TU
TECHNISCHE
UNIVERSITÄT
WIEN

DISSERTATION

Earth-abundant co-catalysts for photocatalytic hydrogen generation

ausgeführt zum Zwecke der Erlangung des akademischen Grades einer Doktorin der Naturwissenschaften unter der Leitung von

Uni. Prof. Dominik Eder
und
Asst. Prof. Alexey Cherevan

E165
Institut für Materialchemie

eingereicht an der Technischen Universität Wien
Fakultät für Technische Chemie

von

Jasmin Sophia Schubert

01500686

Wien, am 30 Oktober 2023

"Success is the ability to go from one failure to another with no loss of enthusiasm"

Winston Churchill

Acknowledgement

Many different people have influenced me on the way until here. From each of them I could learn different things and accompanied me along this way. I learned and improved not only professionally, but also personally. I definitely can say that over the course of these years, becoming a chemist and now a doctorate in natural science, I went through many ups and downs and learned how to deal better with frustration, stress as well as success. Definitely, I would make the same choices again.

Said that, I want to first thank Uni. Prof. Dominik Eder, as he made it possible in the first place that I could do this PhD, offering me the position as an "Universitäts assistentin". In our discussions and meetings, we had our agreements and disagreements, yet in all of them, each discussion, each meeting I got fruitful ideas on how to proceed and continue my work. Also I want to thank him, for the freedom to do almost whatever I wanted. This enabled me to learn by myself many things, such as proposal writing, starting and having collaborations, etc. Thanks a lot.

I also want to thank Asst. Prof. Alexey Cherevan, for his close supervision and always flexible availability during my PhD, always ready to have a meeting when required and questioned the work I presented him, helping me to clarify my thoughts and ideas. Also, and very important, for all and each text writing correction he performed. For being patient in showing me how to write a comprehensive, easy-to-read text. He gave me the basic understanding and tools to become with each text a better writer. But also in showing me tools and tricks to better organize myself and my time. Thanks a lot, as these are gifts for every aspect of my life. Additional thanks for his motivation when I needed it and the fruitful discussion, to be more critical about my initial enthusiasm.

Noelia Barrabés, she always gave me advice on how things could be done, how to write a good proposal, where to go to get information, always positive and easy with thoughts that I had and providing me with tools on how to get there. Also for introducing me to FemChem, from where I learned many things such as organization, coordination among different groups and people and also to rethink what is feminism and about the problems that women have in society.

Markus Sauer and Annette Foelske, first for letting me use the XPS machine as much as I needed/wanted. For their trust. But also, and specially, for their help and always being available when I needed help with the measurements and data evaluation. I definitely learned a lot from them about the XPS method. Furthermore, for trusting me and letting me transfer and show everything I learned about XPS to Hannah Rabl. That was a pleasant experience, as she was an excellent student which I enjoyed showing her everything I know. I'm happy that all I learned can continue to be used by others, so she can start from another starting point than I did, and get better than I was. Thanks Hannah for your motivation and for letting me mentor you with this method.

Stephen Nagaraju Myakala and Pablo Ayala Leiva, both of them for all their help, lab work, extra experiments, etc. that they did during my pregnancy and later when I had to pick up my daughter. This meant a lot to me, the help and support that I got, which enabled me to continue working without getting into a lab. This might look like a minor thing, but for me,

it meant a lot. As being an experimental scientist and pregnant requires the collaboration and cooperation of others, to not fall behind in work. Thanks a lot for providing this to me, as unfortunately, this is not granted.

Shun Kashiwaya for the fruitful discussion and collaboration, even though it hasn't gone in the direction that originally was planned. I definitely learned a lot from his feedback. Werner Artner, for always being ready to help and patient to explain it more than once when required, and for all his XRD expertise. All co-authors of my papers and students for the measurement and material screenings they did. This definitely made my work more efficient and greatly contributed to the finally published papers. The glass-blower for always making quick the required reactors and repairs needed. This means a lot, as work could continue quickly after I broke a reactor or needed a new one. The coffee club, making always sure that coffee was available and ready to make when urgently needed. Also a big thanks to all the taxpayers and the Austrian system, which provided a lot of opportunities to my career. This looks like granted for those who are used to such a system, but definitely is not. In most of the places and countries, even other European countries, this is definitely not the case. And a big thanks to all of them that I haven't mentioned, but have also been there.

And finally, to my beloved life partner, Daniel Moseguí González, and daughter, Iris. Sous el regal més gran de la meva vida, el meu suport, la meva motivació de millorar. Sous la meva família, l'amor de la meva vida. Sense tu, amor meu, no estaria on estic, ja que sempre m'has donat el suport, l'empenta que necessitava, inclús si no estaves d'acord. Cosa que no has dubtat en fer-me saber. Sent sovint un "agua fiestas", confrontant-me amb aquells punts que no havia considerat. Gràcies, amor meu. I la meva filla, la meva vida, que m'ha fet veure, entendré, i col·locar les coses importants i les que no en la vida. Ella està fent que vulgui millorar, perquè ella tingui un millor inici del que he tingut jo. Aquesta tesis doctoral la dedico a aquestes dues persones, les més importants en la meva vida. La meva família. Us estimo. Però també a la resta de la meva família, ja que ells han fet qui soc jo avui. El meu pare i germà, Desmond Schubert, que no han dubtat de les coses que volia fer. Però també la resta, que dubtaven i no creien que podria. Ambdós m'han donat la força d'aconseguir els meus objectius. Estic on estic gràcies a totes aquestes persones i altres que no he mencionat. Gràcies a tots i cada un d'ells.

Contents

i

Abstract

Photocatalytic water splitting is a promising strategy for green and renewable H_2 generation. However, the benchmark materials are still noble-metal-based, which constrains large-scale industrial applications due to their scarcity and, therefore, high costs. Hereby, in this thesis earth abundant Ni, Cu, Fe, Co, and Mn were investigated as co-catalyst for the photocatalytic hydrogen and oxygen evolution reactions (HER and OER). The co-catalyst were analysed and fully characterized to elucidate the effect of post-synthetic calcination on their performance, endorsed by investigating mechanistic changes that affect photocatalytic activity trends.

In the first part of this thesis, we compared Co, Mn, Ni, Cu, and Fe as co-catalysts that were prepared by wet impregnation of the corresponding salts precursors onto model TiO_2 substrate, followed by their calcination. The HER and OER test of the composites revealed that only Cu and Ni are HER active, while Co and Fe are OER active.

In the second part, we examined electronic and structural changes induced by post-synthetic calcination that are in control of the photocatalytic HER activity of the Ni and Cu-based co-catalytic systems. The Cu/TiO_2 photocatalysts – as revealed by a plethora of characterization methods in combination with DFT calculations – showed that by gradually increasing the calcination temperature (from no calcination to 400 °C), a gradual temperature-dependent surface-to-bulk diffusion of Cu – in form of Cu^+ – takes place. This leads to interstitial Cu defects that are associated with the decrease in H_2 generation. In the case of the Ni/TiO_2 photocatalyst – as revealed by long-term HER test (17 h of experiments) – the active Ni^0 HER sites were generated in-situ upon light exposure. A more in-depth analysis, by applying different calcination (non-, 250 and 400 °C) revealed that not only Ni^0 plays a key role in catalysing HER, but rather a combination of Ni^0 and Ni^{2+}. The reaction mechanism involves the dynamic conversion of $Ni^{2+} \leftrightarrow Ni^0$, allowing for efficient H^+ reduction, which is strongly affected by the choice of calcination temperatures. The as-prepared (non-calcined) sample showed a more dynamic $Ni^{2+} \leftrightarrow Ni^0$ conversion, while at 250 and 400 °C, Ni^0 and Ni^{2+}, respectively, was partially stabilized. The loss of the dynamic $Ni^{2+} \leftrightarrow Ni^0$ transformation due to Ni stabilization on the substrate was shown to lead to a drop in the overall potential of the photocatalyst to generate H_2.

In the present thesis, we emphasize the significance and influence of thermal treatments on the dynamic nature of Cu and Ni active state formation and HER mechanism, required to achieve superior HER performances. Herby, our results underline the importance of controlling and optimizing the right synthetic parameters, as thermal treatments can have a detrimental effect on the photocatalytic H_2 evolution performance and co-catalyst active state formation mechanism.

Zusammenfassung

Die photokatalytische Wasserspaltung ist eine vielversprechende Strategie für eine umweltfreundliche und erneuerbare H_2-Erzeugung. Die Referenzmaterialien basieren jedoch nach wie vor auf Edelmetallen, was die großtechnische Anwendung aufgrund ihrer Knappheit und der damit verbundenen hohen Kosten einschränkt. In dieser Arbeit wurden daher die in der Umwelt reichlich vorkommenden Ni, Cu, Fe, Co und Mn als Co-Katalysatoren für die photokatalytische Wasserstoff- und Sauerstoffentwicklung (HER und OER) untersucht.

Die Co-Katalysatoren wurden analysiert und vollständig charakterisiert, um die Auswirkung der postsynthetischen Kalzinierung auf ihre Leistung zu klären und die mechanistischen Veränderungen zu untersuchen, die die Trends der photokatalytischen Aktivität beeinflussen.

Im ersten Teil dieser Doktorarbeit haben wir Co, Mn, Ni, Cu und Fe als Co-Katalysatoren verglichen, die durch Nassimprägnierung der entsprechenden Salzvorläufer auf einem Modellsubstrat aus TiO_2 und anschließender Kalzinierung hergestellt wurden. Der HER- und OER-Test der Materialien ergab, dass nur Cu und Ni HER-aktiv sind, während Co und Fe OER-aktiv sind.

Im zweiten Teil untersuchten wir die elektronischen und strukturellen Veränderungen, die durch die Kalzinierung nach der Synthese hervorgerufen werden und die für die photokatalytische HER-Aktivität der Ni- und Cu-basierten Co-Katalysatorsysteme verantwortlich sind. Die Cu/TiO_2-Photokatalysatoren zeigten - anhand einer Fülle von Charakterisierungsmethoden in Kombination mit DFT-Berechnungen -, dass durch eine schrittweise Erhöhung der Kalzinierungstemperatur (von keiner Kalzinierung bis 400 °C) eine allmähliche temperaturabhängige Diffusion von Cu von der Oberfläche in die TiO_2 Krystallstruktur - in Form von Cu^+ - stattfindet. Dies führt zu interstitiellen Cu-Defekten, die mit dem Abfall der H_2-Erzeugung in Verbindung stehen. Im Falle des Ni/TiO_2-Photokatalysators wurden - wie ein Langzeit-HER-Test (17 Stunden Experimente) zeigte - die aktiven Ni^0 HER-Stellen bei Bestrahlung in-situ gebildet. Eine detailliertere Analyse durch unterschiedliche Kalzinierung (nicht, 250 und 400 °C) ergab, dass nicht nur Ni^0 eine Schlüsselrolle bei der HER-Katalyse spielt, sondern vielmehr eine Kombination aus Ni^0 und Ni^{2+}. Der Reaktionsmechanismus beinhaltet die dynamische Umwandlung von $Ni^{2+} \leftrightarrow Ni^0$, was eine effiziente H^+-Reduktion ermöglicht, die stark von der Wahl der Kalzinierungstemperaturen beeinflusst wird. Die unkalzinierte Probe zeigte eine dynamischere $Ni^{2+} \leftrightarrow Ni^0$ Umwandlung, während bei 250 und 400 °C Ni^0 bzw. Ni^{2+} partiell stabilisiert war. Es wurde gezeigt, dass der Verlust der dynamischen $Ni^{2+} \leftrightarrow Ni^0$-Umwandlung aufgrund der Ni-Stabilisierung auf dem Substrat zu einem Abfall der H_2 Erzeugung des Photokatalysators führt.

In der vorliegenden Doktorarbeit werden die Bedeutung und der Einfluss thermischer Behandlungen auf die dynamische Natur der Cu- und Ni-Aktivzustandsbildung und den HER-Mechanismus hervorgehoben, die erforderlich sind, um überlegene HER-Leistungen zu erzielen. Dabei unterstreichen unsere Ergebnisse die Bedeutung der Kontrolle und Optimierung der richtigen synthetischen Parameter, da sich thermische Behandlungen negativ auf die photokatalytische H_2 Bildung und den Mechanismus der aktiven katalytischen Form auswirken können.

Aim and structure of this thesis

Hydrogen plays a crucial role in our society, being utilized in ammonia synthesis, as a precursor for fertilizer production, and in various industries, including fossil fuel refineries. Moreover, the growing interest in hydrogen as a green and renewable fuel and energy storage system is driving the development of policies to implement it in future societies. In light of this context, this thesis focuses on investigating different photocatalysts capable of synthesizing green hydrogen from water by the use of light energy.

The primary objective of this thesis is to assess the OER (oxygen evolution reaction) and HER (hydrogen evolution reaction) capacity of non-noble metal-based co-catalysts (Co, Fe, Mn, Ni, and Cu) and to determine their active state and reaction mechanism. To achieve this, TiO_2 was employed as a model photocatalyst, and a wide array of analytical characterization methods and theoretical calculations were applied.

The first section of this thesis provides a fundamental introduction and motivation for this research. In the second part, the necessary theoretical background is presented to comprehensively understand the rationale and conclusions derived from the main scientific work, as discussed in the results and discussion section. The third part, being a cumulative thesis, showcases the published manuscripts and highlights their fundamental contributions to the state-of-the-art. Lastly, the fourth and final chapter of this thesis presents the conclusions drawn from the research and outlines future experimental possibilities and open questions for further scientific exploration.

Introduction

Since 1975, the demand for hydrogen has tripled, reaching a current annual demand of 70 million tonnes (Mt) per year (Figure 1.1).[1-3] Its primary uses are in the oil refinery industry and ammonia synthesis, primarily for fertilizers. However, hydrogen is also indispensable in various other industries, including chip manufacturing, chemical manufacturing, and the steel industry.[1,4-6] In recent times, hydrogen has also gained increasing attention in the energy market, finding applications as both a fuel and a chemical energy storage system. As a result, hydrogen has become a cornerstone in modern society, and its importance is expected to grow even further in the future.
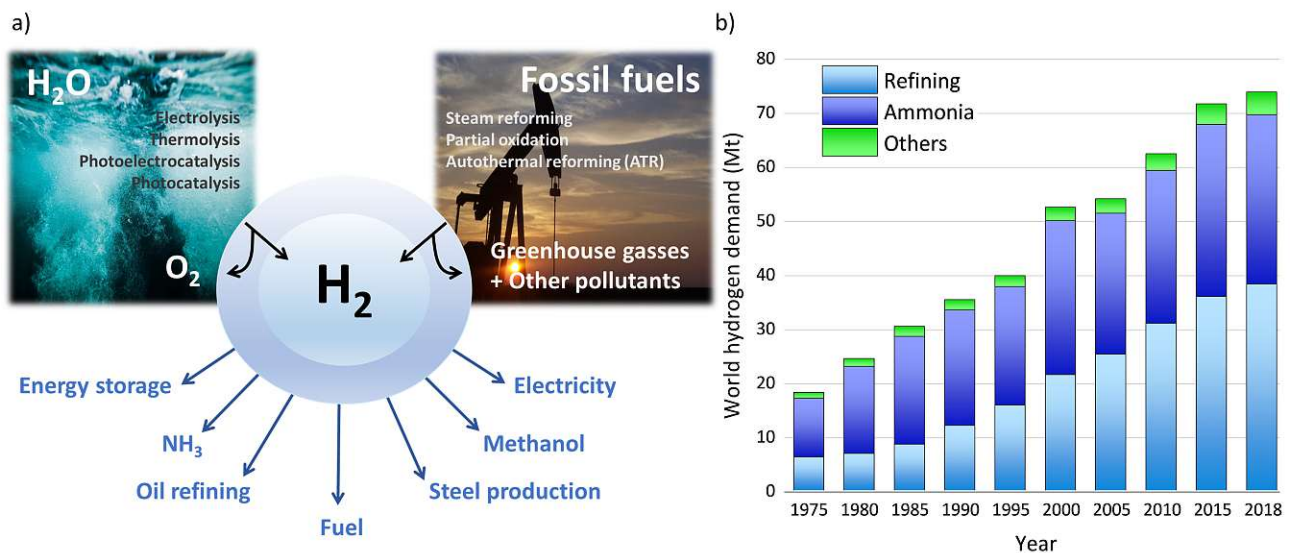

Figure 1.1: a) Hydrogen feedstock and applications. b) World H_2 demand (in million tonnes, Mt) from 1975 to 2018. Data source: IEA, licence: CC BY 4.0.[7]

However, the primary global hydrogen feedstock is still derived from fossil fuels, with the major contributions coming from natural gas (76 %) and coal (23 %), while water electrolysis accounts for a minor share (2 %). As a result, the hydrogen production market is responsible for approximately 830 million tonnes of CO_2 emissions annually, which is equivalent to the combined CO_2 emissions of the United Kingdom and Indonesia. Clearly, there is an undeniable need for increased investment in the development of new technologies for green hydrogen production. In this context, ambitious international climate policies for green hydrogen production have been implemented since 2017.[1-3] The first country with a national hydrogen strategy was Japan, planning to expand its hydrogen production from 2 million tonnes in 2017, to 12 million tonnes in 2040. This expansion involves utilizing hydrogen in fuel cell vehicles, residential fuel cells, and various industries.[8,9] Today, in 2023 the number of countries that implemented a national hydrogen strategy has grown to 30, showing the increasing interest.

1

The demand for hydrogen for fuel applications is also on the rise due to the increasing need for clean and renewable energy sources and storage systems. Molecular hydrogen, H_2, holds immense potential with an energy density of 120 $MJ\,kg^{-1}$, surpassing that of fossil fuels such as methanol or kerosene (19.7 and 43.5 MJ kg^{-1}, respectively).[1,3,10,11] Additionally, the combustion of H_2 produces only clean water, making it pollutant and CO_2 free. The highly exothermic nature of this reaction results in a combustion heat of $1.4 \cdot 10^8\,J\,kg^{-1}$, making hydrogen a promising energy storage solution due to the substantial amount of energy stored in its chemical bonds. Given these advantages, generating hydrogen through the water splitting reaction is a promising approach for green hydrogen production.

Various strategies, such as thermolysis, electrolysis, photoelectrocatalysis, and photocatalysis, can be employed for this purpose.[1,2] Thermolysis uses heat and catalysts to split water. Electrolysis involves using an electric current to crack water molecules. Photoelectrochemical systems can absorb light energy to split water but also require an external voltage contribution to facilitate the process. Hereby, all these systems rely on previously generated electricity for H_2 production. Photocatalysis, on the other hand, combines water splitting and light absorption in the same material, eliminating the need for an external energy source to drive the reaction, making it an all-in-one system.

With these considerations in mind, the focus of this work is on investigating photocatalytic systems for H_2 generation through photocatalytic water splitting, aiming to contribute to the advancement of green hydrogen technologies.

Theoretical background

This section aims to provide the required theoretical background of the data discussed in the results and discussions section.

2.1 Principles of photocatalysis

A photocatalyst is a material able to absorb light, i.e. photons, and use this energy to carry out certain chemical reactions. In 1972, Fujishima and Honda were the first ones to observe this phenomenon.[12] By illuminating with ultraviolet light a TiO_2 electrode – connected to a platinum electrode – they were able to split water into H_2 and O_2. This breakthrough gave birth to the up-to-date field of photocatalysis.

The word "photocatalysis" comes from the Greek word "*photo*", light, and "*catalysis*". The IUPAC defines a catalyst as *"a substance that increases the rate of a reaction without modifying the overall standard Gibbs energy change in the reaction"*.[13] In other words, a catalyst is a substance that affects the rate (kinetics) of a reaction – not being consumed during the reaction – without modifying the thermodynamics. This definition fits with a photocatalyst, as long as the reaction is exergonic ($\Delta G^o < 0$), yet when the reaction is endergonic ($\Delta G^o > 0$) – such as for water splitting or CO_2 reduction – the thermodynamics of the reaction is also altered, as the photon energy is consumed by the reaction without being recovered (see Figure 2.1).[14] Herby, a photocatalyst is not a catalyst in the classical definition. The IUPAC definition for photocatalysis is *"change in the rate of a chemical reaction or its initiation under the action of ultraviolet, visible or infrared radiation in the presence of a substance—the photocatalyst—that absorbs light and is involved in the chemical transformation of the reaction partners"*,[15] i.e. it is a light-driven catalyst, where the photon energy is consumed but the photocatalyst can be recovered after the reaction. For this reason, some authors claim that the term 'photocatalytic' should be corrected to only apply when a downhill reaction is carried out ($\Delta G^o < 0$) and 'photo-synthetic' when the reaction is uphill ($\Delta G^o > 0$).[16,17] In this thesis, however, we used the term photocatalysis, as it is the term by far most often used in the community for photocatalytic water splitting.

2.1.1 Photosynthesis as inspiration

Over millions of years, nature has learned and optimized how to store sunlight energy in chemical bonds with photosynthesis. As a general idea, plants and other organisms store the photon energy from sunlight in chemical bonds. With this strategy, they are capable to power uphill reactions – i.e. thermodynamically endergonic ($\Delta G^o > 0$) reactions – to convert CO_2 and H_2O into carbohydrates. With that, even though the maximum efficiency is approximately 11 %, the yearly amount of energy stored by photosynthesis is about three times the global power consumption.[18,19]
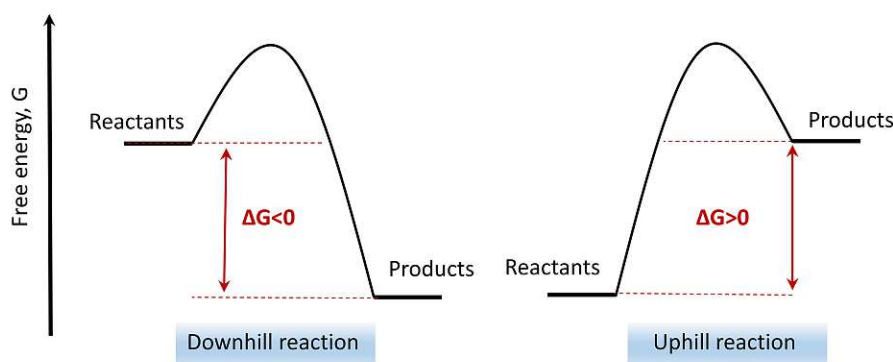
Figure 2.1: Energy diagram of a downhill and uphill reaction.

Nature accomplishes this task through a well-engineered assemblage of pigments, molecules, and proteins.[19,20] Although there are substantial differences among the different photosynthetic organisms, this process can be summarized in the need for an efficient energy flow, electron flow and certain chemical reactions. For simplicity, we will use the discussion of the oxygenic photosynthesis, used by most of the plants. This includes mainly two key components, PSI (photosystem I) and PSII (photosystem II). When a photon hits the PSII an electron is excited, and extracted by a cascade of molecules – losing a certain amount of the energy – that transfers it to the PSI. Once there, another photon excites this electron and by a new cascade of molecules this electron is extracted and finally used in the synthesis of NADPH, an intermediate molecule to store that highly energetic electron. Ultimately, the electron (in form of NADPH) is then used in the Calvin cycle to generate carbohydrates from CO_2. To start the whole process again, however, PSII needs to recover that lost electron. This is achieved by splitting water, carried out by a Mn cluster – called oxygen-evolving complex (OEC) – with an overall reaction

$$2\,H_2O \xrightarrow{\text{hv}} O_2 + 4\,e^- + 4\,H^+$$
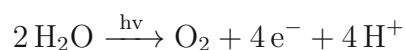
Since the photosynthetic system shows to be robust, enabling the capture of photons and storing them in chemical bonds, scientists have the dream to replicate it, emerging the field of artificial photosynthesis.[21] A term used for all kinds of systems that can capture and store energy from sunlight in a chemical bond. Photocatalysis, thus, is a major research topic of artificial photosynthesis.

2.1.2 Material requirements

A photocatalyst to be a light-driven catalyst, it needs to be activated under light; while under dark conditions, it should be inactive. This requisite can be achieved with a material that has an energy gap between the highest occupied and lowest unoccupied electronic levels, such as a semiconductor.[22,23] This bares the intrinsic property of having a band gap and; thus, a certain energy has to be surpassed to bring an electron from the valence band (VB) to the conduction band (CB). This required energy can come from many sides, one form is electromagnetic radiation. Yet, the required energy has to be above this band gap. Accordingly, to carry out a photocatalytic reaction, 4 steps are required (see Figure 2.2): (1) light absorption to generate an electron-hole pair (exciton), (2) separation of the excited charges, (3) transfer of the electrons/hole to the photocatalyst surface, and (4) utilization of the charges on the surface for a certain chemical redox reaction.[19] The reaction efficiency, thus, is limited by the incident photon flux, the light absorption, the exciton lifetime, and the catalytic active sites of the material. A good photocatalyst should ideally fulfil all these requirements. These points, however, are often in contradiction, as for optimal light absorption the band gap of the semiconductor

should be small, yet, to carry out most of the reactions greater energy is necessary. Thus, a large band gap would be required. Furthermore, to obtain optimal performance, an active surface is necessary, yet such surface could also be more prone to photocorrosion events, and thus is less stable. Additionally, large exciton lifetimes are required, so the excited charges can migrate to the catalyst surface to perform the required reaction, without recombining before. All these aspects, are just to mention some. To overcome these issues, however, two approaches are possible: homogenous and heterogeneous photocatalysts, which will be discussed in the next section.
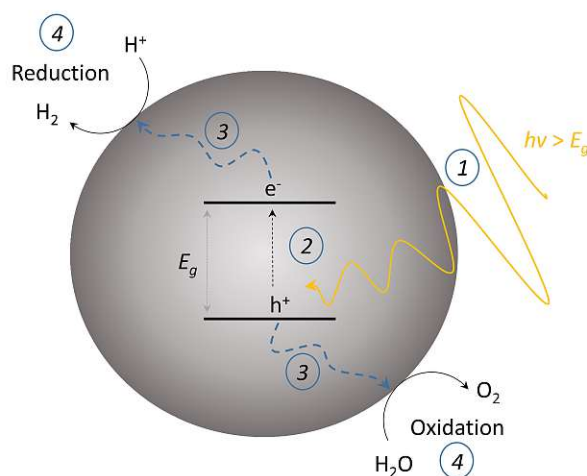

Figure 2.2: Photocatalytic process on a semiconductor, showing the four steps required for a photocatalytic reaction: (1) light absorption, (2) exciton generation, (3) diffusion of the excited charges to the surface and (4) the corresponding chemical reaction.

2.1.2.1 Heterogeneous vs homogeneous photocatalysis

The photocatalytic process may be homogeneous or heterogeneous, depending on the photocatalyst type.[24,25] For the homogeneous approach, both catalyst and reaction medium are in the same phase – for instance, the photocatalyst is a molecule (usually transition metal complexes) dissolved in the reaction solution. The heterogeneous approach is when they are in different phases. For example, the photocatalyst is a nano-particulate powder suspended in the reaction solution.

An ideal photocatalyst, as we have seen before, should fulfil at least three requirements: (I) efficient light absorption (ideally broad and in the visible range), (II) high photocatalytic activity and (III) stability towards photocorrosion.[19] With this in mind, the homogeneous photocatalyst show different drawbacks. Only a small portion of the spectrum can be absorbed, as the HOMO-LUMO levels are well-defined.[24,26] They generally show rapid deactivation and degradation, due to the molecular nature of the photocatalyst, as well as, limited re-usability after reaction, due to great solubility of the molecular photocatalyst in the reaction solution. In contrast, the heterogeneous approach enables a broader light absorption, as the VB and CB are composed of a density of states. They bear greater stability towards photocorrosion/photodegradation, as well as, a higher degree of re-usability.

In the heterogeneous photocatalyst, after excitation by electromagnetic radiation, an exciton is generated, which needs to migrate to the surface to react with the reactants.[19] On this way, many charge recombination issues can take place induced by defects (that can act as charge recombination centres), long migration path (increasing the recombination probability), strong coulomb forces between the electron-hole pair (inhibiting long migration paths and favouring

charge recombination), etc.[17,19] All these phenomena can substantially lower the photocatalyst efficiency. Concomitantly, the ideal photocatalyst (efficient light absorber, high activity and stable), is a challenging task, and engineering of all these parameters is of uttermost importance to achieve high performances.

2.1.2.2 Engineering of photocatalytic efficiency

There are several ways to engineer the photocatalyst's performance by effectively improving charge extraction and preventing recombination.[17,19,27,28] Some of those approaches are by reducing the photocatalysts size and using co-catalyst. The photocatalysts size has an effect on the photon absorption and on the charge recombination phenomena.[19,27–29] Domen et al. showed with theoretical calculations the smaller the particle size is – assuming a spherical shape –, the fewer photons strike the material. This enhances greatly the performance, as the excited charges can react with the reactants before the next exciton is being generated. Thus, leading the improved efficiencies due to more efficient charge extraction by the reactants. Further advantage of reducing the photocatalyst size is that the excited charges can reach the surface much quicker, and, thus, reducing drastically the charge recombination probability. Another approaches to enhance photocatalysts efficiency, is using co-catalysts. They are capable of effectively extracting generated charges – acting as an electron sink – inhibiting charge recombination.[30–32] Additionally, co-catalyst can fine-tune and enhance the catalytic active site, by lowering the activation energy, separating the redox reactions and improving selectivity for certain chemicals.[33,34] This leads to improved stability, as the chemical reaction is taking place on the co-catalyst and not on the semiconductor.[34] Additionally, broader light absorption can be achieved, if the co-catalyst is a semiconductor that enables light absorption, or due to plasmonic effects.[19,33] Hence, the use of a nanoparticulate photocatalyst and co-catalyst can greatly enhance photocatalysts performance.

2.1.2.3 Thermodynamics of interfaces

A hybrid heterogeneous photocatalytic system that involves a combination of a semiconductor and a co-catalyst, will generate an interface between the two material, that comes along with different physical properties than the corresponding bulk material.[19,22,33,35–39] This will generate new energy transfer and exciton migration processes. Hence, the interface plays a key role in charge management, and; thus, being in control of the interface engineering is crucial for photocatalytic efficiency.

Different kinds of heterostructured interfaces will exist depending on the materials' combination (Figure 2.3a):[22,33,35–40] (a) semiconductor/semiconductor interface (between different semiconductors), (b) metal/semiconductor interface (when a semiconductor and a metal are combined), or a (c) semiconductor/electrolyte interface (when a semiconductor is in solution with dissolved electrolytes). At these interfaces, charge transfer processes will take place until reaching an equilibrium situation where the Fermi levels are equilibrated, i.e. same energy level (Figure 2.4). 1.6This new situation will lead to a positively charged area (depleted of negative charges) and a negatively charged area (depleted of positive charges), called the depletion layer. In consequence, a dipole is generated, building an internal electric field (E-field) and inhibiting – in equilibrium situation – the flow of electrical charges. Yet, under illumination, electrons and holes can bypass this potential barrier and a net-one directional electric charge transfer takes place. This enables efficient charge extraction and restricts charge recombination. However, there are differences among the systems by combining different materials.

We can differentiate between three types of semiconductor/semiconductor interface (Figure 2.3b).[33,35,36,39,40] In Type I (straddling gap), two semiconductors (A and B) are combined with one having a smaller band gap, being the CB of semiconductor A above semiconductor
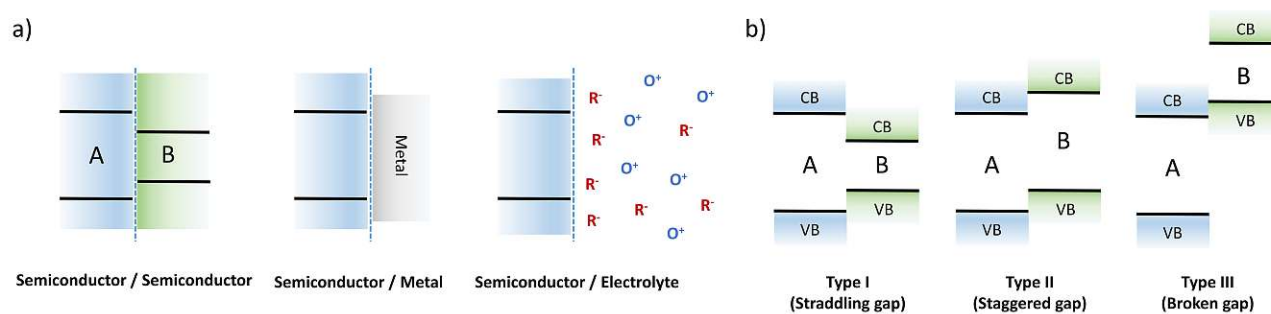
Figure 2.3: a) Schematic representation of a semiconductor/semiconductor, semiconductor/metal and semiconductor/electrolyte interfaces. b) Semiconductor junction types.

B, and the VB of A below B. Here, both charges – electron and hole – are extracted from semiconductor A to B. Accordingly, not achieving selective charge extraction to avoid charge recombination. Yet, this approach can be useful, to combine a more catalytic active material with a better light absorber. In a more common Type II (staggered gap), the CB and VB of the semiconductor A are above B, enabling electron migration from A to B, and the holes from B to A, due to the internal electric field that is generated effectively extracting and separating the generated charges. Furthermore, the chemical reactions are also carried out on the different semiconductors. Hereby, enabling the separation of the catalytic active side too. Type III (broken gap), is the same as type II, but with the difference that the VB and CB offset is much greater. In all three types, band alignments and the equilibration of the Fermi level occur at the semiconductors interface. For instance, when a p-type and n-type semiconductors are combined (i.e. a p-n junction), their Fermi levels will equilibrate until they reach the same level. Consequently, band bending of the CB and VB occurs – by the same proportion as the Fermi level difference ΔE_F – generating a potential barrier (Figure 2.4a). As a result, a depletion layer and an internal electric field are formed, enhancing charge separation in one direction upon illumination of the semiconductors.

The metal/semiconductor junction is generated by combining a metal – generally as a co-catalyst, such as Pt, Au, or Pd – and a semiconductor (see Figure 2.4c and d). Again, the Fermi level of the semiconductor and the metal equilibrate, generating band bending of the CB and VB of the semiconductor. This can result in two situations, depending on whether the semiconductor is an n- or p-type.[14] Downward band bending for an n-type/metal interface, and upwards band bending for a p-type/metal interface. This leads to a depletion layer at the interface – forming a potential – which inhibits charge backflow from the metal co-catalyst to the semiconductor (Schottky barrier, Φ_{SB}). Hereby, enabling effective charge separation

The semiconductor-electrolyte interface is built when a semiconductor is in a suspension with a dissolved electrolyte (Figure 2.4b). This situation is similar to the semiconductor/metal interface, yet with the difference that the electrolyte electrons are not free to move – like in a metal – and instead they are localized on the ions. Hereby, the reducing ion (R) bares the electrons, while the oxidizing ion (O) bares the holes. The relative position of the Fermi levels (the equivalent of the electrochemical potential of the reacting ions) determines what will happen between the semiconductor and the electrolyte. If the Fermi level of the semiconductor is above the Fermi level of the electrolyte, then electrons will be transferred until reaching equilibrium, leading to a depletion layer in the semiconductor, and the same situation as explained previously. However, in this situation to carry out chemical redox reactions, also the CB and VB position play a key role, as the CB minimum has to be above (i.e. more negative) than the reduction potential of the desired reaction, while the VB should be below (i.e. less negative) than the oxidation potential – resembling a type I junction – to carry out the reaction. More details will be explained in the following section.
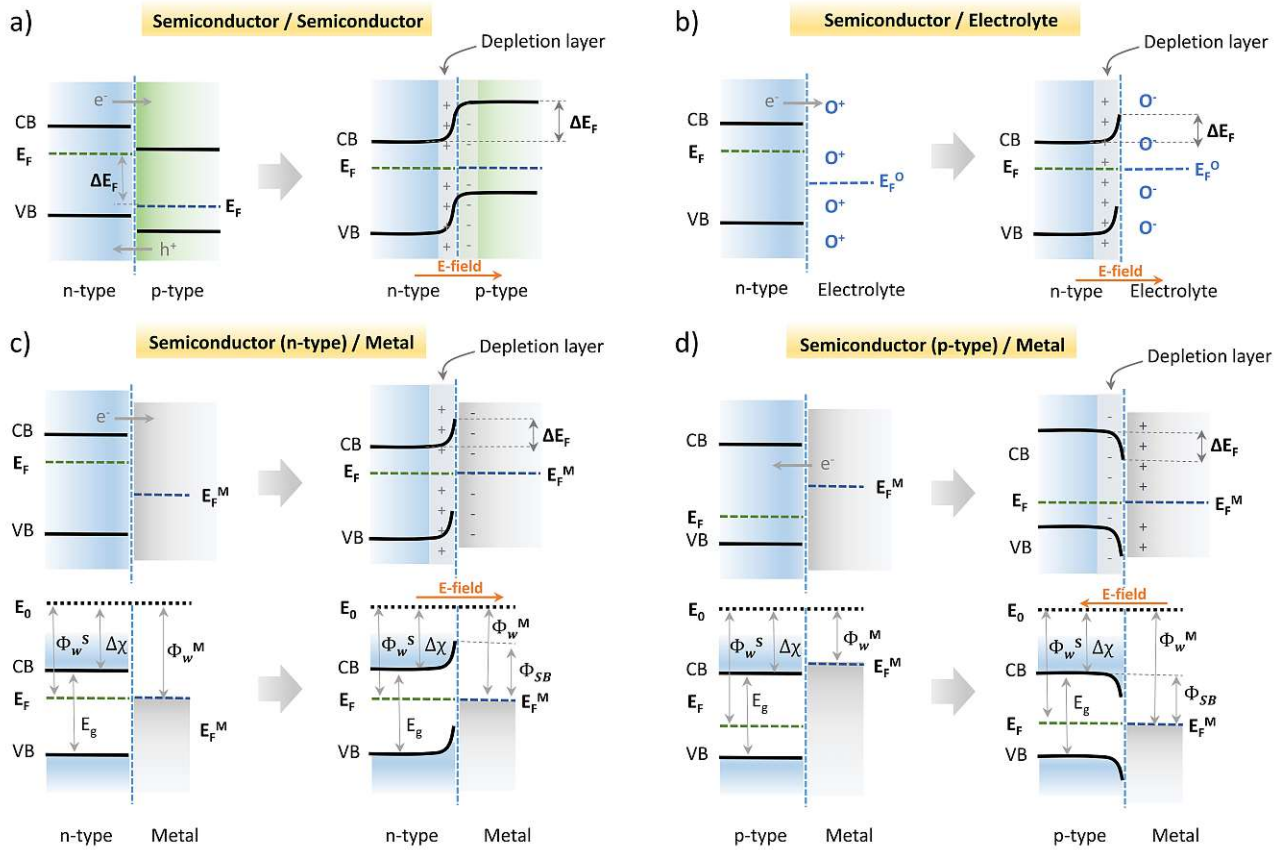
Figure 2.4: Schematic representation of the band diagrams generated at the interface by the different material's combination. E_0 Vacuum level; $\Delta\chi$ Electron Affinity; Φ_{SB} Schottky barrier; Φ_W^S and Φ_W^M Work function of the semiconductor and metal, respectively; E_g Band gap; E_F and E_F^M Fermi level of the semiconductor and metal, respectively; CB and CV Conduction and Valence Band, respectively; E-field electrical field.

In summary, depending on the material combination, we will have different physical properties at the interface, affecting the charge transfer process and; thus the overall photocatalytic performance.

2.2 Photocatalytic hydrogen generation

2.2.1 Reaction requirements

In order for a particular reaction to occur, it is required a total energy (E) that is at least equal to the sum of the standard free energy (ΔG) and the activation energy (E_a) of the overall reaction (i.e. the reduction and oxidation reaction, respectively),[19,27,41–43]

$$E \geq \Delta G + E_a \tag{2.1}$$

Thus, a thermodynamic and a kinetic factor needs to be bypassed (Figure 2.5a and b). Therefore, the photocatalyts band gap and its associated VB and CB positions (i.e. the energy difference between the electron and hole) are crucial in enabling the photocatalyst for a particular chemical reaction (Figure 2.5c). For the photocatalytic water splitting reactions, this would require a theoretical band gap of the semiconductor >1.6 eV.[19] However, due to kinetic overpotential requirements, the minimum required band gap would rather be 2.0 eV. Furthermore, the VB has to be more positive than the required oxidation potential (O_2 / H_2O, 1.23

V vs. NHE at a pH 0)), and the CB minimum needs to be more negative than the required reduction potential (H^+/H_2, 0.00 V vs. NHE at a pH 0). Thus, for photocatalytic water splitting (and any other reaction), the semiconductor band gap and the VB and CB positions are of paramount importance.
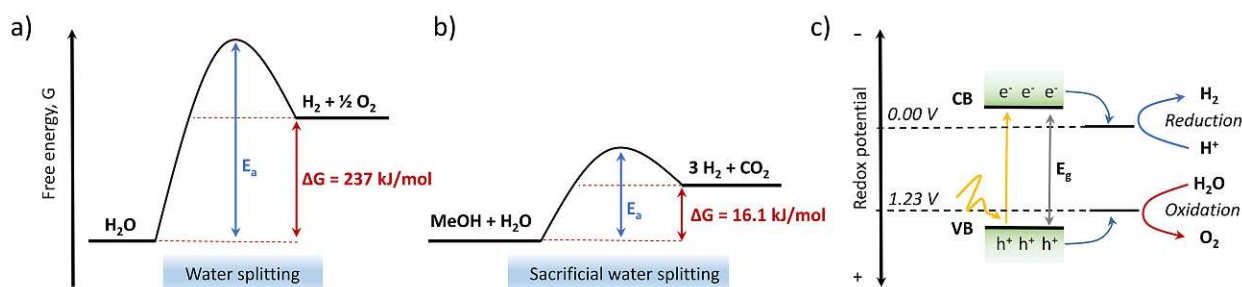

Figure 2.5: Schematic representation of a) energy diagram of the water splitting reaction, showing the Gibbs free energy (ΔG) and the activation energy E_a, and b) band diagram requirements for the water splitting reaction.

2.2.2 Sacrificial vs overall water splitting

The overall water splitting reaction, as a main source for clean and renewable H_2 with photocatalysis, is a challenging task.[19, 22, 27, 44] The main reasons are the intrinsic constraints of the photocatalyst (catalytic active site, charge recombination problems, light absorption efficiencies, etc.), explained in previous sections, and the nature of the reaction itself. The main reaction obstacles are (a) thermodynamic limitations, being water splitting an uphill reaction that requires a free Gibbs energy of 231 kJ/mol (see Figure 2.5a); thus, (b) the back reaction of H_2 and O_2 to H_2O is much more favourable, leading to a considerably lower amount of H_2 to be generated; and (c) both reduction and oxidation reactions,

$$2\,H^+ + 2\,e^- \longrightarrow H_2 \tag{2.2}$$

$$2\,H_2O + 4\,h^+ \longrightarrow 4\,H^+ + O_2 \tag{2.3}$$
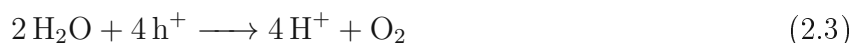
are multistep reactions, involving 4 holes for the oxidation reaction – being the main bottleneck – and 2 electrons for the reduction reaction. One strategy to bypass some drawbacks of the overall water splitting reaction is using sacrificial agents, such as methanol (MeOH).[44–47] In this setup, called sacrificial water splitting, a mixed solution of MeOH and H_2O is used (reaction 2.4),

$$H_2O + CH_3OH \longrightarrow CO_2 + 3\,H_2 \tag{2.4}$$

The advantage of sacrificial water splitting is a much lower Gibbs free energy (16.1 kJ/mol) due to the more favourable CO_2 generation (figure 2.5b); restriction of the back reaction, as CO_2 instead of O_2 is generated (see reaction 2.4); and decreased charge recombination by a more efficient hole extraction by MeOH and/or water (different mechanism have been proposed, dependent on the photocatalyst system used, MeOH concentration, the used co-catalyst and the amount of co-catalyst).[44, 47, 48] Thus, sacrificial water splitting is a widely extended method to investigate a photocatalyst for its HER capacity.

2.3 State of the art of the used materials

2.3.1 TiO₂ as water splitting photocatalyst

For photocatalytic water splitting, TiO_2 has the right band gap (above 2.0 eV) and the right VB and CB edges position – more negative than 0 eV (H^+/H_2) and more positive than 1.23 eV (O_2/H_2O), respectively.[27,49,50] Furthermore, TiO_2 bares great advantages due to high stability in different environments, low cost, non-toxic, excellent optoelectronic properties and high versatility.[38,41–43,51,52] For this reason, TiO_2 – an n-type semiconductor – is widely investigated, and not only for photocatalytic water splitting but also for many other applications (self-cleaning materials, photodegradation of pollutants, photocatalytic dye degradation, etc.).[53]

TiO_2 exists in nature in three crystalline structures. Mainly anatase, brookite and rutile. Anatase and rutile have a tetragonal crystalline form, while brookite is orthorhombic.[54] All three polymorphs are photocatalytically active, even though most of the research is done on rutile and anatase (the most active one). The band gap of anatase is 3.2 eV, while for rutile it is 3.0 eV, being the minimum required λ to generate an exciton 387 nm and 410 nm, respectively.[55] This means that both TiO_2 crystalline structures are only capable of absorbing light in the UV range. Additional drawbacks are short exciton lifetimes, i.e. quick charge recombination.[41,52] Many efforts, however, have been done to overcome these issues, such as doping, combining with other semiconductors or metals, and other structural changes.[38,42,43,55] For instance, combining anatase and rutile, or the use of a co-catalyst, has greatly improved charge recombination issues. In both cases, a heterojunction is generated that enables effective charge separation. Additionally, the use of different polymorphs and co-catalyst add new catalytic active sides, further improving the performance. Another approach has been shifting the light absorption into the visible range, by methods such as doping (adding new energy levels in the band gap), combining it with other light absorbers with a lower band gap (photosensitization) or the creation of different morphological structures (such as nanoporous thin films, nanobelts, thin films, nanotubes, spheres, nanorods, etc.), to mention few.[51,53] For all these reasons, and the great amount of work invested, TiO_2 is a good model material to investigate the effect of co-catalyst.

2.3.2 Transition metals as co-catalysts

The advantage of using co-catalyst to enhance photocatalytic performance are many, as co-catalyst are able (1) to reduce the overpotential required for the H_2 generation, (2) enhance the reaction selectivity, (3) suppress charge recombination by effectively extracting the photo-generated charges and (4) bare the potential to increase the hydrogen production dramatically by suppressing the back reaction of H_2 and O_2 to H_2O.[55,56]

The most efficient and highly investigated co-catalysts are noble metals such as Pt, Pd, Au, Rh and Ag.[39,55–57] These metals have the advantage of an inherent low overpotential for the HER, thus enabling this reaction with much more efficiency, than, for instance, pure TiO_2.[55,56] Unfortunately, noble metals are rare and expensive, limiting large-scale industrial applications. That means cost-efficient and widely available alternatives are greatly needed. Promising results have given metals such as Ni, Cu, Fe or Co, to mention a few.[56] However, there are huge discrepancies in the scientific community about the catalytic active state of each metal, or which is the best metal as a co-catalyst.[56,58,59] This is because the photocatalytic efficiency enhancement using a co-catalyst is highly affected by the deposition method, the amount of co-catalyst loaded, the distribution, particle size and the chemical nature of the ultimate active form of the metal.[34,55] In this thesis, the focus was to compare and investigate Ni, Cu, Fe, Mn and Co as co-catalyst for photocatalytic H_2 generation. Hereby, the following

section will provide a concise literature overview that demonstrates the potential of these metals as co-catalysts for photocatalytic water splitting reactions. However, as manuscript No. 1 (results and discussion section) was dedicated to compare the hydrogen-generating capacity of Ni, Co, Mn and Fe; and because manuscript No. 2 and No. 3 were entirely dedicated to Cu and Ni, respectively – as only Ni and Cu showed to be HER active – we will dedicate separate sections for Ni and Cu, and another for Fe, Mn and Co together.

2.3.2.1 Ni as co-catalysts

Ni as a co-catalyst is widely reported in many different systems (different chemical forms, substrates, etc.) to enhance the photocatalytic performance.[58,60–63] Several works have tried to elucidate the catalytic active state of Ni. For instance, Chen et al.[64] showed that the previous reduction of NiO to Ni^0 on a TiO_2 substrate, leads to a remarkable increase in the amount of hydrogen generated, concluding, that the active Ni form is Ni^0. Indra et al.[65] came to similar results by using in-situ EPR – even though graphitic carbon nitride (g-CN) was used as the semiconductor substrate. The authors, further show that the photo-excited electrons in the g-CN CB reduce Ni^{2+} to Ni^0 and consequently reduce the H^+ to H_2. Yu et al.[66] investigated $Ni(OH)_2$ on TiO_2 coming to the same conclusion. Lv et al.[67] elucidated by a plethora of methods, that Ni is attached in form of Ni^{2+}-O to the TiO_2 lattice. Again, they claimed that the excited electrons in the CB are responsible for the H_2 production, even though without specifying if Ni^{2+} gets reduced or if Ni is actively participating in the reaction. In summary, the general consensus is that the photoexcited electrons upon illumination are transferred from the conduction band to the attached Ni species, forming metallic Ni, which then react with the protons and form H_2. Therefore, being the photocatalytic active form for hydrogen generation Ni^0. However, to which degree metallic Ni and/or Ni^{2+} is required and the question of the role that each of Ni's oxidation states play, has not been addressed so far. Hereby, further research is needed to fully understand and elucidate which role plays the different Ni oxidation states to achieve maximum performance.

2.3.2.2 Cu as co-catalysts

Photocatalytic hydrogen production improvements have also been archived employing Cu as co-catalyst.[57,58,68] Cu can exist in nature in three stable oxidation states Cu^0, Cu^+ and Cu^{2+}, and has been used as a co-catalyst in many different forms - CuO, Cu_2O, $Cu(OH)_2$, incorporated in the substrate lattice, attached on the surface, etc. – all showing an increase in the overall hydrogen generation, compared to the bare semiconductor (such as TiO_2). However, which is the photocatalytic active form or structure of Cu is strongly debated. For instance, Zhang et al.[69] investigated Cu single atoms on TiO_2, where Cu^{2+} was photoreduced to Cu^+ and then reducing H^+ to H_2. Lee et al.[70] and Wu et al.[71] came to similar results, attributing the increased hydrogen production to Cu^+. However, Wu et al., further claimed that a higher amount of Cu^{2+} had a detrimental effect, while Cu^0 had no apparent impact (even though possibly enhancing electron extraction and transfer). Yet, other studies have shown a positive effect of the use of metallic Cu, due to the generation of a Schottky junction, enhancing the charge extraction.[72–77] Thus, the ultimate Cu form – location, oxidation state, chemical environment, etc. – to enhance photocatalytic hydrogen generation is strongly debated in the scientific community, making it imperative to conduct more dedicated studies.

2.3.2.3 Fe, Co and Mn as co-catalysts

While for Cu and Ni as co-catalyst for photocatalytic H_2 generation plethora of publications are found in literature, for Fe, Co and Mn the amount of research is much less extensive,

especially for pure metals or oxides.[34] However, as a dye or organic pollutant degradation photocatalysts, much more research can be found.[68] In this thesis, we investigated the co-catalyst ability and effect on the H_2 generation capacity. Hereby, we will discuss and present only the research related to the hydrogen evolution reaction. Along these lines, Fe revealed to improve the photocatalytic H_2 performance by the synthesis of a double-core-shell nanocomposite by using $Fe_3O_4@C@TiO_2$, or the fabrication of a $FePS_2$ nanosheet anchored on TiO_2 nanoparticles forming an s-scheme heterojunction.[78,79] Other hybrid systems were synthesized by combining TiO_2 with an iron-titania mixed oxide on graphene oxide sheets, or FeO doped TiO_2 onto fibrous annealed carbon.[80,81] Tada and co-workers archived increased activities by attaching FeO_x on TiO_2.[82] All these systems, show the potential of Fe to enhance the H_2 generation under visible light, as well as effective charge extraction.

Cobalt-based co-catalysts for HER in different forms and systems have also given promising results.[34] For instance, Co_3O_4 is widely used in hybrid systems, such as p-n junctions, to enhance photocatalytic performance. For example, Si et al.[83] anchored Co_3O_4 clusters to 2D ultra-thin TiO_2 nanosheets. In this system, Co was reduced to metallic Co by electrons transfer from the TiO_2-CB, leading to comparable HER values to Pt. Chen et al.[84] investigated Co_3O_4/CdS/$SrTiO_3$ core-shell junctions, revealing improved performance due to the variable oxidation state of Co, accelerating the h^+ migration in the ternary system. Other authors used Co single atoms – acting as the catalytic active side and attached to TiO_2 nanosheets – to enhance the hydrogen evolution reactions.[67,85] These studies, show the variety and capability of Co-containing photocatalysts for the HER.

The use of manganese, whether in its pure oxide or metal form, however, is not widely studied as a HER co-catalyst, but it is rather used for the oxygen evolution reaction, such as in photosynthesis as a Mn_4CaO_x cluster.[34] Also, Fe and Co have shown promising results for the OER.[34,86–88] For instance, Li and coworkers synthesized a system containing MnO_x attached to a hollow sphere TiO_2.[89] The authors used MnO_x for the OER and Pt for the HER, generating a spatial separation of the two catalytic centres, as Pt was on the inside of the sphere and MnO_x on the outer side. Liu et al.[88] attached different metals (MnO_x, FeO_x, CoO_x, NiO_x and CuO_x) on TiO_2 nanosheets, and investigated the samples for OER, showing the highest performance for Co and Mn loaded TiO_2, with activities even higher than Ru and Ir. Other authors used these metals for band gap engineering, shifting the adsorption edge to the visible light range by doping TiO_2 with Fe^{3+}, Mn^{3+} or Co^{3+}.[87] Thus, Fe, Co and Mn are promising candidates to enhance the photocatalytic performance as a co-catalyst for photocatalytic water splitting for both half-reactions.

Methodology

The aim of this section is to complement and provide a broader understanding of the data and reasoning conceptualized in each manuscript in the results and discussion section, as well as to provide the details of the used setup development and optimization. For this reason, the corresponding chemicals used, the synthesis details of the corresponding photocatalyst and the exact machine used (with the corresponding measuring setup details) are found in the corresponding sections in each manuscript.

3.1 Photocatalytic setup

In this thesis, we used a gas flow in-situ detection system (figure 3.1). This setup has the advantage that H_2 – and other gases – can be detected in-situ – and simultaneously – over a prolonged time, enabling to investigate reaction activation/deactivation kinetics, overall reaction mechanisms, photocatalyst lifetimes and each change that happens to the system over time. This is not possible with the standard gas chromatographic method used in the community, as the gas to be analysed needs to be injected manually from the reactor. Thus, only the amount of H_2 can be evaluated, but not the dynamic nature of the process.

To investigate the hydrogen evolution reaction (HER) upon time, we used the standard method established in our group – engineered by previous colleges in their corresponding PhD thesis – and we designed and optimized a new setup for the specific experiments carried out in this thesis. The details of the standard method and the developments of the new photocatalytic setups will be discussed in this section.
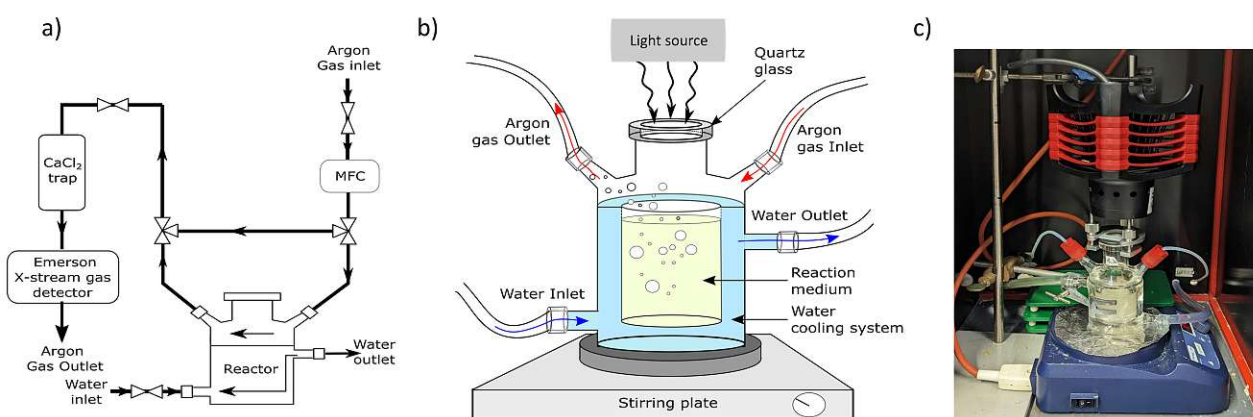

Figure 3.1: Schematic of the standard HER detection system. a) Schematic of the experimental setup. MFC: Mass flow controller. b) Schematic of the custom build glass reactor. c) Photo of the reactor setup showing the Thorlabs LED light source, the glass reactor, stirring plate and the black box where the experiments are carried out.

3.1.1 The standard photocatalytic setup

3.1.1.1 The reactor

The photocatalytic HER experiments were carried out in a custom-built flow reactor, enabling the in-situ detection of hydrogen. The reactor, shown in Figure 3.1, was designed with two necks – serving as in and outlet of the carrier gas, argon (Ar) – and a top illumination made of quartz (material transparent to UV light). The reactor is equipped with a water-cooling jacket around the reaction solution to maintain a constant temperature – aided with a cryostat – during reaction.

3.1.1.2 The excitation light source

The excitation light source used in this thesis, shown in figure 3.1c, was a SOLIS-356C LED lamp from Thorlabs with an excitation wavelength of 365±20 nm, and a 3.0 W minimum and 4.0 W maximum collimated power output. The maximum current of the LED lamp is 4500 mA, with a forward voltage of 4.0 V and a bandwidth (FWHM) of 10 nm. The maximum irradiance – at a distance of 20 cm from the light source – was measured to be 2.8 mW/mm^2.

3.1.1.3 The detector

The detector used for the in-situ H_2 detection upon experimental conditions is an Emerson X-Steam analyser able to simultaneously detect H_2, CO, CO_2 and O_2 by three different integrated detectors. A thermal conductivity detector (TDC, for the H_2 detection), a photometric non-dispersive IR sensor (for the CO and CO_2 detection) and a paramagnetic O_2 detector (for the O_2 detection).

3.1.2 Development of photocatalytic setups

In the photocatalytic water splitting process, two chemical species are generated: H_2 (HER) and O_2 (oxygen evolution reaction, OER). Yet, to investigate the OER our standard method bares the intrinsic problem that the reactor setup is not completely airtight, condition necessary to detect the generated O_2 by the investigated system. Thus, to accomplish the work in this thesis, we needed to develop a new detection system to reliably evaluate the OER rate from our samples under investigation (OER experiment in manuscript no. 1). Additionally, determining the HER rate over a prolonged time range, revealed to be challenging with the standard setup used in our laboratories, as the system revealed to have leaks. This was not relevant for short therm experiments (< 3 h), yet for longer experiments, such as 17 to 24 h, this had a substantial effect on the baseline. Thus, the system needed optimization to enable reproducible and reliable experiments (HER experiment in manuscript No. 3). The creation of a new setup and optimization of the existing one was – as always in science – not done alone, instead with the collaboration of my colleagues Sreejith P Nandan (for OER setup) and Stephen Myakala (for HER setup).

3.1.2.1 Experimental setup for the O_2 evolution reaction rate detection

For the OER rate determination we designed a new photocatalytic setup with a new O_2 in-situ detection system. For the detector, we used an optical oxygen meter (FireStingO2, Pyroscience, Germany) with a needle-like oxygen-sensitive optical sensor (OXF900PT-OI) that could collect data with intervals of one second (figure 3.2).[90] The O_2 detection is based on the luminescence quenching of the REDFLASH indicator by O_2. As more O_2 is present in the system, more will the luminescence of the dye indicator be quenched. The amount of O_2 is then provided in

%. This detection system provides the advantage that O_2 can be detected in-situ inside the reactor (in its head space) with high precision, high reliability, low power consumption, low cross-sensitivity and fast response time.
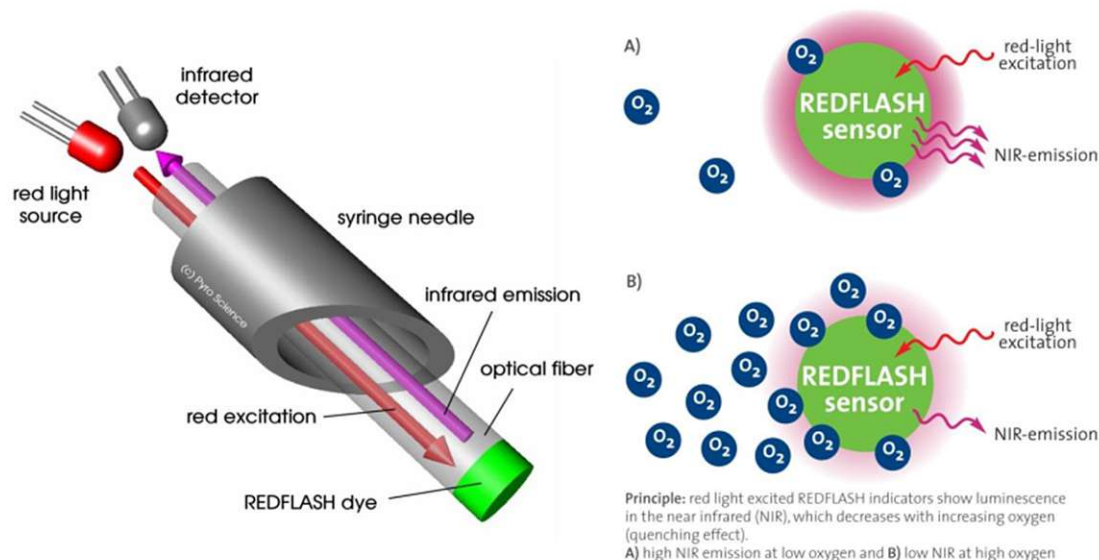

Figure 3.2: Schematic of the OER detection system showing the working principle of the optical sensor and the REDFLASH indicator (Image taken from Pyroscience GmbH[90]).

To convert the O_2 % to μmol we first needed to determine how much O_2 % corresponds to how much μmol of O_2. For this, we injected 100 μL of air with a Hamilton syringe into the reactor, previously purged with Ar (repeating this step several times to obtain an analytically accurate value). In the particular case of our OER reactor, this injected amount corresponded to 0.53 O_2 %, which could be translated to 20.66 μL (amount of O_2 in air) of O_2. Thus, to convert the experimental O_2 % values to μL we used the factor,

$$\mu\text{L } O_2 = \text{X}(\%) \frac{20.66}{0.53} = \text{X}(\%)\, 38.98, \qquad (3.1)$$

where X is the experimental value obtained. Then, to convert this value to μmol we used the ideal gas equation,

$$n(\mu mol) = \frac{V(\mu L)P(mbar)}{R(Lmbar/molK)T(K)}, \qquad (3.2)$$

where V (volume) are the obtained value from the experiment, P (pressure) and T (temperature) are constant values set by our experimental conditions, and R (the gas constant) is a constant.

For the reactor vessel, we needed to design and develop a new setup, as we required it to be completely airtight, to avoid interference of atmospheric O_2. For this, we made a two neck custom-build reactor at the TU Wien glass-blower workshop (see figure 3.3). One neck was to insert the Ar purging needles, and the other neck for the O_2 sensor. The latter one was covered with a black tape and Aluminium foil to avoid interference between the light sensor and the excitation light source used. The neck apertures were sealed with a central borehole screw cap that was closed with a 1 mm thick Viton septum. This septum material holds the right elasticity to self recover/close after the removal of the Ar purging needles, and is chemical inert. Additionally, the reactor included a water cooling jacket to keep a constant temperature in the system, as the product concentration detected is temperature-dependent.
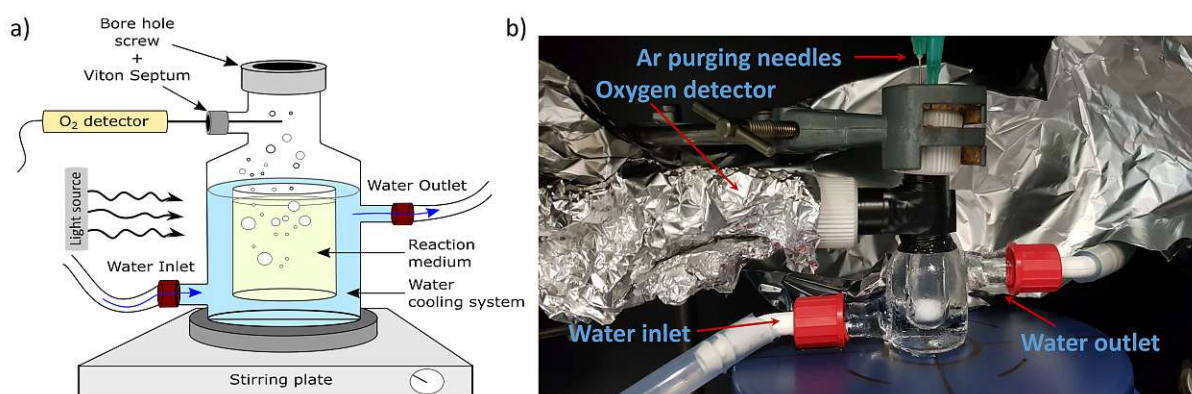
Figure 3.3: a) Schematic of the OER detection system and b) photo of the setup, showing the black tape and the aluminium foil to avoid interference with the excitation light source.

3.1.2.2 Long therm HER rate experimental setup optimization

To perform long-term reactions ($>$3 h) we needed to optimize the reactor and experimental setup. For the standard flow setup (Figure 3.1), we used a reactor with a total reaction volume of 50 ml and added 10 mg of the corresponding sample to be investigated. The Ar gas flow was 30 ml/min connected to the reactor by a central borehole screw connected to the Ar gas in- and outlet tubes. The system was closed by a quartz glass cap and during the experiment a top-side illumination was used. For the new setup (Figure 3.4a and b), we designed a new custom-built reactor with a total reaction volume of 10 ml, adding 10 mg of the investigated photocatalysts, which allowed to reduce the Ar flow to 15 ml/min, and the gas in- and outlet were substituted by a syringe system. To make the system completely airtight, a central borehole screw cap with a 1 mm Viton septum was used, which was additionally sealed with wax after the insertion of the Ar gas in- and outlet syringes. We used here a side illumination, as the light intensity loss due to the material nature of the reactor (glass) and the water cooling jacket, resulted to be negligible. With this setup, we achieved a substantial improvement of the data acquisition and reproducibility of the baseline, shown in figure 3.4c.

3.2 Characterization methods

3.2.1 Electron spectroscopic methods

Electron spectroscopic methods include x-ray Photoelectron Spectroscopy (XPS), Ultraviolet Photoelectron Spectroscopy (UPS) and Auger Electron Spectroscopy (AES). These characterization methods are surface sensitive (up to few nm of depth) and are used to extract qualitative and quantitative information about the chemical composition (XPS and AES) but also to obtain electronic information (XPS and UPS) of the analysed specimen surface.[91] XPS uses x-rays, while UPS ultraviolet light to excite the photoelectrons (see figure 3.5). AES is based on the Auger effect, i.e. the analysed electrons are expelled from the atoms by a series of internal relaxation processes after an initial excitation (electrons or x-rays) of the system. Thus, the binding energy (BE) of the analysed electrons in XPS and UPS is dependent on the light source used, while in AES not. Equation 3.3 shows the dependence of the BE and Kinetic energy (KE) of the electrons, the excitation light source and the work function (ϕ) of the detector

$$E_{Binding} = E_{Kinetic} - h\nu + \phi, \tag{3.3}$$

As the ϕ is a constant for the detector used, the BE depends solely on the KE and the light source used. This is true for emitted photoelectrons (UPS and XPS), but not for the
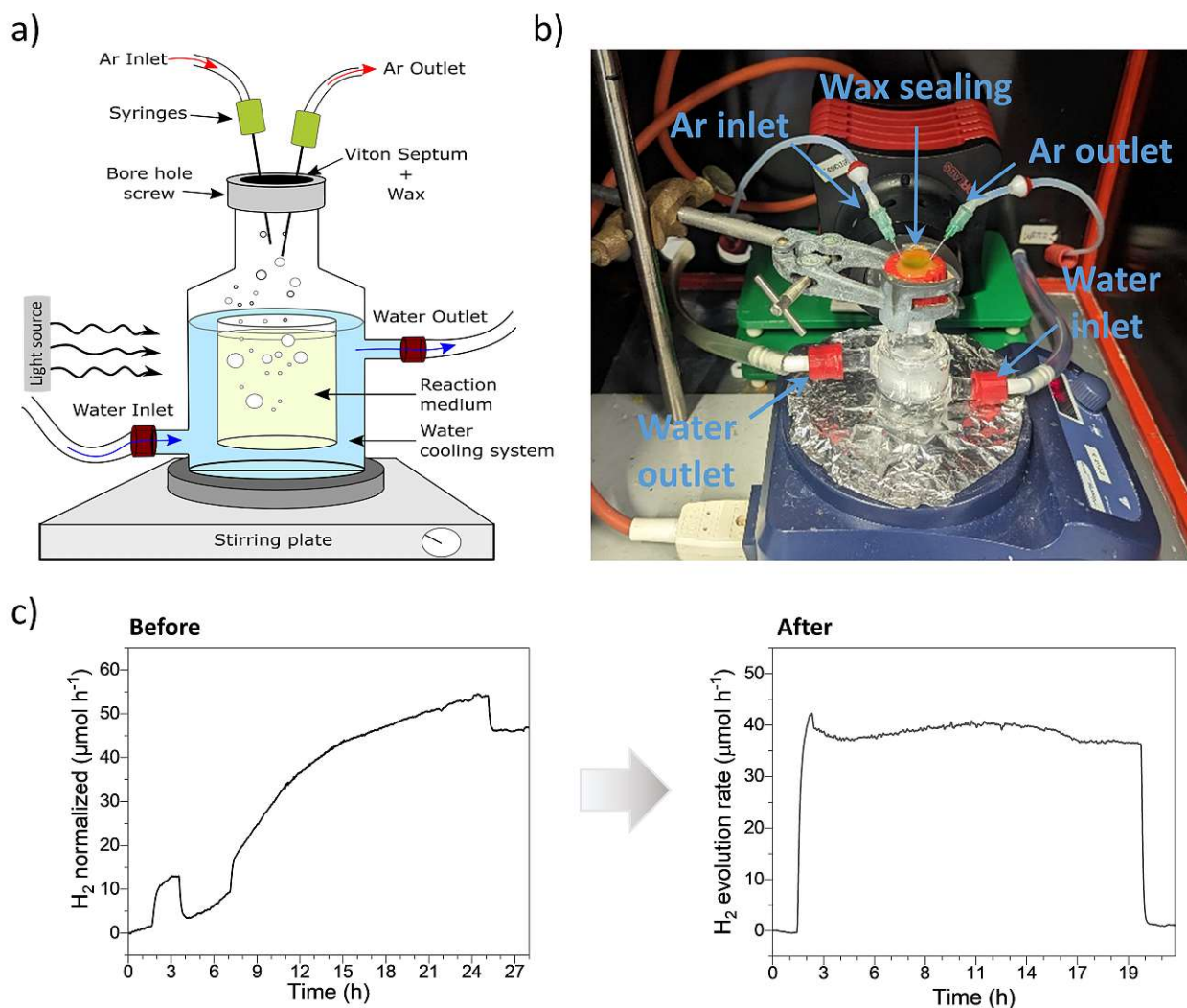
Figure 3.4: a) Schematic representation and b) photo of the new designed HER reactor setup for long term (>3 h) experiments. c) Data showing the difference of the acquired data and baseline with the standard (before) and new (after) reactor setup.

auger electrons (AES), where the BE = KE. Hence, by changing the light source the BE of the photoelectrons will change, while the Auger electron will appear at the same BE (see figure 3.5b). Accordingly, XPS and UPS are always shown in BE, while AES in KE. In this thesis, manuscript No.2, this physical phenomenon was used to obtain the Auger spectra of the Cu LMM. By using the excitation source Al K_α (1486.6 eV), the Cu LMM peak and the Ti 2s overlapped, yet by using the Mg K_α (1253.6 eV), the Ti 2s peak was shifted while the Cu LMM not, enabling its evaluation.

In this thesis, different XPS machines were used to acquire the datasets for the different manuscripts. Manuscript No. 1, we used a custom-built SPECS XPS-spectrometer equipped with a monochromatised Al-K_α x-ray source (ν 350) and a hemispherical WAL-150 analyser (acceptance angle: 60°). In manuscript No. 2 we used two machines, one to achieve the Auger spectra and the other for the XPS data. The Auger spectra were obtained using a Thermo Fisher Microlab 310/350-spectrometer equipped with a twin anode Al/Mg-K_α x-ray source (XR3) and a hemispherical analyser. The XPS spectra were acquired using an Axis Ultra DLD instrument from Kratos Analytical (UK) with a monochromatic Al-K_α radiation with the anode power set to 150 W. The UPS experiment was carried out in a home-built MOSES spectrometer equipped with a monochromatic He-I radiation source (hv=21.22 eV). In manuscript No.3 we used the same XPS machine as in Manuscript No. 2. For the data analysis in all manuscripts,
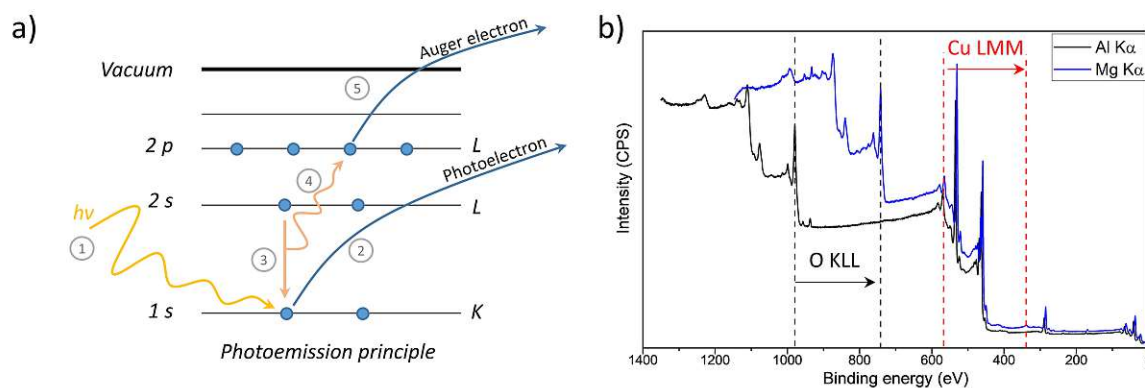
Figure 3.5: a) Schematic representation of the photoemission process principle. 1. Generation of the photoelectron by the incoming x-rays, 2. ejection of the photoelectron, 3. relaxation of an outer layer electron, 4. release of the excess energy and 5. ejection of an auger electron. b) XPS Survey spectra measured with two different excitation sources (Al Kα and Mg Kα), showing the shift of the auger electrons.

we used the CASA XPS software with a charge correction to the adventitious carbon peak (C-C peak was shifted to 284.8 eV BE). For further details of the machines, measurement details and data analysis, see the corresponding manuscript.

3.2.2   X-ray Fluorescence spectroscopy

X-ray Fluorescence Spectroscopy (XRF) is an elemental analysis method to determine chemical composition by using x-rays to excite the sample and detect the secondary x-rays (fluorescence x-rays, shown in figure 3.5 step 4) emitted by the sample to be analysed. In this thesis, the measurements were performed in a total reflection mode, where the source is in a critical angle and the detector at 90°, with respect to the sample. The advantage of this setup is that a higher chemical sensitivity is achieved. Furthermore, due to the nanoparticulate nature of the sample, the high penetration depth of the excitation x-rays and the highly energetic fluorescent x-rays, it provides information about the entire sample composition. Thus, in this thesis, it was defined as a "bulk sensitive" method in some parts.

The measurements were performed with an Atomika 8030C x-ray fluorescence analyser with a molybdenum x-ray source monochromatised K$_\alpha$-line. The excitation conditions were with a total reflection geometry and an energy-dispersive Si(Li)-detector. For further details, see the corresponding manuscript.

3.2.3   Thermogravimetric analysis

Thermogravimetric analysis (TGA) provides information about the sample mass changes over time by applying a constant temperature or a temperature gradient.[92] This provides information about phase transitions, changes in the chemical composition induced by thermal decomposition, as well as adsorption, absorption and desorption phenomena, among others. Hence, in this work we used this method to analyse the decomposition of the acetate and acetylacetonate anions, changes in the oxidation state of the analysed metals (Mn, Fe, Co, Ni, Cu), and generally mass changes induced upon calcination. For this, we used a PerkinElmer Thermogravimetric Analyser TGA 8000. For further details, see the corresponding section in the manuscripts.

3.2.4 Attenuated total reflection Fourier transform Infrared spectroscopy

Attenuated total reflection Fourier transform Infrared Spectroscopy (ATR-FTIR) analyses the absorption of infrared light by the natural vibration of a molecular bond.[93] In ATR-FTIR, the spectra are recorded using the ATR sampling mode. The physical phenomena used here is the attenuation of the evanescent field that is generated by the total reflection of the incident IR-beam. With this, this method enables the identification of functional groups and chemical bonds in the analysed samples. Furthermore, it enables to detect changes in the chemical bond vibration induced by adsorption of a certain species on a substrate.
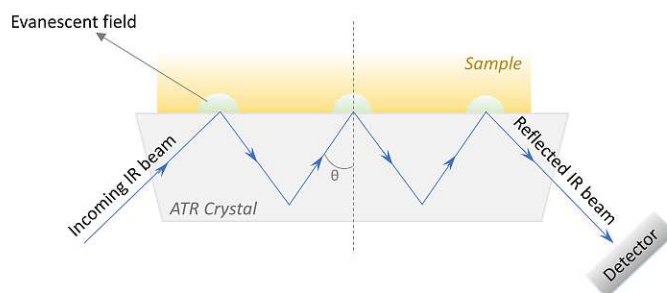
Figure 3.6: Schematic representation of the ATR sampling mode in ATR-FTIR spectroscopy

The used machine in all three manuscripts was a PerkinElmer FTIR Spectral UATR-TWO with a spectrum two Universal ATR (Single Reflection Diamond) accessory.

3.2.5 Raman spectroscopy

Raman spectroscopy uses scattered photons to analyse the change in polarizability of the electron cloud of a molecule bond.[94] The polarizability depends on the molecule geometry, and thus, provides information about the chemical structure, crystallinity, polymorph type, and molecular interactions.

In Raman spectroscopy there are three main parameters that provide information about the sample: the position (in Raman shift, cm^{-1}), the FWHM (cm^{-1}) and the intensity of the peak. The positions indicate what kind of vibrational modes the sample has and can be used as a sample identification. The FWHM and band intensity provides information about the crystallinity, i.e. changes in the polarizability of the molecular vibrations, phonons and other excitations, indicating lattice changes, such as doping.[95] Yet, the intensity of a Raman peak can also be affected by instrument artefacts and the sampling. Thus, to avoid these contributions, it is necessary to normalize the data to a standard, in our case we used TiO_2.

The data acquisition in this thesis was conducted with a LabRAM HR800 (HORIBA Co.Ltd), with the use of a Ne:YAG dio

3.2.6 Ultraviolet-Visible spectroscopy

Ultraviolet-Visible spectroscopy (UV-Vis) is a characterisation method that provides chemical information such as oxidation state, molecular symmetry, charge transfer processes (CT), localized surface plasmon resonance (LSPR), interband gap states and electronic information.[96] However, these electron transitions need to be in the ultraviolet, visible, or IR range to be detected by the UV-Vis spectrometer. This is the case for most d-d transitions of transition metals, or CT processes between metal and ligand (ligand to metal charge transfer (LMCT),

interfacial charge transfer (IFCT) or metal to ligand charge transfer (MLCT)). Yet, d-d transitions generally show a weak intensity, as they are forbidden by the Laporte section rule, while the CT processes are more intense being Laporte allowed. For example, in TiO_2, we only see LMCT (O^{-2} to Ti^{+4}), as no d-d transitions are possible (Ti^{+4} is a d^0). While for $Ni(acac)_2$ we can see both transitions, the LMTC of $acac^-$ to Ni^{+2}, and the d-d transition of Ni^{+2} ($3\,d^8\,4\,s^0$) (see figure 3.7a).
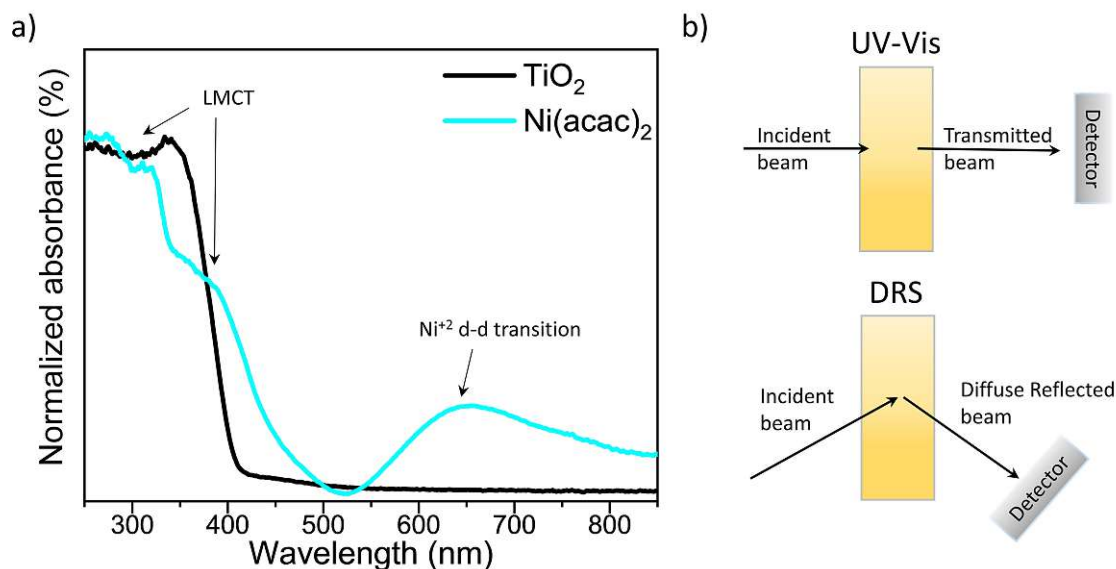
Figure 3.7: a) DRS spectra of TiO_2 and $Ni(acac)_2$ showing the corresponding MLCT and d-d transitions. b) Schematic representation of the different data collection modes of UV-Vis and DRS.

In UV-Vis spectroscopy, there are two methods for data collection, depending on the state of the sample (figure 3.7b). The standard method, when the specimen to be analysed is in solution or suspended in a solvent; or diffuse reflectance spectroscopy (DRS), when the sample is a solid. In the standard method, the suspension/solution is in a cuvette and the light beam goes through the solution. Thus, the data is collected in transmission mode. For DRS, the data is collected by the diffuse reflected, scattered light from the sample to be analysed. In this thesis, for all analysed samples we used the DRS mode, with a Jasco V-670 UV-Vis photo spectrometer.

3.2.7 Transmission electron microscopy

Transmission electron microscopy (TEM) provides microscopical information down to the atomic resolution.[97] The higher the energy of the electrons, the shorter their wavelength, and higher resolution can be achieved. For this, the electron beam energy range is 100-400 keV. The sample analysis takes place in transmission mode. Hence, the morphological information is obtained by the electrons transmitted and scattered by the specimen. The contrast in TEM is generated by the different electron density, providing information of the sample thicknesses, the crystal structure or orientation, and the atomic number of the constituting elements.

A plethora of methods exists that use electrons for materials characterization, as electrons can provide a diffraction pattern, or generate different electronic excitations. These methods include electron diffraction (ED), electron energy loss spectroscopy (EELS), Energy dispersive x-rays (EDX), among others. In this thesis, EDX was used for elemental analysis and chemical characterization, complementary to XRF. Both techniques, are based on the same physical phenomena (explained in section 3.2.2 XRF), with the main difference between these two methods

being the excitation source (electrons or x-rays), and that in EDX we analysed the sample in a scanning mode, thus, enabling elemental mapping of the atoms distribution on the substrate.

In this thesis, the TEM images and the EDX mapping were obtained using a FEI TECNAI F20 transmission electron microscope equipped with a field emission gun in bright field mode using 200 kV acceleration voltage.

Results and discussion

This thesis is written in a cumulative form and includes three peer-reviewed manuscripts reprinted with the permission of the corresponding journals.

4.1 Overview of Contributed Articles

In the work of this thesis, three manuscripts where prepared. The link between the articles is the investigation of structural and catalytic properties of metal-based co-catalyst (mainly Ni, Cu, Fe, Mn and Co) attached on TiO_2 towards the hydrogen evolution reaction (HER). Manuscript No.1 investigates and compares Co, Fe, Ni and Mn as co-catalyst for both water splitting half-reactions. The study shows that – out of this set – only Ni is able to enhance the HER performance of bare TiO_2, while Co and Fe are capable of co-catalysing the oxygen evolution reaction (OER). We further show that the photocatalytically-active Ni species is generated in-situ upon illumination, as a steady hydrogen evolution rate increase is observed correlated with a gradual conversion of Ni^{2+} to metallic Ni, the HER-active oxidation state. In Manuscript No.2, Cu is investigated as a co-catalyst and – compared to the previously described Ni-containing photosystem – is shown to have an even higher HER capacity. Besides its outstanding performance, Cu was not included in the first systematic study as a different Cu precursor, $Cu(ac)_2$ – in comparison to $M(acac)_x$ used for Co, Fe, Ni and Mn – was used due to its advantageous solubility characteristics. These facts led to a separate, more fundamental study of Cu-based photosystem, which was then published separately. This work demonstrates that post-synthetic temperature treatments (i.e. calcination in ambient air) have a detrimental effect on the overall photocatalytic performance, showing that the highest HER activities were achieved by the as-prepared (i.e. non-calcined) and low-temperature-calcined (>200°C) samples. The thermal treatment is shown to induce Cu ions – in the form of Cu^+, generated via spontaneous reduction by the negatively-charged surface of TiO_2 – to diffuse into the TiO_2 sub-surface lattice, leading to a fraction of Cu being non-accessible for the photocatalytic reaction. We further show that another fraction of surface-attached Cu – in the form of Cu^{2+} – requires optimal electronic interaction with the TiO_2 surface to be able to accept (extract) the photoexcited electrons and get reduced to metallic Cu species being responsible for the excellent HER performance. In manuscript No.3, we take a closer look at the dynamic nature of Ni-based photosystem - discovered in our first work - and further investigate its HER mechanism by analysing the effect of calcination on catalysis. Once again, high-temperature treatments are shown to induce strong attachment of Ni to the TiO_2 lattice, hindering Ni^{2+} from being effectively reduced to metallic Ni. Furthermore, we show that not only Ni^0 is important for HER, but that the right proportion of Ni^{2+} and Ni^0 is required to attain optimal photocatalytic performance. Overall, in this thesis, different transition metals are investigated as co-catalyst, and the effect of synthetic parameters and their structure/composition on the ultimate capacity to generate hydrogen is analysed in detail, leading me to propose several metal-dependent HER

23

mechanisms.

This thesis is summarized in the following manuscripts:

Manuscript No.1:

"Immobilization of Co, Mn, Ni and Fe oxide co-catalysts on TiO$_2$ for photocatalytic water splitting reactions"

Jasmin S. Schubert, Janko Popovic, Greta M. Haselmann, Sreejith P Nandan, Jia Wang, Ariane Giesriegl, Alexey S. Cherevan, Dominik Eder

Manuscript No.2:

"Elucidating the formation and active state of Cu co-catalysts for photocatalytic hydrogen evolution"

Jasmin S. Schubert, Leila Kalantari, Andreas Lechner, Ariane Giesriegl, Sreejith P. Nandan, Pablo Ayala, Shun Kashiwaya, Markus Sauer, Annette Foelske, Johanna Rosen, Peter Blaha, Alexey Cherevan and Dominik Eder

Manuscript No.3:

"Nature of the active Ni state for photocatalytic hydrogen generation"

Jasmin S. Schubert, Eva Doloszeski, Pablo Ayala, Stephen Nagaraju Myakala, Jakob Rath, Bernhard Fickl, Ariane Giesriegl, Dogukan H. Apaydin, Bernhard C. Bayer, Shun Kashiwaya, Alexey Cherevan, Dominik Eder

4.2   Original Manuscripts

4.2.1   Manuscript No.1

"Immobilization of Co, Mn, Ni and Fe oxide co-catalysts on TiO$_2$ for photocatalytic water splitting reactions"

Jasmin S. Schubert, Janko Popovic, Greta M. Haselmann, Sreejith P. Nandan, Jia Wang , Ariane Giesriegl, Alexey S. Cherevan and Dominik Eder

J. Mater. Chem. A, 2019, 7, 18568-18579

The corresponding Supplementary information of the manuscript can be found on page 38.

Reproduced from Ref.[98] with permission from the Royal Society of Chemistry.

In this work, the O$_2$ evolution rate setup was newly design for this experiment. Details can be found in section 3.1.2.

PAPER

Check for updates

Immobilization of Co, Mn, Ni and Fe oxide co-catalysts on TiO$_2$ for photocatalytic water splitting reactions†

Jasmin S. Schubert, Janko Popovic, Greta M. Haselmann, Sreejith P. Nandan, Jia Wang, Ariane Giesriegl, Alexey S. Cherevan [iD] * and Dominik Eder [iD] *

Here we report a systematic study of a series of non-noble-metal co-catalysts based on Co, Mn, Ni and Fe oxides that were prepared by wet impregnation of the corresponding acetylacetonate precursors onto a model TiO$_2$ substrate, followed by their oxidative decomposition. We analyze thermal evolution of the impregnated M(acac)$_x$–TiO$_2$ composites with a combination of analytical methods and reveal strong differences in the precursor decomposition onsets and the resulting product composition, compared to the case of pure M(acac)$_x$ precursors. Consequent electron microscopy analyses of the resulting MO$_x$–TiO$_2$ composites indicate the presence of small (1–5 nm) amorphous MO$_x$ nanoparticles that are homogeneously distributed on the surface of the substrate TiO$_2$. Complementing Raman and photoluminescence (PL) spectra confirm pronounced effects of MO$_x$ deposition on the state of TiO$_2$ substrate and suggest strong electronic communication between the components. The composites obtained at 350 °C were further tested towards sacrificial hydrogen evolution reaction (HER) and oxygen evolution reaction (OER) demonstrating the dynamic nature of the NiO$_x$–TiO$_2$ photocatalyst whose Ni^0 active HER sites were generated *in situ* upon light exposure. In contrast, FeO$_x$–TiO$_2$, CoO$_x$–TiO$_2$, and NiO$_x$–TiO$_2$ were all active towards OER, featuring water oxidation ability in descending order, while XPS data of the samples after reaction indicate that partial oxidation of M species takes place during the course of the photocatalytic experiment. This work provides detailed insights on the wet chemistry-based preparation of MO$_x$ co-catalysts decorating oxide nanopowders including optimization of the thermal treatment, potential substrate effects and synergy as well as further prospects in photocatalysis.

Introduction

As of now, renewable energy systems are not mature enough to cover the ever-increasing world energy demands. As a result, the main energy production still comes from non-clean and non-renewable sources, such as fossil fuels, which further contribute to global warming. In addition, the intermittent nature of many renewable energy sources – like in the case of photovoltaics, whose performance depends on the sunlight availability – implies a need for alternative energy storage systems.[1] H$_2$ has been identified as a promising candidate potentially able to become a base chemical as well as an energy storage system (with its high energy density of 120 MJ kg^{-1} and a non-intermittent supply)[2–4] for our future economy. However, given the fact that the majority of industrial H$_2$ production is currently still based on natural gas reforming,[5,6] renewable

methods of H$_2$ generation require further development and implementation.

A prodigious approach for clean H$_2$ production is water splitting, however, in order to induce this reaction using electro- or thermal catalysis, an extensive amount of energy has to be invested.[7] One approach to circumvent this issue relies directly on the renewable energy of sunlight by means of photocatalysis. In this case, the light photons are used to break the water molecules assisted by a photocatalyst, a substance that generates photoexcited charge carriers, delivers them to the solid–liquid interface and catalyzes the redox half-reaction of water oxidation and reduction, the latter yielding the desired H$_2$ product.[8–10] Although the hydrogen evolution reaction (HER) is given much more attention in the community of heterogeneous photocatalysts,[11] it is the oxygen evolution reaction (OER) that – being kinetically far more complicated (4 electron–4 proton transfer) – often becomes a limiting step for the overall process.

A well-suited model compound for photocatalytic water splitting studies is TiO$_2$, as it features high chemical stability, shows no toxicity, is cheap, widely available and has a suitable band gap for both half-reactions.[8,9,12–14] However, TiO$_2$ has several drawbacks that keep it from becoming an efficient water

Institute of Materials Chemistry, Technical University of Vienna, Getreidemarkt 9, Vienna, 1060, Austria. E-mail: alexey.cherevan@tuwien.ac.at; dominik.eder@tuwien.ac.at

† Electronic supplementary information (ESI) available. See DOI: 10.1039/c9ta05637h

18568 | *J. Mater. Chem. A*, 2019, 7, 18568–18579

This journal is © The Royal Society of Chemistry 2019

splitting photocatalyst.[13,14] These limitations include fast electron–hole recombination rates, poor and unselective catalytic sites on its surface, and a wide band gap that only allows absorption in the UV light range. A number of strategies have been explored to address these issues, such as the use of co-catalysts.[11,13] These surface-attached species (mostly nanoparticles) provide new catalytic sites and simultaneously induce separation of photoexcited electrons and holes.[15] The most widely used co-catalysts are Pt, Pd and IrO₂, RuO₂ for the photocatalytic reduction and oxidation of water, respectively. These are expensive materials based on rare noble metals.[11,16,17] To achieve large scale industrial application of photocatalytic water splitting the development of new co-catalysts based on cheap and widely available elements remains an important issue.

With regard to novel abundant co-catalysts for photocatalytic water splitting, research efforts have focused on d-block transition metals of the fourth period, which are known for their excellent catalytic properties and applications in industry, research and nature.[7,11,14,17] These elements – especially in their oxide form – can undergo quick and reversible redox shuttling, accept, accumulate and release electrons – conditions necessary to generate a self-recovering system. Besides this, their surface structure and chemistry can be varied through synthetic conditions (e.g. different oxides can be generated) allowing to further tune adsorption/desorption properties and thus their catalytic function – an aspect rarely investigated so far. For this reason, in this work we explore the nature of Ni, Mn, Co and Fe oxide based co-catalysts and directly compare their potential in both water splitting reactions (OER and HER).

Metal oxide co-catalysts are typically deposited on the photocatalyst surface by sol–gel processes or via the use of surfactants.[18–25] These methods allow for a certain degree of control over the size and shape of the co-catalytic species;[19] however,

they are often limited when one-pot synthesis is desired. Wet impregnation routes, on the other hand, are simple and cost-effective: for example, by using metal salt impregnation followed by thermal decomposition.[26–29] Although some previous works have reported the synthesis and application of such co-catalyst-loaded TiO₂ powders in photocatalysis,[11,14,17,30–37] many inconsistencies, originating from the wide variety of synthetic and calcination conditions, remain. Furthermore, the lack of comparative activity evaluations leave a gap in the fundamental understanding of their actual active state. Besides these, most of the co-catalysts have been tested solely for HER, and no data on OER performance have been reported.

In order to complement this knowledge gap, in this work, we used a wet impregnation route to prepare Mn, Co, Fe and Ni-based co-catalysts immobilized on TiO₂ nanoparticles (NPs) and systematically investigated their prospects in photocatalytic water splitting reactions. We first analyzed the thermal evolution of pure metal salt precursors and the corresponding composites using thermogravimetric analysis (TGA) and in situ X-ray diffraction (XRD) to determine the optimal calcination temperature and product composition. We then elucidated the morphology, crystallinity and oxidation state of the prepared co-catalyst species with a combination of electron microscopy and diffraction as well as XRD, X-ray photoelectron spectroscopy (XPS) and attenuated total reflection Fourier-transform infrared spectroscopy (ATR-FTIR) analyses and correlated these characteristics with their performance towards HER and OER.

Results and discussion

The metal oxide species were synthesized directly on the surface of TiO₂ NPs following the wet impregnation – thermal decomposition method depicted in Fig. 1a. In a typical experiment,
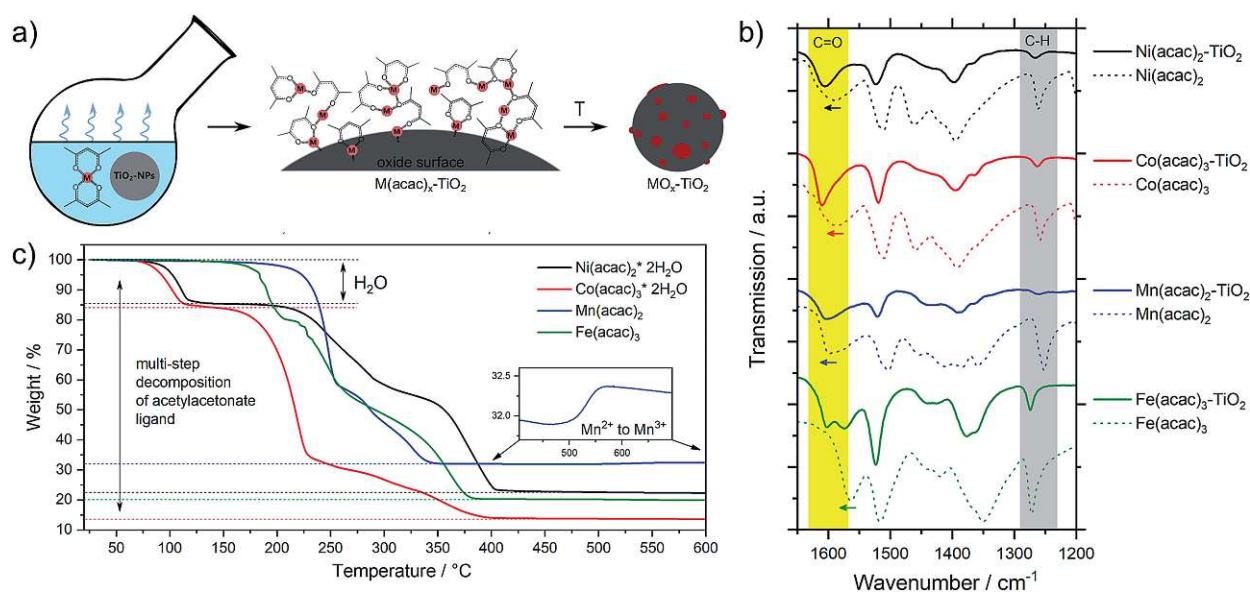

Fig. 1 (a) Schematic description of the synthetic protocol, (b) FTIR spectra of the M(acac)ₓ–TiO₂ composites and the corresponding precursors and (c) TGA data of the pure M(acac)ₓ precursor salts (heating rate: 5 °C min⁻¹ in air; temperature range: 25 °C to 600 °C, M = Fe, Mn, Ni and Co).

This journal is © The Royal Society of Chemistry 2019

J. Mater. Chem. A, 2019, **7**, 18568–18579 | **18569**

27

a given amount of TiO_2 powder was dispersed in a solvent by ultrasonication, to which a pre-made solution of fully solubilized $M(acac)_x$ species (M = Fe, Mn, Co, Ni; acac = acetylacetonate) was slowly added. The solution was stirred until the solvent was completely evaporated, yielding the corresponding $M(acac)_x$–TiO_2 composites, which were converted into the respective MO_x–TiO_2 composites upon subsequent heat treatment. More details can be found in the Experimental section.

The presence of the $M(acac)_x$ salts in TiO_2 powder after the impregnation can be confirmed by ATR-FTIR spectroscopy (Fig. S1†). The spectra of the composites constitute a superposition of the organic part (most pronounced are ligand-related IR bands) and the TiO_2 substrate (broad absorption below 1000 cm^{-1}), however, a closer look at the 1700–1000 cm^{-1} region (Fig. 1b) indicates that the original peaks of acetylacetonate species are shifted to higher wavenumbers, suggesting a strong binding (chemisorption) of the salt precursors with the substrate material. In addition, the formation of the composites is also apparent from the colour changes – brown, blue, green and red for the Mn, Co, Ni and Fe-based composites, respectively – of the originally white TiO_2 powders observed after impregnation (Fig. S1†).

The composites have been further subjected to thermal treatment in ambient air to oxidatively decompose the metal precursors and yield the corresponding metal oxide co-catalysts on the TiO_2 NPs. However, since there is no consensus in the literature as to which conditions generate which species,[30,31,33,35,36,38–44] we systematically varied the calcination temperature and analysed thermal evolution of both, the pure $M(acac)_x$ precursors and the impregnated $M(acac)_x$–TiO_2 composites.

Thermal analysis

Pure $M(acac)_x$. We first investigated thermal decomposition of pure $M(acac)_x$ precursors. The TGA data in Fig. 1c correspond well to the thermal behaviour observed for similar organic salts reported elsewhere:[45,46] (a) the moderate mass loss at low temperatures (<200 °C) is related to the removal of crystallization water that is present in $Ni(acac)_2$ and $Co(acac)_3$; (b) the large weight loss in the temperature window of 200–400 °C corresponds to the multi-step decomposition of the acetylacetonate species (precursor oxidation).[45] The weight profiles reach a stable plateau after complete salt oxidation, which indicates the formation of stable MO_x species. The only exception is $Mn(acac)_2$, which experiences a small mass gain above 500 °C corresponding well with the partial oxidation of Mn^{2+} to Mn^{3+}.

The TGA data were further complemented by *in situ* XRD using the same heating conditions. Fig. 2 shows that the thermal decompositions of all precursor salts coincide well with the formation of crystalline oxides (full data sets can be found in Fig. S2†).

$Mn(acac)_2$. Fig. 2a shows the characteristic peaks of the original crystal structure of the precursor up to a temperature of about 150 °C, while at 200 °C all diffractions corresponding to the acetylacetonate have vanished, instead showing new diffractions corresponding to Mn_3O_4 (ICDD: 04-007-9641). Both, crystal phase and product composition remain unchanged up to temperatures of around 500 °C, above which the orthorhombic bixbyite Mn_2O_3 appears (ICDD: 04-007-0856), accompanied by corresponding Mn^{2+} oxidation. Both observations are in agreement with TGA (Fig. 1c). Interestingly, no apparent crystal growth is observed for the Mn_3O_4 particles upon calcination at high temperatures, as indicated by the absence of any peak narrowing. Instead, more and more of the Mn^{2+} is oxidized to Mn^{3+} and both oxide phases, Mn_3O_4 and Mn_2O_3, co-exist up to at least 800 °C.

$Co(acac)_3$. The multi-step decomposition of acetylacetonate takes place between 200 and 400 °C according to TGA. The XRD results show that the original crystal structure of the salt

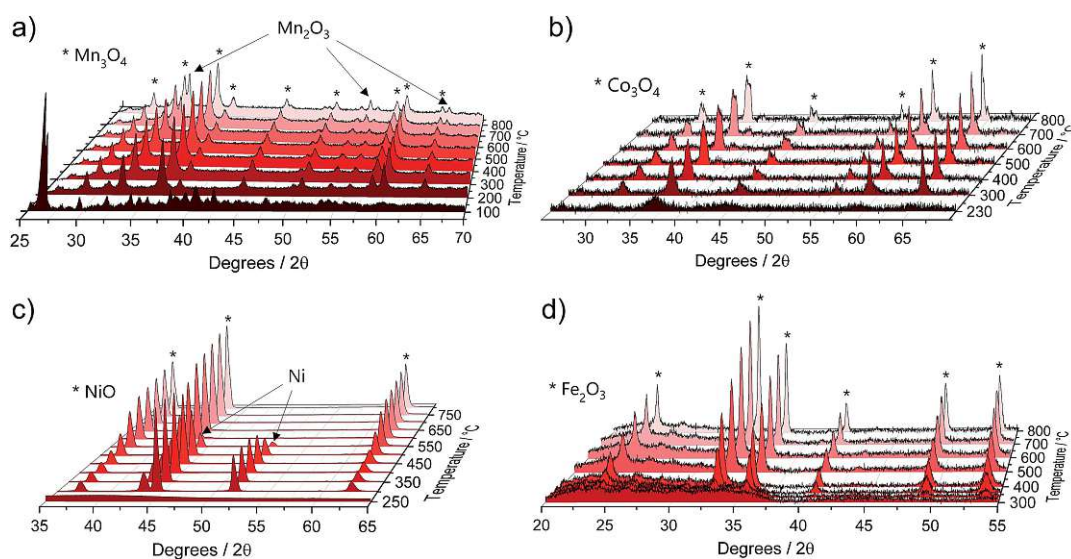**Fig. 2** Selected *in situ* XRD spectra of the pure $M(acac)_x$ (M = Mn, Co, Ni and Fe) precursors acquired in air within a temperature range of 25 °C to 800 °C and heating rate of 5 °C min^{-1} for (a) $Mn(acac)_2$, (b) $Co(acac)_3$, (c) $Ni(acac)_2$ and (d) $Fe(acac)_3$. Full data sets can be found in Fig. S2.†

18570 | *J. Mater. Chem. A*, 2019, **7**, 18568–18579

This journal is © The Royal Society of Chemistry 2019

28

degrades into an amorphous state already at 100 °C (see Fig. S2†) – temperature at which the removal of crystallization water takes place. At temperatures above 200 °C a broad diffraction at 36.8 degrees – corresponding to crystalline Co_3O_4 (ICDD: 04-014-7747) – appears and gets narrower up to 300 °C indicating gradual growth of the crystallites. The conversion of Co^{3+} species to the mixed-valent oxide is likely induced by the acetylacetonate species through radical formation in a similar way as has been suggested for Cu acetate.[47] No apparent changes in crystal structure take place thereafter up to 800 °C; however, the splitting of the peaks at higher temperatures (>600 °C) may be related to the formation of non-stoichiometric oxides.

Ni(acac)$_2$. The diffractograms in Fig. 2c indicate the formation of a mixed product consisting of metallic Ni (ICDD:04-010-6148) and NiO (ICDD:04-005-4393) in the temperature window of 220–400 °C, which is in agreement with the TGA in Fig. 1c. At temperatures above 250 °C Ni remains the major component up to 500 °C, after which the re-oxidized product starts to dominate the composition. This indicates that the presence of carbonaceous species in metal–organic salt precursors (*e.g.* acetylacetonate) can induce strong Ni^{2+} reduction to purely metallic species during the decomposition phase.[47]

Fe(acac)$_3$. Fig. 2d shows that the decomposition proceeds in a way predicted by TGA. There is no reduction of the metal between 230 and 400 °C, while the single product of rhombohedral hematite Fe_2O_3 (ICDD: 04-002-7501) appears above 300 °C.

These results were further complemented by *quasi in situ* ATR-FTIR performed after subjecting the precursor salts to calcination at different temperatures. The spectra in Fig. S3† confirm that the decomposition of the original acetylacetonates and removal of the intermediate organic species for all composites finish at temperatures above 300 °C.

M(acac)$_x$–TiO$_2$ composites. Next, we investigated the impregnated composites with TGA to see whether the presence of TiO_2 substrate affects the thermal decomposition behavior and the final state of the respective MO_x co-catalyst species.

Interestingly, Fig. 3 not only shows large differences in the decomposition behavior (*e.g.* mechanism of acetylacetonate oxidation), it also indicates strong differences in the decomposition onsets and stability windows (up to 100 °C) for all precursors when impregnated on TiO_2. For example, the $Mn(acac)_2$ species do not undergo a two-step decomposition process within a narrow temperature interval anymore (Fig. 3a compared to Fig. 1c); instead we observe only one strong mass loss in the range between 200 and 250 °C. The final product of decomposition forms already above 250 °C, which is about 100 °C lower than for the pure precursor. In the case of the $Co(acac)_3$–TiO_2, the main weight loss takes place just below 300 °C and likely corresponds to the oxidation of acetylacetonate, which – in the case of the pure precursors – does not finish
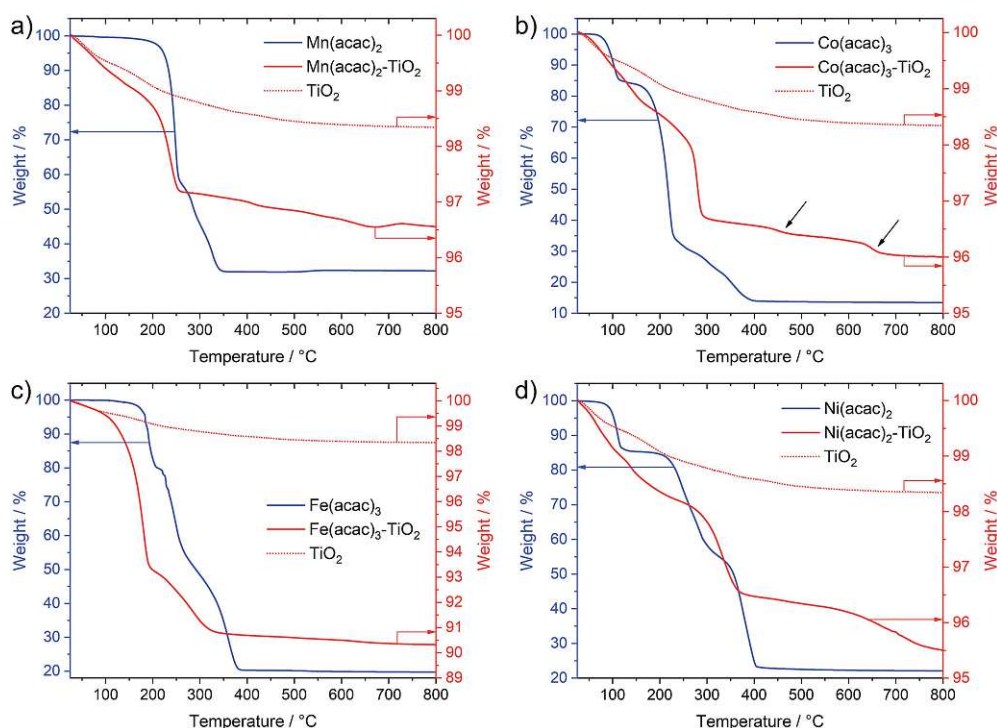

Fig. 3 TGA data of the Mn(acac)$_2$−TiO$_2$ (a), Co(acac)$_3$−TiO$_2$ (b), Fe(acac)$_3$−TiO$_2$ (c) and Ni(acac)$_2$−TiO$_2$ (d) composites overlapped with that of the pure precursors and the TiO$_2$ reference. The left *y*-axis corresponds to the weight loss of the pure precursors, the right *y*-axis corresponds to the weight loss of the composite and the reference TiO$_2$. Data were recorded in air, heating rate 5 °C min^{-1} and in a temperature range from 25 °C to 800 °C. Note the differences in the scale of the *y*-axes. The minor weigh loss observed for the reference TiO$_2$ in the range from 25 °C to 300 °C is attributed to the presence of physisorbed and chemisorbed species left from the synthesis and processing.

until 400 °C. Besides this, we see at least two additional minor weight losses at roughly 450 °C and 650 °C (see black arrows in Fig. 3b) for the composite with respect to the pure precursor salt.

Similar discrepancies can be observed for the other samples and indeed confirm different kinetics and stages for the decomposition of the immobilized $M(acac)_x$ precursors. More detailed investigations are required to gain full understanding for each individual composite. Our results further suggest that one needs to take care when applying heat treatment protocols, developed for the pure salts, unscrutinized to the corresponding nanocomposites.

After revealing thermal behavior of the impregnated $M(acac)_x$–TiO_2 composites, we have chosen calcination conditions for the thermal treatments aiming to fully decompose the acetylacetonate species, but avoid potential particle growth and possible crystallinity changes of the substrate TiO_2. Considering differences between precursors, an optimum treatment of 350 °C that suited all $M(acac)_x$–TiO_2 samples was applied (see Experimental section) and yielded corresponding NiO_x–TiO_2, MnO_x–TiO_2, CoO_x–TiO_2 and FeO_x–TiO_2 nanocomposites that will be the focus of the following sections.

Morphological investigation

The calcined MO_x–TiO_2 composites were analysed by scanning electron microscopy (SEM) and transmission electron microscopy (TEM). The SEM images in Fig. S4† confirm that the samples are composed of small nanoparticles (NPs) that are similar to the reference TiO_2 (not shown), with no apparent changes in size and shape upon impregnation and calcination. There are also no signs of larger particles, thus we can exclude the formation and growth of unattached MO_x. EDX further indicates a homogeneous distribution of the M elements over the TiO_2 material on the microscale (Fig. S5†). Both observations suggest that no phase segregation upon calcination has occurred and the samples indeed are nanocomposites with M species dispersed across all TiO_2 NPs.

Fig. 4a and b show TEM image of the reference TiO_2 NPs that range between 10 and 50 nm in size and constitute close-to-spherical highly crystalline particles with sharp edges. The electron diffraction (ED) pattern of the reference TiO_2 shows diffuse rings that correspond well to polycrystalline, nanosized anatase and rutile particles (Fig. S6a†). In contrast, TEM images of the composites in Fig. 4 indicate strong changes in surface morphology of the substrate TiO_2 and appearance of surface-attached species.

In the case of MnO_x–TiO_2 (Fig. 4c), the images clearly show the presence of dark spots with sizes between 2 and 5 nm, which likely correspond to the newly formed MnO_x NPs. TEM of the CoO_x–TiO_2 composite in Fig. 4d indicates the presence of smaller 2–3 nm surface-attached CoO_x NPs densely decoration the substrate. A similar morphology is found for NiO_x–TiO_2 (Fig. 4f) where the surface of TiO_2 particles got covered with even smaller (1–2 nm) NiO_x NPs of surprisingly uniform size
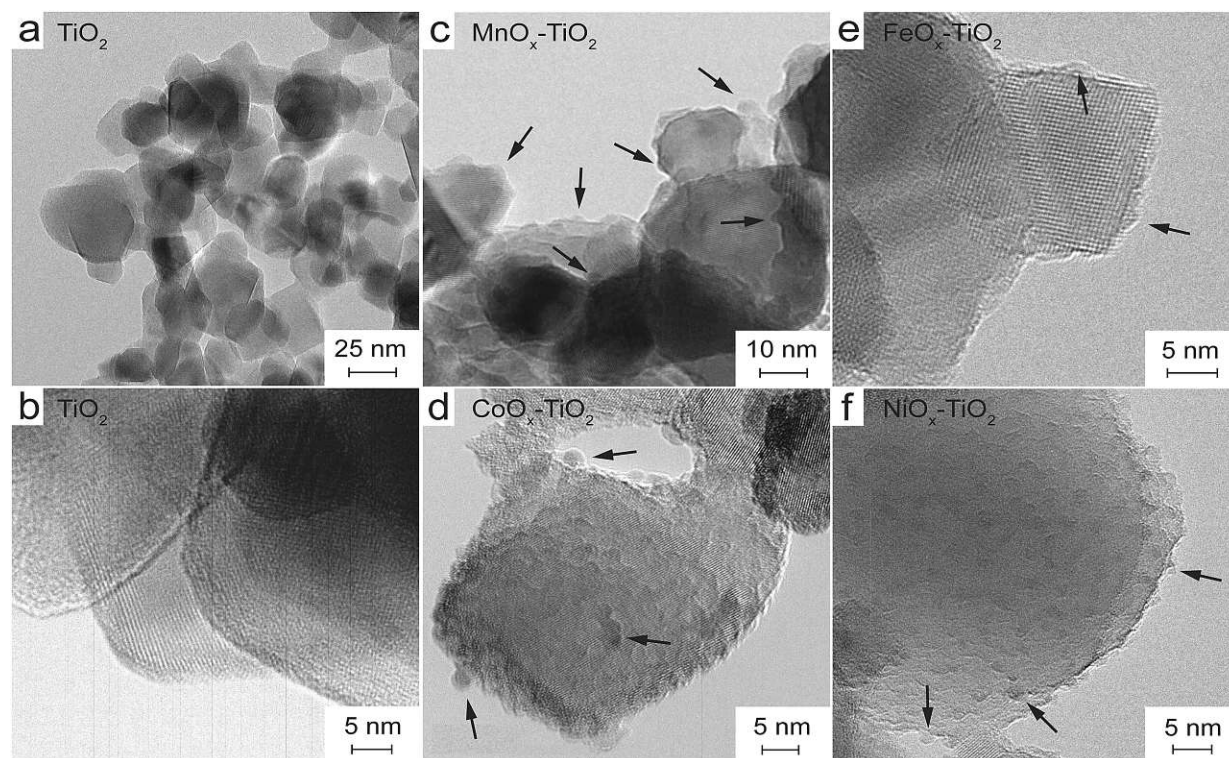

Fig. 4 TEM pictures of the TiO_2 NPs (a and b) as well as MnO_x–TiO_2 (c), CoO_x–TiO_2 (d), FeO_x–TiO_2 (e) and NiO_x–TiO_2 (f) composites prepared at 350 °C. Arrows indicate examples of clearly visible MO_x species.

18572 | *J. Mater. Chem. A*, 2019, **7**, 18568–18579

This journal is © The Royal Society of Chemistry 2019

30

and shape. For FeO$_x$–TiO$_2$ (Fig. 4e), the morphology of the deposits rather resembles a surface shell consisting of small particles sized below 5 nm.

Importantly, we can presently not exclude additional presence of atomic MO$_x$ species on TiO$_2$ surface, but the majority of the visible MO$_x$ NPs appear to be uniform in size and homogeneously distributed on the surface sharing an intimate interface with the substrate.

Interaction with the matrix

To further elaborate on the state of the MO$_x$ in TiO$_2$ matrix and on the differences between the composites, we have performed additional Raman and photoluminescence (PL) measurements.

Fig. S7† shows Raman spectra of all as-prepared composites demonstrating that MnO$_x$–TiO$_2$, CoO$_x$–TiO$_2$ and FeO$_x$–TiO$_2$ samples feature strong peak shifts and peak broadening of the anatase-related E$_g$ band with respect to the TiO$_2$ reference (Table S1†). With regard to our composite systems, these can be assigned to the presence of surface-adsorbed species on TiO$_2$, creation of O vacancies or even doping with M ions, which cannot be excluded based on ionic radii comparison. In contrast, Raman spectrum of the NiO$_x$–TiO$_2$ sample resembles that of the TiO$_2$ suggesting no strong effect on TiO$_2$ upon NiO$_x$ immobilization (detailed discussions of Raman data can be found in ESI†).

PL emission spectrum of the substrate TiO$_2$ powder in Fig. S8† exhibits strong overlapping bands centred at 417, 432 and 461 nm. While the first peak (2.97 eV) can be assigned to band-to-band recombination of rutile component, the latter two (2.87 eV and 2.69 eV) can be attributed to sub-band gap emission characteristic for TiO$_2$ NPs and related to shallow electronic states associated with *e.g.* oxygen vacancies, structural defects or dopants; in line with Raman results. Spectra of the composites still contain PL peaks of TiO$_2$, however, they also feature new bands appearing at higher wavelength and characterized by broad emissions centred at 478 nm, 490 nm and 497 nm for the FeO$_x$–TiO$_2$, CoO$_x$–TiO$_2$ and NiO$_x$–TiO$_2$ respectively. The emergence of the additional emission bands at lower energies (2.60 eV, 2.53 eV and 2.49 eV) for all composites can be assigned to the appearance of new relaxation pathways for the carriers originally photoexcited in TiO$_2$. Judging from TEM and Raman data, one such possibility could be that the electrons or holes are extracted by the surface-attached MO$_x$ species leading to new PL bands related to radiative recombination at MO$_x$ sites or the interface.

This result confirms active electronic communication between the components of the composites and further indicates the ability of the MO$_x$ species to facilitate charge separation in TiO$_2$.

Crystallinity of the obtained MO$_x$ NPs

Further analysis of the MO$_x$ state and composition with HRTEM has proven to be complicated since the deposited NPs were mostly – with some rare exceptions found in TEM – of amorphous nature. This was further confirmed from the analysis of

ED patterns (Fig. S6†) that indicate no additional diffraction spots corresponding to the expected MO$_x$ NPs.

To elucidate more on the amorphous nature of the surface-deposited species in our MO$_x$–TiO$_2$ composites, we performed additional XRD measurements (see Fig. S9†). The data in Fig. S9a† shows no diffractions other than that of the TiO$_2$ substrate for all calcined samples; however, this can also be explained by the low amounts of the MO$_x$ species, thus reaching the detection limit of the XRD technique. To further investigate this, we prepared a set of model samples where the impregnation was done using a much greater amounts of the precursor salts (up to 24.4 wt%) and diffractograms were recorded for the model composites before and after thermal treatment. Still, the XRD did not reveal any peak associated with newly formed oxide species even after calcination (Fig. S9b and c†), thus confirming the TEM and ED data and the conclusion that the MO$_x$ species in the final MO$_x$–TiO$_2$ composites are of amorphous nature regardless of the calcination protocol (see ESI for more details†). This amorphous nature of the generated NPs is surprising, because XRD of the pure precursors clearly indicated that the products of the acetylacetonate decomposition, obtained at this calcination temperature, were crystalline (see again Fig. 2). This different behaviour of the composites against the pure precursor is possibly related to surface effects, where TiO$_2$ restricts the mobility of the surface-bound metallic species and thus prohibits bond rearrangement and formation of a crystalline lattice.

Confirming the oxidation state

Considering the strong differences in the thermal decomposition of the pure precursors and precursors immobilized on the surface of TiO$_2$, we sought to verify the oxidation state and composition of the surface-deposited species (so far only suggested from *in situ* XRD of pure precursor salts) after thermal treatments using surface-sensitive XPS analyses. Measuring conditions and information about data treatment can be found in the Experimental section.

Survey spectra of all composites are presented in Fig. S10† and reveal the presence of expected elements: Ti and O (mainly from the TiO$_2$ substrate) as well as Co, Ni, Mn and Fe in the relevant composites. The characteristic C 1s signals correspond very well to adventitious carbon observed in the TiO$_2$ reference indicating complete decomposition of the acetylacetonate ligand after the applied calcination.[48]

More importantly, Fig. 5 presents the detailed spectra of the Co 2p, Ni 2p, Mn 2p and Fe 2p regions and allows elucidating the oxidation state of the incorporated metals on the surface of TiO$_2$. XPS analyses of these transition metals is quite complex due to multiplet splitting and different shake-up structures. Thus, the signal of a species can be deconvoluted into various different components that have been analysed in detail previously. This also means that the analysis of the oxidation state of these transition metals is not straight-forward and in some cases can only be seen as indicative. Our analysis is largely based on the work by Biesinger *et al.*[49] Detailed fitting parameters can be found in Table S2.†
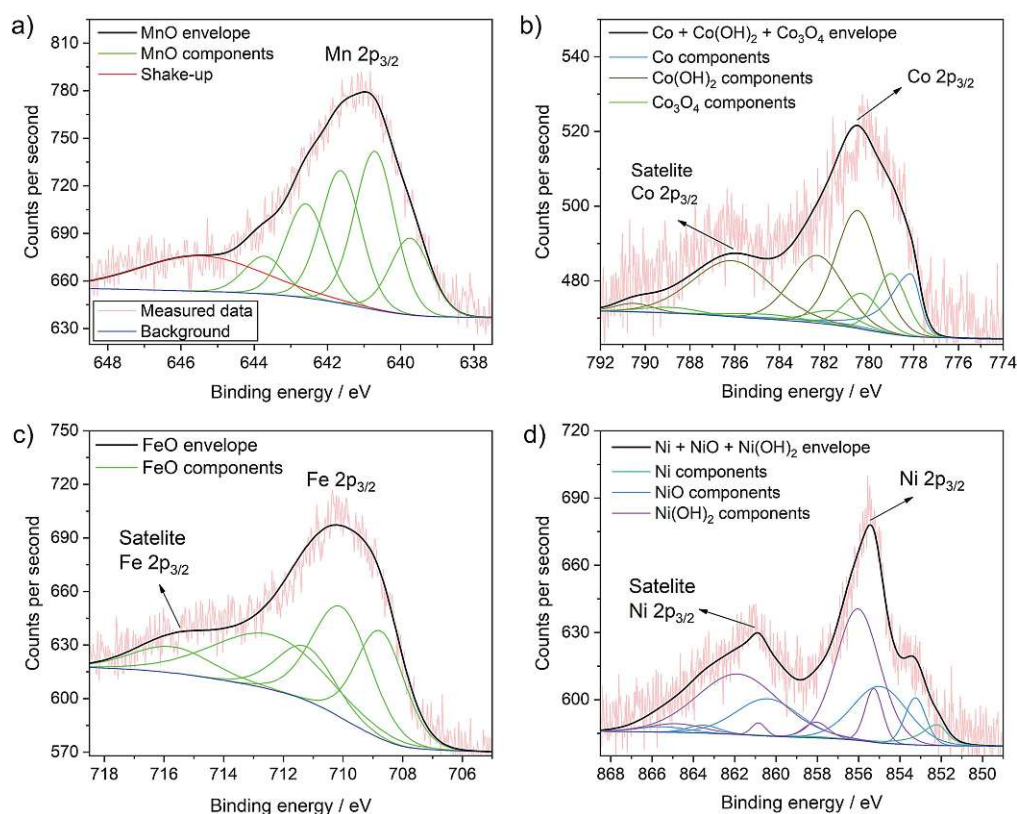
This journal is © The Royal Society of Chemistry 2019

J. Mater. Chem. A, 2019, **7**, 18568–18579 | **18573**

Fig. 5 Detailed XPS spectra of the MnO_x–TiO_2 (a), CoO_x–TiO_2 (b), FeO_x–TiO_2 (c) and NiO_x–TiO_2 (d) samples with the corresponding fits of the different species and mixture of species. Further fits are shown in Fig. S11.†

The Mn 2p spectrum most reliably confirms the presence of Mn^{2+} in the MnO_x–TiO_2 composite (Fig. 5a).[49] We can further clearly exclude the presence of Mn^0 species. Additionally fitting of Mn^{3+} – either from Mn_2O_3 as suggested by XRD, residual precursor salts or due to a partial hydroxylation, i.e. MnOOH – result in only a very low percentage (~2%) of the overall signal, which indicates that the concentration of Mn^{3+} – if present at all – is negligible (Fig. S11a and b†). Furthermore, considering multiplet splitting, a Mn^{4+} species is not needed for peak deconvolution.[49] Therefore, we can exclude the presence of Mn^{4+}, in contrast to previous reports on Mn-doped TiO_2.[50,51] In conclusion, Mn^{2+} is the major component in the MnO_x–TiO_2 composite with a negligible contribution of Mn^{3+} due to Mn_2O_3 or MnOOH.

The analysis of the Co 2p signal in Fig. 5b reveals that Co^{2+} and Co^{3+} species coexist in the CoO_x–TiO_2 composite, most likely in the form of oxides, mixed oxide or hydroxides. However, in contradiction to the pure salt XRD and TGA data, we cannot reliably exclude the formation of metallic Co species. The best fit was obtained for a combination of Co metal, $Co(OH)_2$, and Co_3O_4.

In the case of FeO_x–TiO_2 sample, shown in Fig. 5c, the Fe 2p spectrum clearly indicates the presence of Fe^{2+} with a characteristic satellite at 714 eV.[49] From these data, we can suggest that Fe^{3+} is only present as minority species, as we cannot observe

pronounced characteristic satellite features at 719 and 735 eV. This supports our previous findings that the thermal evolution of $Fe(acac)_3$ is strongly altered by the TiO_2 substrate resulting in the formation of partially reduced $Fe^{II}O$.

Finally, the XPS data for NiO_x–TiO_2 (Fig. 5d) show mainly Ni^{2+} in the form of NiO or $Ni(OH)_2$. Although not required (Fig. S11c†), the addition of a Ni^0 component improves the fit further and indicates the possible presence of a small fraction of metallic Ni in the final composition, which would also be expected from the data on the pure precursors.[49,52]

In summary, we have produced NiO_x–TiO_2, MnO_x–TiO_2, CoO_x–TiO_2 and FeO_x–TiO_2 composite samples with homogeneously distributed nanoparticles of uniform sizes (2–5 nm) as revealed by electron microscopy and EDX. The results further suggest that the MO_x NPs are of amorphous nature, in contrast to the data on pure precursors, thus indicating substrate effects. XPS analyses shows that Co likely coexists in a mixture of Co^{2+} and Co^{3+}, while major contributors of Mn and Fe species are of +2 oxidation state, again contrary to what has been observed for pure precursors. In the case of NiO_x–TiO_2, XPS additionally indicates a small proportion of metallic species, aside from Ni^{2+}.

Photocatalytic water splitting

We investigated the performance of all samples for photocatalytic water splitting, namely, hydrogen evolution reaction

32

(HER) and oxygen evolution reaction (OER), by means of sacrificial water splitting. To compare with literature, we used methanol as an electron donor to facilitate HER[53] and $AgNO_3$ as an electron acceptor to support OER.[54,55] Detailed description of the experimental procedure can be found in Experimental section.

Hydrogen evolution reaction

Fig. 6 shows H_2 evolution profiles (on-line H_2 evolution rate *vs.* time) of the as-prepared NiO_x–TiO_2, MnO_x–TiO_2, FeO_x–TiO_2 and CoO_x–TiO_2 composites from water–methanol mixtures under UV light. The results show that only NiO_x–TiO_2 was active towards HER. Hydrogen evolution rates of about 4 μmol h^{-1} were reached after 10 minutes of light exposure in our flow reactor (Fig. S12†). The rest of the composites showed no activity indicating incapability of the generated MnO_x, FeO_x and CoO_x species to act as co-catalysts for H^+ reduction, which is in stark contradiction to some of the literature reports.[34,41]

We have further investigated the active NiO_x–TiO_2 system in long run HER experiments to identify the maximum activity and investigate the performance stability. Fig. 6b shows a HER profile over 60 minutes under illumination: interestingly, no stable evolution rate was reached within this period; instead, the H_2 evolution rate continued to increase, reaching more than 13 μmol h^{-1} at the end of the illumination cycle. We purged the reactor with Ar to remove the reaction products and proceeded with UV illumination for another 14 h. Fig. 6c shows the resulting HER profile revealing two important observations: (a) the activity increased rapidly to a level of 13 μmol h^{-1} within the first hour of illumination, (b) the increase in activity continued in an almost linear fashion to reach rates as high as 27 μmol h^{-1} after 10 h.

This unusual behaviour indicates that either the catalytic sites of the NiO_x–TiO_2 system become more active or their number increases with time. Furthermore, it appears that this behaviour is triggered by light illumination. Although the Ni/ NiO system has been investigated as co-catalyst for HER before,[7,11,14,17,56] the question as to which Ni oxidation state is more active remains controversial. Our experimental setup is unique in that it allows for on-line activity detection within the first seconds of light illumination, and our data suggest that the increase in metallic Ni, which can gradually form from Ni^{2+} upon photoreduction, is likely the reason for the observed activity increase.[57] This was confirmed by XPS measurements of the NiO_x–TiO_2 composite recovered immediately after the HER experiment, which revealed a substantial increase in the relative content of Ni^0 compared to Ni^{2+} from 3.4 at% to 16.7 at% at the end of the illumination cycle (Table S3†). To the best of our knowledge, this has not been reported before. The results highlight the dynamics nature of this photocatalyst, and we
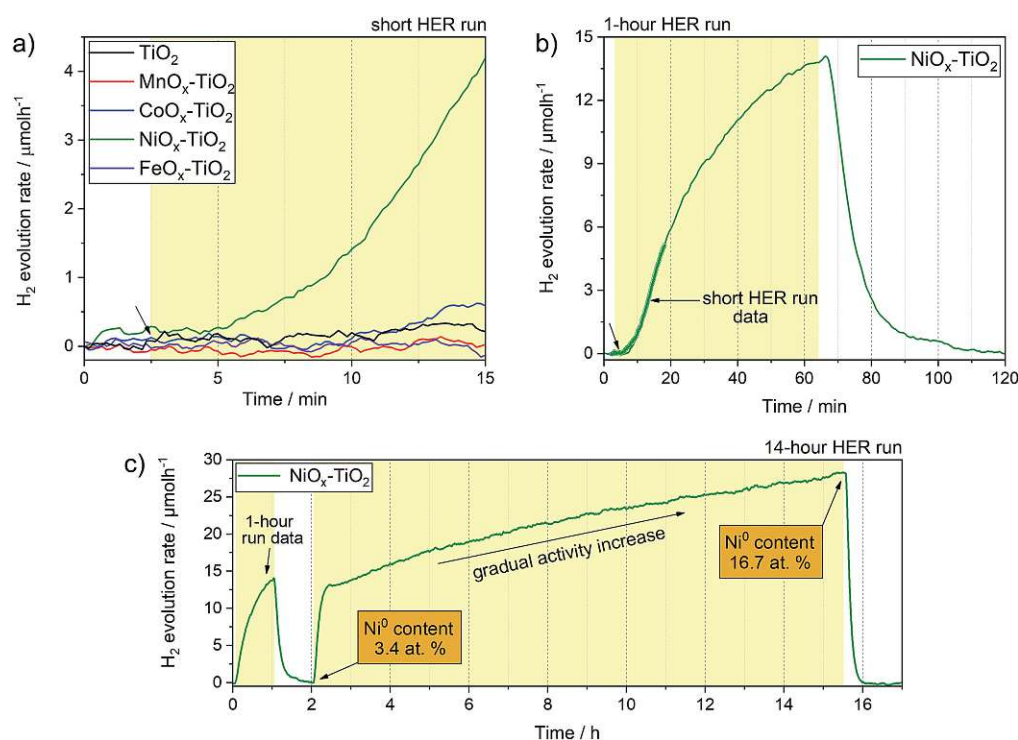

Fig. 6 (a) Short run HER profiles of the NiO_x−TiO_2, MnO_x−TiO_2, FeO_x−TiO_2 and CoO_x−TiO_2 composites along with the reference TiO_2 powder performed using flow-reactor. Arrow indicates the start of illumination, yellow box – illumination period. (b) 1 hour run HER profile of the active NiO_x−TiO_2 photocatalyst along with the corresponding short run data as well as (c) 14 hour run (long run) HER profile showing that the H_2 production rate slowly increases with increasing illumination time. The 1 hour and 14 hour runs have been performed during the same experiment. The reactor was purged with Ar for 1 h in between the runs to remove the reaction products.

This journal is © The Royal Society of Chemistry 2019

J. Mater. Chem. A, 2019, **7**, 18568–18579 | **18575**

33

emphasize that active species can form upon illumination not only during the first stages of a photocatalytic reaction, but even during extended periods of hours and days.

Based on our TGA, *in situ* XRD and XPS data, we further suggest that NiO_x–TiO_2 composites prepared at lower calcination temperatures (<350 °C) can offer a greater potential for photocatalytic HER as they preserve a higher fraction of metallic Ni species.

Oxygen evolution reaction

We have further tested the composites towards OER previously rarely reported for these series of co-catalysts. Again, we followed the typical conditions for sacrificial OER and used $AgNO_3$ as an electron acceptor as well as a closed reactor system (see Experimental section and Fig. S12†). Fig. 7a reveals that three of the composite photocatalysts were active towards water oxidation, namely, FeO_x–TiO_2, CoO_x–TiO_2 and NiO_x–TiO_2, with the corresponding O_2 evolution rates reaching 34.3, 31.4 and 19.9 µmol h^{-1} after 20 min of illumination, respectively (see Fig. 7b). Noteworthy, pure TiO_2 powder without being loaded with any co-catalyst also exhibited respectable OER performance with the rate of 20.8 µmol h^{-1}, suggesting that surface of bare TiO_2 – with Ti^{4+} in d^0 type configuration – also provides suitable sites for water oxidation.[58] In contrast to other samples, the OER on TiO_2 was completely suppressed in the case of the MnO_x–TiO_2 composite.

Enhanced OER rates recorded in the presence of surface-attached CoO_x and FeO_x species can be ascribed to their active role in facilitating the charge separation and/or acting as water oxidation sites; in line with other literature reports where Co- and Fe-oxide-based co-catalysts have been shown to possess some photo- or electrocatalytic activity towards water oxidation.[11,59–63] To further elaborate on the active state and stability of these OER-active co-catalysts, we performed XPS measurements after the OER experiments (see ESI†). Fig. S13a† clearly suggests that some of the initial Fe^{2+} species of the FeO_x–TiO_2 composite oxidized during the photocatalytic process resulting

in a higher proportion of Fe^{3+}, as can be seen from the appearance of the characteristic satellites at 719 and 737 eV. Nevertheless, judging from the stable rate of O_2 evolution in Fig. 7a, we can suggest that no severe activation/deactivation process has taken place during the reaction and Fe^{2+} can still be considered as one of the OER-active components of the composite. With regard to CoO_x–TiO_2, XPS data of the sample after OER (Fig. S13b†) show that oxidation of the initially present Co species takes place during the photocatalytic reaction without any apparent activity loss. This suggests that high-oxidation state Co species are likely to be responsible for the OER performance. Elucidation of this question will require further dedicated investigations.

In the case of the NiO_x–TiO_2 composite, we observed no apparent increase in OER rate compared to bare TiO_2, despite the fact that NiO – that is present in our composite – and various Ni oxyhydroxides are known for their excellent water oxidation performance.[64,65] However, it has also been reported, that performance of Ni-based co-catalysts is strongly dependent on the calcination conditions and may need to be optimized to obtain desired OER rates. Nevertheless, the as-prepared NiO_x–TiO_2 composite containing both metallic Ni and NiO can be considered as a promising candidate for overall water splitting as it contains both HER and OER sites whose initial ratio can be controlled during the synthesis.

The rather negative result obtained for the MnO_x–TiO_2 case (Fig. 7b) can be related to well-known sensitivity of Mn-based oxides OER performance to their structure and Mn oxidation state.[66] Our XPS data suggest that the MnO_x co-catalyst NPs are mainly composed of Mn^{2+}, while a number of literature reports suggest that the presence of Mn^{3+} and Mn^{4+} is required for the accumulation of the required oxidizing equivalents necessary to drive water oxidation.[67,68] Judging from our TGA and *in situ* XRD data, we could suggest that much higher calcination temperatures (>600 °C) will be required to produce MnO_x species with higher content of Mn in higher oxidation states, that could be of interest for photocatalytic OER.
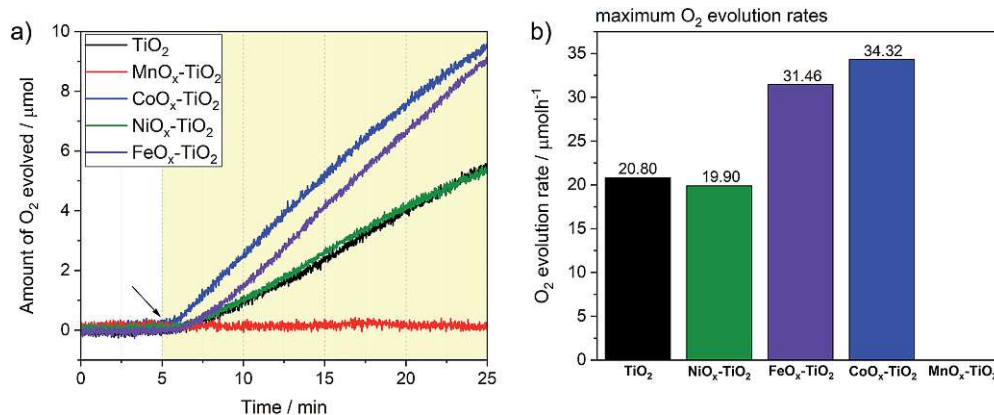

Fig. 7 (a) OER evolution profiles for the NiO_x–TiO_2, MnO_x–TiO_2, FeO_x–TiO_2 and CoO_x–TiO_2 composites along with the reference TiO_2 powder performed using a closed reactor. The arrow indicates start of illumination. The coloured area corresponds to the illumination period. (b) Bar chart presenting maxima of O_2 evolution rates extracted from derivative analysis.

Conclusions

In this contribution, we systematically studied a series of NiO_x–TiO_2, MnO_x–TiO_2, CoO_x–TiO_2 and FeO_x–TiO_2 photocatalysts prepared by wet impregnation of $M(acac)_x$ salts (M = Ni, Fe, Mn and Co) onto high surface area TiO_2 NP substrate, followed by their oxidative decomposition. A combination of TGA, *in situ* XRD, ATR-FTIR as well as XPS revealed strong differences in thermal decomposition of the $M(acac)_x$–TiO_2 in comparison to pure $M(acac)_x$ salts. When loaded on TiO_2, the M precursors undergo decomposition at substantially lower temperatures, *via* different mechanism and often result in the formation of otherwise unstable M species, such as Fe^{2+} in the case of FeO_x–TiO_2. Consequent SEM and TEM analyses along with EDX mappings showed that the morphology of the created MO_x–TiO_2 composites feature small (1–5 nm) MO_x NPs homogeneously decorating the TiO_2 NPs. In addition, XRD and ED suggested that the MO_x co-catalysts prepared at 350 °C are of amorphous nature, while combined Raman and PL spectra indicate the possibility of M doping and strong electronic communication between the components of the composites.

We further evaluated the potential of the composites towards photocatalytic water splitting reactions. We show that among all samples, NiO_x–TiO_2 was active towards hydrogen evolution reaction (HER) with metallic Ni species – gradually generated *in situ* upon light illumination – being the active site. In contrast, FeO_x–TiO_2, CoO_x–TiO_2, and NiO_x–TiO_2 were all active towards oxygen evolution reaction (OER), featuring water oxidation ability in descending order. XPS data of the OER-active samples after reaction indicated that mild oxidation of M species takes place during the course of the photocatalytic experiment. However, Fe^{2+} species could still be considered as one of the OER-active components of the FeO_x–TiO_2 composite.

This contribution provides a systematic study on the specifics of the wet chemistry-based synthesis of small MO_x NPs directly onto the surface of TiO_2, which can be expanded to other inorganic substrates. Besides, we show that some of the prepared catalysts are of interest for photocatalytic water splitting reactions and that their activity could be further controlled by modifying synthetic conditions.

Experimental section

Chemicals

All materials used for the syntheses were obtained from commercial suppliers. As such, P25 TiO_2 from Degussa, $Mn(acac)_2$ from Sigma-Aldrich (99.8% pure), $Co(acac)_3 \cdot 3H_2O$ from Fluka (99.9% pure), $Ni(acac)_2 \cdot 2H_2O$ from Sigma-Aldrich (99.8% pure) and $Fe(acac)_3$ from Sigma-Aldrich (97% pure). The used solvent for the syntheses were deionized water and absolute ethanol (from Chem-Lab NV) and for photocatalytic experiments deionized water and HPLC-gradient grade methanol (from VWR).

Synthesis of the composites

The metal oxide species were synthesized directly on the surface of TiO_2 NPs following the wet impregnation – thermal decomposition method depicted in Fig. 1a. The general synthesis procedure used for all samples included (a) suspending the TiO_2 powder (400 mg, 5 mmol) in 20 mL of ethanol; (b) stirring the suspension for 10 minutes; (c) adding the corresponding precursor salt: $Mn(acac)_2$ (0.248 mmol, 62.7 mg), $Co(acac)_3$ (0.297 mmol, 75.6 mg), $Ni(acac)_2$ (0.113 mmol, 29.1 mg), or $Fe(acac)_3$ (0.26 mmol, 92.0 mg); and (d) subjecting the resulting suspension to sonication to assist salt dissolution and homogenisation of the suspension components. The resulting mixture was left stirring at 60 °C until complete evaporation of the solvent. The remaining powder was then dried at 80 °C for 5 h and grinded. Afterwards, the samples were heat-treated at 350 °C for 10 h in ambient air to generate the corresponding oxides resulting in MO_x–TiO_2 composites.

Characterisation methods

Scanning electron microscopy (SEM) images were acquired using FEI Quanta 250 FEG at 200 keV scanning electron microscope to obtain visual information on the morphology of the samples. Typically acceleration voltage of 2 kV and secondary electron detection mode were used. Energy dispersive X-ray spectroscopy (EDX) was performed using the SEM to obtain elemental maps.

Transmission electron microscopy (TEM) images were obtained using FEI TECNAI F20 transmission electron microscope equipped with a field emission gun in bright field mode using 200 kV acceleration voltage. The sample was prepared from a suspension in ethanol without ultrasonication, using a copper holey carbon coated grids (Plano, 200 mesh).

X-ray diffraction (XRD) was performed using an XPERT III: PANalytical XPert Pro MPD (Θ–Θ Diffractometer) for the *in situ* experiments and an XPERT II: PANalytical XPert Pro MPD (Θ–Θ Diffractometer) for the *ex situ* experiments. The sample was placed on a sample holder and irradiated with a Cu X-ray source (8.04 keV, 1.5406 Å). The signal was acquired with Bragg–Brentano Θ/Θ-diffractometer geometry ranging from 5° to 80° degrees. The detector system was a semiconductor X'Celerator (2.1°) detector. The *in situ* experiment was performed under air flow and temperatures ranging from 25 °C to 800 °C.

The thermogravimetric (TGA) measurements were carried out on a PerkinElmer Thermogravimetric Analyser TGA 8000. The samples were placed into an Al_2O_3 crucible and heated with a dynamic method at a heating rate of 5 °C min^{-1} under air from 25 °C to 800 °C.

The chemical composition of the samples was obtained with X-ray photoelectron spectroscopy (XPS) using a custom-built SPECS XPS-spectrometer equipped with a monochromatised Al-K$_\alpha$ X-ray source (μ 350) and a hemispherical WAL-150 analyser (acceptance angle: 60°). All samples were mounted onto the sample holder using double-sided carbon tape. Pass energies of 100 eV and 30 eV and energy resolutions of 1 eV and 100 meV were used for survey and detail spectra, respectively (excitation energy: 1486.6 eV, beam energy and spot size: 70 W onto 400 μm, angle: 51° to sample surface normal, base pressure: 5×10^{-10} mbar, pressure during measurements: 2×10^{-9} mbar). To reduce charging effects, a broad-spot low energy

35

electron source (SPECS FG 22 flood gun, 8–12 eV/15–30 μA) was used for charge compensation in some samples (containing Mn and Fe). Data analysis was performed using CASA XPS software, employing transmission corrections (as per the instrument vendor's specifications), Shirley backgrounds and Scofield sensitivity factors. Charge correction was applied so the adventitious carbon peak (C–C peak) was shifted to 284.8 eV binding energy (BE). All content values shown are in units of relative atomic percent (at%), where the detection limit in survey measurements usually lies around 0.1–1 at%, depending on the element. For the attenuated total reflection Fourier-transform infrared spectroscopy (ATR-FTIR) measurements a PerkinElmer FTIR Spectral UATR-TWO with a spectrum two Universal ATR (Single Reflection Diamond) accessory was used.

Fluorescence steady state measurements of the TiO_2 and MO_x–TiO_2 NPs were carried out using PicoQuant FluoTime 300 spectrophotometer. For PL spectra, the excitation source was Coaxial UV-Xe arc lamp (ozone free – with 300 W power) coupled with a computer-controlled double-grating monochromator and the detection system comprised of PMA Hybrid 07 detector and a high resolution emission double monochromator. For all the measurements, the excitation wavelength was kept to be the 377 nm (corresponding to 3.29 eV photon energy), and the PL data was collected using the EasyTau2 software.

Raman measurements were conducted with LabRAM HR800 from Horiba. Ne:YAG diode was used as the 532 nm laser source and the characteristic Raman peak of Si at 520.8 cm^{-1} was used as the calibration peak. The laser intensity was keep at 5 mW.

Photocatalytic experiments

Hydrogen evolution experiments were performed using a top irradiation gas-flow slurry type home-made reactor equipped with a LED lamp light source centred at 365 nm (Thorlabs). In a single experiment, 10 mg of a powdered photocatalyst was dispersed in 50 mL 50 vol% MeOH–water solution by stirring. During the experiment, the reactor was continuously purged with argon (flow rate of 30 mL min^{-1}, controlled with a mass flow controller from MCC-Instruments) to deliver the gaseous products to the online gas analyzer (X-Stream, Emerson Process Management) equipped with a thermal conductivity detector (TCD) for H_2 quantification. The temperature of the reactor was kept constant through a water cooling system (Lauda). In a single experiment, the suspension was first stirred for 30 min in the dark, then illuminated for 15 min. A typical H_2 evolution profile (e.g. in Fig. 6) obtained with our flow reactor includes an "induction" period (increasing H_2 evolution rate during the first 5–10 min) that is due to the fact the H_2 gas first needs to fill the dead volume (e.g. reactor volume, tubing volume) to reach the detector. When the illumination is stopped, the signal returns to its baseline. The H_2 evolution rates were normalized by subtracting the H_2 evolution rate measured in the blank experiment (no catalyst present in the MeOH–H_2O mixture) as a result of UV-assisted MeOH oxidation (photo-reforming).

Oxygen evolution experiments were performed in a home-made top illumination closed reactor using the same light source and water cooling system. The experiments were carried out using a 2 mL water solution containing 1 mg of a photo-catalyst (dispersed via stirring) and $AgNO_3$ (0.1 M) as electron scavenger. The reactor was first purged with Ar to remove the air and the O_2 detection was started using a fibre-optic oxygen sensor (PyroScience) inserted in the reaction volume. The suspension was stirred for 30 min in the dark to allow for O_2 signal stabilization followed by 20 minutes of UV illumination.

Conflicts of interest

There are no conflicts to declare.

Acknowledgements

Notes and references

1 H. Ibrahim, A. Ilinca and J. Perron, Renewable Sustainable Energy Rev., 2008, 12, 1221–1250.
2 K. T. Møller, T. R. Jensen, E. Akiba and H. Li, Prog. Nat. Sci.: Mater. Int., 2017, 27, 34–40.
3 S. E. Hosseini and M. A. Wahid, Renewable Sustainable Energy Rev., 2016, 57, 850–866.
4 P. Millet, in Hydrogen Production, John Wiley & Sons, Ltd, 2015, pp. 63–116.
5 M. Serban, M. A. Lewis, C. L. Marshall and R. D. Doctor, Energy Fuels, 2003, 17, 705–713.
6 B. E. Logan, Environ. Sci. Technol., 2004, 38, 160A–167A.
7 I. Roger, M. A. Shipman and M. D. Symes, Nat. Rev. Chem., 2017, 1, 0003.
8 Nanocomposites for Visible Light-induced Photocatalysis, ed. M. M. Khan, D. Pradhan and Y. Sohn, Springer International Publishing, 2017.
9 Photocatalysis, https://www.crcpress.com/Photocatalysis-Principles-and-Applications/Ameta-Ameta/p/book/9781482254938, accessed January 22, 2019.
10 J. Schneider, D. Bahnemann, J. Ye, G. L. Puma and D. D. Dionysiou, Photocatalysis: Fundamentals and Perspectives, Royal Society of Chemistry, 2016.
11 X. Li, J. Yu, J. Low, Y. Fang, J. Xiao and X. Chen, J. Mater. Chem. A, 2015, 3, 2485–2534.
12 A. O. Ibhadon and P. Fitzpatrick, Catalysts, 2013, 3, 189–218.
13 M. Ni, M. K. H. Leung, D. Y. C. Leung and K. Sumathy, Renewable Sustainable Energy Rev., 2007, 11, 401–425.
14 T. Jafari, E. Moharreri, A. S. Amin, R. Miao, W. Song and S. L. Suib, Molecules, 2016, 21, 900.
15 Z. Zhang and J. T. Yates, Chem. Rev., 2012, 112, 5520–5551.
16 T. Kawai and T. Sakata, J. Chem. Soc., Chem. Commun., 1980, 694–695.

36

17 B. M. Hunter, H. B. Gray and A. M. Müller, Earth-Abundant Heterogeneous Water Oxidation Catalysts, *Chem. Rev.*, 2016, **116**(22), 14120–14136.

18 Sol-Gel Derived Nanomaterials and It's Applications, https://www.researchgate.net/publication/288630167_Sol-Gel_Derived_Nanomaterials_and_It's_Applications_A_Review, accessed January 22, 2019.

19 R. Nagarajan and T. Alan Hatton, *Nanoparticles: Synthesis, Stabilization, Passivation, and Functionalization*, American Chemical Society, 2008, vol. 996, pp. i–v.

20 H. Chen, X. Y. Liu, X. D. Hao and Y. X. Zhang, *Ceram. Int.*, 2016, **42**, 19425–19428.

21 P. Praveen, G. Viruthagiri, S. Mugundan and N. Shanmugam, *Spectrochim. Acta, Part A*, 2014, **120**, 548–557.

22 W. Xin, D. Zhu, G. Liu, Y. Hua and W. Zhou, *Synthesis and Characterization of Mn–C–Co-doped Nanoparticles and Photocatalytic Degradation of Methyl Orange Dye under Sunlight Irradiation*, https://www.hindawi.com/journals/ijp/2012/767905/, accessed January 22, 2019.

23 C. Karunakaran, P. Vinayagamoorthy and J. Jayabharathi, *Superlattices Microstruct.*, 2013, **64**, 569–580.

24 Y. Wan, Z. Xu, W. Chao and J. Zhang, *J. Exp. Nanosci.*, 2013, **8**, 782–787.

25 W. Liu, Z. Liu, G. Wang, X. Sun, Y. Li and J. Liu, *Sci. China Mater.*, 2017, **60**, 438–448.

26 S. G. Babu, P. Karthik, M. C. John, S. K. Lakhera, M. Ashokkumar, J. Khim and B. Neppolian, *Ultrason. Sonochem.*, 2019, **50**, 218–223.

27 A. M. Antolín, S. Contreras, F. Medina and D. Tichit, *Top. Catal.*, 2017, **60**, 1156–1170.

28 T. Harifi and M. Montazer, *Appl. Catal., A*, 2014, **473**, 104–115.

29 J. Lasek, Y.-H. Yu and J. C. S. Wu, *Environ. Technol.*, 2012, **33**, 2133–2141.

30 J.-D. Lin, S. Yan, Q.-D. Huang, M.-T. Fan, Y.-Z. Yuan, T. T.-Y. Tan and D.-W. Liao, *Appl. Surf. Sci.*, 2014, **309**, 188–193.

31 J. Yu, Y. Hai and B. Cheng, *J. Phys. Chem. C*, 2011, **115**, 4953–4958.

32 A. T. Montoya and E. G. Gillan, *ACS Omega*, 2018, **3**, 2947–2955.

33 P. D. Tran, L. Xi, S. K. Batabyal, L. H. Wong, J. Barber and J. S. C. Loo, *Phys. Chem. Chem. Phys.*, 2012, **14**, 11596–11599.

34 J. Si, S. Xiao, Y. Wang, L. Zhu, X. Xia, Z. Huang and Y. Gao, *Nanoscale*, 2018, **10**, 2596–2602.

35 H. Tada, Q. Jin, H. Nishijima, H. Yamamoto, M. Fujishima, S. Okuoka, T. Hattori, Y. Sumida and H. Kobayashi, *Angew. Chem., Int. Ed.*, 2011, **50**, 3501–3505.

36 H. Yu, H. Irie, Y. Shimodaira, Y. Hosogi, Y. Kuroda, M. Miyauchi and K. Hashimoto, *J. Phys. Chem. C*, 2010, **114**, 16481–16487.

37 A. Li, T. Wang, X. Chang, W. Cai, P. Zhang, J. Zhang and J. Gong, *Chem. Sci.*, 2016, **7**, 890–895.

38 M. Higashi, K. Domen and R. Abe, *J. Am. Chem. Soc.*, 2012, **134**, 6968–6971.

39 A. Singh, S. L. Y. Chang, R. K. Hocking, U. Bach and L. Spiccia, *Energy Environ. Sci.*, 2013, **6**, 579–586.

40 W.-T. Chen, A. Chan, D. Sun-Waterhouse, T. Moriga, H. Idriss and G. I. N. Waterhouse, *J. Catal.*, 2015, **326**, 43–53.

41 W. Wang, S. Liu, L. Nie, B. Cheng and J. Yu, *Phys. Chem. Chem. Phys.*, 2013, **15**, 12033–12039.

42 H. Yu, J. Tian, F. Chen, P. Wang and X. Wang, *Sci. Rep.*, 2015, **5**, 13083.

43 Z. Yan, X. Yu, Y. Zhang, H. Jia, Z. Sun and P. Du, *Appl. Catal., B*, 2014, **160–161**, 173–178.

44 M. Nolan, A. Iwaszuk and H. Tada, *Aust. J. Chem.*, 2012, **65**, 624–632.

45 B. Pal and M. Sharon, *Thin Solid Films*, 2000, **379**, 83–88.

46 S. A. Sadeek, *An. Asoc. Quim. Argent.*, 2005, **93**, 165–176.

47 Z. Lin, D. Han and S. Li, *J. Therm. Anal. Calorim.*, 2012, **107**, 471–475.

48 T. L. Barr and S. Seal, *J. Vac. Sci. Technol., A*, 1995, **13**, 1239–1246.

49 M. C. Biesinger, B. P. Payne, A. P. Grosvenor, L. W. M. Lau, A. R. Gerson, R. St and C. Smart, *Appl. Surf. Sci.*, 2011, **257**, 2717–2730.

50 M. Chandra Sekhar, B. Purusottam Reddy, S. V. Prabhakar Vattikuti, G. Shanmugam, C.-H. Ahn and S.-H. Park, *J. Cluster Sci.*, 2018, **29**, 1255–1267.

51 Q. R. Deng, X. H. Xia, M. L. Guo, Y. Gao and G. Shao, *Mater. Lett.*, 2011, **65**, 2051–2054.

52 M. C. Biesinger, B. P. Payne, L. W. M. Lau, A. Gerson and R. S. C. Smart, *Surf. Interface Anal.*, 2009, **41**, 324–332.

53 J. K. Stolarczyk, S. Bhattacharyya, L. Polavarapu and J. Feldmann, *ACS Catal.*, 2018, **8**, 3602–3635.

54 R. Niishiro, R. Konta, H. Kato, W.-J. Chun, K. Asakura and A. Kudo, *J. Phys. Chem. C*, 2007, **111**, 17420–17426.

55 G. Hitoki, T. Takata, J. N. Kondo, M. Hara, H. Kobayashi and K. Domen, *Chem. Commun.*, 2002, 1698–1699.

56 W. Zhang, Y. Li, X. Zeng and S. Peng, *Sci. Rep.*, 2015, **5**, 10589.

57 I. Majeed, M. A. Nadeem, E. Hussain, G. I. N. Waterhouse, A. Badshah, A. Iqbal, M. A. Nadeem and H. Idriss, *ChemCatChem*, 2016, **8**, 3146–3155.

58 J. Sato, N. Saito, H. Nishiyama and Y. Inoue, *J. Phys. Chem. B*, 2001, **105**, 6061–6063.

59 F. Meng, J. Li, S. K. Cushing, J. Bright, M. Zhi, J. D. Rowley, Z. Hong, A. Manivannan, A. D. Bristow and N. Wu, *ACS Catal.*, 2013, **3**, 746–751.

60 N. Zhang, J. Shi, S. S. Mao and L. Guo, *Chem. Commun.*, 2014, **50**, 2002–2004.

61 D. M. Jang, I. H. Kwak, E. L. Kwon, C. S. Jung, H. S. Im, K. Park and J. Park, *J. Phys. Chem. C*, 2015, **119**, 1921–1927.

62 M. Okazaki, Y. Wang, T. Yokoi and K. Maeda, *J. Phys. Chem. C*, 2019, **123**, 10429–10434.

63 M. S. Burke, S. Zou, L. J. Enman, J. E. Kellon, C. A. Gabor, E. Pledger and S. W. Boettcher, *J. Phys. Chem. Lett.*, 2015, **6**, 3737–3742.

64 H. Kato and A. Kudo, *J. Phys. Chem. B*, 2001, **105**, 4285–4292.

65 C. K. Mavrokefalos and G. R. Patzke, *Inorganics*, 2019, 7, 29.

66 R. Pokhrel, M. K. Goetz, S. E. Shaner, X. Wu and S. S. Stahl, *J. Am. Chem. Soc.*, 2015, **137**, 8384–8387.

67 M. Wiechen, M. M. Najafpour, S. I. Allakhverdiev and L. Spiccia, *Energy Environ. Sci.*, 2014, **7**, 2203–2212.

68 P. Kurz, *Top. Curr. Chem.*, 2016, **371**, 49–72.

This journal is © The Royal Society of Chemistry 2019

J. Mater. Chem. A, 2019, **7**, 18568–18579 | 18579

37

Electronic Supplementary Information

Immobilization of Co, Mn, Ni and Fe oxide co-catalysts on TiO₂ for photocatalytic water splitting reactions

Jasmin S. Schubert,[a] Janko Popovic,[a] Greta M. Haselmann,[a] Sreejith P. Nandan,[a] Jia Wang ,[a] Ariane Giesriegl,[a] Alexey S. Cherevan*[a] and Dominik Eder*[a]
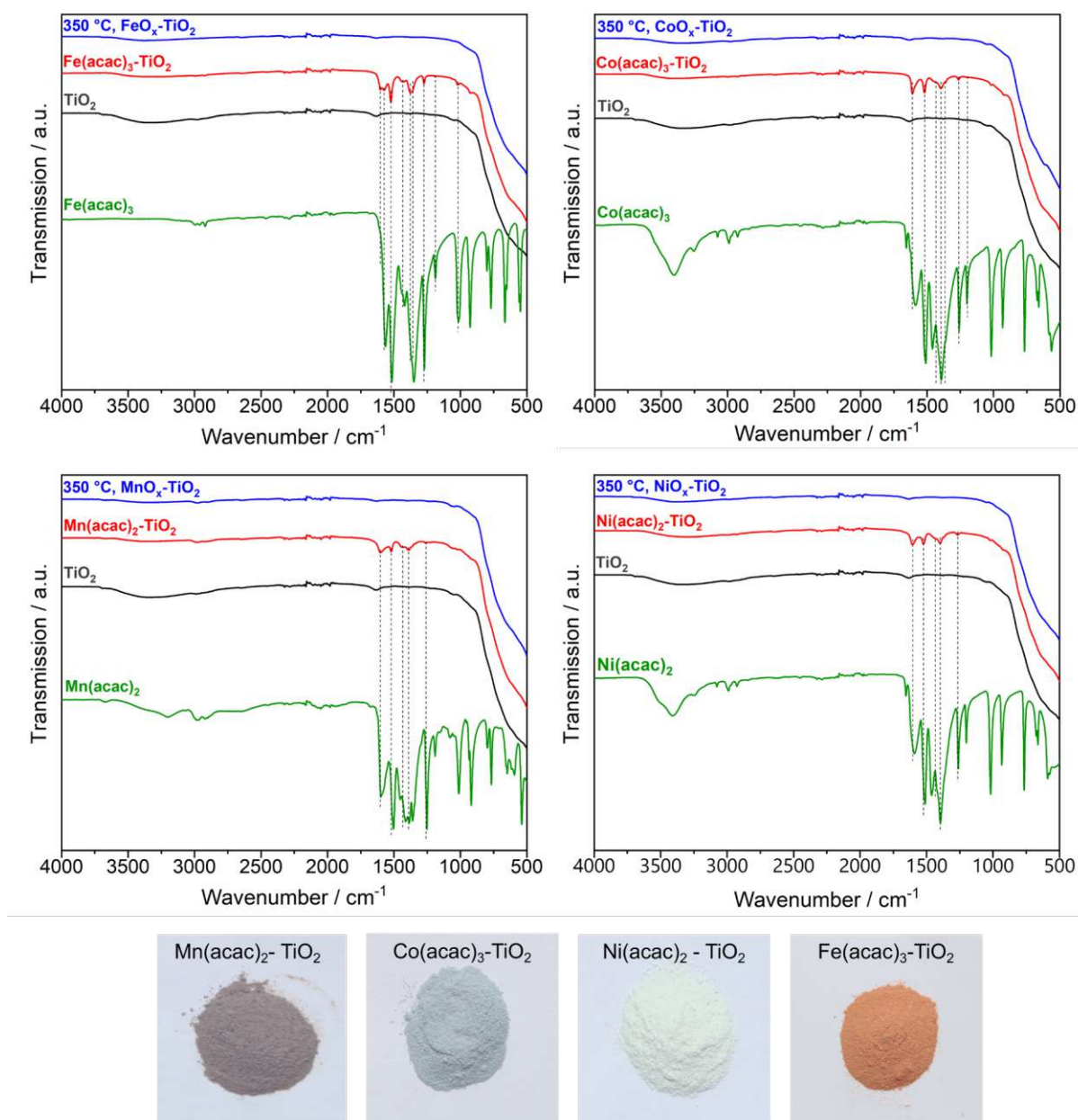
[a] Institute of Materials Chemistry, Technical University of Vienna, Getreidemarkt 9, 1060, Vienna, Austria

A list of supplementary Figures:

## A list of supplementary Tables:

39

Figure S1. *On the top:* ATR-FTIR spectra of the obtained composites along with the original salts, reference TiO_2, photocatalyst powder before calcination (M(acac)$_x$-TiO$_2$, with M corresponding to Co, Mn, Fe and Ni) and after calcination (MO$_x$-TiO$_2$). The reference M(acac)$_x$ salts show the characteristic C=O band (1572.5 cm^{-1} for Fe(acac)$_3$, 1589.2 cm^{-1} for Co(acac)$_3$, 1598.8 cm^{-1} for Mn(acac)$_2$ and 1594.0 cm^{-1} for Ni(acac)$_2$) and the fingerprint region from 1700 cm^{-1} to 500 cm^{-1} of the organic ligand. The presence of the acetylacetonate is also visible in the M(acac)$_x$-TiO$_2$ composites between 1700 cm^{-1} and 1120 cm^{-1}. The band at 3412.7 cm^{-1} for Ni(acac)$_2$ and 3409.5 cm^{-1} for Co(acaca)$_3$ correspond to the presence of crystalline water. After calcination at 350 °C, the absence of acetylacetonate signals can be assigned to its complete oxidation. *On the bottom:* photographs of the TiO$_2$ composites after impregnation with the different metal precursors before calcination.

3

40
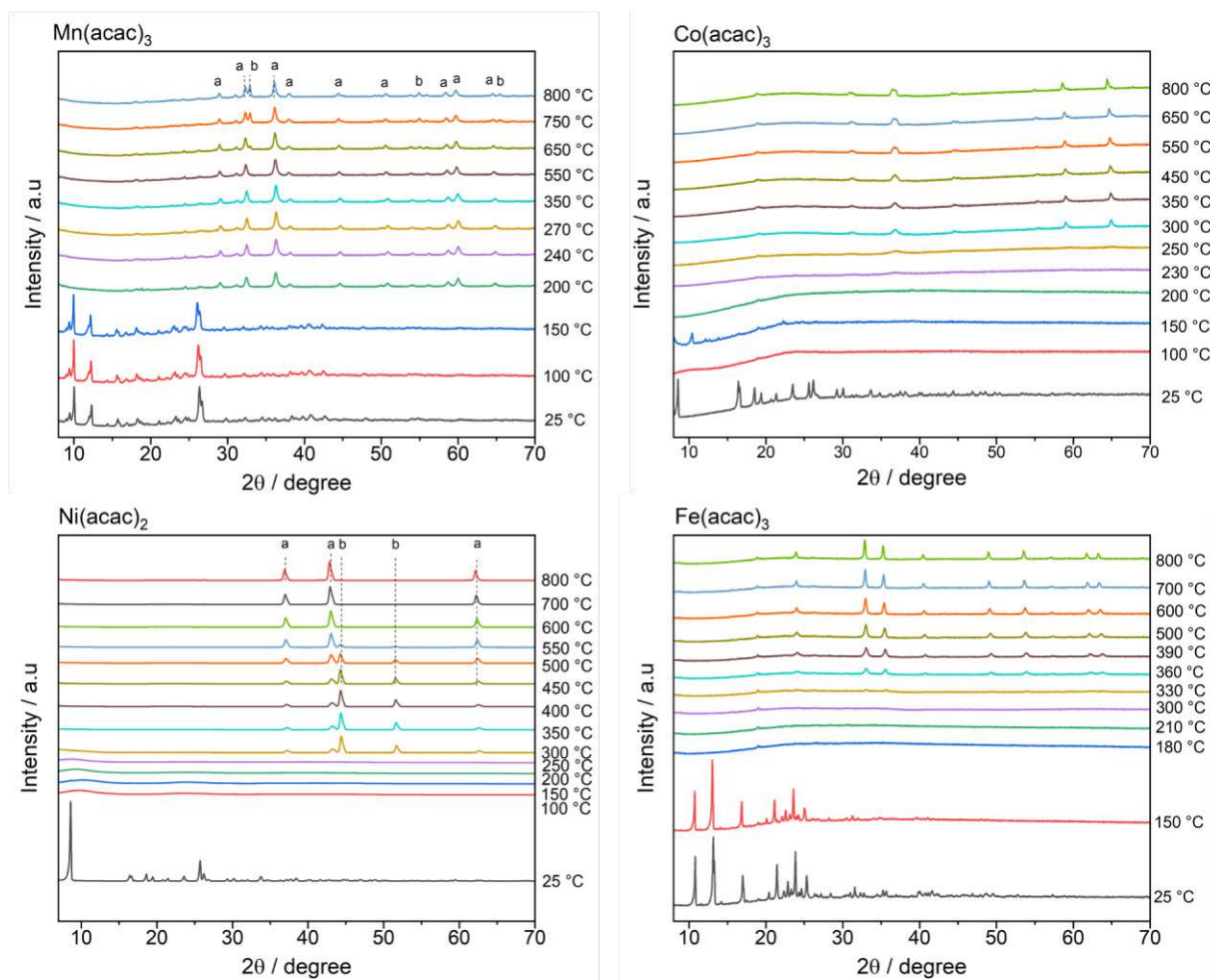
Figure S2. Complete data sets of the in situ XRD experiments performed for pure acetylacetonate precursors (Mn(acac)$_2$, Co(acac)$_3$, Ni(acac)$_2$ and Fe(acac)$_3$). The data was recorded at air with a 5°C/min heating rate and temperature range from 25 °C to 800 °C. Legend: **a**: Mn$_3$O$_4$, NiO , **b**: Mn$_2$O$_3$, Ni.

41
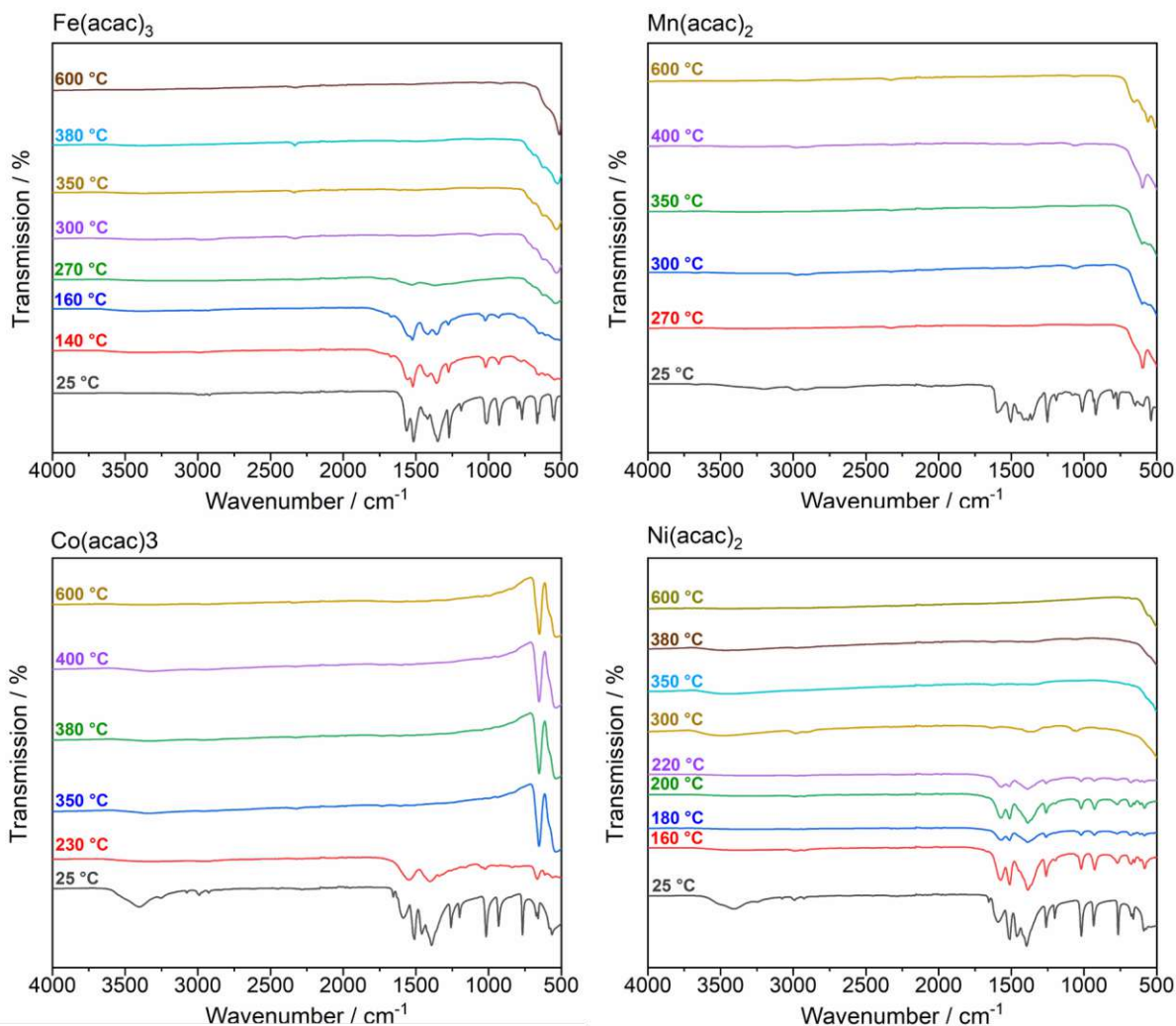
Figure S3. *Quasi in situ* ATR-FTIR spectra showing the thermal decomposition of the original salt precursors precursors ($Mn(acac)_2$, $Co(acac)_3$, $Ni(acac)_2$ and $Fe(acac)_3$) calcined at a temperature range from 25 °C to 600 °C.
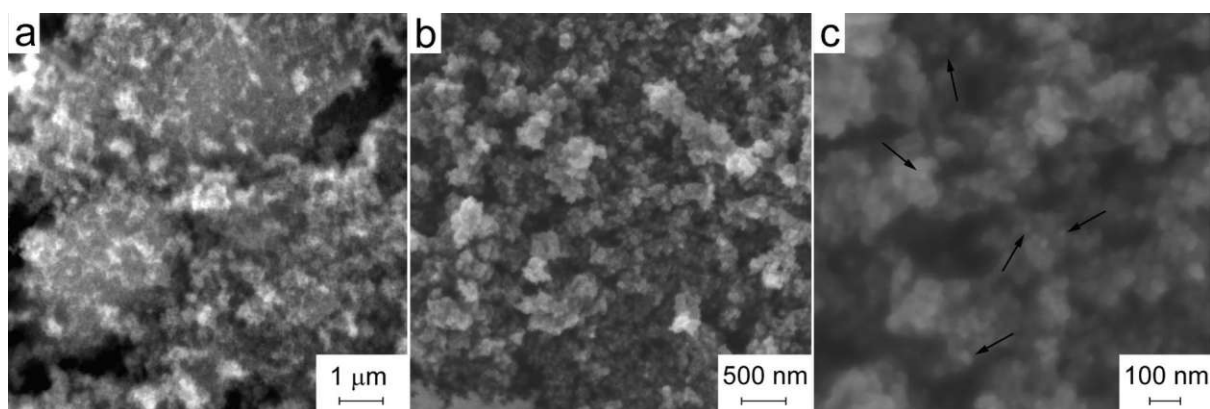
Figure S4. SEM of the FeO_x-TiO_2 sample representative for the rest of the composites. The images reveal the presence of nanoparticle aggregates corresponding to typical TiO_2 nanopowder. Image (c) shows individual TiO_2 nanoparticles with expected dimensions (20-50 nm). No foreign particles has been generated upon the composite formation.

42
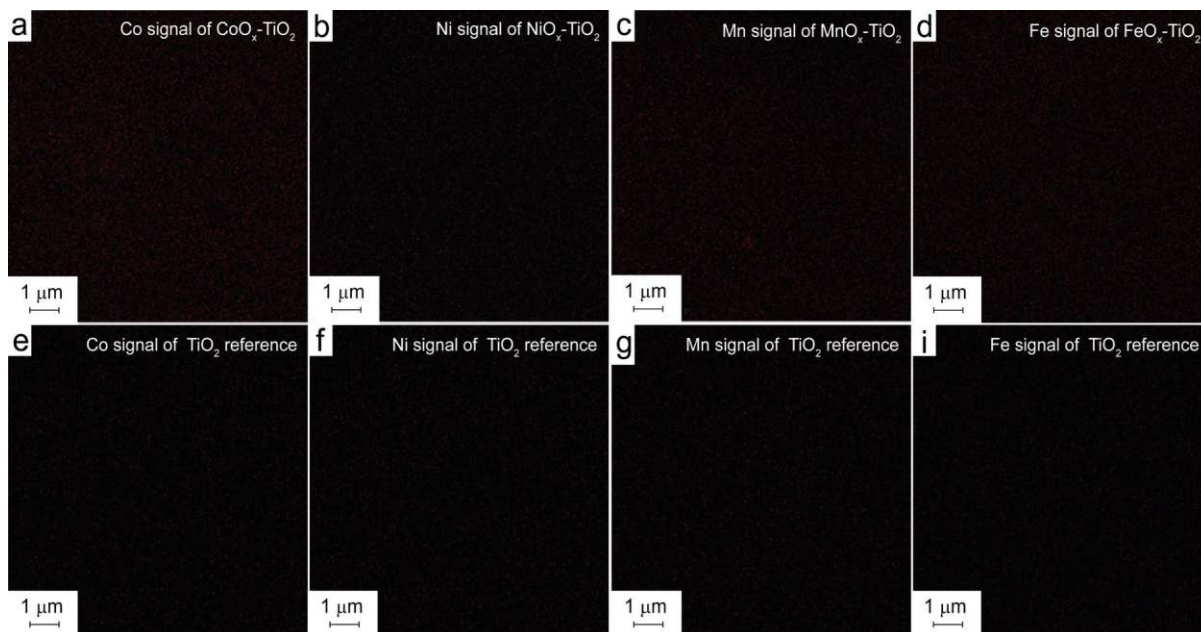
Figure S5. EDX mapping of the CoO_x-TiO_2 (a), NiO_x-TiO_2 (b), MnO_x-TiO_2 (c), and FeO_x-TiO_2 (d) nanocomposites along with the Co (e), Ni (f), Mn (g) and Fe (i) EDX signals acquired for pure reference TiO_2 powder. The images on the bottom are not related to the actual presence of these elements in TiO_2, but rather originate from the data acquisition process and "non-zero" background signal of the EDX scans.
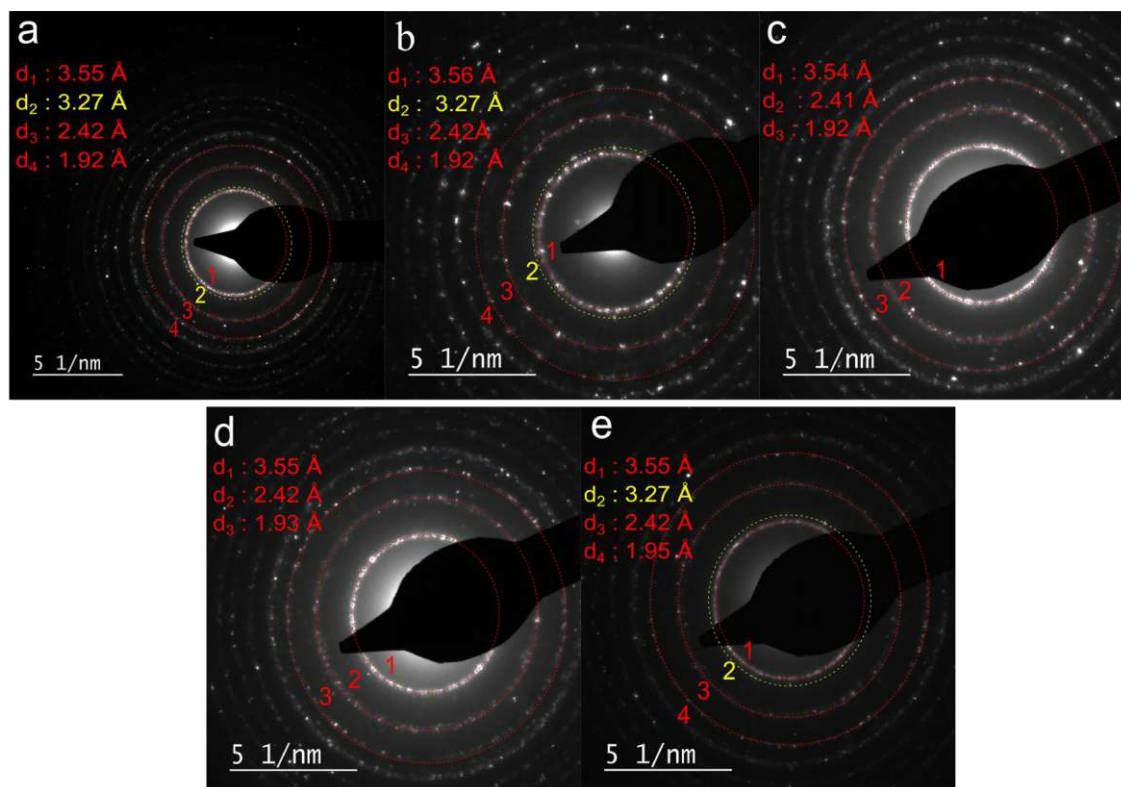
Figure S6. Electron diffraction (ED) pattern of the MO_x-TiO_2 composite. (a) Pure TiO_2, (b) NiO_x-TiO_2, (c) MnO_x-TiO_2, (d) FeO_x-TiO_2 and (e) CoO_x-TiO_2 revealing that all samples show the corresponding d values of the TiO_2 anatase phase (red) and rutile (yellow). The anatase phase is much more intense in all samples indicating a much higher concentration in the sample, while the rutile phase is present in a much lower amount, as can be seen by the much less intense signal.

6

43

Discussion of Raman data
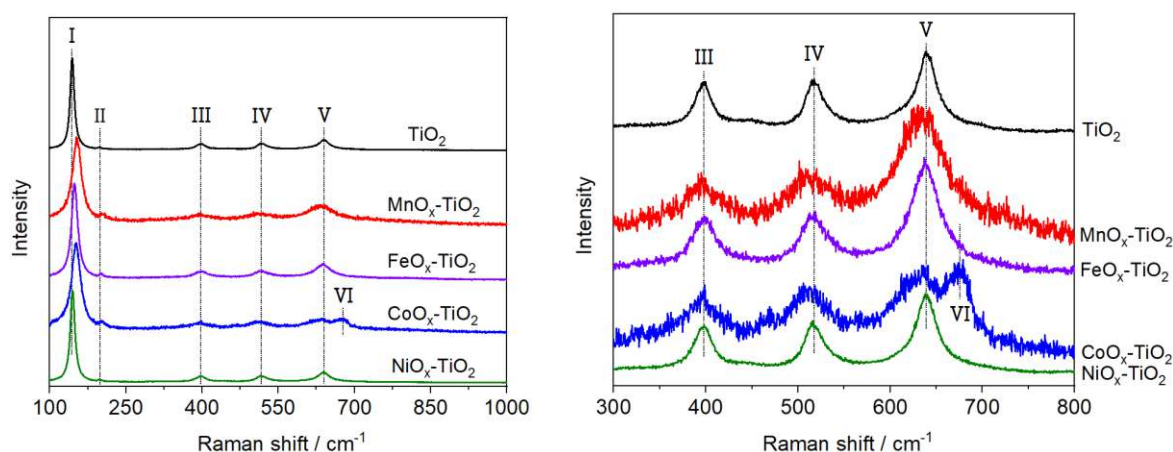
Figure S7. Raman spectra of the MnO$_x$-TiO$_2$, FeO$_x$-TiO$_2$, CoO$_x$-TiO$_2$ and NiO$_x$-TiO$_2$ composites along with the TiO$_2$ reference. (a) Overview spectra. (b) Magnified regions.

In TiO$_2$ reference spectrum, peaks present at around 144, 198, 397, 517 and 640 cm^{-1} can be assigned to the E$_g$, E$_g$, B$_1$, A$_{1g}$+B$_{1g}$ and E$_g$ modes of anatase phase, respectively (**Figure S7**), while the peak present at 448 cm^{-1} can be attributed to the E$_g$ mode of rutile phase, in line with TiO$_2$ composition. **Table S1** presents a summary of the peak positions and peak full-width at half-maxima (FWHM) of the strongest anatase E$_g$ band of the TiO$_2$ reference as well as the rest of the MO$_x$-TiO$_2$ composites:

Table S1. Peak analysis of the as-prepared MO$_x$-TiO$_2$ composites along with TiO$_2$.

	I (E$_g$)	II (E$_g$)	III (B$_{1g}$)	IV (A$_{1g}$+B$_{1g}$)	V (E$_g$)	VI	FWHM of peak I (E$_g$)
TiO$_2$	144	198	397	517	640		9.5
MnO$_x$-TiO$_2$	153	203	397	512	636		22.3
FeO$_x$-TiO$_2$	150	202	398	515	637		17.3
CoO$_x$-TiO$_2$	152	204	396	512	631	673	22.3
NiO$_x$-TiO$_2$	144	198	398	517	639		10.5

It can be seen from **Table S1** that, compared with TiO$_2$, all MO$_x$-TiO$_2$ samples demonstrate substantial peak shifts (blue-shifts for peak 'I' and 'II', red-shifts for peak 'IV' and peak 'V'), except for NiO$_x$-TiO$_2$ sample. As an example, the shift of the most intense E$_g$ band (I) can be considered.

It is known that the peak shift in Raman can be caused by different reasons, including the crystallite size,[1] crystal strain,[2] non-stoichiometry/doping,[3] surface adsorbed species,[1] etc. It is also known that the FWHM of the anatase E$_g$ mode (~ 146 cm^{-1}) reflects the stoichiometric ratio of O/Ti.[4] In the oxidation annealing experiment of TiO$_{2-x}$ performed by Parker and Siegel,[4] the authors have discovered that the FWHM above 13 cm^{-1} indicates that the oxide is oxygen deficient (x > 0); and the higher the FWHM value is, the higher does the oxygen deficiency (x) get. The substantially larger FWHM values of MO$_x$-TiO$_2$ (for Mn, Fe, Co) therefore suggest that the samples may have oxygen deficiency.

Overall, considering our composite systems, the data for MnO$_x$-TiO$_2$, CoO$_x$-TiO$_2$ and FeO$_x$-TiO$_2$ may suggest the presence of additional (apart from those observed in TEM) surface-adsorbed species on TiO$_2$, creation of O vacancies or bulk doping with M ions.

More specifically for each of the composites (see **Figure S7**):

MnOₓ-TiO₂:

The observed broadening/shoulder of the peak IV at 512 cm⁻¹ and peak V at 640 cm⁻¹ can be assigned to newly formed MnO_x species decorating TiO_2 surface. These bands may be caused by various MnO_x phases incl. manganite, pyrolusite or todorokite.[5] However, given the similarity in the band position of different MnO_x species,[5] especially in light of the amorphous nature of the MnO_x clusters in our composites, it seems incorrect to make any assumption about the possible phase or even oxidation state of Mn species. Besides this, MnO_x have low Raman activity and are known for their high sensitivity to the laser-induced heating, which can easily cause shifts and broadening of the Raman peaks and thus unreliable interpretation of the Raman data.

FeOₓ-TiO₂:

Compared with the Raman spectra of TiO_2, no additional band corresponding to FeO_x have been detected. On the other hand, the observed peak broadenings of TiO_2 bands is also unlikely caused by the potential Raman bands of FeO_x due to the position mismatch. No further conclusions can be made.

CoOₓ-TiO₂:

Additional shoulder and peak arising at 470 cm⁻¹ and 673 cm⁻¹, respectively, can be assigned to the Co_3O_4,[6] in line with our expectations. Compared with the standard position of the A_{1g} band of crystalline Co_3O_4 expected at 680 cm⁻¹, the shifted vibrational band at 673 cm⁻¹ of our CoO_x-TiO_2 may indicate for the highly defective structure,[6] in line with the amorphous nature, surface distribution and mixed composition of our CoO_x clusters. In addition, referring to XPS data, Co^{2+} could be present as dopant in the TiO_2 lattice. Due to the larger ionic radius of Co^{2+} (0.885Å), substitutional Co^{2+} dopants would tend to distribute on the surface of TiO_2, which would further lead to the formation of surface oxygen vacancies and surface disorder reflected in the shift of the TiO_2 E_g band in the Raman spectra.[7] Surface Co^{2+} species could also take part in the observed OER.[7]

NiOₓ-TiO₂:

Especially interesting result was observed for NiO_x-TiO_2 composites whose Raman spectra did not resemble the behaviour observed for the rest of the composites (i.e. peak shifts and broadening of main TiO_2 bands), but looked rather identical to the reference TiO_2 powder.

Typically, signal broadening, decreased intensity and the peak shifts of TiO_2 bands may be indicative of the presence of doping, oxygen vacancies and other structural defects and disorders as well as crystal strain and surface adsorbed species. As mentioned before, some of these effects can take place in our MO_x-TiO_2 composites, but, surprisingly, there is no indication of these for the NiO_x-TiO_2 sample. Why does not this particular samples exhibit this kind of behaviours that could be expected for surface-immobilized amorphous MO_x species?

According to our TEM results, NiO_x-TiO_2 sample features extremely small, but well defined NPs with the size of about 1 to 2 nm. Such homogeneity of the particle size and their fine distribution may indicate that the formed NiO_x NPs are thermodynamically stable and have reached a certain optimal size during the precursor decomposition, followed by nucleation and growth of the NiO_x. If this process is energetically favourable, all Ni species would be consumed to form these NPs and one could expect neither Ni incorporation into the TiO_2 matrix (doping) nor presence of atomic Ni-based species over the TiO_2 surface, thus explaining no shifts or peak broadenings of the substrate TiO_2. Further investigation is required to understand this exceptional behaviour.

45
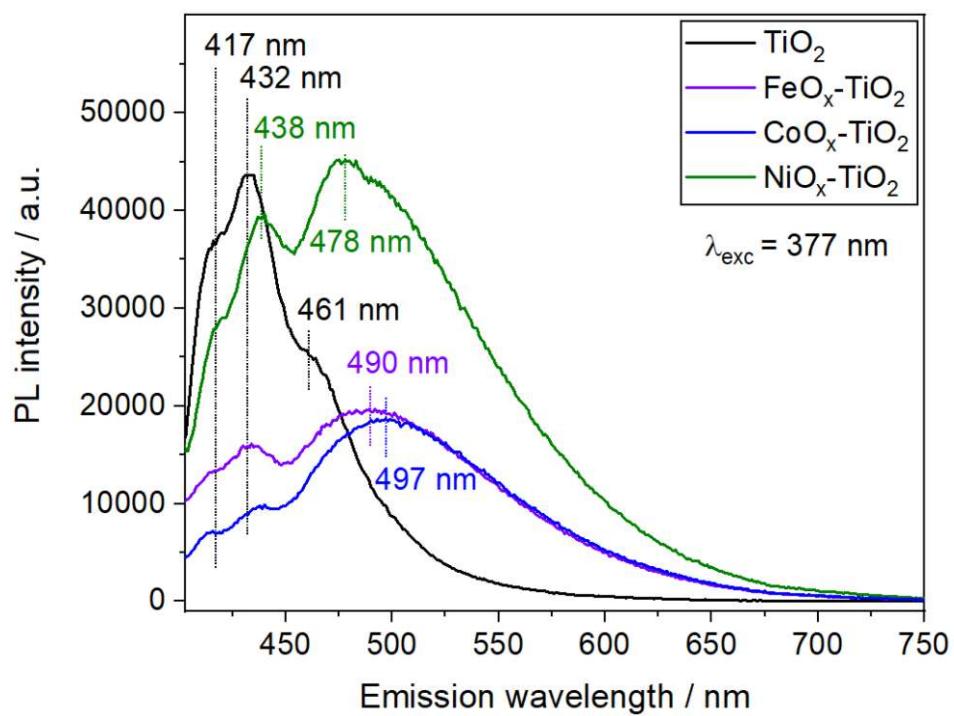
**Figure S8.** Steady-state photoluminescence (PL) spectra of the FeO$_x$-TiO$_2$, CoO$_x$-TiO$_2$ and NiO$_x$-TiO$_2$ composites along with the TiO$_2$ reference.

9

46

## Discussion about the crystallinity of the obtained MO$_x$ species

To elucidate a possible reason why the resulting composites feature amorphous MO$_x$ NPs, we have subjected the pure Ni(acac)$_2$ salt precursor to the same synthetic procedure than the composites (but without TiO$_2$ present) and analysed the dried product after solvent evaporation with XRD. The data in **Figure S9b** revealed that indeed the salt losses its crystalline structure after being recollected as a powder. This, in turn, can explain why the resulting oxides after calcination may be of amorphous nature. The amorphous nature was also confirmed by synthesised model composites - using Ni(acac)$_2$-TiO$_2$ - with an increased amount of Ni(acac)$_2$ up to 24.4 wt. %. The x-ray diffractograms of these model systems showed only the presence of TiO$_2$ (rutile and anatase, **Figure S9b** and **c**) for both thermal treated and untreated samples. Thus, with these model system investigations, it can be confirmed that the generated metal species in our composites are indeed amorphous.
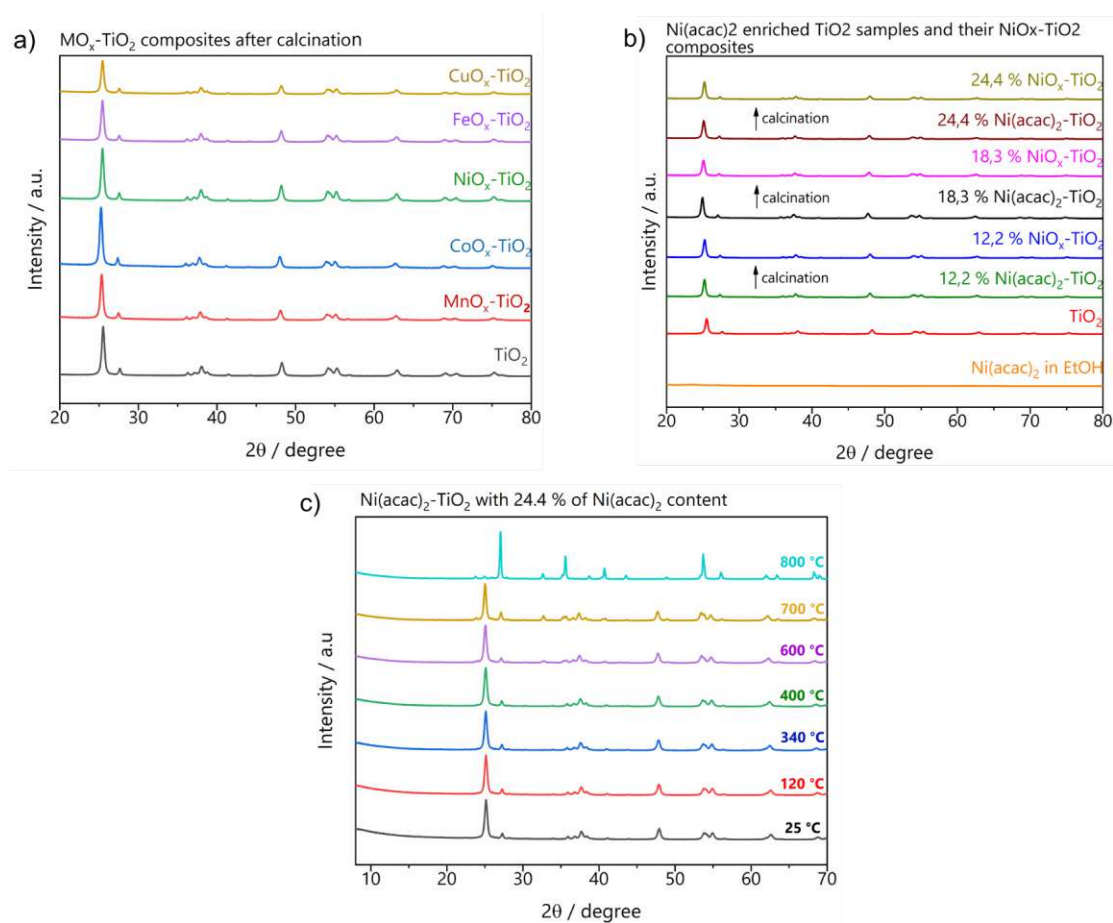
Figure S9. (a) XRD data of the MO$_x$-TiO$_2$ composites (prepared at 350 °C) and the TiO$_2$ reference to demonstrate the incapability of XRD to detect the newly deposited species. (b) Pure TiO$_2$ as reference material and the corresponding Ni(acac)$_2$-TiO$_2$ as well as NiO$_x$-TiO$_2$ composites after calcination demonstrating that even higher precursor loadings do not yield XRD signals that can be attributed to NiO$_x$ species. The diffractogram on the bottom corresponds to the Ni(acac)$_2$ salt after dissolution in ethanol showing that the originally crystalline salt loses its crystal structure after being recollected. (c) *In situ* XRD data of the Ni(acac)$_2$-TiO$_2$ composite with 24.4 wt. % Ni(acac)$_2$ content (heating rate 5°C/min at air) from 20 °C to 800 °C: only signals corresponding to TiO$_2$ (anatase and rutile) are visible in the spectra. Importantly, XRD profile starts changing (new peaks appear) above roughly 500 °C, which is exclusively related to gradual anatase-to-rutile conversion.

47
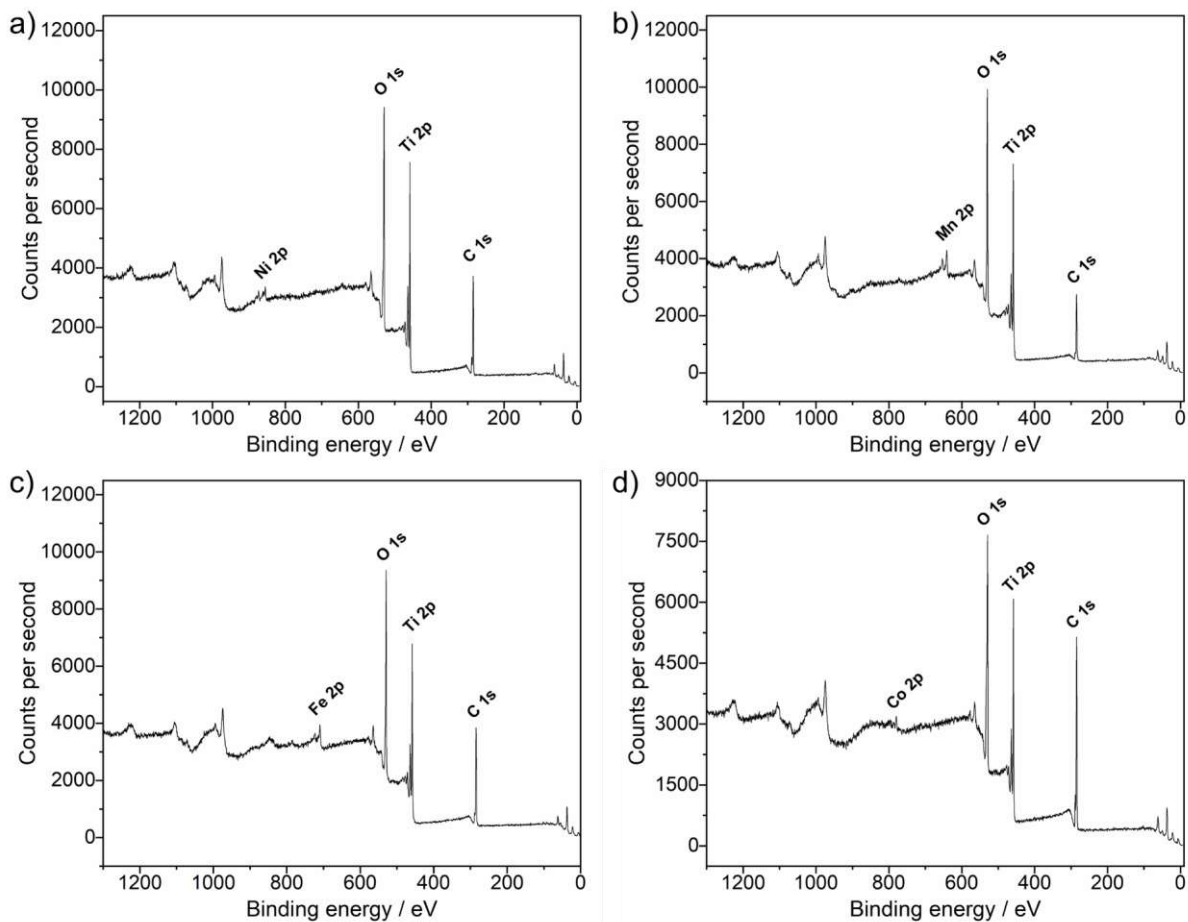
Figure S10. Survey XPS spectra of the (a) NiO_x -TiO_2, (b) MnO_x -TiO_2, (c) FeO_x -TiO_2 and (d) CoO_x -TiO_2 composites.
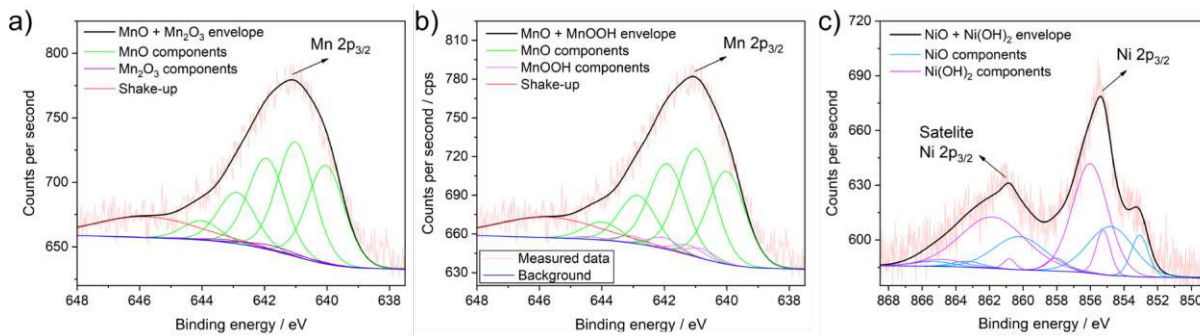
Figure S11. XPS spectra with the corresponding fits. a) and b) 2p Mn from the MnO_x-TiO_2 composite. c) Ni 2p spectra of NiO_x-TiO_2 composite.

11

48
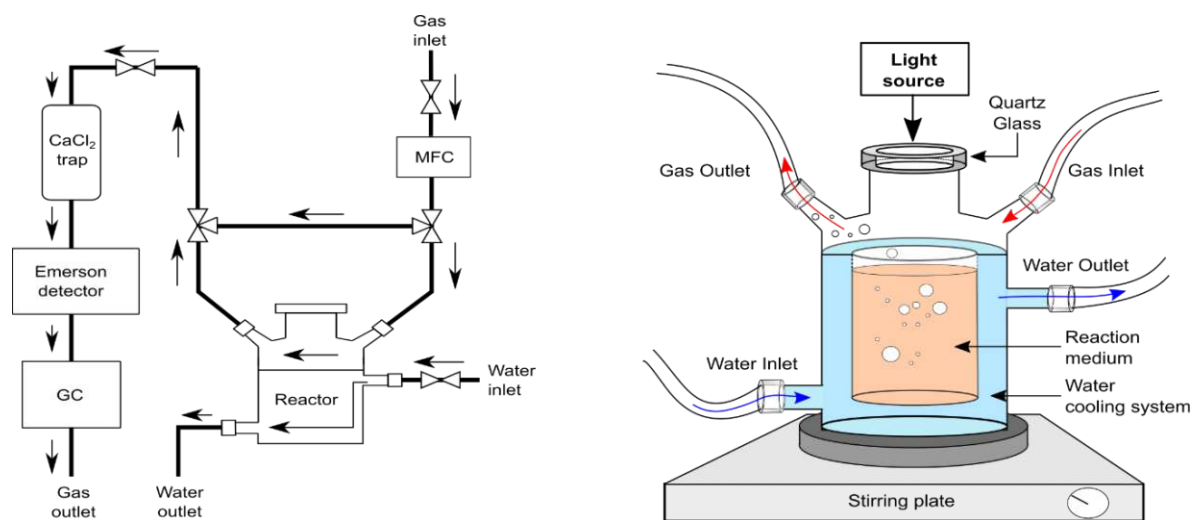
Figure S12. Experimental setup for the hydrogen evolution reaction (HER) experiments that were performed in flow-mode (see Methods). The oxygen evolution reactions (OER) experiments were performed in the same reactor, but without any gas flow. The oxygen sensor was introduced through septum.

Discussion of the XPS data for the samples after OER
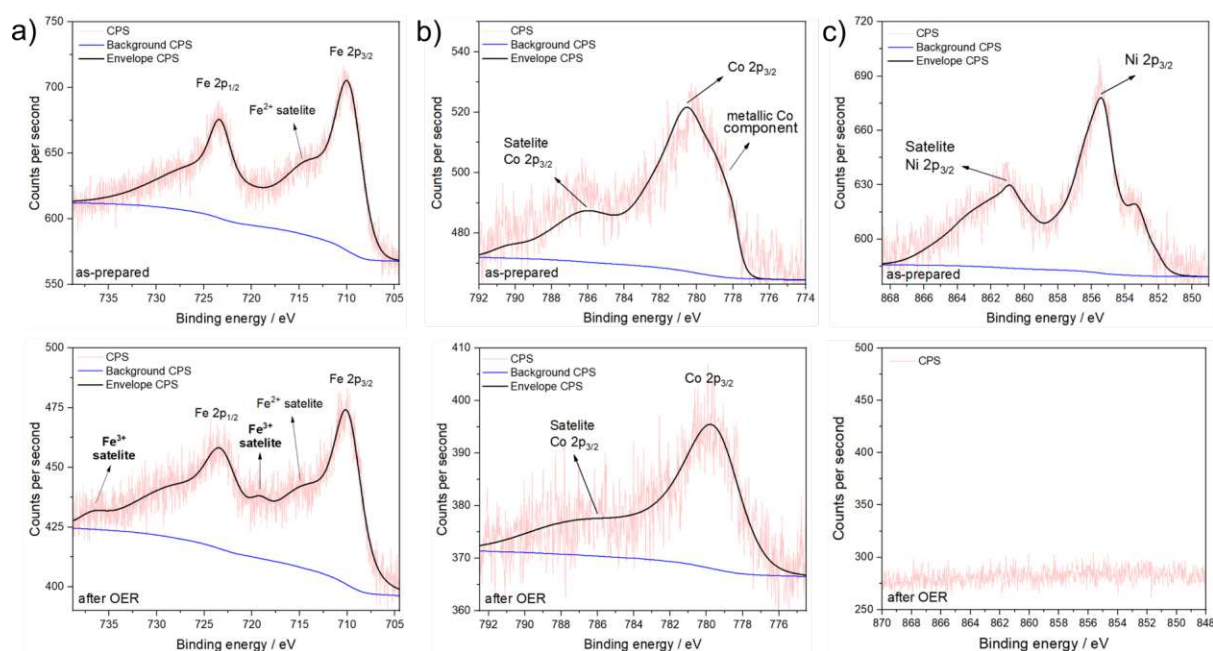
Figure S13. XPS spectra of the (a) FeO_x-TiO_2, (b) CoO_x-TiO_2 and (c) NiO_x-TiO_2 composites before (upper raw) and after OER (lower raw).

XPS spectrum of the FeO_x-TiO_2 after photocatalytic reaction (**Figure S13a**) clearly indicates the increase of the signals corresponding to Fe^{3+} species as can be seen from the appearing of the characteristic satellites at 719 and 737 eV. The spectrum after OER shows that Fe^{2+} is still present in the composite as one of the main components, but we can clearly suggest that some of the initial Fe^{2+} species oxidized during the photocatalytic process (the samples prepared for these XPS measurements were exposed to 1h-long illumination under OER conditions).

XPS spectrum of the CoO_x-TiO_2 after reaction (**Figure S13b**) also indicates that oxidation of the initially present Co species takes place. As such, we do not anymore observe the shoulder at 778 eV (corresponding to small amount of metallic Co potentially present in the as-prepared composite), while the satellite at 786 eV gets effectively reduced implying that some of the Co^{2+} species (e.g. the suggested $Co(OH)_2$) turn into Co^{3+} during the photocatalytic OER.

XPS spectrum of the NiO_x-TiO_2 after OER (**Figure S13c**) marks strong differences to the other samples investigated after reaction: no signal characteristic for NiO/Ni species can be observed anymore. This cannot be related to composite instability or potential leaching of the Ni species into the solution under photocatalytic conditions as the XPS data after HER experiment clearly shows that Ni signal is preserved even after 14 hour light illumination run. We believe that this specialty of the NiO_x-TiO_2 is related to the role of NiO_x species in OER and associated with the electron reduction of Ag^+ that was used as sacrificial agent. Given that XPS is a surface sensitive technique, we suggest that metallic Ag – being the product of Ag^+ reduction, as also confirmed by XPS – gets deposited onto NiO_x sites that act as electron acceptor and release centres. This Ag shell effectively blocks the Ni sites not allowing for any XPS analyses.

This result highlights the differences between NiO_x and the other two co-catalysts active for OER in terms of their role in charge extraction and separation, however, would require an extended investigation to elaborate on this in light of the rest of the data.

50

Table S2. XPS fitting parameters

	MnOₓ-TiO₂	CoOₓ-TiO₂			FeOₓ-TiO₂	NiOₓ-TiO₂		
	MnO	*Co metal**	*Co(OH)₂*	*Co₃O₄*	*FeO*	*Ni metal†*	*NiO*	*Ni(OH)₂*
	Mn^{2+}	Co^0	Co^{2+}	Co^{2+},Co^{3+}	Fe^{2+}	Ni^0	Ni^{2+}	Ni^{2+}
Peak 1 / eV	640.1	778.1	780.5	779.0	708.8	852.2	853.3	855.3
%	22.74	10.87	24.53	8.81	24.23	3.32	4.80	4.58
FWHM	1.40	1.00	2.30	1.61	2.05	1.20	1.20	1.00
Peak 2 / eV	641.0	781.1	782.3	780.3	710.1	855.9	855.0	856.0
Peak 2 - Peak 1 / eV	0.97	3.00	1.80	1.30	1.30	3.65	1.71	0.77
%	26.4	1.47	17.2	6.34	30.08	0.26	14.92	28.05
FWHM	1.40	3.30	2.8	1.97	2.46	3.00	3.10	2.50
Peak 3 / eV	642.0	783.10	786.1	781.6	711.3	858.2	860.4	858.1
Peak 3 - Peak 1 / eV	1.90	5.00	5.59	2.60	2.50	6.03	7.15	2.79
%	20.96	1.08	21.46	3.31	14.57	0.50	11.52	1.88
FWHM	1.40	3.30	4.2	2.60	2.46	3.00	3.60	1.40
Peak 4 / eV	642.9	-	790.5	784.6	712.5	-	863.5	860.8
Peak 4 - Peak 1 / eV	2.85	-	9.99	5.6	3.70	-	10.25	5.58
%	11.85	-	1.56	1.77	25.52	-	1.21	0.88
FWHM	1.40	-	2	4.00	4.50	-	1.80	0.80
Peak 5 / eV	644.1	-	-	788.9	715.8	-	865.5	861.8
Peak 5 - Peak 1 / eV	3.99	-	-	9.9	7.00	-	12.25	6.58
%	4.47	-	-	1.58	5.61	-	1.31	24.45
FWHM	1.40	-	-	3.00	2.55	-	2.80	4.71
Peak 6 / eV	645.8	-	-	-	-	-	-	864.9
Peak 6 - Peak 1 / eV	5.74	-	-	-	-	-	-	9.59
%	13.6	-	-	-	-	-	-	2.31
FWHM	1.40	-	-	-	-	-	-	3.10
% species	100	13.42	64.75	21.81	100	4.08	33.76	62.15

*line shape LA(1.2,5,5)
†line shape LA(1.1,2.2,29)

Table S3. XPS quantification data of the best fits: Ni, NiO and Ni(OH)₂. Ni 2p composition in atomic % before HER, after HER (still wet from the reaction) and after HER dried overnight.

	at.%		
	before	*after(wet)*	*after(dry)*
Ni	3.4	16.7	9.2
NiO	33.6	0.0	31.3
Ni(OH)₂	63.0	83.3	59.5

References

1 C. Y. Xu, P. X. Zhang and L. Yan, *Journal of Raman Spectroscopy*, 2001, **32**, 862–865.
2 G. Liu, C. Sun, H. G. Yang, S. C. Smith, L. Wang, G. Q. (Max) Lu and H.-M. Cheng, *Chem. Commun.*, 2010, **46**, 755–757.
3 X. Cheng, X. Yu, Z. Xing and L. Yang, *Arabian Journal of Chemistry*, 2016, **9**, S1706–S1711.
4 J. C. Parker and R. W. Siegel, *Appl. Phys. Lett.*, 1990, **57**, 943–945.
5 S. Bernardini, F. Bellatreccia, A. C. Municchia, G. D. Ventura and A. Sodo, *Journal of Raman Spectroscopy*, 2019, **50**, 873–888.
6 J. Li, G. Lu, G. Wu, D. Mao, Y. Guo, Y. Wang and Y. Guo, *Catal. Sci. Technol.*, 2014, **4**, 1268–1275.
7 L.-N. Han, L.-B. Lv, Q.-C. Zhu, X. Wei, X.-H. Li and J.-S. Chen, *Journal of Materials Chemistry A*, 2016, **4**, 7841–7847.

4.2.2   Manuscript No.2

"Elucidating the formation and active state of Cu co-catalysts for photocatalytic hydrogen evolution"

Jasmin S. Schubert, Leila Kalantari, Andreas Lechner, Ariane Giesriegl, Sreejith P. Nandan, Pablo Ayala, Shun Kashiwaya, Markus Sauer, Annette Foelske, Johanna Rosen, Peter Blaha, Alexey Cherevan and Dominik Eder

The corresponding Supplementary information of the manuscript can be found on page 68.

Elucidating the formation and active state of Cu co-catalysts for photocatalytic hydrogen evolution†

Jasmin S. Schubert,[a] Leila Kalantari,[a] Andreas Lechner,[a] Ariane Giesriegl,[a] Sreejith P. Nandan,[a] Pablo Alaya,[a] Shun Kashiwaya,[b] Markus Sauer, [c] Annette Foelske,[c] Johanna Rosen,[b] Peter Blaha,[a] Alexey Cherevan [*a] and Dominik Eder [*a]

The design of active and selective co-catalysts constitutes one of the major challenges in developing heterogeneous photocatalysts for energy conversion applications. This work provides a comprehensive insight into thermally induced bottom-up generation and transformation of a series of promising Cu-based co-catalysts. We demonstrate that the volcano-type HER profile as a function of calcination temperature is independent of the type of the Cu precursor but is affected by changes in oxidation state and location of the copper species. Supported by DFT modeling, our data suggest that low temperature (<200 °C) treatments facilitate electronic communication between the Cu species and TiO_2, which allows for a more efficient charge utilization and maximum HER rates. In contrast, higher temperatures (>200 °C) do not affect the Cu oxidation state, but induce a gradual, temperature-dependent surface-to-bulk diffusion of Cu, which results in interstitial, tetra-coordinated Cu^+ species. The disappearance of Cu from the surface and the introduction of new defect states is associated with a drop in HER performance. This work examines electronic and structural effects that are in control of the photocatalytic activity and can be transferred to other systems for further advancing photocatalysis.

Introduction

Photocatalysis can contribute to the development of environmentally-friendly processes relevant to water purification technologies, antibacterial applications, CO_2 reduction as well as the energy sector.[1–4] As such, photocatalytic water splitting towards light-driven hydrogen generation has the capability to be part of the solution to overcome the energy-related challenges of our times. To engineer the most efficient photocatalyst, heterogeneous photocatalysis has shown to be an advantageous approach, as it can combine a solid-state semiconductor – able to absorb light, generate electron–hole pairs and transfer their energy to the catalytic sites – and a co-catalyst with more suitable catalytic properties, which enables the desired oxidation and reduction half-reactions.[2,3,5] Additionally, the co-catalysts can act as a driving force for quick separation of photoexcited charge carriers, by extracting the charge carriers from the bulk and preventing their recombination, leading ultimately to enhanced charge separation and photocatalytic activity.[6] The use of tailor-made co-catalysts deposited on the photocatalyst surface thus, provides a means to control the catalytic sites to enhance and tune efficiency and adsorption–desorption equilibria of the reaction of interest.[6] Therefore, co-catalyst engineering has emerged as one of the most promising strategies to achieve high photocatalytic performance.

The light-to-hydrogen conversion efficiency of the final photocatalyst strongly depends on the electronic interaction and band alignments between the two components, as the photogenerated charge carries need to be effectively transferred between the semiconductor substrate and the catalytic sites.[6] Besides, the accessibility of the co-catalyst to the reactants also defines the final rate of the charge consumption by the desired reaction. Hence, the overall photocatalytic activity is often limited by the degree of electronic communication between the semiconductor and the co-catalyst, and the accessibility of the catalytic active sites. In order to provide more control over the co-catalyst/semiconductor interface, co-catalyst species are often generated on the support surface *via* bottom-up methods such as photodeposition, chemical deposition and growth as well as a selective surface reaction.[6–12] In many cases, the synthesis is accompanied by thermal treatments aiming to generate the desired co-catalyst species *via* oxidation or reduction. However, temperatures can facilitate otherwise kinetically

[a]*Institute of Materials Chemistry, Technische Universität Wien (TU Wien), Getreidemarkt 9, 1060, Vienna, Austria. E-mail: alexey.cherevan@tuwien.ac.at; dominik.eder@tuwien.ac.at*

[b]*Materials Design, Department of Physics, Chemistry, and Biology (IFM), Linköping University, 58183, Linköping, Sweden*

[c]*Analytical Instrumentation Center, Technische Universität Wien (TU Wien), Lehargasse 6, 1060 Vienna, Austria*

† Electronic supplementary information (ESI) available. See DOI: 10.1039/d1ta05561e

54

hindered diffusion processes leading to possible growth of the co-catalyst species or their chemical interaction with the substrate. These processes can reduce the accessibility of the catalytic centers to the reactants and lead to doping which often creates charge recombination centers and introduces localized inter-bandgap states resulting in lower photocatalytic performance.[13,14] It thus becomes important to control the location, chemical state and morphology of the co-catalyst species in the final photocatalytic system, for which more detailed investigations are often desired.

This work examines a series of Cu-based co-catalysts supported on anatase TiO_2 as a model substrate and provides a comprehensive insight into the side effects of thermal pre-treatments on their photocatalytic performance. The results reveal a surprising effect of the heat-treatment temperature on the hydrogen evolution reaction (HER) activity: the HER rates decrease at higher calcination temperatures, while the maximum activity is achieved for the non- and low-temperature treated samples, in contrast to other works.[10,15,16] Aiming to unveil optimal synthetic parameters, we prepared a set of Cu/TiO_2 composites *via* wet-chemical deposition of Cu species and characterized systematically their oxidation state, location and loading. To elucidate and understand the mechanism responsible for the photocatalytic performance, we correlated the rates of HER with the data obtained *via* photoelectron spectroscopy (XPS and UPS), infrared-, Raman- and diffuse reflectance spectroscopy (DRS), as well as microscopic techniques (TEM) and X-ray diffraction (XRD), among others. Overall, our results reveal that higher calcination temperatures (>200 °C) can trigger migration of the Cu species from the TiO_2 surface to its sub-surface and bulk. The disappearance of active sites as well as the introduction of defect sites can both be responsible for the observed HER decline. This work illustrates the importance of considering potential side effects of thermal treatments in the preparation and activation of non-noble-metal-containing co-catalysts and provides a quantitative measure for their impact on photocatalytic performance.

Results and discussion

We investigated the hydrogen evolution reaction (HER) for a series of nanoparticulate anatase TiO_2 powders impregnated with ~1 at% of Cu as a function of thermal treatment. Two sample sets were prepared using different Cu precursors: copper acetate, $Cu(ac)_2$, and copper nitrate, $Cu(NO_3)_2$. The as-prepared $Cu(ac)_2$/TiO_2 and $Cu(NO_3)_2$/TiO_2 powders were subjected to temperature-treatments ranging from room temperature (RT) – *i.e.* no thermal treatment – to 400 °C and evaluated with regard to their HER performance (Fig. 1a). The photocatalytic data revealed a clear trend for both sample sets: the activity first increased with calcination temperature to reach a maximum at 100 °C/150 °C, then by further increasing the temperature a gradual decrease of the HER takes place. The subsequent decrease at higher calcination temperatures, however, was surprising, considering that thermal treatments at those temperatures constitute a standard method required to either eliminate the anion residue, generate the corresponding

oxides, or enhance the interaction between the substrate and co-catalyst.[7,8,10–12,17,18] Yet, our data show that the calcination protocol of the Cu/TiO_2 composites has a detrimental effect on photocatalytic performance. In addition, a similar HER trend was observed for isothermal treatments performed at 250 °C for different periods of time (see Fig. S2†). Hence, not only does the temperature of the treatment play a role but also the time of calcination. For simplicity, as both parameters – temperature and time – led to similar behavior, in this work we focused on the effect of temperature, and thus we set a constant calcination time of 2 h for each thermally treated sample.

The observed HER decline in Fig. 1a can originate from several phenomena: (a) sintering of the Cu species on the TiO_2 surface, (b) generation of less or non-active Cu species (change in the oxidation state/morphology) or (c) diffusion of Cu into the TiO_2 lattice, which may lead to (d) reduced availability of the Cu sites at the solid–liquid interface, (e) formation of thermally induced defects that act as charge recombination centers (doping) or (f) changes of the band gap structure (electronic effect), among others.[6,9–11,13,14,19–21] In order to elucidate the responsible factors for the observed HER trends, we thoroughly characterized and investigated both sample sets, $Cu(ac)_2$/TiO_2 and $Cu(NO_3)_2$/TiO_2, with a plethora of methods.

Thermal and morphological analysis

The thermal gravimetric analysis (TGA) in Fig. 1b of the composites revealed that the decomposition of the anions takes place between 206 °C and 360 °C for $Cu(NO_3)_2$/TiO_2 and 255 °C to 313 °C for $Cu(ac)_2$/TiO_2. The beginning of the anion decomposition coincides well with the start of the HER activity decline, which thus may be related to the precursor transformation. Yet, it is well known that the thermal treatment can also induce sintering of the Cu species that can lead to reduced activity.[19] High-resolution transmission electron microscopy (HRTEM) revealed that no Cu-based clusters or nanoparticles (NP) are present on the TiO_2 surface, independent of the precursor type and the temperature of the thermal treatment (Fig. 1c–f). This suggests that Cu is homogeneously distributed on the TiO_2 support at the nanoscale as atomic layers/species without forming TEM-visible clusters, even at high-temperature treatments. This eliminates sintering as a significant reason for the observed activity drop.

Structural and compositional analysis

The Raman spectrum in Fig. 2a shows only features that correspond to a pure anatase phase with the typical E_g (145.3 cm^{-1}), B_{1g} (397.5 cm^{-1}), A_{1g} + B_{1g} (517.5 cm^{-1}) and E_g (641.1 cm^{-1}) bands, which belong to the O–Ti–O symmetric stretching, symmetric bending and antisymmetric bending vibrations, respectively.[22,23] This indicates that neither the transition to rutile nor the formation of a separate Cu phase took place in any of the samples (further confirmed by XRD, see Fig. S7†). Furthermore, a gradual decrease of the TiO_2 band intensities with increasing calcination temperatures occurred for both samples, accompanied by a broadening of their FWHM, yet with some fluctuations (Fig. 2b and c). The loss of

55
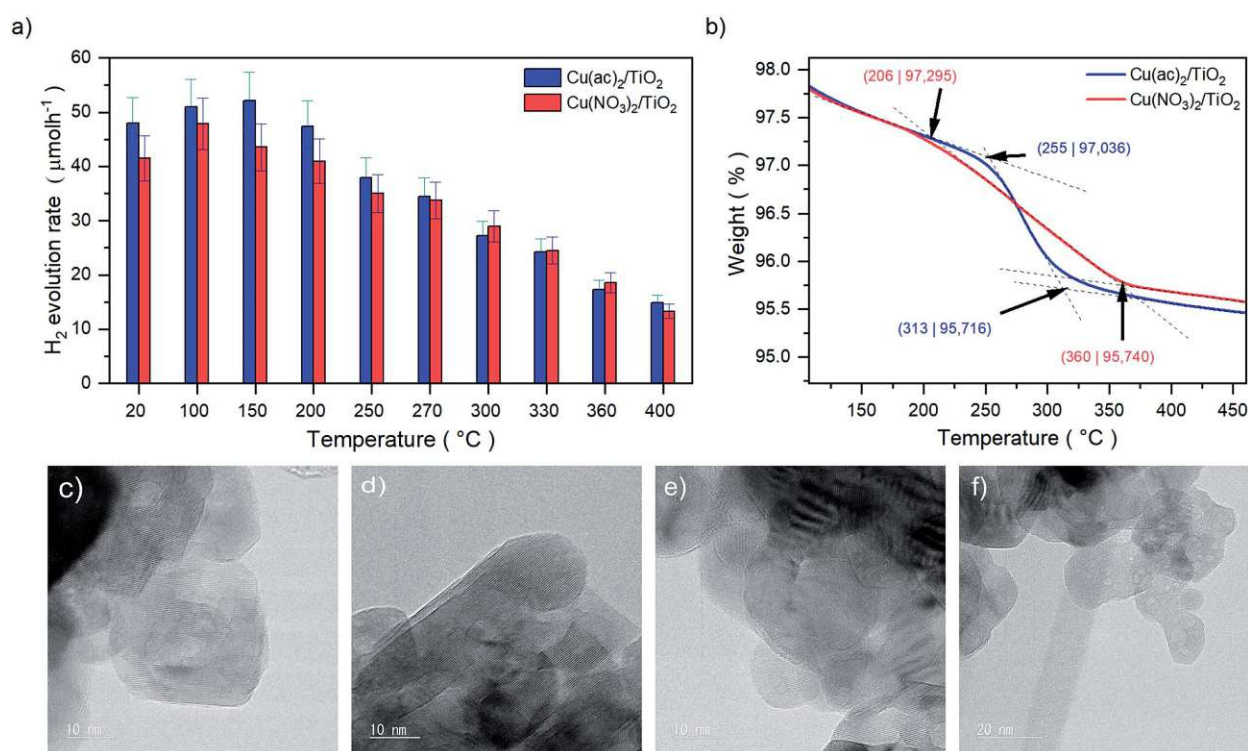
Fig. 1 (a) Values of the HER rates achieved after 20 minutes of illumination of Cu(ac)$_2$/TiO$_2$ and Cu(NO$_3$)$_2$/TiO$_2$ composite series prepared at different temperatures. Full HER evolution profiles over time and illumination are shown in Fig. S1 and Table S1,† HER stability (long-term HER performance) discussion can be found in Fig. S3,† (b) TGA profiles of the Cu(ac)$_2$/TiO$_2$ and Cu(NO$_3$)$_2$/TiO$_2$ composites showing the decomposition ranges from 206 to 360 °C and 255 to 313 °C, respectively. Full profiles from room temperature to 800 °C are shown in Fig. S4.† (c) HRTEM images of anatase-TiO$_2$, (d) the non-calcined, (e) 400 °C (10 nm) and (f) 400 °C calcined (20 nm) Cu/TiO$_2$ composites. Further TEM and complementary SEM micrographs are shown in Fig. S5 and S6.†

Raman band intensity can be related to a decrease in polarizability and symmetry of the vibrational modes and suggests a crystal lattice distortion of TiO$_2$, which is more pronounced at higher temperatures.[22,24–30] The slight FWHM broadening of the Cu/TiO$_2$ samples – in contrast to bare TiO$_2$ – further confirms this assumption (Fig. 2d).[22,25,26] Furthermore, recent DFT studies revealed that Cu incorporation (via interstitial or substitutional Cu:TiO$_2$ doping) does not result in a strong TiO$_2$ lattice distortion.[31] Hence, these observations point to the possible formation of thermally induced Cu–TiO$_2$ lattice defects, via Cu surface-to-bulk diffusion, which – being a kinetically hindered process – can be activated at higher temperatures.[27–29]

Attenuated total reflection infrared (ATR-IR) spectroscopy of the composites, Fig. 3, indicates chemisorption of the Cu precursor species on the TiO$_2$ surface already after impregnation (RT samples). This is evident from the red-shifted COO modes of the acetate ligand (around 1490 and 1600 cm^{-1}), the appearance (1558 cm^{-1}) and decrease (1419 cm^{-1}) of a new acetate binding mode, and the pronounced rise of the intensity of the bidentate bridging nitrate coordination at 1620 cm^{-1}, typical artifacts of surface-binding.[32] Furthermore, at 400 °C we see a complete decomposition of the nitrate and acetate ligands, in line with TGA.

Fig. 1a shows that the highest photocatalytic activity was obtained at 150 °C for Cu(ac)$_2$/TiO$_2$ and 100 °C for Cu(NO$_3$)$_2$/TiO$_2$. Based on the discussion above, Raman signal changes are already visible at these temperatures and ATR-IR indicates strong binding of the precursor species, yet no Cu diffusion is expected at those temperatures. Hence, we suggest that such mild thermal treatments enact densification of the adsorbed precursor layer, resulting in Cu species that are bound more strongly to the TiO$_2$ surface. This in turn induces a slight crystal distortion at the Cu/TiO$_2$ interface (inducing the Raman signal changes) but concomitantly enhances the electronic communication between the support and the co-catalyst, leading to a better overall HER performance.

Surface-to-bulk diffusion

In order to further investigate a possible formation of Cu–TiO$_2$ lattice defects upon calcination (indicated by Raman spectroscopy), we analyzed the samples with X-ray photoelectron spectroscopy (XPS). The idea is that diffusion of Cu from the surface into the bulk would lead to a decreased Cu concentration on the substrate surface and hence to a weaker Cu signal in the surface-sensitive XPS. Moreover, XPS also allows for identifying changes in the oxidation state of Cu and Ti.
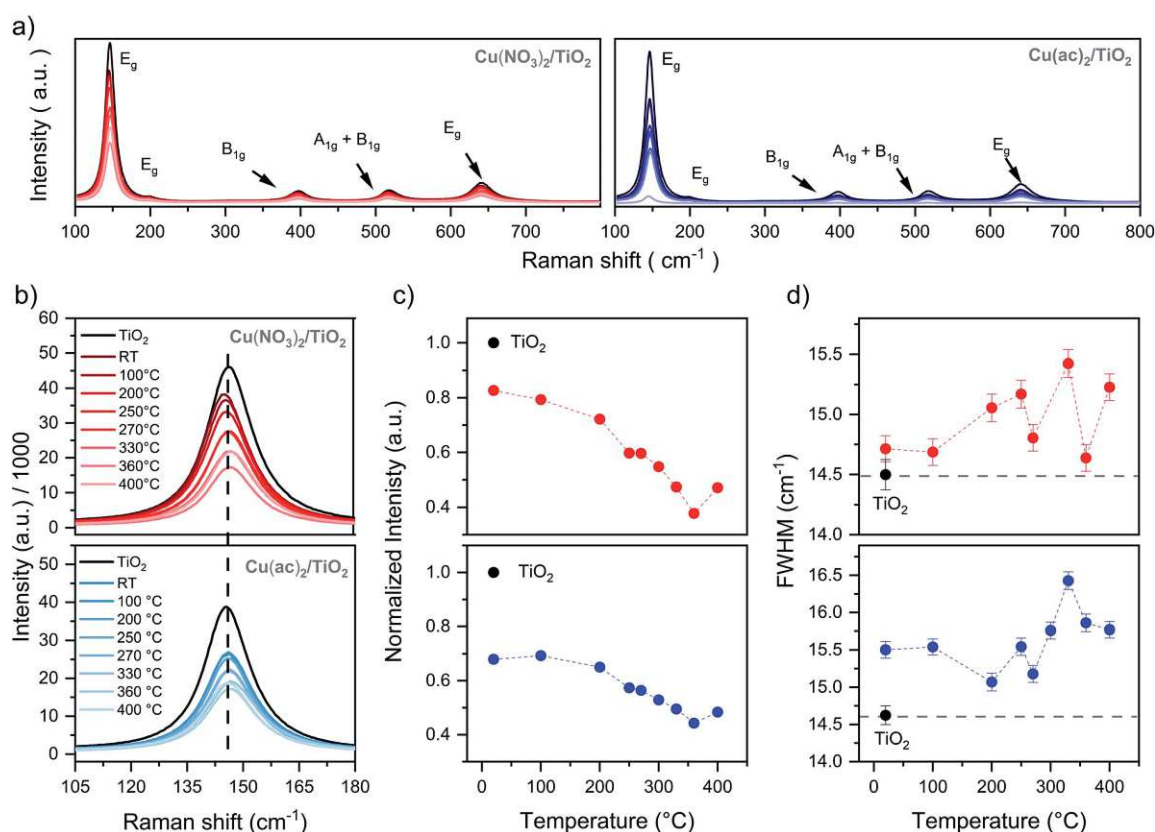
21960 | *J. Mater. Chem. A*, 2021, **9**, 21958–21971

This journal is © The Royal Society of Chemistry 2021

56

Fig. 2 Raman data of the $Cu(NO_3)_2/TiO_2$ (red) and $Cu(ac)_2/TiO_2$ (blue) composites as a function of post-thermal treatment temperature: (a) full range of the $Cu(NO_3)_2/TiO_2$ and $Cu(ac)_2/TiO_2$ composites, (b) E_g band profiles, (c) normalized E_g band intensity – to bare TiO_2 to exclude instrumental artifacts – and (d) E_g band FWHM changes. Details in Table S2.†
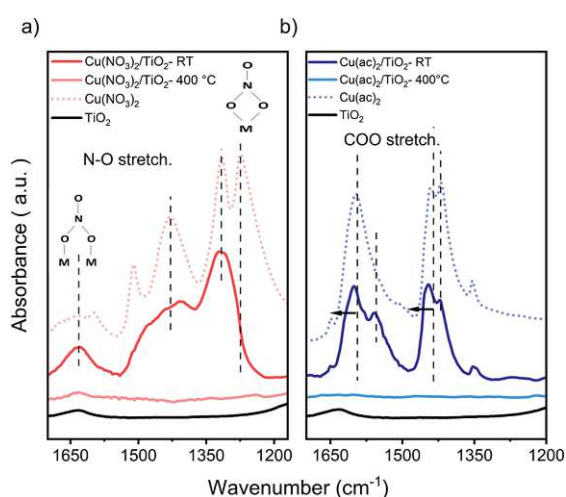

Fig. 3 FTIR-ATR of (a) $Cu(NO_3)_2/TiO_2$ and (b) $Cu(ac)_2/TiO_2$ samples. Main nitrate and acetate peaks, showing the new binding modes and band shift for the non-calcined (RT) and calcined at 400 °C composites *vs.* the pure precursors and TiO_2. Samples contained 5 at% of Cu, to obtain a better visualization. The full range of the pure precursor, 5 at% Cu and 1 at% Cu samples are shown in Fig. S8 and S9.†

The survey spectra acquired show the expected Cu 2p, Cu Auger, Ti 2p, C 1s and O 1s signals for all measured samples. The detail spectra of C 1s and O 1s show the typical carbon species as well as the oxygen from TiO_2 (Fig. S10–S13†). The Ti $2p_{3/2}$ signal (458.8 eV) corresponds to Ti^{4+} in all samples, with no detectable contribution of Ti^{3+} (Fig. 4e). The Cu 2p signals, however, are more complex and surprising, as no characteristic Cu^{2+} satellite features (generally around 942 eV) were detectable, despite Cu^{2+} precursors being used in the synthesis (Fig. 4a and b).[33–35] Thus, the Cu $2p_{3/2}$ peaks, seen in all samples (932.5 eV for $Cu(NO_3)_2/$ TiO_2 and 932.3 eV for $Cu(ac)_2/TiO_2$), indicate the presence of Cu^+, Cu^0 or more likely a combination of both. However, considering the low signal intensity – due to the low (~1 at%) Cu content – and the slight asymmetric broadening of the signal, the presence of small amounts of Cu^{2+} cannot be fully excluded. In fact, DRS – discussed later in the manuscript – confirms the presence of Cu^{2+}. To further clarify the Cu oxidation states in the composites, we also analyzed the Cu LMM Auger signals shown in Fig. 4c. However, it was only possible to obtain a reliable signal for the non-calcined and 250 °C treated samples. Furthermore, as the binding energy and Auger parameters are sensitive to the ligand nature and small particle size, only qualitative analysis was performed to confirm the Cu $2p_{3/2}$ signal analysis.[34,35] The data reveal a sharp and intense peak at 915.1 eV kinetic energy (K.E.),
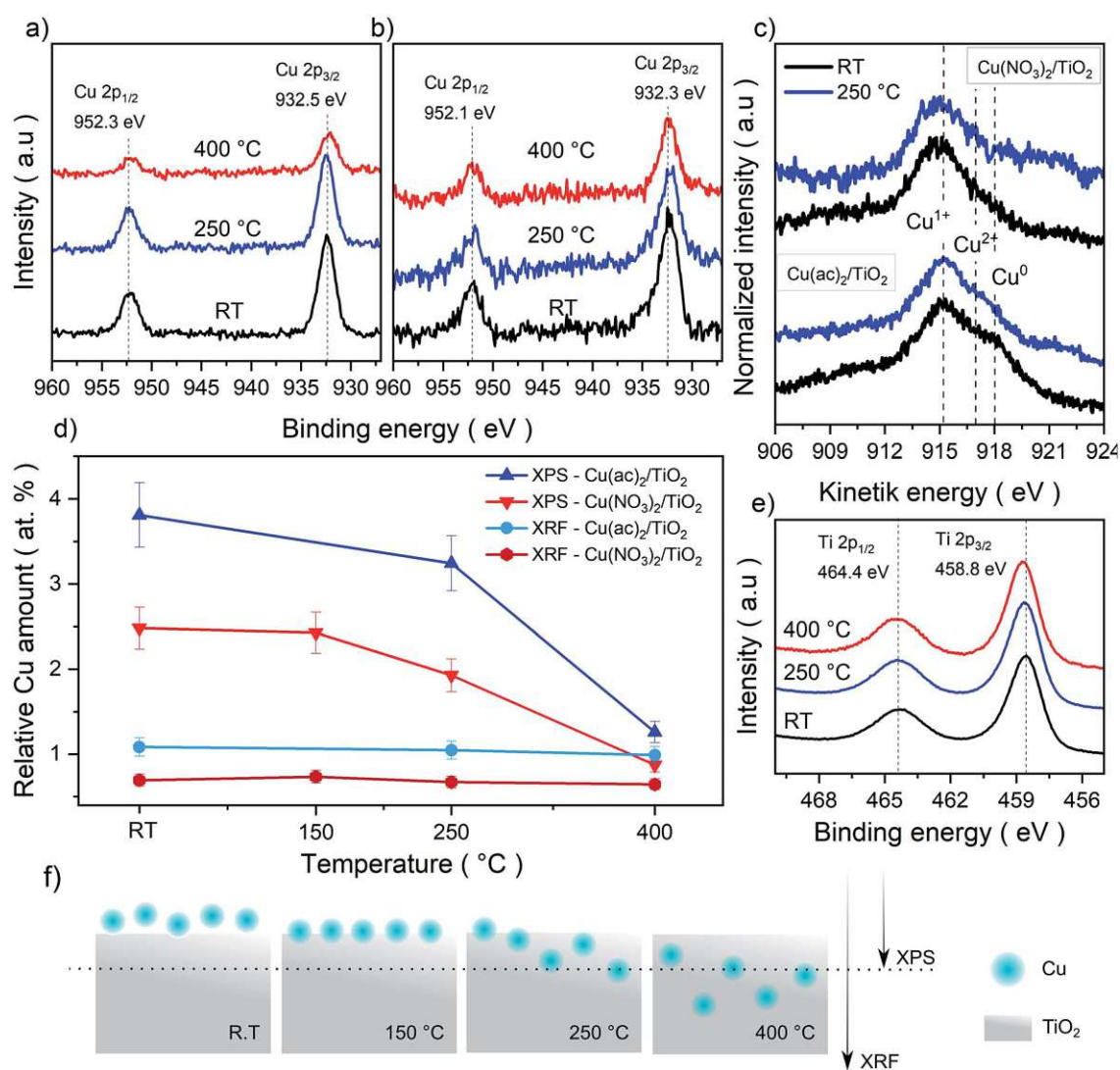
This journal is © The Royal Society of Chemistry 2021

J. Mater. Chem. A, 2021, **9**, 21958–21971 | **21961**

57

Fig. 4 XPS Cu 2p detail spectra of the (a) $Cu(NO_3)_2/TiO_2$ and (b) $Cu(ac)_2/TiO_2$ composites subjected to various temperature treatments. (c) Cu LMM Auger spectra for both composites non-calcined (RT) and at 250 °C. The Cu^{2+}, Cu^+ and Cu^0 reference values were taken from literature reports.[33–35] (d) Elemental Cu contents (Cu-to-Ti ratio in at%) derived from bulk sensitive XRF and surface-sensitive XPS survey data. Absolute values are shown in Table S5.† (e) Ti 2p spectra of the composites and (f) graphical representation of the proposed thermally induced diffusion mechanism and depth penetration of XPS and XRF.

which corresponds to Cu^+.[33,36] At 918 eV K.E. a clear shoulder, typical of Cu^0, is visible for the non-calcined $Cu(ac)_2/TiO_2$; the shoulder, however, almost disappears after the 250 °C treatment. Besides, as Cu^{2+} generally appears around ~917 eV, the broadening in that region of the spectrum further indicates the presence of Cu^0 and Cu^{2+}. Overall, we conclude, that a mixture of Cu^{2+}, Cu^+ and Cu^0 is present in all the Cu/TiO_2 samples with Cu^+ being the most abundant. The presence of a mixed oxidation state implies that a reduction of the original Cu^{2+} precursor takes place already during impregnation most probably induced by the photoelectrons of TiO_2 generated under ambient light (further discussion in the optoelectronic analysis and DFT sections) and by the set of our synthetic conditions (*i.e.* use of vacuum and ethanol).

To further elaborate on the hypothesis of possible Cu diffusion into the substrate lattice, we compared the Cu amounts quantified from XPS (a surface-sensitive method) against the elemental quantification obtained using X-ray fluorescence (XRF) spectroscopy (a bulk-sensitive method, considering the nanometer-sized composites), shown in Fig. 4d and f. The XRF Cu signal of ~1 at% is consistent for all composites (non-calcined and calcined at 150, 250 and 400 °C), while the Cu content in XPS decreased strongly from 2.5 to 0.9 Cu at% (Ti is set to 100% and Cu content is provided in relation to it). Overall, while XRF confirms that no Cu loss from the sample takes place upon calcination, these complementary sets of data suggest that Cu undergoes diffusion into the TiO_2 lattice at higher calcination temperatures.

21962 | *J. Mater. Chem. A*, 2021, **9**, 21958–21971

This journal is © The Royal Society of Chemistry 2021

58

Analysis of the optoelectronic properties

The DRS data in Fig. 5a and b reveal a strong absorption band below 400 nm, which corresponds to the ligand-to-metal charge transfer (LMCT) of oxygen (O^{2-}) to Ti^{4+} and Cu^{n+} ($n = 0$, 1 or 2).[37,38] Next, all samples show a shoulder in the range of 400 to 500 nm, absent in pure TiO_2. The nature of this band is strongly debated in literature and has been attributed to localized

surface plasmon resonance (LSPR) effects of Cu^0 nanoparticles (NP), d–s transition of Cu^0 ($d^{10}s^1$), interfacial charge transfer (IFCT) from the TiO_2 valence band (VB) to the Cu^{2+} ions or Cu_xO-clusters as well as to Cu^+ metal-to-ligand charge transfer (MLCT) absorption.[38–43] In our case, TEM micrographs show no visible Cu nanoparticles. Thus, NP LSPR effects can be excluded. DFT calculations revealed that this shoulder
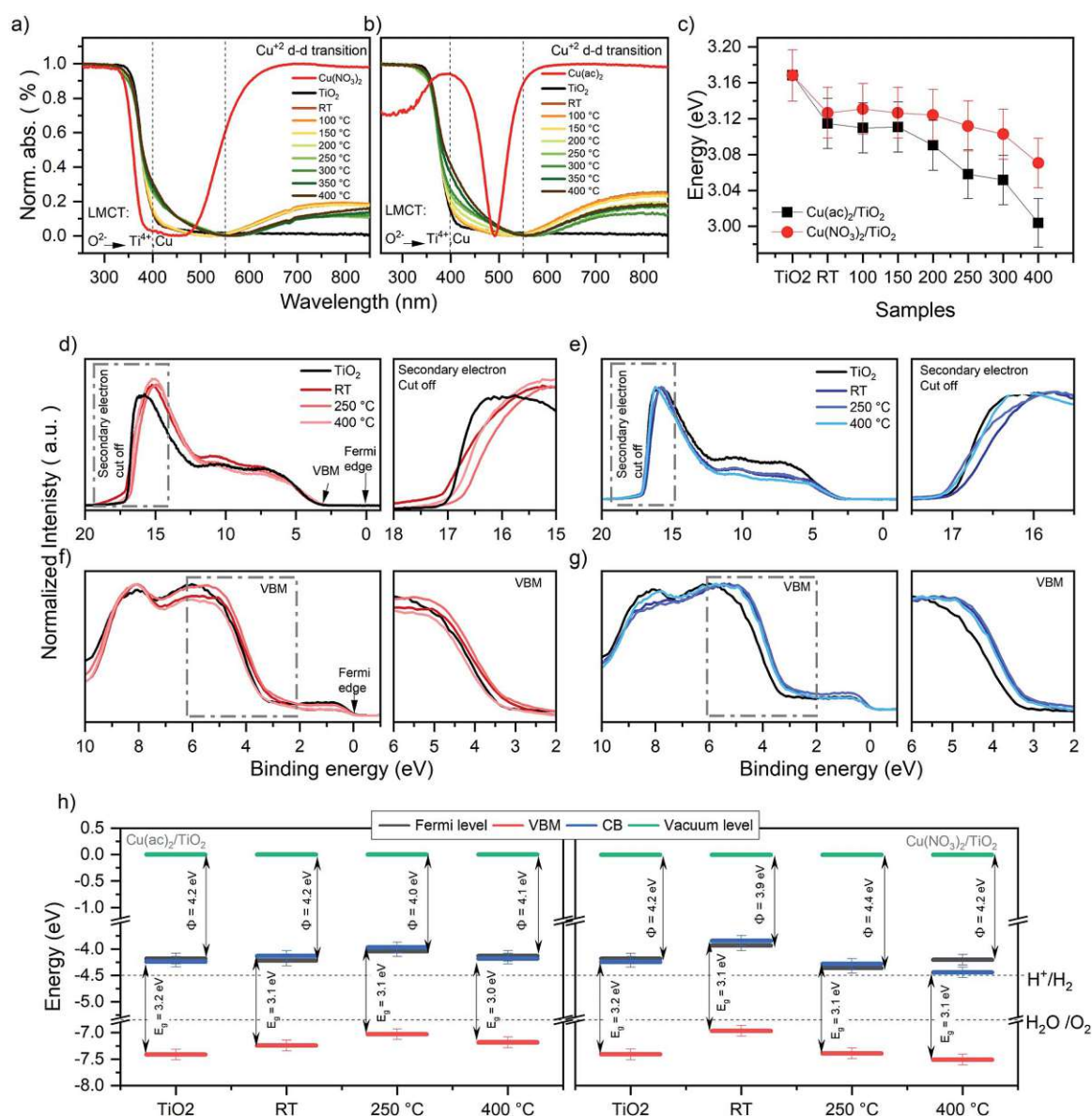

Fig. 5 Normalized DRS data for the (a) $Cu(NO_3)_2/TiO_2$ and (b) $Cu(ac)_2/TiO_2$ composites subjected to various thermal treatments along with the pure anatase TiO_2 and the original Cu precursors. (c) Band gap (E_g) values of the $Cu(NO_3)_2/TiO_2$ and $Cu(ac)_2/TiO_2$ composites as a function of post-treatment temperature. The data is extracted *via* Tauc plot analysis of the DRS spectra. RT = non-calcined sample, LMCT = ligand to metal charge transfer. Further details, absolute values of the composites and thermal evolution of the pure precursors are shown in Fig. S15, S16 and Table S6.† (d) UPS signals of $Cu(NO_3)_2/TiO_2$ and (e) $Cu(ac)_2/TiO_2$ composites prepared at different temperatures. (f) VB-XPS of $Cu(NO_3)_2/TiO_2$ and (g) $Cu(ac)_2/TiO_2$ composites. (h) Energy diagram (energy (eV) *vs.* vacuum level) of $Cu(ac)_2/TiO_2$ and $Cu(NO_3)_2/TiO_2$ constructed from the corresponding UPS, XPS and DRS data (further detail in Fig. S17 and Table S7†) of the bare TiO_2-anatase, the non-calcined sample and the composites obtained *via* calcination at different temperature. H^+/H_2 and H_2O/O_2 potential values taken at standard conditions.[52,53] Note that the values are referenced to the vacuum level ($E_{vac} = 0$ eV).

59

originates from inter-band gap states of Cu-d orbitals caused by Cu^0, Cu^+ and Cu^{2+} (see the corresponding section for further discussion). The strong absorption between 550 and 900 nm is characteristic of Cu^{2+} d–d transitions (d^9s^0) (see pure Cu^{2+} precursors reference in Fig. 5a and b).[37,39,44] This further corroborates the presence of Cu^{2+} in the composites. Furthermore, the d–d Cu^{2+} band intensity decreases by increasing temperature. This reveals that Cu^{2+} vanishes from the composites at higher calcination temperatures, in line with the heat-induced diffusion of Cu into TiO_2, indicated by XPS and XRF as well as DFT models discussed later.

The optical band gaps constructed from the corresponding DRS data, determined by using Tauc plots (Fig. 5c), revealed a clear band gap decrease with increasing temperature.[45] Yet, already a decrease for the non-calcined samples takes place from 3.17 eV, for bare TiO_2, to 3.12 eV and 3.13 eV for $Cu(ac)_2/TiO_2$ and $Cu(NO_3)_2/TiO_2$, respectively. This also confirms the presence of Cu inter-band gap states and suggests that electronic communication between TiO_2 and Cu was established immediately after impregnation – in line with Raman spectroscopy – and gets more pronounced with increasing temperature. These findings align well with the hypothesis of thermally induced diffusion of the Cu species into the TiO_2 lattice and previously reported studies on Cu doped TiO_2.[46,47]

The work function and valence band maximum (VBM) of the samples were determined using UPS and XPS (see Fig. 5d–h and for further detail about the method Fig. S17†).[48] The data show strong fluctuations in the work function values, without following a clear trend, while the VBM shows a decrease for all samples except $Cu(NO_3)_2/TiO_2$ at 400 °C, which increases (see Table 1). Furthermore, the energy diagrams, constructed based on XPS, UPS and DRS, show that the Fermi level of all samples, except $Cu(NO_3)_2/TiO_2$ calcined at 400 °C, is in the same range as the conduction band minimum (CB) (see Fig. 5h), indicating an n-type conductivity of all samples. This can be related to an electron accumulation on the surface, which induces a downward band bending, attributed to defects (oxygen vacancies, titanium interstitials, *etc.*), adsorbed species (type and density of those species), UHV conditions or doping.[49–52] This electron accumulation on the TiO_2 surface would explain the reduction of Cu^{2+} to Cu^+ and Cu^0 seen in XPS even for the non-thermally treated Cu/TiO_2 composites. Furthermore, to fully understand the work function differences between the composites prepared using different Cu precursors is beyond the scope of this study, yet it is well known that the work function depends on the
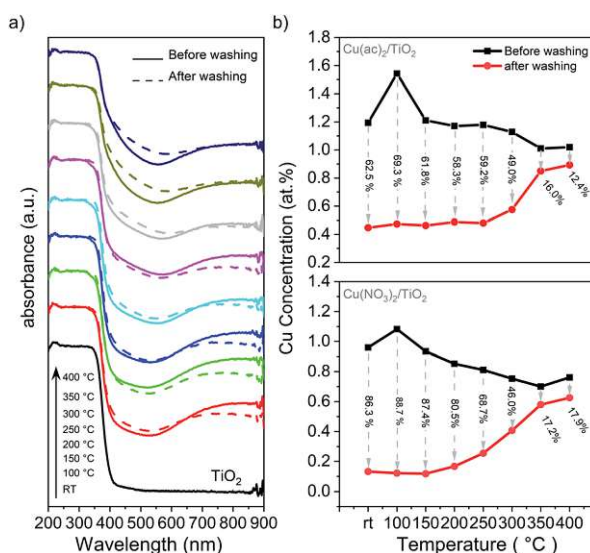
surface structure and nature of the adsorbates.[48,49] Hence, the presence of the different physisorbed anions (nitrate and acetate, that have different charge density and dipole moments), the products of the anion thermal decomposition and the different state and location of Cu is likely to affect the work function differently giving rise to these fluctuations.[48] By correlating these data with the photocatalytic performance, we conclude that the position of the CB levels thermodynamically required to drive proton reduction remains suitable for all composites and does not seem to correlate with the observed HER trend. Yet, doping is known to induce defects that act as charge recombination centers; thus, the observed HER activity decrease can be governed by the Cu-induced defects which increase by increasing temperature, rather than the change in the optoelectronic properties.[13,51,53]

Analysis of the Cu–TiO₂ linkage strength

Diffusion of Cu into the interior of the TiO_2 particles will reduce their accessibility and improve their stability towards leaching into solution. Therefore, we performed washing experiments and analyzed the samples with DRS and XRF. DRS in Fig. 6a shows that the absorption band characteristic of Cu^{2+} (550 to 900 nm) decreased significantly after washing with water for the non-treated sample and those heated at low temperature, suggesting a significant portion of weakly bound Cu^{2+} species. In contrast, a far smaller amount of Cu-species detached in the samples treated at temperatures above 250 °C. XRF (Fig. 6b) confirmed that 62.5% and 86.3% of Cu was removed from the non-calcined samples for $Cu(ac)_2/TiO_2$ and $Cu(NO_3)_2/TiO_2$,

Fig. 6 Washing experiments of the Cu/TiO_2 composites: (a) DRS of the $Cu(ac)_2/TiO_2$ sample before and after washing. The corresponding DRS data of the $Cu(NO_3)_2/TiO_2$ sample, showing the same behaviour, is shown in Fig. S18.† (b) XRF analysis of the Cu content before and after washing with the amount of Cu washed out (in % regarding the original content). Further details are shown in Table S8.†

Table 1 Cut off, work function and valence band maximum (VBM) values obtained from the corresponding UPS and VB-XPS data shown in Fig. 5. All values are in eV. Details of the data evaluation method are shown in Fig. S17. RT = non-calcined sample

	$Cu(NO_3)_2/TiO_2$			$Cu(ac)_2/TiO_2$		
	Cut off	Work function	VBM	Cut off	Work function	VBM
TiO_2	17.0	4.2	3.2	—	—	—
RT	17.3	3.9	3.0	17.0	4.2	3.0
250 °C	16.8	4.4	3.0	17.2	4.0	3.0
400 °C	17.0	4.2	3.3	17.1	4.1	3.1

21964 | *J. Mater. Chem. A*, 2021, **9**, 21958–21971

This journal is © The Royal Society of Chemistry 2021

60

respectively, while the corresponding amounts for the samples treated at 350 °C were only 16.0% and 17.2%, respectively.

These results indicate that most of the Cu species are weakly bound on the surface and that the lower extent of leaching at high temperatures is a result of Cu surface-to-bulk diffusion. However, the observed band gap narrowing, VBM position shifts, as well as FTIR and Raman band changes indicate that Cu-to-support interactions exist to some extent already for the non-calcined sample. Hence, despite Cu being weakly chemisorbed after impregnation, this interaction appears to be strong enough to establish efficient electronic communication with the supporting TiO_2. Accordingly, the HER maximum for the catalysts calcined at mild temperatures can be associated with densification of the adsorbed species on the surface, which leads to a stronger binding that facilitates charge transfer from TiO_2 to the catalytic center, Cu. The increase of calcination temperature above 200 °C, however, triggers Cu diffusion into the TiO_2 lattice, which consequently increases the number of charge recombination centers within TiO_2 and reduces the number of Cu centers available on the surface.[13,14] Previous reports have shown that Cu undergoes redox shuttling between the reactant and the TiO_2 surface by going into solution and redepositing by electron transfer from the TiO_2 CB to Cu.[9,54] Additional photodeposition experiments indicate that this mechanism is relevant to our system (further discussion in ESI and Fig. S19†). Therefore, we can conclude that both, the reduced availability of Cu sites on the surface as well as the introduction of new trap and recombination states in TiO_2 lattice, contribute to the HER performance decline.

DFT calculations

Cu oxidation state and diffusion mechanism. To better understand the surface and sub-surface Cu incorporation, we performed DFT calculations (see details in Methods). We examined the formation stability and analyzed the oxidation states of the corresponding Cu atoms by following the changes in the magnetic moments and Bader charges. We considered various Cu models anchored to the most abundant and stable (101) anatase TiO_2 surface: a single Cu atom, a cluster of Cu atoms and Cu clusters with different numbers of oxygen atoms coordinated to Cu, labeled Cu_yO_x (simulating partially oxidized clusters).

For a single Cu atom, the results show that Cu prefers to adsorb at the bridge site between two unsaturated oxygen atoms (O_{2c}, see Fig. 7a and b) with an almost linear O_{2c}–Cu–O_{2c} bond angle of 161°, similar to findings of previous studies.[55–57] The adsorption energy (E_{ads}) for one single Cu atom on TiO_2 is 2.24 eV, which agrees well with literature.[55–57] Furthermore, the two shortest Cu–O bonds of 1.87 Å are close to the Cu_2O bond length (1.85 Å) but much shorter than for bulk-CuO (1.98 Å) (Table S10†), and the vanishing magnetic moments and the Bader charge of +0.68 (Fig. 7j–l) indicate a Cu-oxidation state of +1. For small Cu_x clusters ($x = 1, 2, 3,$ and 5), when 2 or 3 Cu atoms are added to the surface, the most stable structures are still obtained for a Cu–O_{2c} bridge sites (Fig. 7b). This indicates that Cu can form infinite almost linear Cu–O chains on the TiO_2 surface. Yet, the further addition of Cu atoms tends to destroy

the symmetric chain-like 3-atom structure and results in an irregular 3D-like Cu_5 array (Fig. 7c and d). This is more stable than the corresponding chain-like Cu_5 structures and has the highest E_{ads} of all considered Cu_x-clusters (Table S11†). Furthermore, the charge transfer from Cu_5 to TiO_2 (in the DFT model each time a neutral Cu atom is added to the TiO_2 surface) is in general smaller. As a result, Cu atoms of Cu_5 clusters remain mainly neutral (Bader charges of −0.06 to 0.17), except for the Cu atoms directly attached on TiO_2, which have still very short Cu–O bonds or are coordinated by 2 O_{2c} atoms (Bader charge of 0.41 to 0.66), indicating ionized Cu.

For the Cu_xO_y ($x = 5, y = 0$–5) clusters, we started from the chain-like Cu_5 structure and gradually added oxygen atoms until a fully oxidized Cu cluster has been obtained (Fig. 7g and h). We calculated the E_{ads} of different metal oxide clusters on the surface and computed the cohesive energies of bulk Cu and CuO for comparison (Fig. 7i). For all studied clusters, the obtained E_{ads} are much smaller than the cohesive energy of bulk Cu, while showing more similar values to CuO. The E_{ads} depends only weakly on the oxygen content (or the cluster size); thus, the oxygen partial pressure and kinetic effects will determine the specific oxidation state. Furthermore, a +1 Bader charge and 0.6 μ_B magnetic moments of Cu atoms in the Cu_5O_y structures, indicate that for the Cu_5O_5 cluster Cu is in a +2 state. However, when the number of oxygen atoms gradually decreases, the ionicity also decreases. The largest $Cu_{10}O_9$ cluster has 8 Cu^{2+} and 2 Cu^+ ions and 3 out of the 8 Cu^{2+} ions have already flipped their spin indicating the preferred antiferromagnetic order of CuO. This is further shown by analyzing the dependency of the Cu charge state with the number of O neighbors (coordination number – a bond is counted when the Cu–O distance is below 2.16 Å) shown in Fig. 7j. For simplicity, only the coordination number *versus* the Bader charge is shown, however, also bond angle or bond distances just below/above the cutoff criterion had some minor influence. This shows that Cu without or with one direct O neighbor is neutral, with two it is in the +1 state (Bader charge of ∼0.5) and with 3 or 4 coordinated oxygen atoms Cu is in a +2 state. Hence, by increasing oxygen content, the Cu ionicity increases.

To check the possibility of Cu diffusion into the bulk, we constructed DFT models in which one Cu atom migrates from the surface to different positions in the subsurface. Based on the calculated E_{ads} values, Fig. 7e and f shows the most stable structures of subsurface Cu derived from two different configurations: the single Cu atom and the most stable 3D-like Cu_5 cluster. As expected, when a single Cu atom diffuses into the subsurface there is a small energy loss (E_{ads} decreases from 2.24 eV to 1.90 eV), which suggests that a single Cu atom is not prone to diffusion into the TiO_2 lattice but is rather stable on the surface. Yet, for the larger cluster, migration of a single Cu atom yields virtually no energy difference (1.90 eV to 1.84 eV), which supports the possibility of Cu diffusion into the bulk. In both cases, the most preferable state of Cu incorporation in the subsurface is to be 4-fold coordinated by O and present in the Cu^+ state, which is in line with our DRS and XPS results that indicated the reduction of the Cu^{2+} content.
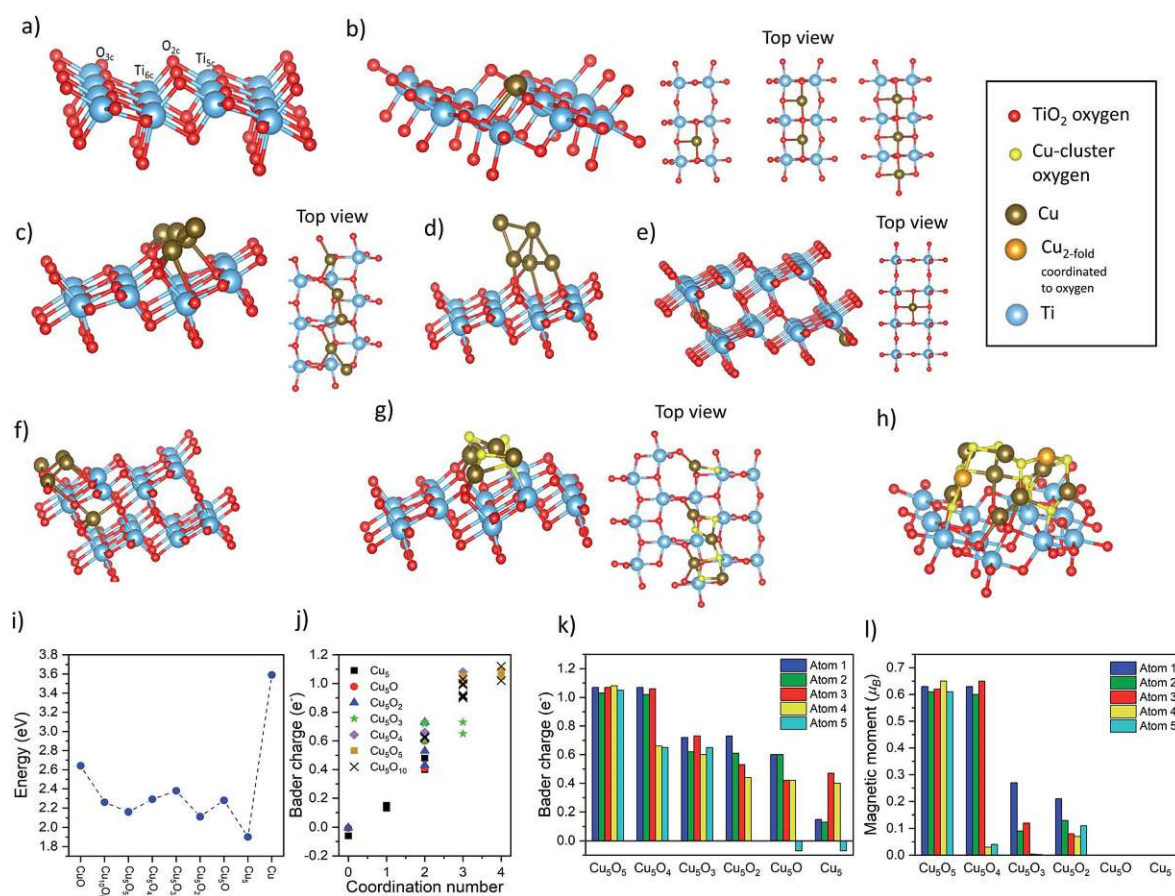
61

Fig. 7 (a) Side view of the anatase TiO_2 (101) surface layer (in the 1×3 supercell). (b) Side and top views of adsorbed Cu_x ($x = 1, 2, 3$) atoms, (c) Cu_5 atoms in the chain-like structure, (d) Cu_5 3D-like structure, (e) subsurface Cu atom, (f) one subsurface Cu atom in the Cu_5-chain structure, (g) Cu_5O_5 cluster and (h) $Cu_{10}O_9$ cluster adsorbed on the anatase TiO_2 (101) surface. (i) Adsorption energy (eV per atom) of Cu_xO_y clusters on the anatase TiO_2 (101) surface, with the cohesive energy of bulk CuO and Cu as references. (j) Bader charges versus Cu coordination number (selected according to Cu–O distances below 2.16 Å). Bader charges <0.4 correspond to Cu^0, 0.4–0.7 to Cu^+ and >0.7 to Cu^{2+}. (k) Bader charges (e^-) and (l) atomic magnetic moment (in μ_B) of Cu atoms in Cu_5O_y ($y = 5, 4, 3, 2, 1, 0$) clusters adsorbed on the anatase TiO_2 (101) surface.

Overall, the DFT results indicate that differently sized Cu clusters of a few atoms can indeed be stabilized on the TiO_2 surface. Analysis of the Cu oxidation state shows that Cu^+ and Cu^0 species are likely to form at the solid–solid interface, while Cu^{2+} species can only be formed as an outer cluster layer when enough oxygen is present, in line with the experimental data and the washing experiments. Furthermore, the models show that the generation of interstitial Cu^+ – surrounded by 4 O atoms of TiO_2 lattice – is the most stable species that can be formed via diffusion in thermally treated samples. Such Cu incorporation results in a minimal crystal structure change, and thus is in line with the Raman and XRD data.

Cu inter-band gap states. The origin of the absorption shoulder in DRS (Fig. 5a, b and 6) between 400 and 550 nm remains a matter of debate in literature. To uncover the nature of this shoulder, we calculated the partial density of state (PDOS) for an ideal TiO_2 (101) surface and for some selected and representative configurations of adsorbed Cu, Cu_5O_2 and Cu_5O_5 clusters, shown in Fig. 8.

The bare TiO_2 surface (Fig. 8a) exhibits a band gap of 2.5 eV (which is lower than the experimental value of 3.2 eV due to the well-known DFT shortcomings), the surface Ti-d states are a bit higher in energy than in the bulk and the Ti–O covalency is reduced (see reduced Ti-surface contribution at the bottom of the valence band). Furthermore, as this TiO_2 model represents an ideal surface without defects, it shows p-type conductivity in contrast to the experimental TiO_2 samples. Then, when a neutral Cu atom is added on the TiO_2-anatase (101) surface (Fig. 8b), the Fermi level moves to the conduction band (the added Cu is in a neutral state, thus, by adding it on the ideal-TiO_2 surface, Cu transfers negative charge to TiO_2) and the system becomes formally metallic (n-type conductivity). Additionally, the Cu-d states show some hybridization with the O-p orbitals closest to the Cu atoms. This is evident in the difference of the O-PDOS of O atoms close/far to Cu atoms, from which in general a downward/upward shift of O-p states for atoms close/far to Cu can be observed. In any case, the main Cu-d peaks are located above the VBM within the TiO_2 band gap

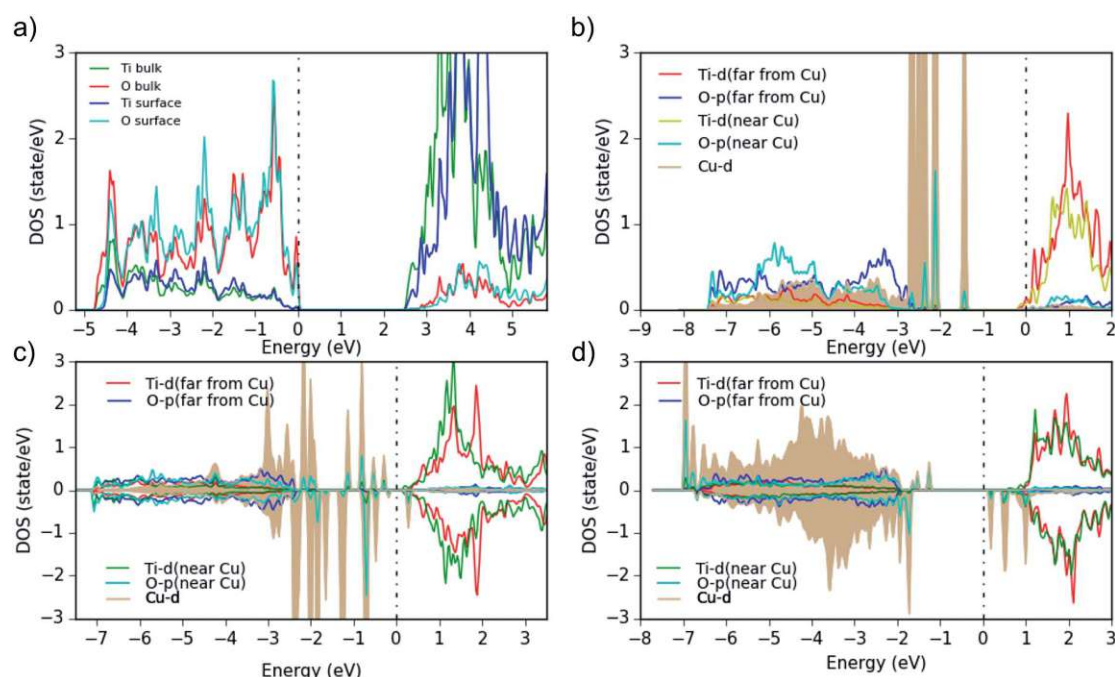21966 | J. Mater. Chem. A, 2021, 9, 21958–21971

This journal is © The Royal Society of Chemistry 2021

62

Fig. 8 Partial density of states (PDOS) for (a) bare anatase TiO_2 (101) surface, showing the surface atoms and the bulk-layer states, (b) one Cu atom, (c) Cu_5O_2 and (d) Cu_5O_5 adsorbed on the surface. All Ti and O PDOS are from surface atoms only. 0 eV indicates the Fermi energy, and the plots are aligned at the TiO_2 CBM.

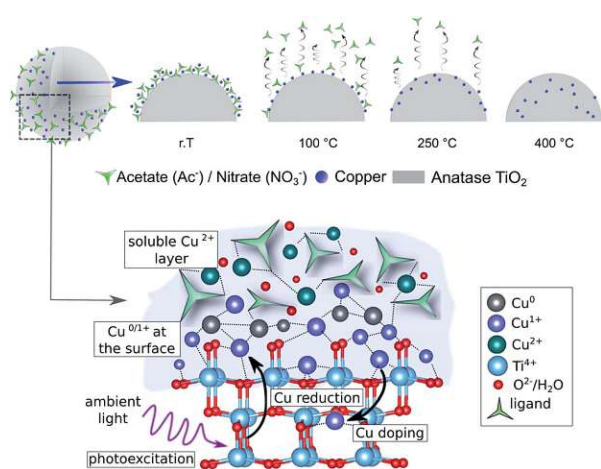**Fig. 9** Proposed mechanism of formation and evolution of Cu/TiO_2 photocatalysts upon thermal treatment, showing the thermally induced densification and diffusion of the Cu species. The bottom scheme illustrates the state of Cu-based co-catalysts during the wet-impregnation synthesis with the outer layer enriched with Cu^{2+}, while the Cu species at the TiO_2 surface partially turn into Cu^+ and Cu^0 via direct electron reduction.

and are fully occupied. Larger Cu clusters or Cu diffused into the subsurface (Cu_5O_2 and Cu_5O_5, Fig. 8c and d), show that the Cu-PDOS behaves qualitatively similarly. When more oxygen is added to the Cu_5O_x clusters, no electron transfer takes place anymore from the Cu 4s (and partly 3d) to the Ti-d states at the

CBM, but to the additional O atoms and the Fermi level moves down to the top of the Cu-d bands within the TiO_2 gap. In addition, spin-polarization sets in, magnetic moments on (some) Cu atoms appear, and the Hubbard U shifts fully (partially) occupied Cu-d states down (up) in energy (Fig. 8d), indicating typical Cu^{2+} behavior. This moves a lot of Cu-d states down into the O-p band (e.g. in Cu_5O_2 and Cu_5O_4, Fig. 8c) and eventually in Cu_5O_5 leads to clear lower (below the O-p band) and upper (above E_F) Hubbard bands with all Cu in the +2 state.

We conclude, the band gap reduction and the adsorption band between 400 and 550 nm of $Cu(NO_3)_2/TiO_2$ and $Cu(ac)_2/TiO_2$ – compared to pure TiO_2 – is related in all cases to Cu-d states in the band gap of the composites. In the case of Cu_5O_5, where Cu is mainly in the +2 state, we can also see some d states above the Fermi level, which can cause d–d excitations. The transitions from the highest occupied Cu-d states into the TiO_2 conduction band may also explain the observed adsorption above 600 nm in Fig. 5a, b and 6.

Proposed diffusion mechanism and active Cu state

The combined experimental and theoretical results confirm that thermal pretreatment can indeed initiate the diffusion of Cu species into the TiO_2 lattice, and that this process plays a key role in decreasing the photocatalytic activity towards HER. Moreover, Cu diffusion induces charge recombination centers, and results in lower availability of the Cu sites for the HER. Additionally, a mixed oxidation state of Cu^+, Cu^{2+} and Cu^0 is found to be in the composites at any thermal treatment; while Cu^{2+} is only weakly bound to the outer surface and can leach

This journal is © The Royal Society of Chemistry 2021

J. Mater. Chem. A, 2021, **9**, 21958–21971 | **21967**

63

when in solution. Thus, we propose the following formation mechanism, which is summarized in Fig. 9: first, during the synthesis, the Cu^{2+} precursor species are weakly chemisorbed onto the TiO_2 surface in a multilayer manner, in which the Cu atoms directly attached to the surface get reduced to Cu^+ and Cu^0, facilitated by the reduction with electrons accumulated on the TiO_2 surface. The low-temperature treatments of the as-prepared composites (≤150 °C) densify the network and enhance the electronic coupling between the Cu and the substrate resulting in increased HER performance (peak activity). Higher calcination temperatures (>150 °C) induce the decomposition of precursor anions and facilitate the diffusion of Cu^+ species into the TiO_2 lattice, which in turn introduces charge recombination centers and reduces the accessibility of the Cu co-catalyst at the catalyst–reactant interface leading to a strong decrease in the photocatalytic performance.[13,58]

Conclusions

This work sheds light on the thermally induced Cu diffusion into the TiO_2 lattice that has a detrimental effect on photocatalytic performance. We show that calcination temperatures below 200 °C enhance the HER activity, yet treatments at higher temperatures have a surprisingly detrimental effect. Using a comprehensive set of experimental and theoretical state-of-the-art techniques, we critically examined various possible reasons for this observation. HRTEM and XPS showed that sintering and change in the oxidation state of the Cu species can be excluded, as they reveal the absence of larger Cu clusters on the TiO_2 substrate even for the high-temperature treated samples, and all samples show a mixed Cu oxidation state – Cu^0, Cu^+ and Cu^{2+} – even for high-temperature calcined samples under air. Washing experiments show that at lower calcination temperatures Cu is weakly bounded and can leach off by 88.7%, yet at temperatures above 250 °C the percentage drops down to 12.4% of leached Cu. The combined assessment of XPS and XRF indicates that the drop of HER activity is not induced by leaching, but by diffusion of Cu into the TiO_2 lattice, as XRF – a bulk sensitive method, considering the nanometer-sized composites – shows a constant Cu concentration for all samples, while XPS – a surface-sensitive method – reveals a strong drop of the Cu amount on the surface. This is further supported by Raman, DRS and DFT calculations. Furthermore, the data demonstrate that a reduction of the Cu^{2+} precursor to mainly Cu^+ and partially to Cu^0 takes place already after impregnation – without any further post-treatment – which indicates a photoreduction of the precursor species by TiO_2 and that Cu^+ is stabilized as an interstitial dopant. From the results, we propose a mechanism as follows: (a) after impregnation Cu^{2+} is weakly bound on the substrate and get reduced by TiO_2 to Cu^+ and Cu^0, (b) by increasing temperature Cu densifies on the substrate and (c) at temperatures >200 °C Cu^+ diffuses into the TiO_2 lattice. The drop in photocatalytic performance is thus related to the diffusion of the co-catalyst species into the substrate, which generates charge recombination centers and depletes the number of co-catalyst species available on the surface for the redox reaction. This work demonstrates that

mild thermal treatments of photocatalytic systems are considerably more complex than previously believed. Thus, future studies on other co-catalysts and materials need to consider the potential side effects induced by calcination.

Experimental

Synthesis of the composites

All materials used for the syntheses were obtained from commercial suppliers. As such, anatase TiO_2 from Sigma-Aldrich, $Cu(ac)_2$ (98% pure) and $Cu(NO_3)_2$ from Sigma Aldrich (98% pure). The used solvent for the syntheses was absolute ethanol (from Chem-Lab NV) and for photocatalytic experiments deionized water and HPLC-gradient grade methanol (from VWR). The composites were synthesized by a wet impregnation method with a post-synthesis thermal treatment. The general synthesis procedure used for all samples included (a) suspending the TiO_2 powder (400 mg, 5 mmol) in ethanol (20 mL); (b) stirring the suspension for 5 minutes; (c) adding the corresponding precursor salt: $Cu(ac)_2/Cu(NO_3)_2$ (0.05 mmol) and stirring for another 5 min, (d) subjecting the resulting suspension to sonication to assist salt dissolution and homogenization of the suspension components for 15 minutes, (e) the resulting mixture was left stirring for 30 minutes; and (f) the ethanol was extracted under vacuum. The remaining powder was then ground. Afterwards, the samples were heat-treated at the corresponding temperature with a heating ramp of 2 h until reaching the desired temperature, in ambient air.

Characterisation methods

Transmission electron microscopy (TEM) images were obtained using FEI TECNAI F20 transmission electron microscope equipped with a field emission gun in bright field mode using 200 kV acceleration voltage. The sample was prepared from an ethanol suspension, using a copper holey carbon-coated grid (Plano, 200 mesh). X-ray diffraction (XRD) was performed using an XPERT III: PANalytical XPert Pro MPD (θ–θ Diffractometer) for the *in situ* experiments and an XPERT II: PANalytical XPert Pro MPD (θ–θ Diffractometer) for the *ex situ* experiments. The sample was placed on a sample holder and irradiated with a Cu X-ray source (8.04 keV, 1.5406 Å). The signal was acquired with Bragg–Brentano θ/θ-diffractometer geometry ranging from 5° to 80° degrees. The detector system was a semiconductor X'Celerator (2.1°) detector. The *in situ* experiment was performed under air flow and temperatures ranging from 25 °C to 800 °C. The *ex situ* experiments were performed with a Si NIST certified standard reference material (SRM 640d) as an internal standard. The internal standard was required in order to detect the crystal parameter changes of the samples. Refinements were done according to the instruction provided by the standard. The thermogravimetric (TGA) measurements were carried out on a PerkinElmer Thermogravimetric Analyser TGA 8000. The samples were placed into an Al_2O_3 crucible and heated with a dynamic method at a heating rate of 5 °C min^{-1} under air from 25 °C to 800 °C. The chemical composition of the samples was obtained with two different X-ray photoelectron spectroscopy

21968 | *J. Mater. Chem. A*, 2021, **9**, 21958–21971

This journal is © The Royal Society of Chemistry 2021

64

(XPS) machines. The Auger spectra were determined using a Thermo Fisher Microlab 310/350-spectrometer equipped with a twin anode Al/Mg-Kα X-ray source (XR3) and a hemispherical analyzer. Pass energies of 70 eV and 20 eV, as well as energy resolutions of 1 eV and 100 meV, were used for survey and detail spectra respectively (excitation energy: 1486.6 eV/1253.6 eV, beam power: 100 W, angle: 60° to sample surface normal, base pressure: 2×10^{-8} mbar, pressure during measurements: 3×10^{-8} mbar). All measurements were carried out with the sample in normal emission angle with respect to the analyzer. The samples were mounted onto the sample holder using double-sided carbon tape. The XPS spectra were acquired using an Axis Ultra DLD instrument from Kratos Analytical (UK) with the base pressure during spectra acquisition better than 1.1×10^{-9} torr (1.5×10^{-7} Pa), achieved by a combination of turbomolecular and ion pumps. Monochromatic Al-Kα radiation ($h\nu = 1486.6$ eV) is employed with the anode power set to 150 W. All spectra are collected at normal emission angle. Ultraviolet photoemission spectroscopy (UPS) experiment was carried out in home-built MOSES spectrometer under a base pressure of 5×10^{-10} mbar equipped with a monochromatic He-I radiation source ($h\nu = 21.22$ eV). All spectra were collected at normal emission and at room temperature. The total resolution of UPS is about 0.1 eV estimated from the width of the Fermi edge of a sputter-cleaned Au film. The signal was calibrated by using the Fermi edge of this sputtered Au. To extract sample work function, a bias of -50 V was applied to the sample during the UPS measurement. Data analysis was done using the CasaXPS Version 2.3.19PR1.0 software package employing Shirley/Shirley Tougaard backgrounds and Scofield sensitivity factors.[59,60] Curve fits using combined Gaussian–Lorentzian peak shapes (GL(30)) were used to discern the components of detail spectra if not stated otherwise. For the peak analysis a charge correction was applied to the adventitious carbon peak (C–C peak) shifting to 284.8 eV binding energy (BE) due to the absence of a clear Fermi edge and for comparison to literature values, while for the VBM, where the indium foil was used, a charge correction was done to the Fermi level. All content values shown are in units of a relative atomic percent (at%), where the detection limit in survey measurements usually lies around 0.1–0.5 at%, depending on the element. The accuracy of XPS measurements is around 10–20% of the values shown. Assignment of different components was primarily done using ref. 61 and 62. For the attenuated total reflection Fourier-transform infrared spectroscopy (ATR-FTIR) measurements a PerkinElmer FTIR Spectral UATR-TWO with a spectrum two Universal ATR (Single Reflection Diamond) accessory was used. Raman measurement was conducted with LabRAM HR800 (HORIBA Co. Ltd). Ne:YAG diode was used as 532 nm laser source and the characteristic Raman peak of Si at 520.8 cm^{-1} was used as the calibration peak. The laser intensity was kept at 5 mW. The obtained signal intensity was normalized to the anatase sample to avoid measuring artifacts. The X-ray Fluorescence Spectroscopy (XRF) chemical quantification analysis was performed with an Atomika 8030C X-ray fluorescence analyzer in total reflection geometry (XRF) with a molybdenum X-ray source (monochromatized Kα-line). The excitation conditions were 50 kV and 47 mA for 100 s irradiation time and an

energy-dispersive Si(Li)-detector was employed. For the sample preparation, all reflectors were washed thoroughly and measured to account for true blanks. 1 mg of the solid nano-powder was loaded on the clean reflectors and sealed with 5 μL of a 1% PVA solution to avoid contamination of the detector. After drying for 5 min on a hot plate and cooling, the reflectors with the loaded samples were measured. For the data evaluation, Ti was set as a matrix with 100% (wt%) and relative amounts of Cu were acquired (wt%). The Diffuse Reflectance Ultra-violet Spectroscopy (DRS or DR-UV-vis) a Jasco V-670 UV-Vis photo spectrometer has been used to measure diffusive reflectance spectra. The optical band gap was determined with the Tauc plots and with the exponent value, $n = 1/2$ for direct allowed transition.

Photocatalytic experiments

Hydrogen evolution experiments were performed using a top irradiation flow-reactor (total volume of 100 mL) equipped with an LED light source with incident light intensity of 0.488 W centred at 365 nm $\pm$ 15 nm (192 mW cm^{-2}, Thorlabs SOLIS). In a single experiment, the powdered photocatalyst (10 mg) was dispersed in 40 mL 1 : 1 vol% MeOH–water solution. During the experiment, the reactor was continuously purged with argon (flow rate of 30 mL min^{-1}, controlled with a mass flow controller from MCC-Instruments) to deliver the gaseous products to the online gas analyzer (X-Stream®, Emerson Process Management) equipped with a thermal conductivity detector (TCD) for H$_2$ quantification with an unmatchable sensitivity (down to ppm level) and time-resolution (one data point per second, see Fig. S1†). A typical H$_2$ evolution profile obtained with our flow reactor includes an "induction" period (increasing H$_2$ evolution rate during the first minutes) that is purely related to the fact the H$_2$ gas first needs to fill the dead volume (e.g., reactor volume, tubing volume) to reach the detector. The temperature of the reactor was kept constant through a water-cooling system (Lauda).

Computational methods

To understand the experimental observations regarding the influence of the copper oxidation state on H$_2$ production activity, spin-polarized DFT calculations of the model Cu$_x$O$_y$ clusters ($x = 1, 2, 3, 5, 10$ and $y = 0, 1, ..., 5, 9$) adsorbed on the anatase TiO$_2$ (101) surface were performed using the full-potential augmented plane wave plus local orbitals method as implemented in the WIEN2k code.[63–65] The TiO$_2$-anatase (101) surface was chosen as it is the most abundant and stable anatase surface.[66,67] We employed the PBEsol exchange–correlation functional, which is a generalized gradient approximation (GGA) and yields lattice parameters of bulk anatase TiO$_2$, $a = b = 3.77$ Å and $c = 9.54$ Å which are in good agreement with experimental data.[68] In order to treat the correlated 3d electrons a Hubbard U correction was used.[69] A value of $U_{\text{eff}} = U - J = 5$ eV has been used for Cu 3d e$^-$, which is chosen deliberately smaller than what is typically used in strongly correlated Cu oxides, since in our case also less ionic (neutral) clusters were investigated and the correlation may not be always so strong.

This journal is © The Royal Society of Chemistry 2021

J. Mater. Chem. A, 2021, 9, 21958–21971 | 21969

65

The (101) surface was modeled by a symmetric slab with a thickness of three layers of TiO_2 (Fig. S20†), where only one layer is shown for better visibility and a vacuum region of 16 Å between the slabs. In order to reduce the interactions between the adsorbed clusters in neighboring cells, a 1×3 supercell was used for all surfaces with adsorbed clusters. Moreover, such a supercell is also helpful to release the interfacial strain energy and find more stable configurations. A $2 \times 2 \times 1$ Γ-centered mesh of k-points was used during relaxation (a $5 \times 4 \times 1$ mesh for the final results) and a basis-set size corresponding to $R_{MT}^{min}K_{max} = 7$ was used for the Cu_x models (atomic sphere radii R_{MT} of Ti = 1.7, Cu = 1.65, O = 1.4 bohr), while the Cu_xO_y models used $R_{MT}^{min}K_{max} = 5.45$, because the O spheres had to be reduced to 1.09 bohr. All surface models were relaxed until the residual forces were below 1 mRy bohr^{-1}. Consistent R_{MT} and $R_{MT}^{min}K_{max}$ values were used for calculating the adsorption energy per atom E_{ads} of clusters on the anatase surface, which is defined as

$$E_{ads} = \frac{1}{x+y}\left[E(TiO_2(101)) + xE(Cu) + y\frac{1}{2}E(O_2)\right.$$
$$\left. - E\left(Cu_xO_y/TiO_2(101)\right)\right], \quad (1)$$

where $E(Cu)$ and $E(O_2)$ are the total energies of the free Cu atom and the O_2 molecule in the gas phase, $E(TiO_2 (101))$ is for the bare TiO_2 (101) surface, and $E(Cu_xO_y/TiO_2 (101))$ is the total energy of anatase with the surface-attached cluster. To calculate the oxidation state and the magnetic moment of each atom, we used Bader's method, which uses the electron density to calculate the gradient vector field and the atomic basins by searching for surfaces of zero flux.[70,71] An integral of the electron (spin) density enclosed within these basins defines the total electronic charge (magnetic moment) of an atom. To provide reference values for oxidation states, calculations for bulk Cu, Cu_2O, and antiferromagnetic CuO were also done.

Author contributions

Jasmin S. Schubert: methodology, validation, formal analysis, investigation, writing – original draft, data curation, visualization. Leila Kalantari: investigation, formal analysis, writing – review & editing, data curation, software, visualization. Andreas Lechner: investigation, formal analysis, visualization. Ariane Giesriegl: investigation. Sreejith P. Nandan: investigation. Pablo Alaya: investigation. Shun Kashiwaya: investigation, writing – review & editing. Markus Sauer: writing – review & editing, resources. Annette Foelske: writing – review & editing, resources. Johanna Rosen: writing – review & editing. Peter Blaha: supervision, writing – review & editing. Alexey Cherevan: conceptualization, methodology, supervision, project administration, writing – review & editing. Dominik Eder: conceptualization, supervision, writing – review & editing, project administration, funding acquisition, resources.

Conflicts of interest

There are no conflicts to declare.

References

1 T. Jafari, E. Moharreri, A. S. Amin, R. Miao, W. Song and S. L. Suib, *Molecules*, 2016, **21**, 900.
2 A. Kudo and Y. Miseki, *Chem. Soc. Rev.*, 2008, **38**, 253–278.
3 X. Li, J. Yu, J. Low, Y. Fang, J. Xiao and X. Chen, *J. Mater. Chem. A*, 2015, **3**, 2485–2534.
4 I. Roger, M. A. Shipman and M. D. Symes, *Nat. Rev. Chem.*, 2017, **1**, 0003.
5 B. M. Hunter, H. B. Gray and A. M. Müller, *Chem. Rev.*, 2016, **116**, 14120–14136.
6 S. Bai, W. Jiang, Z. Li and Y. Xiong, *ChemNanoMat*, 2015, **1**, 223–239.
7 M.-K. Jeon, J.-W. Park and M. Kang, *J. Ind. Eng. Chem.*, 2007, **1**, 84–91.
8 N.-L. Wu and M.-S. Lee, *Int. J. Hydrogen Energy*, 2004, **29**, 1601–1605.
9 A. J. J. Lennox, P. Bartels, M.-M. Pohl, H. Junge and M. Beller, *J. Catal.*, 2016, **340**, 177–183.
10 M. Jung, J. Scott, Y. H. Ng, Y. Jiang and R. Amal, *Int. J. Hydrogen Energy*, 2014, **39**, 12499–12506.
11 Y. Wu, G. Lu and S. Li, *Catal. Lett.*, 2009, **133**, 97.
12 H.-J. Choi and M. Kang, *Int. J. Hydrogen Energy*, 2007, **32**, 3841–3848.
13 M. Nolan, A. Iwaszuk, A. K. Lucid, J. J. Carey and M. Fronzi, *Adv. Mater.*, 2016, **28**, 5425–5446.
14 L. Zhang, Q. Zheng, Q. Xie, Z. Lan, O. V. Prezhdo, W. A. Saidi and J. Zhao, *Nano Lett.*, 2018, **8**.
15 Q. Hu, J. Huang, G. Li, Y. Jiang, H. Lan, W. Guo and Y. Cao, *Appl. Surf. Sci.*, 2016, **382**, 170–177.
16 M. Jung, J. N. Hart, J. Scott, Y. H. Ng, Y. Jiang and R. Amal, *Appl. Catal., A*, 2016, **521**, 190–201.
17 J. Yu, Y. Hai and M. Jaroniec, *J. Colloid Interface Sci.*, 2011, **357**, 223–228.
18 J. Bandara, C. P. K. Udawatta and C. S. K. Rajapakse, *Photochem. Photobiol. Sci.*, 2005, **4**, 857–861.
19 T. Akita, P. Lu, S. Ichikawa, K. Tanaka and M. Haruta, *Surf. Interface Anal.*, 2001, **31**, 73–78.
20 N. Waiskopf, Y. Ben-Shahar and U. Banin, *Adv. Mater.*, 2018, **30**, 1706697.

21970 | *J. Mater. Chem. A*, 2021, **9**, 21958–21971

This journal is © The Royal Society of Chemistry 2021

66

21 F. A. L. Laskowski, S. Z. Oener, M. R. Nellist, A. M. Gordon, D. C. Bain, J. L. Fehrs and S. W. Boettcher, *Nat. Mater.*, 2020, **19**, 69–76.

22 A. El Mragui, Y. Logvina, L. Pinto da Silva, O. Zegaoui and J. C. G. Esteves da Silva, *Materials*, 2019, **12**(23), 3874.

23 T. Ohsaka, F. Izumi and Y. Fujiki, *J. Raman Spectrosc.*, 1978, **7**, 321–324.

24 W. Li, L. Fang, G. Qin, H. Ruan, H. Zhang, C. Kong, L. Ye, P. Zhang and F. Wu, *J. Appl. Phys.*, 2015, **117**, 145301.

25 A. Chanda, K. Rout, M. Vasundhara, S. R. Joshi and J. Singh, *RSC Adv.*, 2018, **8**, 10939–10947.

26 J. I. Garza-Arévalo, I. García-Montes, M. H. Reyes, J. L. Guzmán-Mar, V. Rodríguez-González and L. H. Reyes, *Mater. Res. Bull.*, 2016, **73**, 145–152.

27 A. A. Kashale, A. S. Rasal, G. P. Kamble, V. H. Ingole, P. K. Dwivedi, S. J. Rajoba, L. D. Jadhav, Y.-C. Ling, J.-Y. Chang and A. V. Ghule, *Composites, Part B*, 2019, **167**, 44–50.

28 M. R. Joya, K. M. Fonseca and J. Barba-Ortega, *AIP Conf. Proc.*, 2014, **1627**, 42–45.

29 P. Colomban and A. Slodczyk, *Acta Phys. Pol., A*, 2009, **116**, 7.

30 J. Halim, M. R. Lukatskaya, K. M. Cook, J. Lu, C. R. Smith, L.-Å. Näslund, S. J. May, L. Hultman, Y. Gogotsi, P. Eklund and M. W. Barsoum, *Chem. Mater.*, 2014, **26**, 2374–2381.

31 A. M. Alotaibi, B. A. D. Williamson, S. Sathasivam, A. Kafizas, M. Alqahtani, C. Sotelo-Vazquez, J. Buckeridge, J. Wu, S. P. Nair, D. O. Scanlon and I. P. Parkin, *ACS Appl. Mater. Interfaces*, 2020, **12**, 15348–15361.

32 M. Y. Mihaylov, V. R. Zdravkova, E. Z. Ivanova, H. A. Aleksandrov, P. St. Petkov, G. N. Vayssilov and K. I. Hadjiivanov, *J. Catal.*, 2021, **394**, 245–258.

33 V. Krylova and M. Andrulevičius, *Int. J. Photoenergy*, 2009, **2009**, e304308.

34 M. C. Biesinger, B. P. Payne, A. P. Grosvenor, L. W. M. Lau, A. R. Gerson, R. St and C. Smart, *Appl. Surf. Sci.*, 2011, **257**, 2717–2730.

35 M. C. Biesinger, *Surf. Interface Anal.*, 2017, **49**, 1325–1334.

36 J. Y. Park, Y. C. Kang, K. A. Lim and R. D. Ramsier, *Bull. Korean Chem. Soc.*, 2011, **32**, 3395–3399.

37 L. P. Bevy, *Focus on Catalysis Research*, Nova Publishers, 2006.

38 X. Qiu, M. Miyauchi, K. Sunada, M. Minoshima, M. Liu, Y. Lu, D. Li, Y. Shimodaira, Y. Hosogi, Y. Kuroda and K. Hashimoto, *ACS Nano*, 2012, **6**, 1609–1618.

39 S. Pande, M. G. Weir, B. A. Zaccheo and R. M. Crooks, *New J. Chem.*, 2011, **35**, 2054–2060.

40 A. Dikhtiarenko, P. Villanueva-Delgado, R. Valiente, J. R. García and J. Gimeno, *Polymers*, 2016, **8**(2), 48.

41 B. Viswanathan, *Catalysis: Principles and Applications*, CRC Press, 2002.

42 H. Irie, K. Kamiya, T. Shibanuma, S. Miura, D. A. Tryk, T. Yokoyama and K. Hashimoto, *J. Phys. Chem. C*, 2009, **113**, 10761–10766.

43 H. Irie, S. Miura, K. Kamiya and K. Hashimoto, *Chem. Phys. Lett.*, 2008, **457**, 202–205.

44 K. Wang, L. Yang, W. Zhao, L. Cao, Z. Sun and F. Zhang, *Green Chem.*, 2017, **19**, 1949–1957.

45 P. Makuła, M. Pacia and W. Macyk, *J. Phys. Chem. Lett.*, 2018, **9**, 6814–6817.

46 I. Ganesh, P. P. Kumar, I. Annapoorna, J. M. Sumliner, M. Ramakrishna, N. Y. Hebalkar, G. Padmanabham and G. Sundararajan, *Appl. Surf. Sci.*, 2014, **293**, 229–247.

47 S. Mathew, P. Ganguly, S. Rhatigan, V. Kumaravel, C. Byrne, S. J. Hinder, J. Bartlett, M. Nolan and S. C. Pillai, *Appl. Sci.*, 2018, **8**, 2067.

48 A. Kahn, *Mater. Horiz.*, 2015, **3**, 7–10.

49 S. Kashiwaya, J. Morasch, V. Streibel, T. Toupance, W. Jaegermann and A. Klein, *Surfaces*, 2018, **1**, 73–89.

50 S. Moser, L. Moreschini, J. Jaćimović, O. S. Barišić, H. Berger, A. Magrez, Y. J. Chang, K. S. Kim, A. Bostwick, E. Rotenberg, L. Forró and M. Grioni, *Phys. Rev. Lett.*, 2013, **110**, 196403.

51 K. Ozawa, M. Emori, S. Yamamoto, R. Yukawa, S. Yamamoto, R. Hobara, K. Fujikawa, H. Sakama and I. Matsuda, *J. Phys. Chem. Lett.*, 2014, **5**, 1953–1957.

52 S. Selcuk and A. Selloni, *Nat. Mater.*, 2016, **15**, 1107–1112.

53 U. Diebold, *Surf. Sci. Rep.*, 2003, **48**, 53–229.

54 D. Spanu, A. Minguzzi, S. Recchia, F. Shahvardanfard, O. Tomanec, R. Zboril, P. Schmuki, P. Ghigna and M. Altomare, *ACS Catal.*, 2020, **10**, 8293–8302.

55 S. K. Iyemperumal, T. G. Fenton, S. L. Gillingham, A. D. Carl, R. L. Grimm, G. Li and N. A. Deskins, *J. Chem. Phys.*, 2019, **151**, 054702.

56 A. Alghannam, C. L. Muhich and C. B. Musgrave, *Phys. Chem. Chem. Phys.*, 2017, **19**, 4541–4552.

57 N. Seriani, C. Pinilla and Y. Crespo, *J. Phys. Chem. C*, 2015, **119**, 6696–6702.

58 Z. Lin, D. Han and S. Li, *J. Therm. Anal. Calorim.*, 2012, **107**, 471–475.

59 S. Tougaard, *Surf. Interface Anal.*, 1997, **25**, 137–154.

60 D. A. Shirley, *Phys. Rev. B: Solid State*, 1972, **5**, 4709–4714.

61 C. D. Wagner, A. V. Naumkin, A. Kraut-Vass, J. W. Allison, C. J. Powell and J. R. Rumble, *NIST standard reference database*, 2003, vol. 20, ch. 3, pp. 251–252.

62 G. Beamson and D. Briggs, *Anal. Chem.*, 1992, **64**, 1729–1736.

63 P. Blaha, K. Schwarz, G. K. H. Madsen, D. Kvasnicka, J. Luitz, R. Laskowsk, F. Tran, L. Marks and L. Marks, *WIEN2k: An Augmented Plane Wave Plus Local Orbitals Program for Calculating Crystal Properties*, Techn. Universitat, 2019.

64 D. J. Singh and L. Nordstrom, *Planewaves, Pseudopotentials, and the LAPW Method*, Springer US, 2nd edn, 2006.

65 P. Blaha, K. Schwarz, F. Tran, R. Laskowski, G. K. H. Madsen and L. D. Marks, *J. Chem. Phys.*, 2020, **152**, 074101.

66 M. Lazzeri, A. Vittadini and A. Selloni, *Phys. Rev. B: Condens. Matter Mater. Phys.*, 2001, **63**, 155409.

67 M. Lazzeri, A. Vittadini and A. Selloni, *Phys. Rev. B: Condens. Matter Mater. Phys.*, 2002, **65**, 119901.

68 J. P. Perdew, A. Ruzsinszky, G. I. Csonka, O. A. Vydrov, G. E. Scuseria, L. A. Constantin, X. Zhou and K. Burke, *Phys. Rev. Lett.*, 2008, **100**, 136406.

69 V. I. Anisimov, J. Zaanen and O. K. Andersen, *Phys. Rev. B: Condens. Matter Mater. Phys.*, 1991, **44**, 943–954.

70 R. F. W. Bader, *Chem. Rev.*, 1991, **91**, 893–928.

71 R. F. W. Bader, *Atoms in Molecules: A Quantum Theory*, Oxford University Press, Oxford, New York, 1994.

This journal is © The Royal Society of Chemistry 2021

J. Mater. Chem. A, 2021, **9**, 21958–21971 | **21971**

67

Supporting Information

Elucidating the formation and active state of Cu co-catalysts for photocatalytic hydrogen evolution

Jasmin S. Schubert, Leila Kalantari, Andreas Lechner, Ariane Giesriegl, Sreejith P. Nandan, Pablo Alaya, Shun Kashiwaya, Markus Sauer, Annette Foelske, Johanna Rosen, Peter Blaha, Alexey Cherevan* and Dominik Eder*

List of Sections and Figures/Tables

2

1. Hydrogen evolution reaction (HER)

A typical H_2 evolution profile obtained with our flow reactor (**Figure S1a**) includes an "induction" period that is related to the fact the H_2 gas needs to fill the dead volume (e.g., reactor volume, tubing volume) to reach the detector (see **Figure S1b,c** for the experimental setup). The delay in H_2 increase (2-3 minutes after illumination start) thus corresponds to the first H_2 species reaching the detector cell. A stable evolution rate is typically reached after 40-60 minutes of illumination.
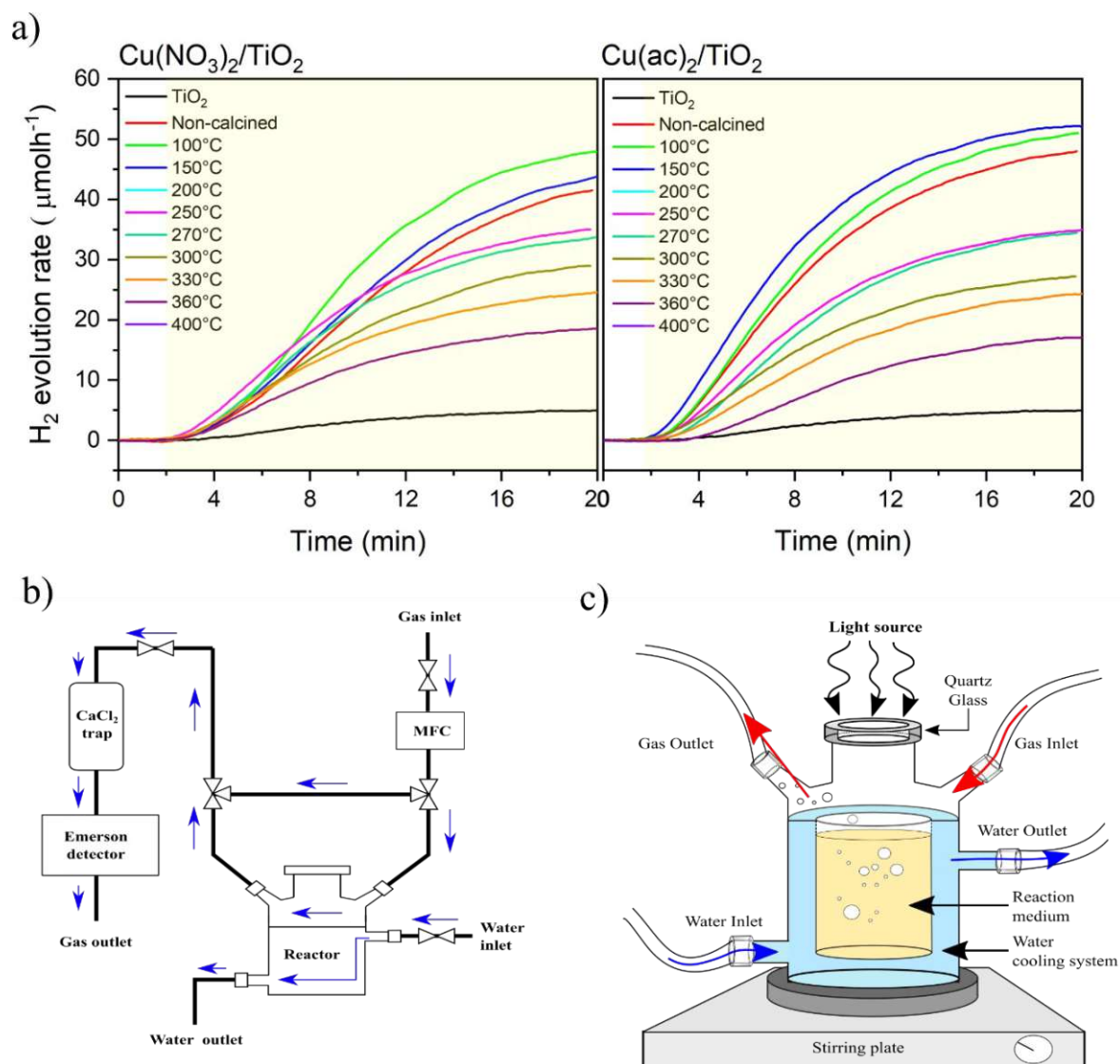
Figure S1: a) HER activity rates obtained for the different thermally treated Cu/TiO_2 composites along with the reference sample, TiO_2. The yellow region indicates the time of illumination. The bar graph, **Figure 1a**, in the main manuscript was constructed from these profiles at 20 minutes of illumination. b) Scheme of the photocatalytic setup used to evaluate HER rates (MFC: mass flow controller) and b) top-irradiation, flow-reactor used.

3

For this particular work, we were not interested in measuring the ultimate activities of the samples (e.g. waiting until the H_2 evolution rate reached a plateau), but - in order to speed up the photocatalytic evaluation - we only measured the activity value reached after 20 minutes of illumination (i.e. in the middle of the ascending slope). The values are reported in **Figure 1a** and allow for qualitative evaluation and comparison between the samples. The values are also representative of the absolute activity rates.

Table S1: HER rate maximum after 20 minutes of illumination. Values are taken from **Figure S1a** and represented in **Figure 1a,** in the main manuscript.

	H_2 evolution rate, $\mu mol\ h^{-1}$	
	$Cu(ac)_2/TiO_2$	$Cu(NO_3)_2/TiO_2$
TiO_2	5.03	5.03
RT	47.97	41.47
100 °C	50.98	47.88
150 °C	52.18	43.55
200 °C	47.44	40.94
250 °C	37.88	35.01
270 °C	34.48	33.71
300 °C	27.22	28.98
330 °C	24.23	24.51
360 °C	17.29	18.55
400 °C	14.81	13.25

71

1.1. Calcination time effect on the HER activity

HER trend for the $Cu(ac)_2/TiO_2$ sample hold from 44 to 655 minutes at 250 °C. This data shows that at constant temperature but longer calcination times, the activity decreases. Hence, this shows the same behavior than by increasing temperature but constant time. This data agrees with the hypothesis of doping, as longer calcination time would led to more time the system to equilibrate, i.e. Cu has more time to incorporate into the TiO_2 lattice. The amount of doping depends on the kinetics (time that it has to diffuse) and thermodynamics (temperature/energy).
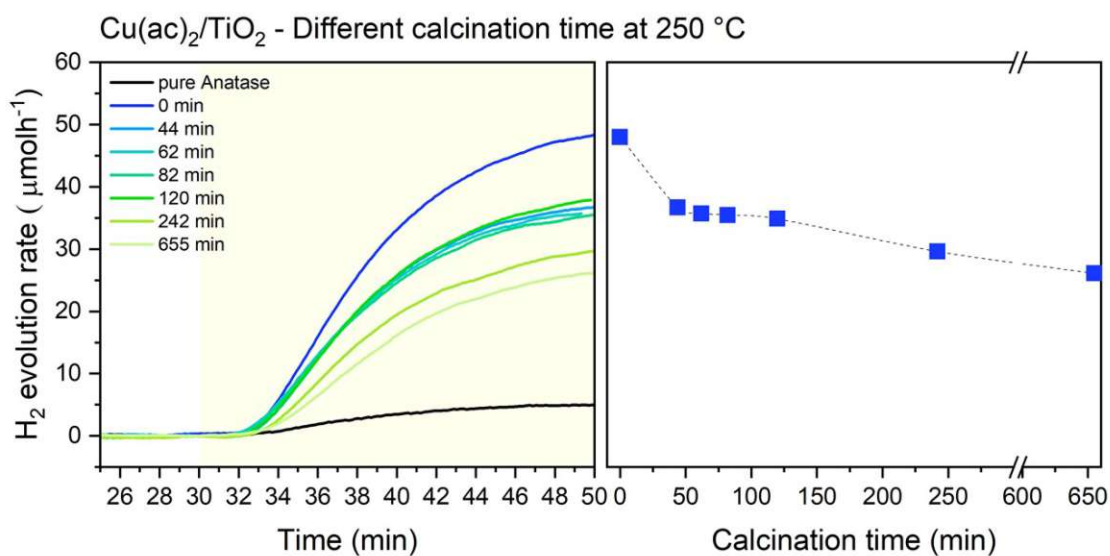

Figure S2. Time-depended HER at a constant calcination temperature of 250 °C. a) HER vs reaction time. The yellow region is the illumination time. b) The HER at different calcination time after 20 minutes of illumination.

1.2. Long-term performance (stability)

With regard to the stability issue, long-term performance of our catalysts has been investigated using a combination of our flow-reactor and H_2 detection flow-cell by Emerson. **Figure S3** shows a 25 h HER run composed of two illumination cycles conducted for one of our Cu/TiO_2 samples. As clarified in the setup description, we observe a quick rise of "activity" that riches a plateau within the first hour. Over the course of the next 17 h of illumination, H_2 evolution rate undergoes a slight but gradual drop (ca 18% of the max value) and reaches a new stability level. After the light is off (end of the first illumination cycle), we observe the expected drop of the H_2 evolution rate to zero. The second illumination cycle (the mutually compensating positive and negative spikes at 20 h point are related to carrier-gas supply change) yields activity similar to the second stability regime. Overall, these data illustrate a minor deactivation of the composite photocatalyst, however, they also indicate the overall stable long-term performance.
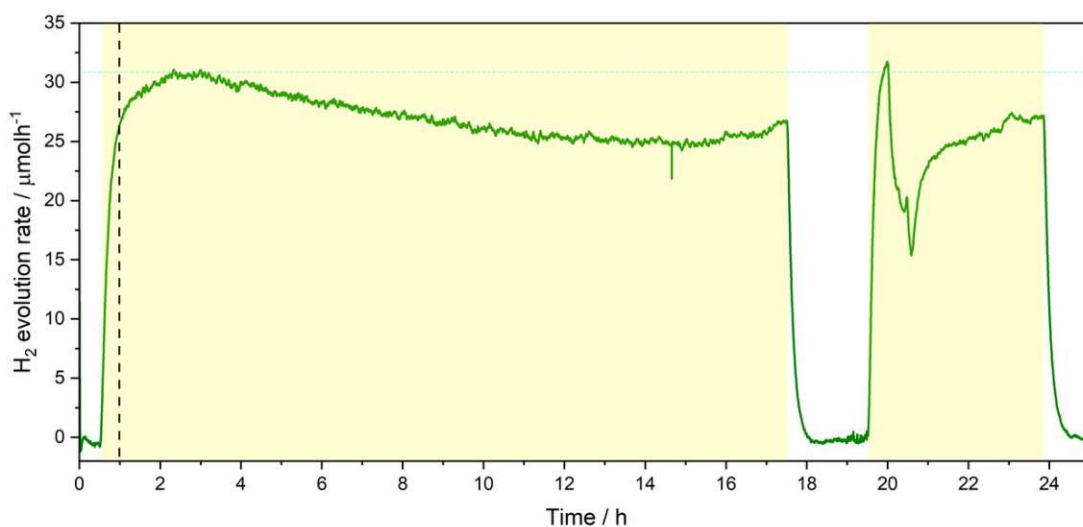
Figure S3. Long-term time-depended HER stability test of one of the Cu/TiO_2 samples.

73

2. Thermal behavior of the composites

We examined the pure precursors - $Cu(ac)_2$ and $Cu(NO_3)_2$ – and the obtained composite $Cu(ac)_2/TiO_2$ and $Cu(NO_3)_2/TiO_2$ powders with TGA (in air) to reveal the decomposition behavior. **Figure S4** shows the obtained weight loss profiles for the pure precursors, the composites and the reference TiO_2 powder. The continuous mass loss of the reference TiO_2 in the entire temperature range can be ascribed to slow removal of adsorbed (physisorbed and chemisorbed) solvent and other species; and, importantly, this reference profile can be treated as a baseline to quantitatively describe the behavior of composites. The analysis of the pure precursors shows that the first decomposition step starts at 82.3°C for both precursors and ending at 147.8 °C for $Cu(ac)_2$ and 179.9 °C for $Cu(NO_3)_2$, corresponding to the evaporation of water molecules.[1] The second step ranges from 251.5 °C until 288.9 °C for $Cu(ac)_2$ and 213.2°C to 261.7 °C for $Cu(NO_3)_2$. Corresponding to the decomposition of the acetate and nitrate ions, respectively. In the case of $Cu(ac)_2$ the acetate ion undergoes decomposition via radical formation which leads to the formation of metallic Cu as an intermediate product before it gets re-oxidized at higher temperatures (see **Figure S4** from 288.9 to 800 °C).[2]
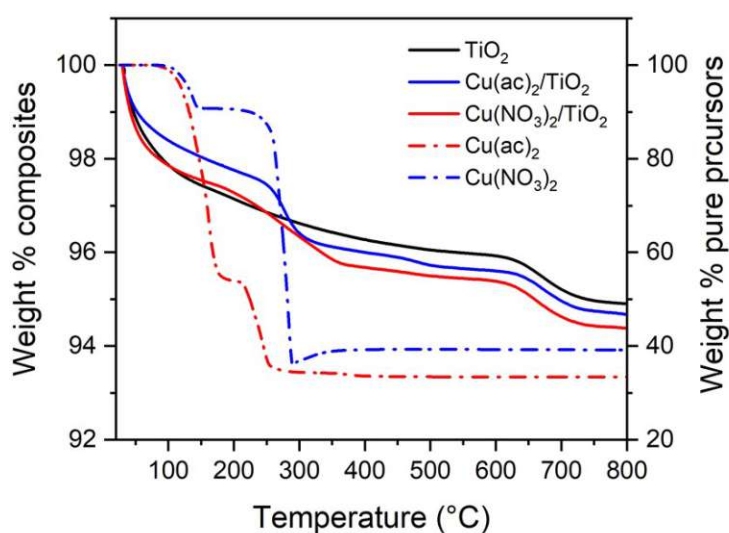
Figure S4: TGA data from 20 °C to 800 °C with a heating rate of 5 °C min^{-1} of the reference TiO_2, the pure precursors - $Cu(ac)_2$ and $Cu(NO_3)_2$ – and the composites $Cu(ac)_2/TiO_2$ and $Cu(NO_3)_2/TiO_2$. Note: The left y-axes correspond to the composites while the right y- axes to the pure precursors.

3. SEM and further TEM of the samples for Cu quantification
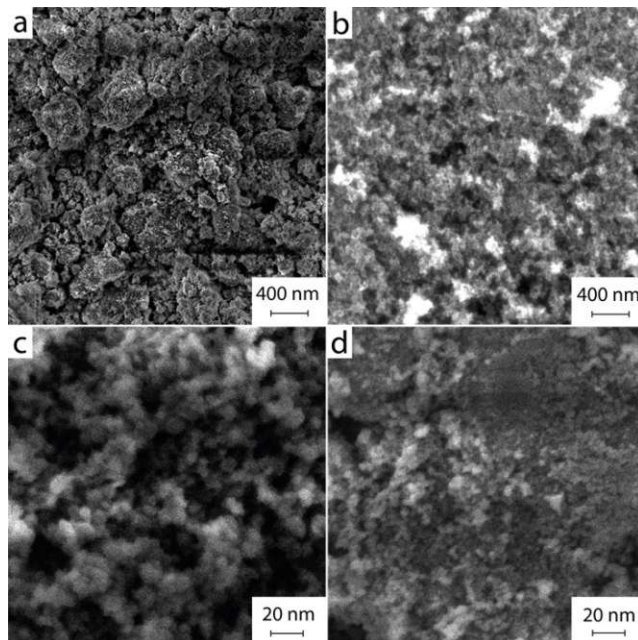
Figure S5: (a-d) SEM images of the as-prepared $Cu(ac)_2/TiO_2$ composites.

Figure S6: TEM pictures corresponding to $Cu(ac)_2/TiO_2$ ranging from non-calcined to 400 °C (left to right).

8

75

4. Raman

Table S2. Raman peak positions, FWHM and Intensity maximum values. The FWHM error was obtained from the mathematical model used to determine the values from the raw data and was estimated to be $\pm$ 0.1 cm^{-1} for both sample sets.

	Cu(ac)$_2$/TiO$_2$			Cu(NO$_3$)$_2$/TiO$_2$		
	Peak position cm^{-1}	FWHM cm^{-1}	Intensity maximum a.u.	Peak position cm^{-1}	FWHM cm^{-1}	Intensity maximum a.u.
TiO$_2$-anatase	145.6	14.6	38825.7	146.3	14.5	46155.2
RT	146.1	15.5	26373.3	144.7	14.7	38156.0
100 °C	146.1	15.5	26908.0	145.3	14.7	36622.2
200 °C	146.1	15.1	25247.7	145.8	15.1	33309.5
250 °C	146.6	15.5	22275.3	146.3	15.2	27572.4
270 °C	146.6	15.2	21890.7	146.3	14.8	27534.5
330 °C	146.6	16.4	19226.7	146.8	15.4	21843.3
360 °C	146.1	15.9	17179.3	146.3	14.6	17432.8
400 °C	146.1	15.8	18781.0	146.8	15.2	21725.2

9

5. XRD

Pure precursor: In-situ XRD diffractograms were taken from the pure precursors, $Cu(ac)_2$ and $Cu(NO_3)_2$ (**Figure S7**). The precursor maintains a crystalline structure over the whole calcination temperature range (from non-calcined to 800 °C). The diffractogram of $Cu(ac)_2$ is shown at 25°C and then its decomposition from 100°C to 200°C. At 220°C we see the formation of mixed metallic Cu, Cu_2O and CuO species – known from previous work that acetate decomposes through a radical formation – then by gradually increasing the calcination temperature, all Cu oxidizes to CuO. For $Cu(NO_3)_2$ the same trend is observable - yet, without reduction intermediates - where a gradual decomposition of the nitrate salt takes place until all Cu is transformed to CuO. [1,2]

Composites: The XRD analysis further confirmed the exclusive presence of the anatase phase (**Figure S7** and **Table S3**), in line with Raman Spectroscopy. The patterns show no significant peak broadening or peak shift, even for the 400°C treated sample, while only small changes of the crystal parameters upon the thermal treatment can be explained by the relatively small Cu amount present in the samples (~1 at. %). This is in line with recent DFT studies which suggest that a potential Cu incorporation (via interstitial or substitutional $Cu:TiO_2$ doping) does not result in a pronounced TiO_2 lattice distortion.[3] Both, Raman and XRD results are merely hints for potential interstitial doping of Cu into the TiO_2 lattice at elevated temperatures.

Table S3: Crystal parameters from the $Cu(ac)_2/TiO_2$ sample shown in **Figure S7**. Pure anatase *vs.* non-calcined (RT) and at 400 °C treated $Cu(ac)_2/TiO_2$ samples. As a standard reference material was used Si with a certified lattice parameter of 0.543123 ± 0.000008 nm (SRM 604d) at 22.5 °C in order to determine the crystal lattice parameter changes.

	XRD Crystal lattice parameters		
	a	c	Si
TiO_2-anatase	3.779	9.491	5.431
Cu/TiO_2 - RT	3.788	9.510	5.431
Cu/TiO_2 - 400 °C	3.790	9.509	5.431

10
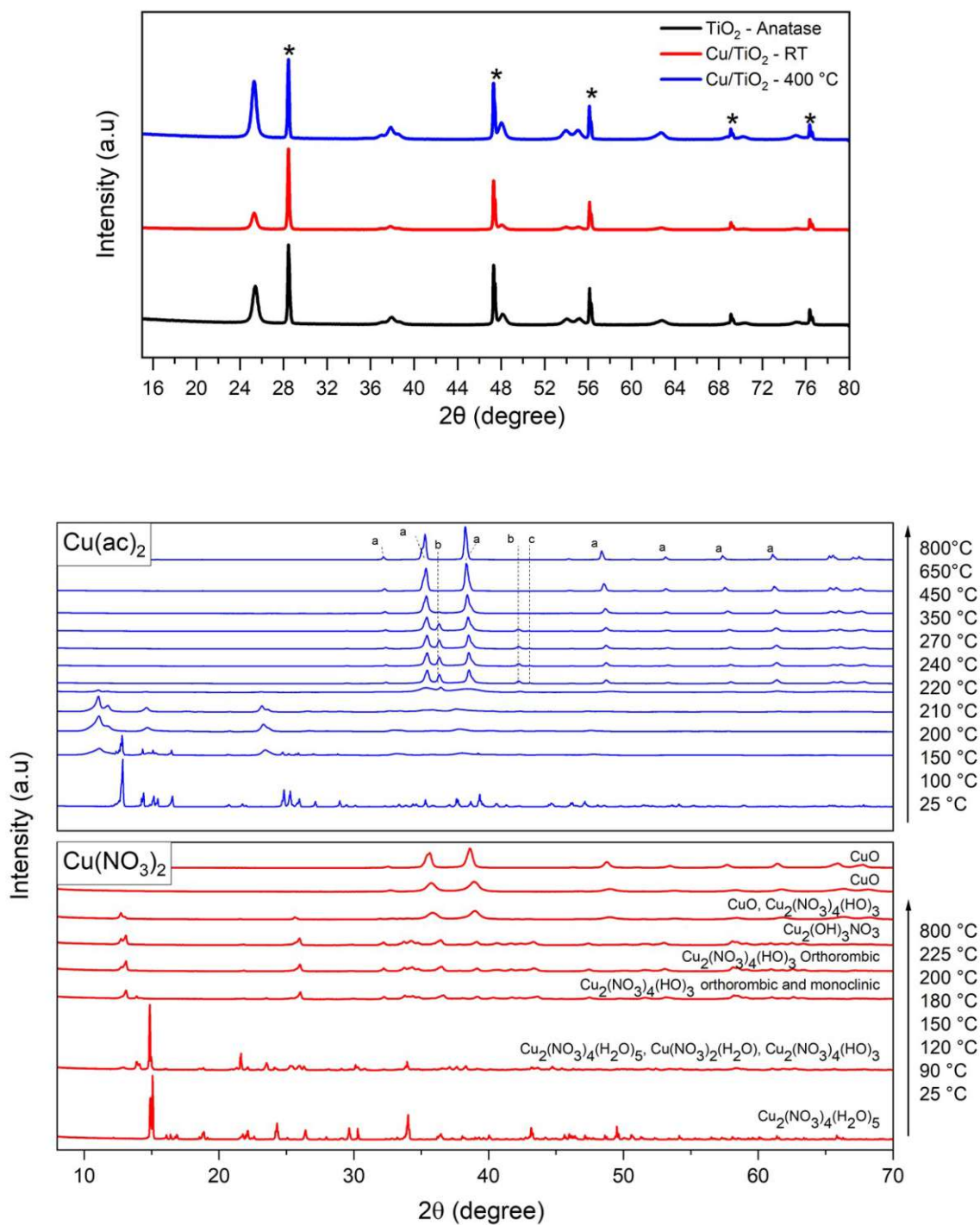
Figure S7: Top: XRD of the non-calcined and 400 °C treated Cu(ac)$_2$/TiO$_2$. The (*) indicates the Si phase used as internal standard to determine the crystal lattice parameters changes. All other phases belong to anatase TiO$_2$. Bottom: in-situ XRD; thermal decomposition evolution of the pure precursors. (a) Cu(ac)$_2$ and (b) Cu(NO$_3$)$_2$.

11

6. Infrared spectroscopy (FT-IR)

We analyzed for comparison the pure precursors and the composites at different thermal treatments to determine correlations of their behaviors.
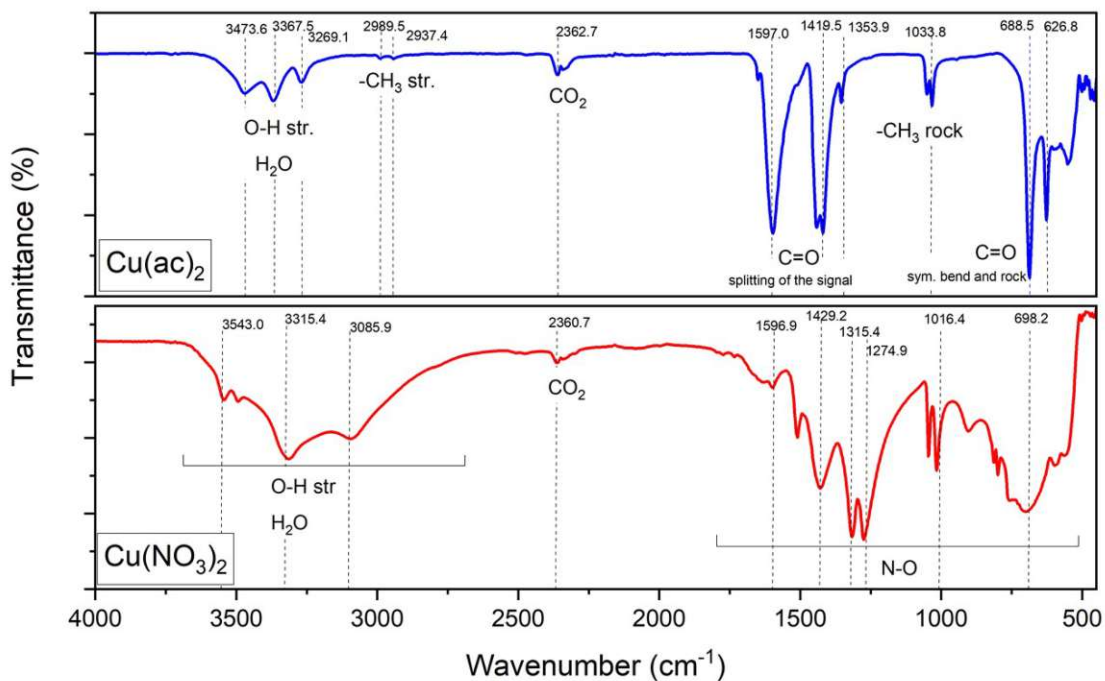
Figure S8: IR-ATR of the pure precursors, $Cu(ac)_2$ and $Cu(NO_3)_2$.
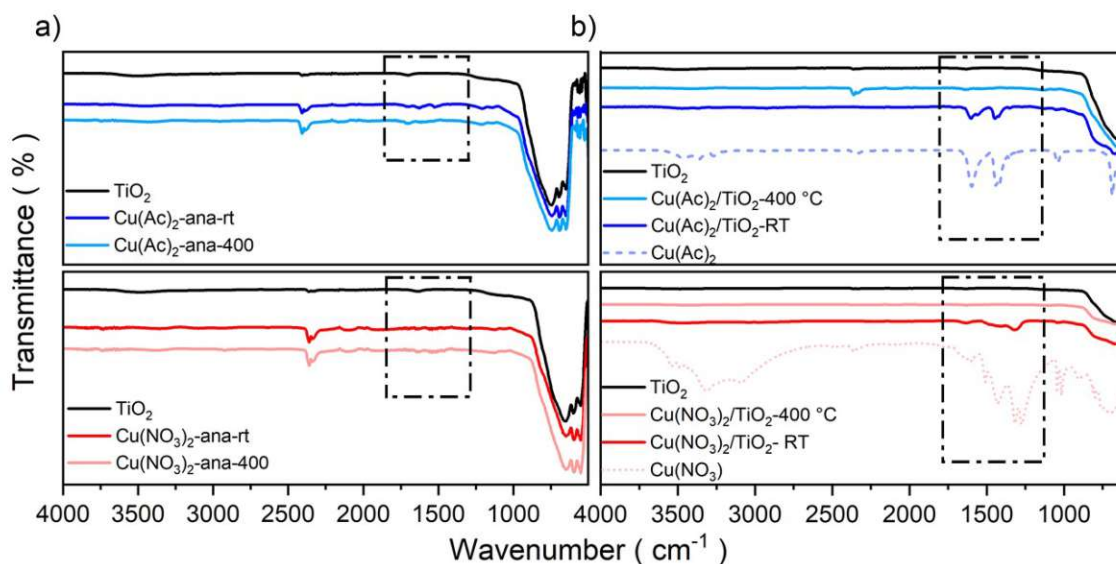
**Figure S9:** Full range FTIR-ATR of the $Cu(ac)_2/TiO_2$ and $Cu(NO_3)_2/TiO_2$ samples at different calcination temperatures. a) 1 at. % of Cu and b) 5 at. % of Cu.

12

79

7. XPS

The XPS measurements were done with two different XPS machines, one with a monochromatic Al-Kα source and one equipped with a dual anode providing Al-Kα and Mg-Kα radiation. Furthermore, measurements were done deposing the samples on an indium foil (measured with the mono source) and on a carbon tape (used for the dual anode). The indium foil was used to avoid charging effects and so to determine a correct work function and valence band. The dual anode was used to resolve the Cu-auger bands (Cu LMM), using the Mg-Kα radiation, due to an overlap of the Ti 2s signals. By using this radiation, an apparent shift of binding energy of the auger band is induced (see the corresponding surveys).

Surveys:
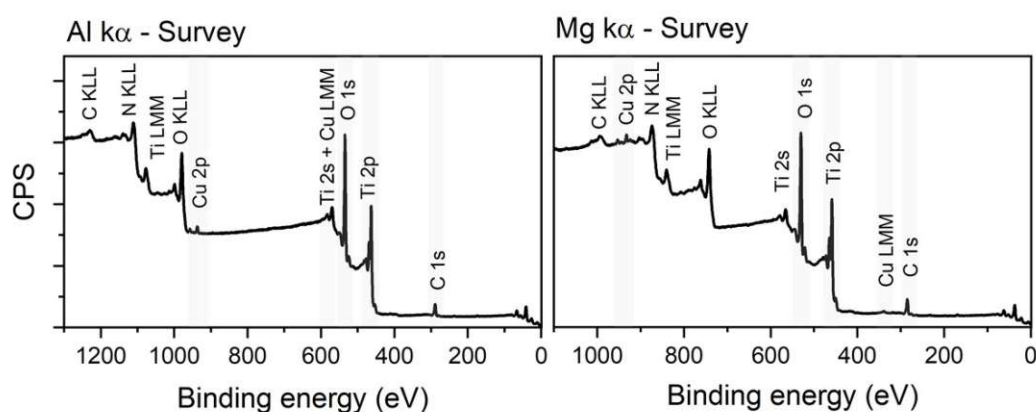
Figure S10: XPS survey spectra of the $Cu(NO_3)_2/TiO_2$ samples. Left: measured with the Al-Kα. Right: measured with the Mg-Kα. Note the shift O KLL, Ti LMM and Cu LMM auger signals.

13
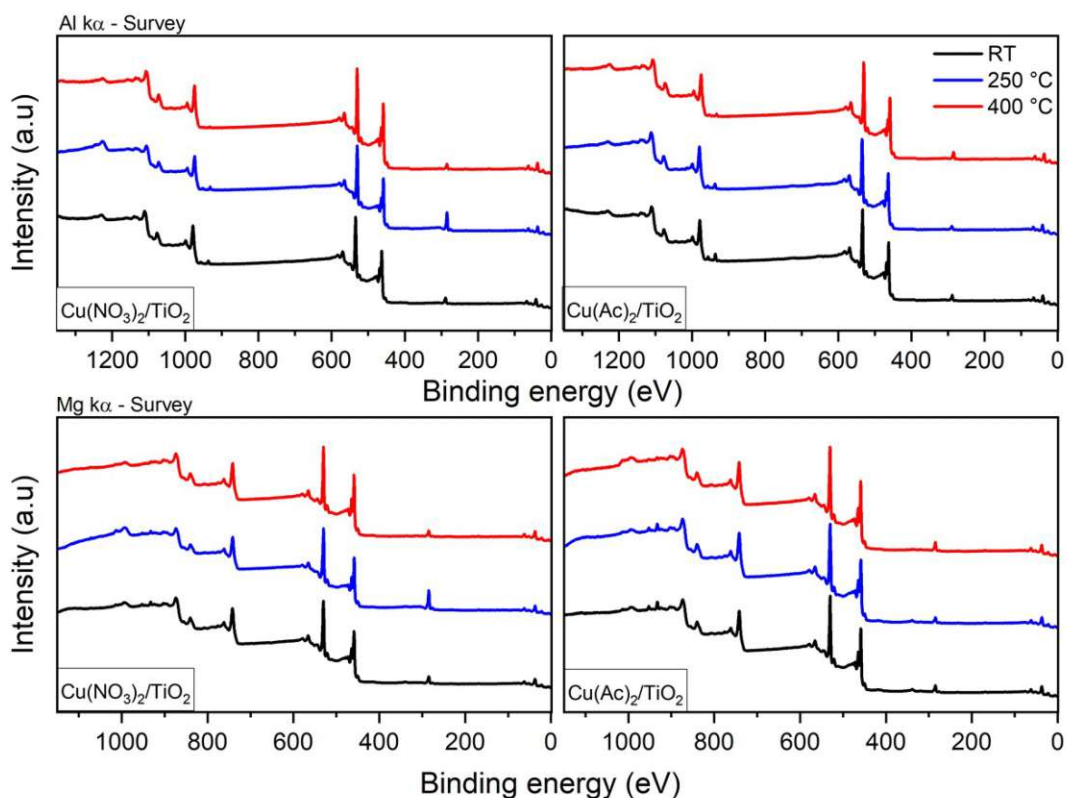
Figure S11: All surveys of the different calcined $Cu(NO_3)_2/TiO_2$ and $Cu(ac)_2/TiO_2$ samples. Top: measured with Al-Kα. Bottom: measured with Mg-Kα.

Table S4: Survey quantifications from the corresponding Al-Kα and Mg-Kα x-ray source.

	Al-k$_\alpha$				Mg-k$_\alpha$			
Cu(ac)$_2$/TiO$_2$	Ti 2p	Cu 2p	C 1s	O 1s	Ti 2p	Cu 2p	C 1s	O 1s
				at %				
RT	23.4	0.9	18.6	57.4	22.7	1.0	20.5	55.8
250 °C	24.4	0.8	14.3	60.6	23.4	1.0	17.3	58.3
400 °C	23.0	0.3	21.2	55.5	22.2	0.3	23.0	54.5

	Al-k$_\alpha$				Mg-k$_\alpha$			
Cu(NO$_3$)$_2$/TiO$_2$	Ti 2p	Cu 2p	C 1s	O 1s	Ti 2p	Cu 2p	C 1s	O 1s
				at %				
RT	22.2	0.6	20.4	56.9	21.3	0.5	23.8	54.4
250 °C	14.5	0.3	42.3	42.9	14.4	0.3	44.0	41.2
400 °C	25.1	0.2	15.4	59.3	24.0	0.2	19.4	56.5

14

81

C 1s:
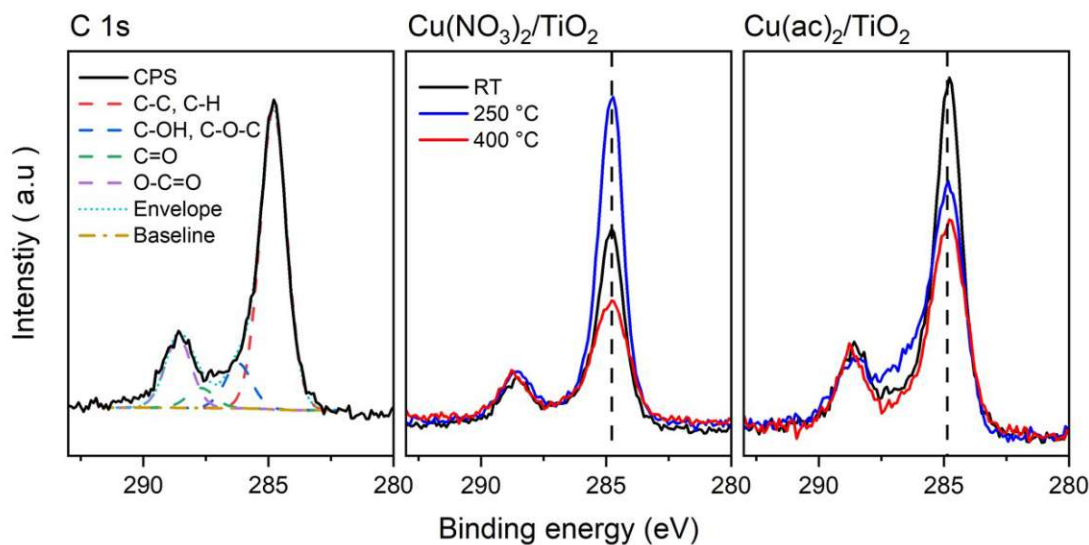
Figure S12: All C 1s of the different calcined $Cu(NO_3)_2/TiO_2$ and $Cu(ac)_2/TiO_2$ samples. From left to right: The deconvoluted data of the non-calcined $Cu(ac)_2/TiO_2$ with the characteristic adventitious carbon species. All $Cu(NO_3)_2/TiO_2$ and $Cu(ac)_2/TiO_2$ C 1s spectra.

O 1s:
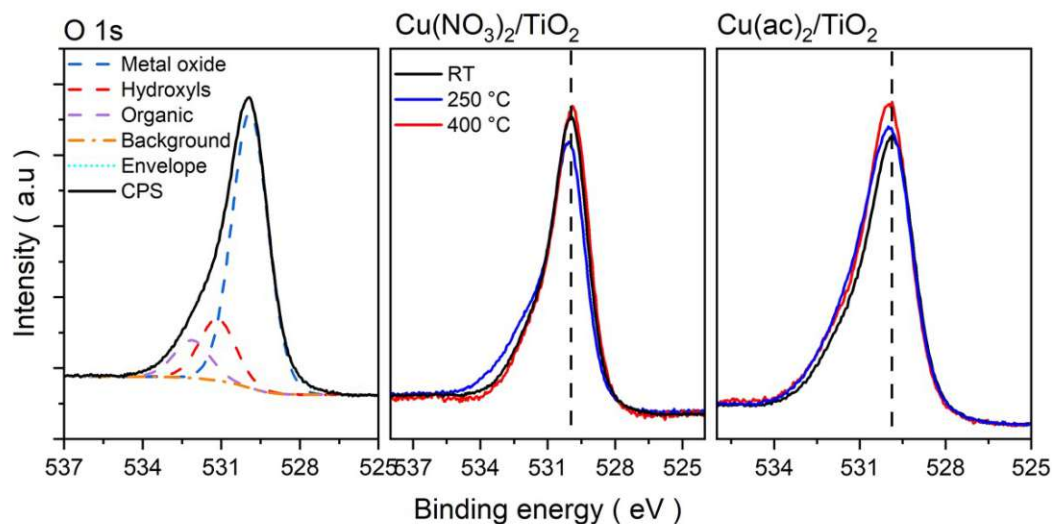
Figure S13: XPS O 1s detail spectra of all different calcined $Cu(NO_3)_2/TiO_2$ and $Cu(ac)_2/TiO_2$ samples. Left to right: the deconvoluted data of the non-calcined $Cu(ac)_2/TiO_2$ sample. All $Cu(NO_3)_2/TiO_2$ and $Cu(ac)_2/TiO_2$ spectra.

8. XPS and XRF

Table S5. XRF vs. XPS (from the surveys and recalculated to set in a ratio to Ti. Ti set to 100) Cu at. % in relation to Ti quantification. Data are shown in **Figure 4** in the manuscript.

	Cu amount in at. %					
	Cu(ac)$_2$/TiO$_2$			Cu(NO$_3$)$_2$/TiO$_2$		
	XPS		XRF	XPS		XRF
	Al-K$_\alpha$	Mg-K$_\alpha$		Al-K$_\alpha$	Mg-K$_\alpha$	
RT	3.8	4.6	1.08	2.5	2.3	0.69
150 °C	-	-	1.07	2.4	2.6	0.73
250 °C	3.2	4.2	1.05	1.9	2.2	0.67
400 °C	1.3	1.3	0.99	0.9	0.7	0.64
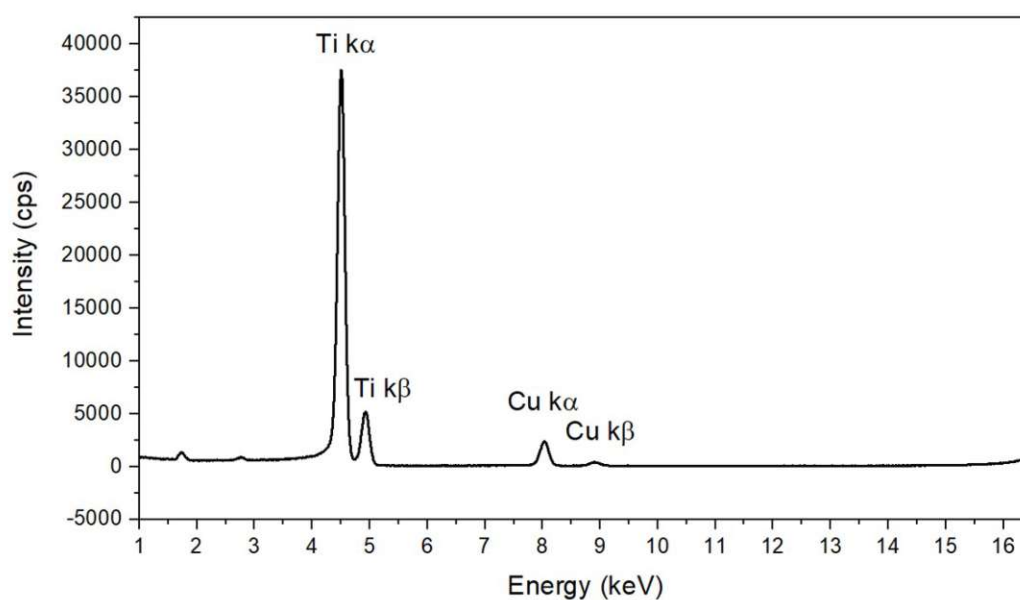
Figure S14: XRF full spectra of one of the analyzed samples, all other samples spectra look the same just with intensity shifts. Corresponding data are shown in **Table S5**. The spectra show the corresponding Ti and Cu peaks without further contribution of other species. The peak at 1.8 keV and 2.9 keV belong to the Si from the detector and Ar from the measuring atmosphere, respectively.

9. DRS, Tauc plots, UPS and VB-XPS

The thermal decomposition of the pure precursors, analyzed by In-situ XRD, see **Figure S7**, show for nitrate that Cu^{+2} stays present for the whole decomposition, while for acetate different oxidation states are generated over thermal treatment until getting fully oxidized to Cu^{+2} again. By analyzing the DRS profiles, we see these changes represented in the absorption range from 500 to 900 nm corresponding to Cu^{2+}.
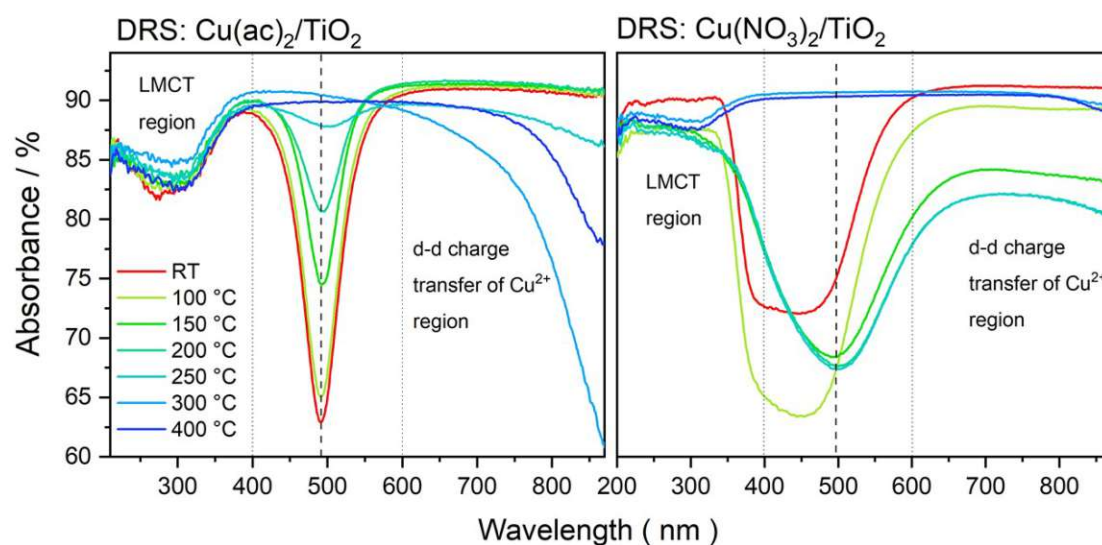
Figure S15. DRS of the pure precursors (a) $Cu(NO_3)_2$ and (b) $Cu(ac)_2$ at different thermal treatments, showing the evolution of the DRS profile by decomposition of the nitrate and acetate ligand and the formation of the different Cu oxides.

The band gap, work function and valence band maximum were determined with a linear fit interpolated to the zero Tauc function and zero Intensity, respectively. The corresponding errors are from the linear fit where 6 different points were taken, and the average was taken as the corresponding value.
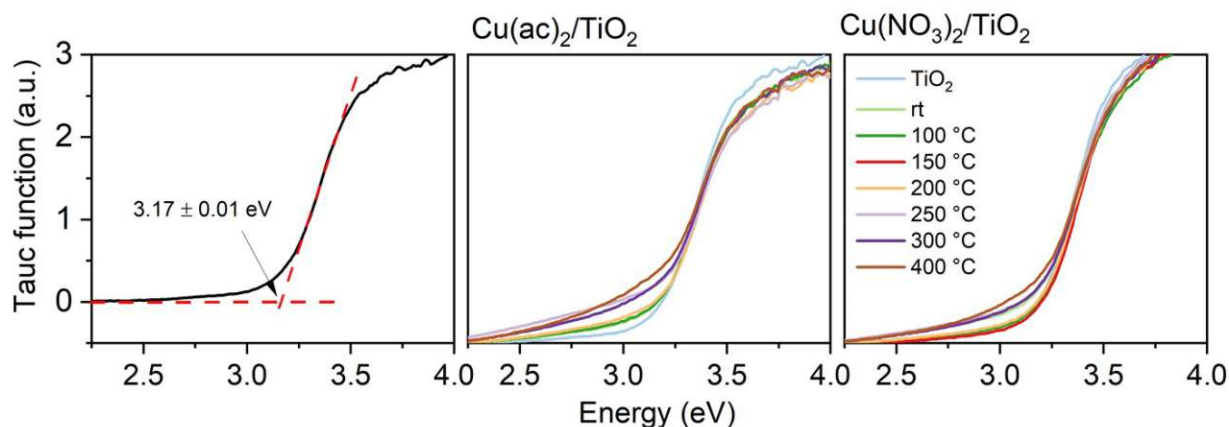
Figure S16. DRS Tauc plots. (a) representation of how the bang gaps were taken by extrapolation to the zero Tauc function. (b) Tauc plots of $Cu(NO_3)_2/TiO_2$ and (c) $Cu(ac)_2/TiO_2$ at different thermal treatments.

Table S6. DRS Tauc plot band gap values table obtained from **Figure S16**.

	$Cu(ac)_2/TiO_2$	$Cu(NO_3)_2/TiO_2$
	E_g - Band gab	E_g - Band gab
	eV	eV
TiO_2	3.17	3.17
RT	3.12	3.13
100 °C	3.11	3.13
150 °C	3.11	3.13
200 °C	3.09	3.12
250 °C	3.06	3.11
300 °C	3.05	3.10
400 °C	3.00	3.07
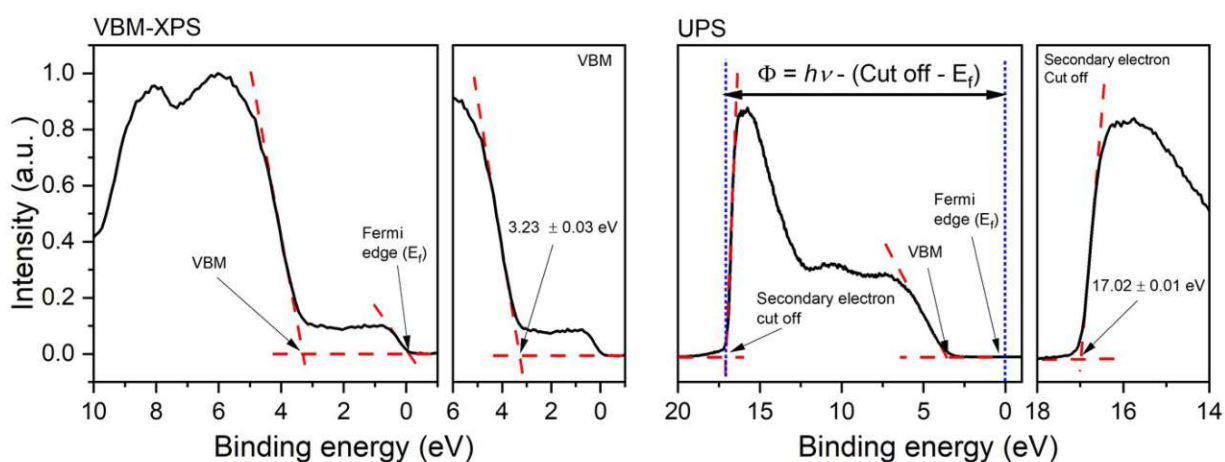
Figure S17. a) VB-XPS and b) UPS to determine the valence band maximum and work function, respectively. Representation of how the values were taken for all samples, here only shown TiO_2. $hv = 21.2$ eV (He-II source) and $E_f = 0$ eV.

Table S7. Data used in **Figure 5h** from the main manuscript. (*) Data calculated from VB-XPS, Work function and E_g by taking the vacuum energy ($E_{vac} = 0$ eV) as the reference. The former values were obtained from the corresponding VB-XPS, UPS and DRS spectra where the fermi edge is the reference ($E_f = 0$ eV). All data in eV.

	Cu(ac)$_2$/TiO$_2$						Cu(NO$_3$)$_2$/TiO$_2$					
	VB-XPS	Work function	E_g	Fermi level*	VBM*	CB*	VB-XPS	Work function	E_g	Fermi level*	VBM*	CB*
TiO$_2$	3.2	4.2	3.2	-4.2	-7.4	-4.2	3.2	4.2	3.2	-4.2	-7.5	-4.3
RT	3.0	4.2	3.1	-4.2	-7.2	-4.1	3.0	3.9	3.1	-3.8	-6.9	-3.8
250 °C	3.0	4.0	3.2	-4.0	-7.0	-4.0	3.0	4.4	3.1	-4.3	-7.3	-4.2
400 °C	3.1	4.1	3.0	-4.1	-7.2	-4.2	3.3	4.2	3.1	-4.1	-7.4	-4.3

10. DRS and XRF before and after washing of Cu(NO₃)₂/TiO₂
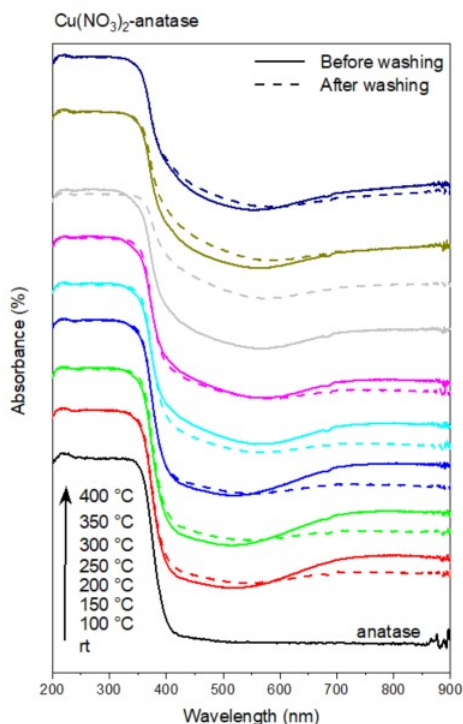
Figure S18: DRS of the $Cu(NO_3)_2/TiO_2$ before and after washing.

Table S8: XRF measurements of the Washing experiment. Cu at. % of the samples before and after washing (Ti is set to 100) and the corresponding decrease of Cu % used in **Figure 6** in the manuscript.

	Cu(ac)₂/TiO₂			Cu(NO₃)₂/TiO₂		
	Cu concentration in at. %		Decrease after washing	Cu concentration in at. %		Decrease after washing
	Before washing	After washing	%	Before washing	After washing	%
RT	1.19	0.45	62.52	0.96	0.13	86.26
100°C	1.54	0.47	69.29	1.08	0.12	88.73
150°C	1.21	0.46	61.78	0.93	0.12	87.42
200°C	1.17	0.49	58.34	0.85	0.17	80.48
250°C	1.18	0.48	59.23	0.81	0.25	68.67
300°C	1.13	0.58	49.02	0.75	0.41	46.03
350°C	1.01	0.85	15.96	0.70	0.58	17.23
400°C	1.02	0.89	12.41	0.76	0.63	17.88

87

11. Cu amount effect on the HER activity

To determine the dependency of the amount of at. Cu % versus HER we prepared a model system by using the photodeposition method. This method consists of preparing a Cu solution with the suspended TiO_2-anatase nanoparticles. Then by UV-light illumination of the system, an excited electron is generated that reacts with the Cu in solution (electron transfer from TiO_2 to Cu, inducing the reduction of Cu). In parallel, it is in-situ detected the amount of Hydrogen that is generated by this photodeposition. In this method, the HER rate is directly dependent on the Cu amount available in the solution able to deposit on TiO_2 (see **Figure 19**). The difference in this method to the wet impregnation is when the HER rate is analyzed under light illumination Cu deposits from the solution on TiO_2 (photodeposition) while in the wet impregnation Cu is already on the TiO_2 surface. Thus, if a Cu redox shuttle takes place, in the first case it goes from solution on TiO_2, in the second it goes from the TiO_2 surface in solution and back. Thus, to further investigate the dependence of HER on the surface availability of Cu, we prepared Cu/TiO_2 photocatalysts with different at. % of Cu on TiO_2 surface – ranging from 0.01 to 1 at. % – using the photo-deposition method (see **Figure S19b**). The reasoning is: in the photodeposition process – TiO_2 is suspended in the HER solution with solubilized Cu - Cu can undergo redox shuttling with the TiO_2 surface. In our systems, prepared by wet impregnation, TiO_2 is impregnated previously with Cu, hence, Cu must go from the TiO_2 surface into the solution to carry out the HER reaction. Thus, if Cu diffuses into the TiO_2 lattice, and is consequently less accessible to the solution to undergo redox shuttling a decreased activity would be expected. In **Figure S19b** we see, for the photodeposition model, that a decreasing amount of Cu available leads to reduced activity. In **Figure 1** (from the main manuscript) we saw a gradual decrease of HER rate by increasing temperature until reaching 72 % of the peak performance at 400 °C, corresponding to HER rate of 14.81 µmol h^{-1} for Cu(ac)$_2$/TiO_2 (**Table S9**). Correlating these data with the photodeposition model study (**Figure S19b**), we see that this corresponds to a Cu at. % less than 0.1 %. The XPS survey quantification further showed that 0.3 and 0.2 at.% for the 400 °C Cu(ac)$_2$/TiO_2 and Cu(NO$_3$)$_2$/TiO_2, respectively, is still present on the TiO_2 surface.
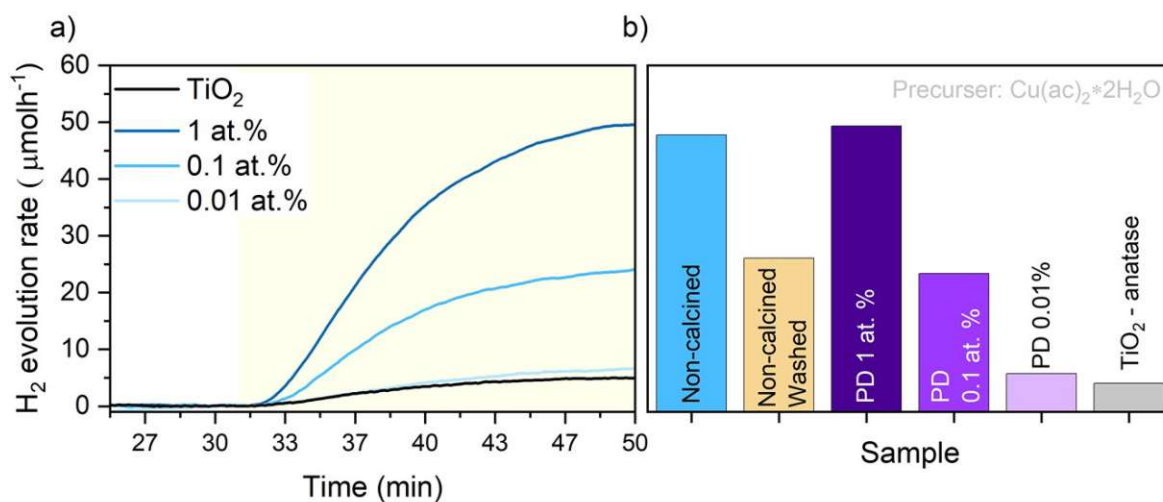
Figure S19. a) HER dependency with different Cu at. % photodeposited on TiO$_2$. Ranging from 0.01 to 1 at. % of photo-deposited Cu. b) Bar diagram showing the absolute HER values for the photodeposited (PD) samples and the non-calcined before and after washing, as well as the reference TiO$_2$.

Table S9: Photodeposition (PD) experiment: HER rate maximum after 20 minutes of illumination. Values are taken from the graphs **Figure S19**.

Cu at %	H$_2$ evolution rate μmol h^{-1}
TiO$_2$-Anatase	4.97
Non-calcined	47.97
Non-calcined Washed	26.63
PD 1%	49.54
PD 0.1%	23.97
PD 0.01%	6.65

89

12. DFT calculations

Perfect anatase TiO₂ surface

Figure S20 shows that the anatase TiO₂ (101) surface has a stepped structure. Threefold coordinated O atoms (O_{3c}) and sixfold coordinated Ti atoms (Ti_{6c}) are fully saturated and have bulk coordination whereas the twofold (O_{2c}) and fivefold (Ti_{5c}) atoms are undercoordinated. The O_{2c} atoms are located at the ridges of the saw-tooth-like structure, and after optimization, they relax inwards by ~0.16 Å with respect to bulk TiO₂. The three-fold coordinated O_{3c} atoms relax outwards by~0.07 Å, while the Ti_{5c} and Ti_{6c} atoms relax inwards by ~0.15 Å and ~0.16 Å respectively, so that the surface exhibits a slightly buckled structure.
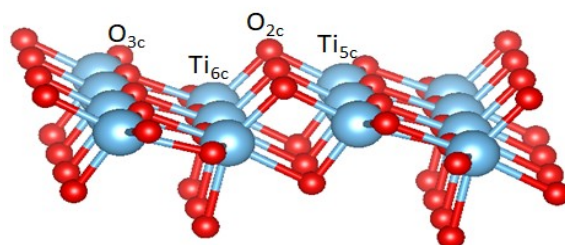
Figure S20: Side view of the top-most layer of the anatase TiO₂ (101) surface (in the 1 x 3 supercell). Red and blue spheres corresponded to O and Ti atoms respectively.

Table S10: Shortest Cu-O bonds between a Cu Atom (of the pure Cu clusters adsorbed on the anatase TiO₂ (101) surface) and O atoms (O_{2c} and O_{3c}) of TiO₂. Cu₅ (1) and Cu₅ (2) refer to chain-like and 3D-like structures, respectively. The results for different Cu atoms are separated by semicolons. "(2)" means two bonds of same length and (*) indicates a Cu in the subsurface.

Compound	Cu-O_{2c} (Å)	Cu-O_{3c} (Å)
TiO₂-Cu	1.87(2)	2.33;2.47
TiO₂-Cu*	1.96(2)*	2.03;2.17*
TiO₂-Cu₂	(1.88,1.89);(1.88,1.89)	(2.34,2.52);(2.34,2.52)
TiO₂-Cu₃	1.90(2);1.90(2);1.90(2)	(2.28,2.46);(2.29,2.46);(2.28,2.46)
TiO₂-Cu₅ (1)	1.97;2.11;(2.09,2.10);(2.04,2.15);2.83	(2.81,2.71);(2.30,2.31);2.30;2.42;-
TiO₂-Cu₅* (1)	1.99;2.02;1.87(2);1.87(2);(2.23,2.24)*	(2.42,2.80);2.31;(2.41,2.53);(2.42,2.53);1.99(2)*
TiO₂-Cu₅ (2)	1.86;-;-;2.94;1.89	-;-;2.00;2.75

23

Table S11: Adsorption energy (eVatom^{-1}) and Bader charge for Cu$_x$ (x=1, 2, 3, 5) clusters adsorbed on the anatase TiO2 (101) surface. Cu$_5$ (1) and Cu$_5$ (2) refer to chain-like and 3D-like structures, respectively. For comparison, the cohesive energy for bulk CuO is 2.75 eV. (*) indicates a Cu in the subsurface. E$_{ads}$ in the subsurface is the equivalent of the binding energy. Bader charges <0.4 correspond to Cu^0, 0.4 – 0.7 to Cu$^+$ and >0.7 to Cu^{+2}.

Compound	E$_{ads}$ (eV atom^{-1})	Bader charge (e$^-$)
TiO$_2$-Cu	2.24	0.68
TiO$_2$-Cu*	1.90*	0.69*
TiO$_2$-Cu$_2$	2.08	0.68,0.68
TiO$_2$-Cu$_3$	1.99	0.68,0.68,0.68
TiO$_2$-Cu$_5$ (1)	1.9	0.15,0.13,0.48,0.41,-0.06
TiO$_2$-Cu$_5$* (1)	1.84	0.17,0.17,0.66,0.66,0.71*
TiO$_2$-Cu$_5$ (2)	2.26	0.33,0.07,-0.12,0.17,0.34

References

[1]   J. S. Schubert, J. Popovic, G. M. Haselmann, S. P. Nandan, J. Wang, A. Giesriegl, A. S. Cherevan, D. Eder, Journal of Materials Chemistry A 2019, 7, 18568.

[2]   Z. Lin, D. Han, S. Li, J Therm Anal Calorim 2012, 107, 471.

[3]   A. M. Alotaibi, B. A. D. Williamson, S. Sathasivam, A. Kafizas, M. Alqahtani, C. Sotelo-Vazquez, J. Buckeridge, J. Wu, S. P. Nair, D. O. Scanlon, I. P. Parkin, ACS Appl. Mater. Interfaces 2020, DOI 10.1021/acsami.9b22056.

91

4.2.3 Manuscript No.3

"Nature of the active Ni state for photocatalytic hydrogen generation"

Jasmin S. Schubert, Eva Doloszeski, Pablo Ayala, Stephen Nagaraju Myakala, Jakob Rath, Bernhard Fickl, Ariane Giesriegl, Dogukan H. Apaydin, Bernhard C. Bayer, Shun Kashiwaya, Alexey Cherevan, Dominik Eder

Advanced Materials Interfaces

The corresponding Supplementary information of the manuscript can be found on page 113.

Reproduced from Ref.[100]

In this work, to determine the long therm hydrogen evolution rate, optimization of the experimental setup design was required. Details can be found in section 3.1.2.

WILEY-VCH

Nature of the active Ni state for photocatalytic hydrogen generation

*Jasmin S. Schubert, Eva Doloszeski, Pablo Ayala, Stephen Nagaraju Myakala, Jakob Rath, Bernhard Fickl, Ariane Giesriegl, Dogukan H. Apaydin, Bernhard C. Bayer, Shun Kashiwaya, Alexey Cherevan, * Dominik Eder ***

J.S. Schubert, E. Doloszeski, P. Ayala, S. N. Myakala, J. Rath, B. Fickl, A. Giesriegl, D. H. Apaydin, B. C. Bayer, A. Cherevan, D. Eder
Institute of Materials Chemistry, Technische Universität Wien (TU Wien), Getreidemarkt 9, 1060, Vienna, Austria
E-mail: alexey.cherevan@tuwien.ac.at, dominik.eder@tuwien.ac.at

S. Kashiwaya
Materials Design, Department of Physics, Chemistry, and Biology (IFM), Linköping University, 58183, Linköping, Sweden

Thermal treatments can have detrimental effects on the photocatalytic hydrogen (H_2) evolution performance and impact the formation mechanism of the active state of surface-supported co-catalysts. In this work, we investigated a range of Ni-based co-catalysts immobilized on TiO_2, evaluated their H_2 evolution rates in-situ over 21 h and analyzed the samples at various stages with a comprehensive set of techniques, including XPS, ATR-FTIR, UV-Vis, HRTEM and XRF. We found that achieving the optimal hydrogen evolution (HER) performance requires the right Ni^0:Ni^{2+} ratio, rather than only Ni^0, and that Ni needs to be weakly adsorbed on the TiO_2 surface in order to create a dynamic state. Under these conditions, Ni is able to undergo an efficient redox shuttle, involving the transformation of Ni^{2+} to Ni^0 and back after releasing the accumulated electrons for H^+ reduction (i.e. $Ni^{2+} \leftrightarrow Ni^0$). Yet, when the calcination temperature of the Ni/TiO_2 photocatalysts increases, resulting in stronger coordination/adsorption of Ni on TiO_2, this process is gradually inhibited, which ultimately leads to decreased HER performances. This work emphasizes the significance and influence of thermal treatments on the Ni active state formation – a process that can be relevant to other HER co-catalysts.

1. Introduction

Photocatalysis utilizes the energy of light under ambient and environmentally-friendly conditions to enable and accelerate thermodynamically challenging processes, such as overall water splitting for light-driven hydrogen (H_2) production.[1,2]

The photocatalyst architecture plays a key role in the ultimate performance and, currently, the most efficient and longevous photosystems are still based on heterogeneous materials.[1–5] This approach combines solid-state semiconductors – able to absorb light, generate electron-hole pairs and transfer their energy to the catalytic sites – and other materials, such as co-catalysts, that offer active sites to promote specific reactions. The combination, can greatly improve the separation of photoexcited charge carriers and their transfer into adsorbed reactant species, enhancing the overall photocatalytic activity.[1,2,5,6] Consequently, co-catalyst engineering to optimize photocatalytic efficiencies of the reaction of interest has become a popular research focus.

The light-to-hydrogen conversion efficiency is governed by the degree of electronic communication between semiconductor and co-catalyst, structural characteristics of their interfaces as well as the accessibility of the catalytically active sites. [1–3,5,7–9] Much effort has been dedicated to designing the ideal co-catalyst/semiconductor interface through various bottom-up methods such as photodeposition, chemical deposition and growth and selective surface reaction.[10–14] In many cases, co-catalysts are further activated through post-synthetic modifications, e.g. by irradiation or thermal treatment in oxidative/reductive environments. However, these conditions can also facilitate the growth and agglomeration of co-catalyst-nanoparticles or instigate changes in their chemical interaction with the substrate.[10,12,15] Consequently, it is crucial to understand how these treatments affect the electronic, chemical, and structural characteristics of the co-catalyst species, the accessibility of the catalytic sites, the potential formation of charge recombination centers along with localized inter-bandgap states at the interfaces, and – ultimately – the resulting photocatalytic performance.[3,5,7–9]

In this context, the utilization of Ni as a co-catalyst has been widely documented across various systems, encompassing diverse chemical compositions (Ni^0, $Ni(OH)_2$, NiO, NiS_2, Ni_2P, etc), substrates (TiO_2, CdS, g-CN, MoS_2, etc) and synthesis methods, all with the overarching aim of enhancing photocatalytic performance. [16–18] Numerous studies have made concerted efforts to unravel the catalytic active state of Ni. For instance, Chen et al.[19] observed that the prior reduction of NiO to Ni^0 – when deposited on a TiO_2 substrate – results in a remarkable augmentation in the quantity of H_2 produced. Furthermore, under photocatalytic conditions they observed a long induction time for the NiO/TiO_2 sample, revealing that NiO gets gradually

2

reduced to Ni^0. Accordingly, their conclusion was that the catalytically active form of Ni is Ni^0. Indra et al. [20] obtained analogous results using in-situ EPR by photodepositing Ni on graphitic carbon nitride (g-CN). The authors demonstrated that photo-excited electrons in the g-CN's conduction band are responsible for reducing Ni^{2+} to Ni^0 and subsequently catalyzing the conversion of H^+ to H_2. Hence, again metallic Ni was suggested as a H_2 generating center. Additionally, the authors observed the formation of metallic Ni only under photocatalytic conditions, hereby coexisting Ni^{2+} and metallic Ni in the whole process. Yu et al.[21] conducted an investigation involving $Ni(OH)_2$ on TiO_2 and reached the same conclusion. In a separate study, Lv et al. [22] utilized a multitude of methods to clarify that Ni is affixed to the TiO_2 lattice in the form of Ni^{2+}-O. Once again, they asserted that the excited electrons in the conduction band are the key players in H_2 production, though they did not specify whether Ni^{2+} is reduced or if Ni actively partakes in the reaction. In our previous study,[23] we also showed how the amount of H_2 produced increased gradually over time when using NiO_x/TiO_2 photocatalyst, which correlated well with a gradual increase of the amount of Ni^0/Ni^{2+} proportion.

In summary, there is a prevailing consensus that photoexcited electrons migrate from the conduction band to the attached Ni species, leading to the formation of metallic Ni.[16–25] This species, in turn, is able to react with protons to generate H_2, thus establishing Ni^0 as the active form for photocatalytic H_2 generation. However, as many reported photocatalytic systems contained a mixture of Ni^0 and Ni^{2+} states, the precise extent to which metallic Ni and/or Ni^{2+} contribute to the activity trends, as well as the distinct roles played by each of Ni oxidation states, remain unaddressed questions. Consequently, further research is imperative to comprehensively unravel the roles played by different Ni oxidation states as well as the effect of photocatalyst synthesis and post-treatments in achieving maximum performances.

In this work, we examine a series of Ni-based co-catalysts supported on TiO_2 – chosen as a model support – and provide a comprehensive insight into the effects of thermal pre-treatments on their structure-property-photocatalytic performance relationships. Using a wide range of techniques, we observe surprising detrimental effects of heat treatments on their photocatalytic performance towards HER. We also unravel the underlying structural, electronic and mechanistic contributions that govern the activity of the photocatalytic reaction and identify the redox activity of Ni/Ni^{2+} and the strength of their coordination to the TiO_2 surface as key criteria.

WILEY-VCH

2. Results and discussion
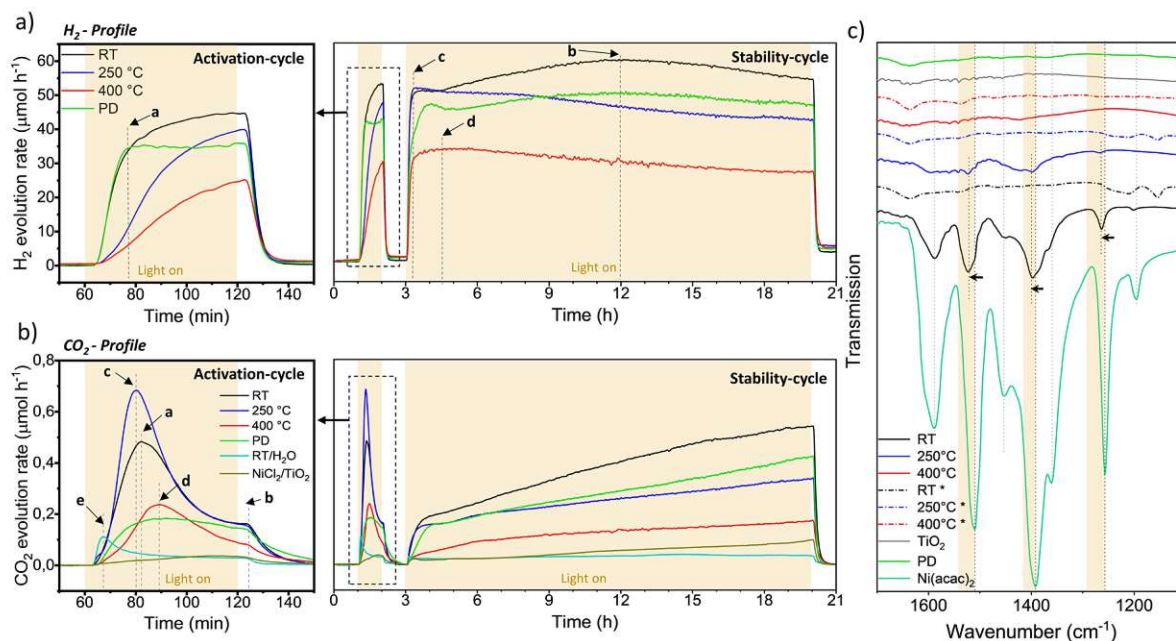
Figure 1. a) Hydrogen evolution reaction (HER) rate profile and b) CO_2 evolution rate profile of different Ni/TiO_2 calcined samples (non-calcined (RT), and calcined at 250 and 400 °C), photodeposited Ni/TiO_2 sample (PD), RT sample tested only in water (i.e. without sacrificial agent, MeOH, RT/H_2O) and $NiCl_2/TiO_2$ sample. Zoom-in of the first 3 h HER (the activation-cycle) and full 21 h HER profile (showing the activation- and stability-cycle) are shown on the left and right, respectively. The illumination (light-on) periods are indicated by the yellow shading. Some points of interest, which are referred to in the main text, are indicated with letters a-d. The total amount of H_2 generated (i.e. the integrated area) and the activation slope values are summarized in **Table S2.** The corresponding HER profiles of the RT/H_2O and $NiCl_2/TiO_2$ are show in **Figure S9.** The short delay between the start of illumination and the rise of hydrogen signal is due to the experimental setup (see experimental section). (c) FTIR-ATR before and after HER for the Ni/TiO_2 samples, PD, $Ni(acac)_2$ and TiO_2. * Spectra acquired for the samples after photocatalysis. Full range FTIR-ATR spectra are shown in **Figure S10**.

Ni was deposited on TiO_2 from $Ni(acac)_2$ via wet impregnation followed by different post-synthesis treatments including room temperature (RT) drying – i.e. no thermal treatment – as well as calcination at 250 °C and 400 °C (Ni/TiO_2 samples). Additionally, a benchmark Ni/TiO_2 composite was also prepared via in situ photodeposition (PD) of Ni from $Ni(acac)_2$.[10,11,26–28] The photocatalytic performance of the catalysts was evaluated using H_2 detection *in-flow* with high temporal resolution (see methods and **Figure S1** for experimental and setup details). Furthermore, three different Ni/TiO_2 sample sets were prepared to explore the impact of

4

synthetic solvents (i.e. H_2O or EtOH) and the influence of atmospheric O_2 on Ni deposition (i.e. ambient and vacuum conditions). In addition, Ni-free benchmark TiO_2 samples: non-calcined (RT) and the one calcined at 400°C – were investigated to account for the effect of calcination on its crystallinity and defect level (see **Figure S2**). Since all sample sets showed similar performance trends independent of these synthetic aspects, and because the highest photocatalytic activity was obtained for the Ni/TiO_2 samples derived from the EtOH-based synthesis *in vacuo* (further details on the synthesis and discussion about the sample sets are in **SI section 3**), for simplicity, we focus here on the representative set of Ni/TiO_2 samples prepared via wet impregnation using EtOH/vacuum conditions.

For each experiment, two illumination periods were carried out (highlighted in **Figure 1**a yellow): a short-term period (the first hour of illumination) which corresponds to the activation cycle of the photocatalyst, and a long-term period (a follow-up 17 h illumination) which allows us to uncover steady-state activity trends and discuss (de)activation behavior. Additionally, we analyzed the CO_2 evolution rates *in situ* (**Figure 1**b) aiming to obtain additional insight into the oxidative behavior of Ni/TiO_2 photocatalysts.

H_2 profiles - Activation cycle (**Figure 1**a): The RT and PD samples show the sharpest evolution rate increase after illumination start. Yet, after 18 minutes of illumination (a in **Figure 1**a), the PD sample reaches the H_2 evolution rate maximum, while RT continues to increase. The 250 °C and 400 °C calcined samples, show a gradual activation rate decrease by 66.7 % and 83.3 %, respectively, when compared to the HER profile of the RT sample. After 1 h of illumination, the total amount of H_2 generated is 39.1 µmol and 32.9 µmol for RT and PD samples, and 26.7 µmol and 15.4 µmol for the samples derived at 250 °C and 400 °C, respectively. Hereby, the data clearly show that increasing the calcination temperature leads to a slower HER rate increase and an overall diminished H_2 generation after 1 h of illumination.

H_2 profiles - Stability cycle: The HER rate slightly increases for the RT sample and reaches a maximum after a total illumination of ~10 h (b in **Figure 1**a). For the samples calcined at 250 °C and 400 °C, the HER rate maximum is reached earlier, already after a total illumination time of 1.5 h (c in **Figure 1a**) and 2.5 h (d in **Figure 1a**), respectively. The HER profile of the PD sample generated *in-situ* under photocatalytic conditions is reminiscent of the RT sample. These results suggest that the RT and PD samples constitute similar composition and structure of the active state. The different activation behaviors are likely of kinetic origin, as in the case of the

5

PD sample Ni/TiO_2 formation requires a rather slow deposition of Ni species from the solution. In contrast, the RT sample already has $Ni(acac)_2$ present on the TiO_2 surface after the synthesis, which facilitates a faster generation of HER-active Ni centers by the photoexcited electrons.[19,21] The ability of Ni species to extract electrons from TiO_2 was further demonstrated by chronoamperometry measurements (**Figure S8**). Overall, the data show that thermal treatments result in a gradual HER rate decline that increases with calcination temperature and leads to different activation/deactivation behavior.

CO_2 profiles - Activation cycle (**Figure 1**b)*:* For the RT sample, the CO_2 evolution reaches a maximum at ~22 minutes of illumination (a in **Figure 1**b), after which it drops abruptly by 71.7 % (b in **Figure 1**b). The samples calcined at 250 °C and 400 °C show similar CO_2 evolution profiles. However, the 250 °C sample generates much more CO_2 (peaking after 20 min of illumination, c in **Figure 1**b), while the 400 °C sample's CO_2 peak maximum appears considerably later and is less intense (peaking after ~30 min of illumination, d in **Figure 1**b). The major contribution to CO_2 generation clearly is due to the oxidation of MeOH, which is used here as a sacrificial agent. [29–31] However, the presence of metalorganic precursors on the catalyst's surface, i.e. $Ni(acac)_2$, is expected to contribute to CO_2 generation as well upon oxidation during the initial stage of the photocatalytic process. Accordingly, we analyzed the samples by FTIR-ATR before and after photocatalysis (**Figure 1**c). *Before photocatalysis*, the RT sample features vibrational bands that correspond well to the fingerprint of $Ni(acac)_2$, however with noticeable shifts of some signals (1512.1 to 1523.7 cm^{-1}, 1390.6 to 1400.2 cm^{-1} and 1257.5 to 1265.2 cm^{-1}), indicating strong interaction of the acac ion with the TiO_2 surface.[23,32] After calcination at 250 °C and 400 °C, the acac intensities gradually decreases by increasing temperature. *After photocatalysis*, the acac bands completely vanish in all samples. Two possibilities can explain these observations: dissolution of the acac ion into the reaction solution and/or complete decomposition of the acac anion by the photocatalytic process. Washing experiments of the RT sample complemented by FTIR-ATR analyses before and after (see **Figure S10**) show that acac is weakly attached on the TiO_2 surface, suggesting that acac gets dissolved into the reaction solution. To further confirm the origin of the CO_2 peaks and the role of the acac anion, we performed two additional benchmark experiments. In the first, we synthesized a sample following an identical synthetic procedure but using an all-inorganic $NiCl_2$ as a precursor ($NiCl_2/TiO_2$) – i.e. the only organic source in the reaction was MeOH. The respective evolution curve clearly shows no peak formation, just a steady slow increase in CO_2 (**Figure 1**b). In the second experiment, we used $Ni(acac)_2$ as the precursor, but performed the

reaction only in water without MeOH (RT/H₂O). Here, the corresponding CO_2 profile shows a sharp evolution peak that drops quickly to almost no CO_2 formation. These data confirm that the observed peak in the first hour of illumination directly relates to the oxidation of the metalorganic precursor or its decomposition intermediates (as seen in ATR-FTIR for the 250 °C and 400 °C sample).

*CO_2 profiles - Stability cycle (**Figure 1b**):* all Ni/TiO₂ samples show a steady increase in the CO_2 evolution rate over time. The activity trend correlates well with the HER rate trend according to RT > 250 °C > 400 °C. The PD sample, again, shows a reaction profile similar to that of the RT sample, but with a lower maximum rate – expected from its lower HER activity – thus further indicating a similar reaction mechanism. The gradual increase of the CO_2 evolution rate over time observed for all samples is related to the conversion of MeOH. The more MeOH and its decomposition intermediates accumulate over time, the stronger the equilibrium shifts to CO_2.

2.1. Ni on TiO₂ attachment strength
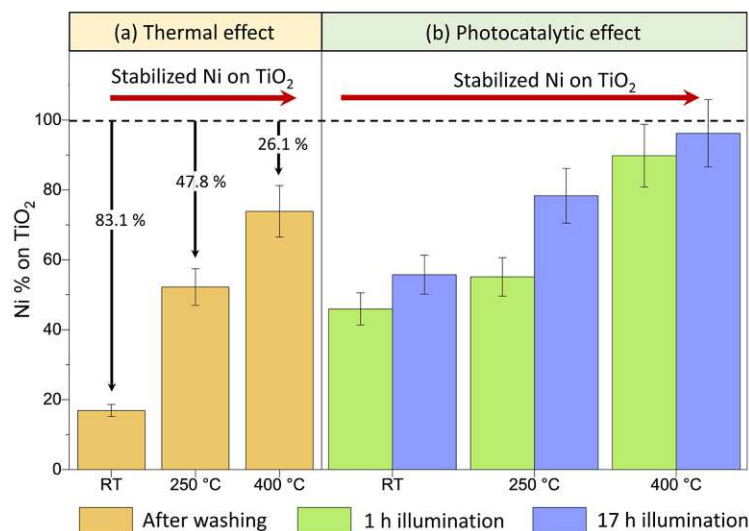
Figure 2. Total Ni % in the Ni/TiO₂ samples - i.e. stabilized Ni on TiO₂ - (a) after washing of the as-prepared samples (see methods for more details) as well as (b) those after photocatalysis (the activation- (1h illumination) and stability-cycle (after 17 h illumination)). The relative Ni content values were calculated from the as-synthesized samples set as 100 % (see **Table S3**).

To gain information about the thermal and photocatalytic effects on the Ni adsorption/coordination strength with the TiO₂ surface, we quantified the Ni amount present in

the as-synthesized samples, after washing them (details in Methods), as well as after the activation- and stability-cycles (i.e. after 1 h and 17 h illumination, HER experiment) (**Figure 2**). For the as-synthesized Ni/TiO$_2$, XRF confirms that the content of Ni is close to the expected 5 at. % for all samples independent on the thermal treatment (for more details see SI, **Table S3**). After washing, 83.1 % of the original Ni amount present in the RT sample got washed off, whereas much less of Ni – 47.8 and 26.1 % – was detached from the samples calcined at 250 and 400 °C, respectively (see black arrows in **Figure 2**a). These values clearly show that calcination at higher temperatures results in stronger adhesion/adsorption of Ni species to TiO$_2$ involving stronger coordination of Ni species to the TiO$_2$ lattice and partial formation of oxy/hydroxide-like species at the TiO$_2$ surface (for more details, see -OH bands in ATR-FTIR shown in SI, **Figure S10**). For the samples after HER, after the activation cycle (1 h illumination in **Figure 2**b), the residual amounts of stabilized Ni on TiO$_2$ – with respect to the initial Ni contents – amount to 45.9, 55.1 and 89.8 % for RT, 250 and 400 °C, respectively. In contrast, the respective Ni content after the stability cycle (17 h illumination in **Figure 2**b) remain significantly higher with 55.7, 78.3 and 96.2 % for RT, 250 and 400 °C, respectively. This shows that the adhesion of Ni on the TiO$_2$ surface becomes stronger with prolonging photocatalytic reaction. Hence, not only the calcination temperature increases the Ni adsorption strength on TiO$_2$, but also the photocatalytic process. Accordingly, the results show a clear adverse correlation between Ni adhesion and photocatalytic performance: the weaker the coordination of Ni, the more H$_2$ is generated.

2.2. Morphological analysis

The morphology of the Ni/TiO$_2$ samples before and after HER was investigated by HRTEM and EDX (figures shown in SI, **Section 4.6**). The HRTEM data show no apparent difference between the samples neither before-after HER nor to bare TiO$_2$. EDX analysis shows a homogenous Ni distribution for the as-prepared Ni/TiO$_2$ samples (before HER) and for RT and 400 °C samples after HER. Yet, we see agglomeration of Ni in the PD sample – phenomenon well known in literature for the photodeposition process [10,11,33] – as well as for the 250 °C composite. These data confirms a homogenous atomic-size distribution of Ni on TiO$_2$, while for the PD and 250 °C-after-HER sample, Ni generates a more dense packed area without forming clusters that are visible in HRTEM. Furthermore, the inconsistency of seeing more agglomeration at 250 °C than at 400 °C is possibly related to the intermediate adsorption strength (between RT and 400 °C, as documented by XRF). This suggests that the adsorption of Ni at 250 °C is weak enough so that Ni is able to diffuse along the TiO$_2$ surface, but strong

enough so that it does not dissolve into the solution and randomly redeposits (such as in the case of the RT sample). Hereby, 250 °C leads to the agglomeration of Ni species.

2.3. Ni chemical state analysis
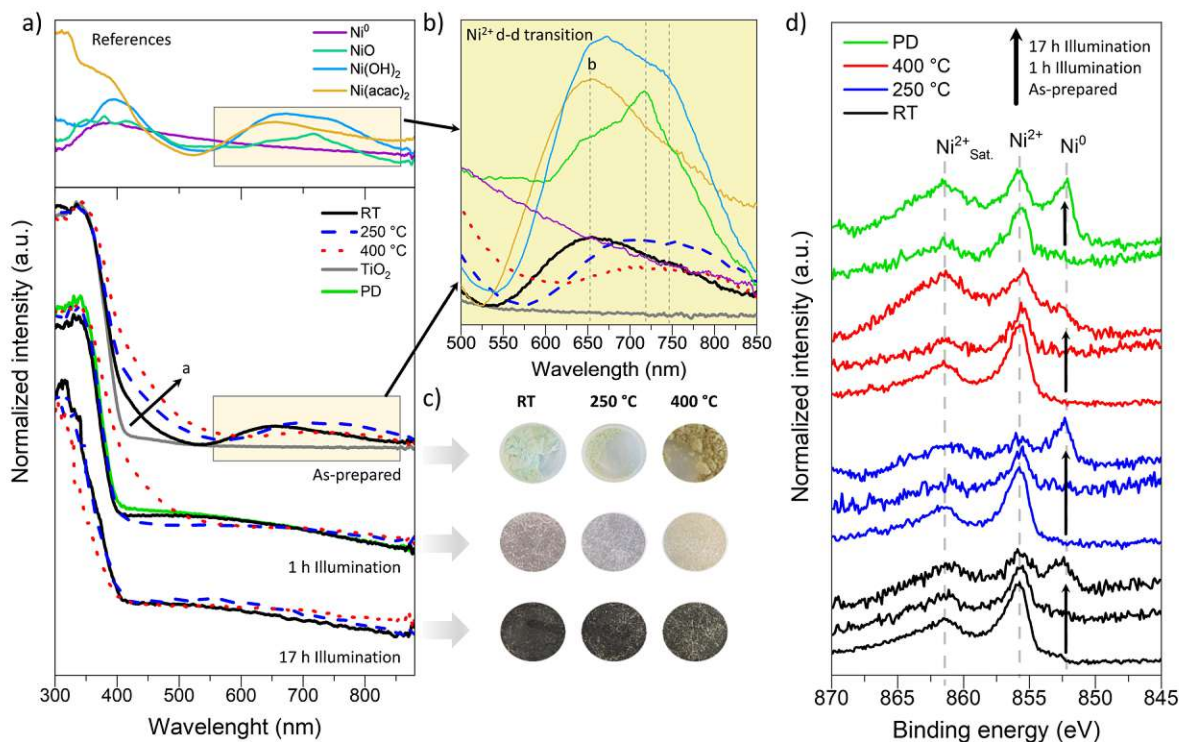
Figure 3. a) UV-Vis of the as-prepared (i.e. before HER) Ni/TiO₂ samples prepared at different temperatures (non-calcined (RT), and calcined at 250 and 400 °C), after the activation-cycle (1 h illumination), after the stability-cycle (17 h illumination) – below – and reference spectra of relevant Ni compounds (above). b) Zoom-in of the 500 to 850 nm region. c) Digital photographs of all the relevant Ni/TiO₂ samples before HER and after the activation- and stability-cycles. d) XPS Ni2p$_{3/2}$ detail spectra of the Ni/TiO₂ samples (RT, 250 °C and 400°C) before (as-prepared) and after HER (activation-, i.e. 1 h illumination, and stability-cycle, i.e. 17 h illumination), and of the PD sample after 1 h and 17 h of illumination.

We used UV-Vis spectroscopy in diffuse reflection mode (DRS) to obtain insights about the chemical state, i.e. chemical surrounding and oxidation state, of Ni before and after HER (**Figure 3**a). A set of references including Ni(acac)₂, NiO, Ni(OH)₂ and metallic Ni were used to complement the data. The pronounced absorption band below 400 nm – visible in all spectra mainly due to the presence of TiO₂ matrix – corresponds to the ligand-to-metal charge transfer (LMCT) of oxygen (O^{2-}) to Ti^{4+} i.e. band-to-band excitation. [34,35]

The samples *before HER* show that the absorption edge shifts (in the as-prepared samples, a in **Figure 3**a) to higher wavelengths with increasing calcination temperature, eventually extending the absorption range well above 500 nm. Such a shift has been related to the presence of dopants within the TiO_2 crystal lattice, which add new energy levels within the band gap.[15,36–39] Alternatively, this apparent shift has also been attributed to interfacial charge-transfer (IFCT) between the photoabsorber's (i.e. TiO_2) valence band (VB) and the surface-grafted metal species.[40–43] In both cases, the increase of the metal concentration (as an impurity in the lattice or grafted) is associated with an increase in absorption in this region. Since NiO, $Ni(acac)_2$ and $Ni(OH)_2$ references also show absorption in this region, we suggest that this absorption shift is likely due to a combination of (a) Ni(II) diffusion into TiO_2, which is facilitated by high-temperature calcination, (b) IFCT between the VB of TiO_2 and surface-grafted Ni(II) and (c) electronic transition of the Ni(II)-complexes formed on TiO_2 surface (e.g. Ni-OH or Ni-O species). **Figure 3**a and b show that in the range from 550 to 850 nm all samples exhibit a characteristic Ni(II) (d^8) d-d transition band.[43,44] The exact spectral shape and the position of the absorption maximum are highly affected by the chemical environment of Ni(II) – i.e. coordination number, geometry and nature of the neighboring atoms – as different ligands influence the ligand field and hence, the splitting and occupation of d-orbitals differently. The RT sample shows an absorption band similar to that of $Ni(acac)_2$ (b in **Figure 3**b), with a minor contribution of $Ni(OH)_2$ that likely arises from partial acac displacement upon adsorption onto TiO_2. For the 250 °C sample, the band resembles more the $Ni(OH)_2$ reference, suggesting that a much larger portion of Ni species is now hydroxylated to the TiO_2 surface -OH groups, Ni-(OH)-Ti. This is in line with partial oxidation of acac as observed in ATR-FTIR spectra of the composites, and aligns well with the stronger adhesion of Ni species to the TiO_2 surface, as suggested by the XRF leaching studies (**Figure 1**c and **2**a). For the 400 °C sample, the absorption band flattens, which suggests further hydroxylation or even formation of Ni-O-Ti bonds, due to possible diffusion of Ni ions into the TiO_2 lattice (suggested by the previous mentioned absorption shoulder, our previous work and literature.[15,36–39]

The DRS data *after 1 h illumination (activation-cycle)* reveals that the absorption shoulder in the 350 to 550 nm range vanishes for all samples except for the 400 °C sample. This indicates that at 400 °C the as-prepared Ni structure is partially preserved, which supports the diffusion of part of Ni into the TiO_2 lattice. Furthermore, the characteristic Ni(II) d-d transition in the 550 to 850 range disappears for all samples. This indicates the formation of Ni^0, which can also be suggested by the gradual color change of the catalyst powders after 1 h illumination and the matching DRS profile of the metallic Ni reference (**Figure 3**b and c).[19,25] *After 17 h*

Illumination (stability-cycle), all DRS spectra and the color of the samples look similar (**Figure 3**a and c), which indicates that all samples have transformed to a similar chemical state and composition.

The samples were further investigated by XPS before and after HER (both activation- and stability-cycle). Briefly, all survey spectra show the expected C1s, O1s, Ti2p and Ni2p components. The detail spectra of the C1s and O1s belong to the acac anion and the characteristic adventitious carbon. The Ti2p spectra show no differences before and after HER, with a typical Ti^{4+} spectral shape at a binding energy of 458.5 eV ($Ti2p_{2/3}$), which further excludes a potential contribution of TiO_2 transformation to the observed HER profiles, also confirmed by XRD (all corresponding XPS graphs are shown in the SI, **section 4.7** and XRD in **Figure S13**). Yet, as preluded by DRS data, the photocatalysts show substantial differences in their $Ni2p_{3/2}$ lines. **Figure 3**d indicates that *before HER* (in the as-prepared samples) no apparent changes are induced by the different thermal treatments. The main $Ni2p_{3/2}$ peak has a binding energy (B.E) of 855.8 eV and a small shoulder around 852.8 eV, typical values for Ni^{2+} and Ni^0, respectively.[23,45–47] Based on the DRS data, the spectral fitting parameters proposed by Biesinger et. al.[47] and according to the measured BEs, the most probable chemical surrounding for Ni in our Ni/TiO_2 samples can be attributed to a combination of Ni-OH and metallic Ni, with a contribution of the latter one of 17, 26 and 13 at. % for the RT, 250 °C and 400 °C samples, respectively (See SI, **section 4.7.5** for more details). Therefore, we can conclude that the main Ni species for the as-prepared samples is Ni^{2+} – in the form of Ni-OH or Ni-acac for the RT sample and with a higher contribution of Ni-OH with increasing calcination temperature – and Ni^0.

For the samples *after 1h illumination (activation-cycle)*, the $Ni2p_{3/2}$ spectra show no major differences between the samples, with the Ni oxidation state still being Ni^{2+} as the main species and with small amounts of Ni^0, yet with an increased proportion of metallic Ni in all samples (see SI, **section 4.7.5**). However, *after 17 h illumination (stability-cycle)*, we observe major differences among the samples with a clear Ni^0 signal intensity increase. In more detail, the RT and PD samples show a similar Ni^{2+}:Ni^0 intensity ratio – i.e. relative amount of Ni^{2+} and Ni^0 – indicating that Ni^0 becomes the dominant species. Furthermore, the similarity among the samples, also seen in DRS (**Figure 3**a, 1 h illumination) indicates a similar Ni^{2+}/Ni^0 formation mechanism. For the 250 °C sample, the Ni^0 signal is much more intense than the Ni^{2+} signal, indicating that in this sample even more Ni^0 was generated than in the RT sample. Then at

400 °C, the opposite is observable: the Ni^0 peak intensity is less than Ni^{2+}. In connection with these observations and the information provided by XRF and EDX, the most probable explanation, again, is the adsorption strength of Ni to TiO_2. Consequently, in the RT sample, Ni is weakly adsorbed, thus Ni can undergo an efficient redox shuttle (transformation of Ni^{2+} to Ni^0 and back by reacting with H^+ to H_2, $Ni^{2+} \leftrightarrow Ni^0$), as the Ni oxidation state is not stabilized by the adsorption to TiO_2, but still strong enough for electron transfer. At 250 °C, Ni starts to get strongly adsorbed (most likely via partial chemical coordination or physisorption), thus enabling efficient electron transfer (more Ni^{2+} gets reduced) and stabilizing Ni^0 on the TiO_2 lattice (still not strong enough to inhibit Ni^0 migration and agglomeration, seen in EDX). At 400 °C, Ni is even more strongly adsorbed (increasing the chemisorption character), being less prone to structural changes. Hence, Ni^{2+} is partially stabilized by the TiO_2 lattice hindering its reduction to Ni^0, its migration and agglomeration.

In summary, the DRS and XPS data show that the main Ni species before HER is Ni^{2+} – in the form of Ni-acac and Ni-OH – with a minor contribution of Ni^0. After the activation-cycle (1 h of HER) the system only slightly increases its metallic Ni content, while after the stability-cycle (17 h of HER) most of the Ni^{2+} (mainly in the form of Ni-O-Ti and Ni-(OH)-Ti) gets converted into metallic Ni. This transformation seems independent of the calcination temperature, but occurs with a different efficiency (250 °C > RT > 400°C). Hence, these results clearly indicate the in-situ formation of metallic Ni from Ni^{2+} upon photocatalytic turnover conditions, but with a different efficiency upon calcination.
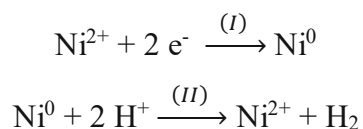
2.4. Proposed mechanism
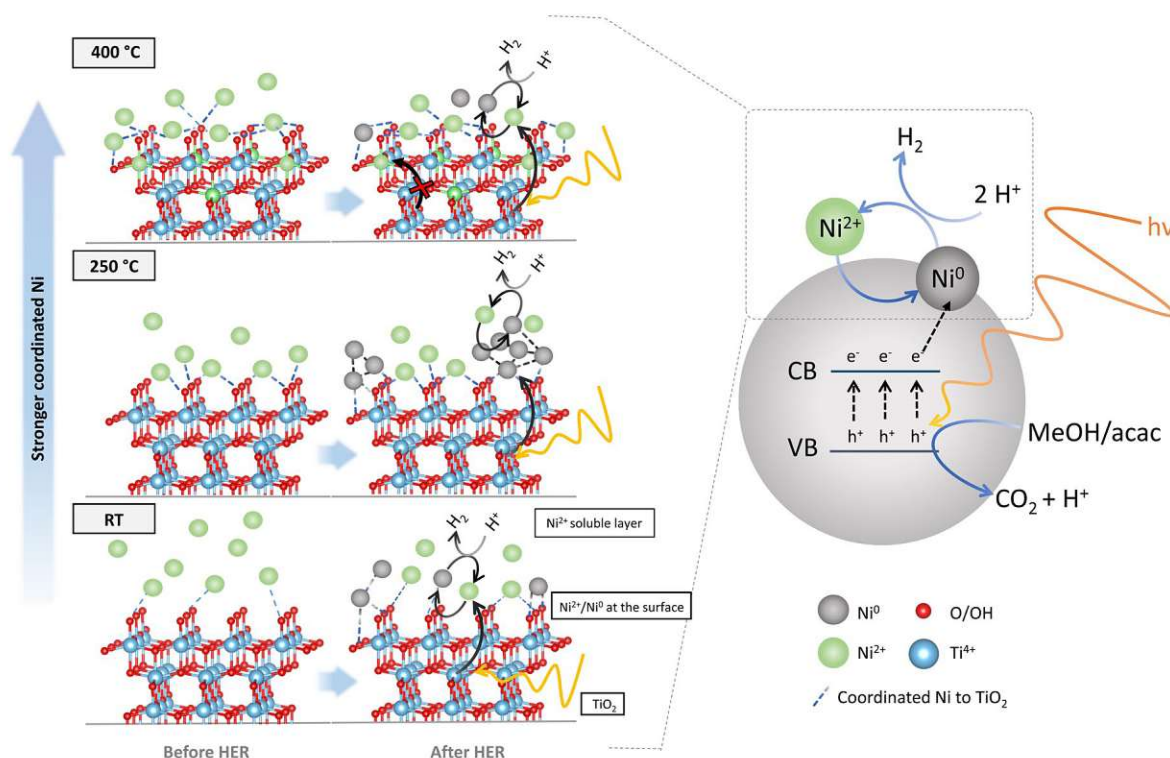
Figure 4. Proposed photocatalytic mechanism and schematic of the Ni/TiO$_2$ system for the case of the non-calcined (RT) and calcined Ni/TiO$_2$ samples (at 250 °C and 400 °C) showing the states of the photocatalytic surface for the as-prepared samples – i.e. before HER – and after the photocatalytic reaction – i.e. after HER.

It is well accepted in literature that Ni^0 constitute the active HER center.[10,11,16,17,19–22,27,33] Furthermore, numerous studies have demonstrated the transformation of Ni^{2+} to Ni^0 upon illumination when in presence of an electron donor. Additionally, photodeposition experiments showed how dissolved Ni^{2+} are able to react with a photo excited electron and deposit on the substrate.[10,11,16,17,27] Hereby, integrating insights from the literature with the findings presented in this study, we can propose a photocatalytic HER active Ni state formation mechanism and the effects of increasing pre-calcination temperature on the photocatalyst's structure and HER activity. Summarizing the key findings of this study as obtained by XRF, TEM/EDX, UV-Vis, and XPS:

1. With increasing temperature, the performance of Ni/TiO$_2$ in HER decreases, coinciding with stronger Ni adhesion/adsorption onto TiO$_2$, as indicated by XRF analysis.
2. During photocatalysis, the efficiency of Ni^{2+} to Ni^0 reduction follows the sequence 250 °C > RT/PD > 400 °C, as revealed by DRS and XPS.

13

3. At 400 °C, the oxidation state of Ni^{2+} is stabilized within the TiO_2 lattice, while at 250 °C, Ni^0 dominates, as indicated by DRS and XPS.

4. RT and PD samples exhibit consistent patterns across various data sets (HER, UV-Vis, XPS), indicating similarities in the composition and structure of the Ni active state.

By correlating these observations with the HER performance, existing literature and a two-step photo-transformation of Ni on TiO_2 surface:

$$Ni^{2+} + 2\ e^- \xrightarrow{(I)} Ni^0$$

$$Ni^0 + 2\ H^+ \xrightarrow{(II)} Ni^{2+} + H_2$$

involving Ni photoreduction and electron release to form H_2, we can propose a formation mechanism of the active Ni species during HER as summarized in **Figure 4**.

Figure 4, the RT sample demonstrates weak physisorption of Ni^{2+} species, which are capable of re-dissolving into the solution during the photocatalytic reaction. Similar to the photodeposition process observed in the PD sample, these re-dissolved Ni species then get photodeposited back onto the TiO_2 surface in the form of Ni^0 through a reaction with the photogenerated electrons in TiO_2 (Ni undergoes reaction step I). Subsequently, H^+ generated from the decomposition of MeOH/acac get adsorbed onto Ni^0 centers and reduced to H_2, which ultimately regenerates the Ni^{2+} state (Ni undergoes reaction step II).

At the calcination temperature of 250 °C (**Figure 4**, 250 °C), stronger Ni adsorption takes place, leading to a partially chemisorption character of the anchoring and stronger electronic communication with TiO_2. Consequently, more electrons can be conducted through this Ni/TiO_2 interface, resulting in an increased degree of Ni reduction. Hence, Ni^0 is stabilized on the TiO_2 surface and continues to grow, acting as an efficient electron trap increasing the Ni^0 content and the undesired growth and agglomeration. That means, at 250 °C the reaction step II is partially inhibited, leading to a Ni^0 accumulation and less efficient HER performance.

At 400 °C (**Figure 4**, 400 °C), we observe that Ni is much stronger adsorbed to the surface -OH/-O groups, with an increased chemisorption character. Additionally, Ni is partially incorporated into the TiO_2 lattice (likely its sub-surface), which leads to a stabilization of the Ni^{2+} state. As a result, reaction step I is partially hindered and less Ni^0 is generated leading to a drop in HER performance.

In summary, for effective extraction of photoelectrons from the TiO_2 support and their injection into adsorbed H^+ to generate H_2, it is crucial for Ni to be weakly adsorbed/adhered to the TiO_2 surface. In this situation, Ni species facilitate a dynamic and reversible redox shuttling ($Ni^{2+} \leftrightarrow Ni^0$) of the electrons between TiO_2 and reactants, similar to the case observed in Ni/TiO_2

samples prepared via Ni photodeposition.[10,11,48] In contrast, when Ni species are strongly adhered to the TiO_2 surface, either by becoming a part of the TiO_2 lattice or by transforming into Ni^0 aggregates, this dynamic process is partially hindered. In such cases, Ni centers are limited in their ability to undergo redox shuttling, resulting in less efficient transformation between Ni^{2+} and Ni^0 states, which consequently, limits their photocatalytic performance.

3. Conclusions

In this study, we demonstrate that post-synthesis calcination of the photocatalyst can negatively impact its photocatalytic performance. Ni, acting as a co-catalyst, was grafted onto TiO_2 nanoparticles (Ni/TiO_2) using a wet impregnation method and then subjected to calcination at 250 and 400 °C. The non-calcined Ni/TiO_2 sample (RT) exhibited the highest performance, with a gradual decrease in hydrogen generation as the calcination temperature increased (RT > 250 °C > 400 °C). XRF analysis and Ni washing experiments revealed that the primary cause of this effect is the increase in the adsorption strength of Ni on the TiO_2 surface. As the calcination temperature increases, Ni becomes more strongly adsorbed (RT < 250 °C < 400 °C), hindering its ability to efficiently undergo a redox shuttle (transformation of Ni^{2+} to Ni^0 and back after reaction with H^+ to H_2, i.e. $Ni^{2+} \leftrightarrow Ni^0$) required to generate H_2 efficiently. At 250 °C, Ni^{2+} adsorption becomes strong enough to facilitate efficient electron transfer between TiO_2 and Ni^{2+}, leading to agglomeration of Ni^0 and acting as an electron sink, thereby inhibiting the dynamic $Ni^{2+} \leftrightarrow Ni^0$ shuttle. At 400 °C, Ni establishes an even stronger adsorption with TiO_2, stabilizing Ni^{2+} state and preventing the formation of Ni^0. Thus, the stabilizing effect of Ni^{2+} or Ni^0 in the various calcined samples detrimentally affects the overall photocatalytic performance. Hereby, this work underscores that not only Ni^0 plays a key role in enabling efficient HER performance, but also the right $Ni^{2+}:Ni^0$ ratio which enables dynamic and efficient $Ni^{2+} \leftrightarrow Ni^0$ shuttling. These findings emphasize that possible side effects of chosen calcination and synthetic methodologies need to be considered when designing a range of photocatalytic materials.

4. Experimental Section/Methods

Synthesis of the composites: All materials used for the syntheses were obtained from commercial suppliers: anatase TiO_2 and $Ni(acac)_2$ from Sigma-Aldrich; absolute ethanol was used for the synthesis (from Chem-Lab NV); deionized water and HPLC-gradient grade methanol (from VWR) were used for the photocatalytic experiments. The composites were synthesized by a wet impregnation method with post-synthetic thermal treatments conducted in

ambient air. The general synthesis procedure used for all samples included (a) suspending the TiO$_2$ powder (12.5 mmol) in 20 ml of the corresponding solvent (ethanol or water). b) Next, the Ni(acac)$_2$ (0.626 mmol) was dissolved separately in the corresponding solvent (70 ml for H$_2$O and 50 ml for EtOH) and sonicated for 5 min. c) The two solutions were then mixed and sonicated for 10 min. d) The sample prepared under air (EtOH/air) was left stirring at 60 °C until complete evaporation of the solvent took place, while the vacuum samples (EtOH/vacuum and H$_2$O/vacuum) the solvent was extracted by a rotary evaporator. e) The remaining powder was then collected and ground. f) Afterwards, the samples were heat-treated in ambient air at the corresponding temperature (no heat treatment (RT), 250 or 400 °C) with a heating ramp of 2 h to reach the desired temperature, and then allowed to naturally cool down. In the case of the photodeposited sample (PD), TiO$_2$ (0.11 mmol) was suspended in a 50:50 vol. % MeOH-water solution and a Ni(acac)$_2$ stock solution was added aiming for 5 at.% Ni. Next, the standard photocatalytic experiments was carried out to allow *in-situ* deposition of Ni on TiO$_2$ and simultaneous H$_2$ detection (see photocatalytic experiment section for details). For the washing experiments, the corresponding samples were suspended in a 10 ml MeOH:H$_2$O solution (same solution as for the HER). After stirring for 5 minutes, the suspensions were vacuum filtered and dried under vacuum yielding powders for XRF analyses.

Photocatalytic experiments: Hydrogen evolution experiments were performed using a side irradiation gas-flow slurry type home-made reactor equipped with a LED lamp light source centered at 365 nm ± 20 nm (Thorlabs) (**Figure S1**) and an *in-situ* product detection system. In a single experiment, 10 mg of the powdered photocatalyst was dispersed in 10 ml 50:50 vol. % MeOH-water solution. During the experiment, the reactor was continuously purged with argon (flow rate of 15 ml min^{-1}, controlled with a mass flow controller from MCC-Instruments) to deliver the gaseous products to the online gas analyzer (X-Stream®, Emerson Process Management) equipped with a thermal conductivity detector (TCD) for H$_2$ quantification and a photometric non-dispersive IR sensor for CO$_2$ detection. The temperature of the reactor was kept constant at 15 °C through a water-cooling system (Lauda). The 3 min delay between the start of illumination and the rise of hydrogen signal in all H$_2$ and CO$_2$ rate graphs is due to the experimental setup as the carrier gas (Ar) needs a certain time to reach from the reactor to the detector (see **Figure S1**).

Characterisation methods: Transmission electron microscopy (TEM) images were obtained using FEI TECNAI F20 transmission electron microscope equipped with a field emission gun in bright field mode using 200 kV acceleration voltage. The sample was prepared from an ethanol suspension, using a copper holey carbon-coated grid (Plano, 200 mesh). The EDX

mapping was performed with the same device in scanning mode with approximately 2 nm resolution and high-angle annular dark-field imaging (HAADF) equipped with a EDAX-AMETEK Apollo XLTW SDD EDX-detector. The chemical composition of the samples was obtained with X-ray photoelectron spectroscopy (XPS). All measurements were carried out with the sample in normal emission angle with respect to the analyzer. The samples were mounted onto the sample holder using double-sided carbon tape and In-foil. The XPS spectra were acquired using an Axis Ultra DLD instrument from Kratos Analytical (UK) with the base pressure during spectra acquisition better than 1.1×10^{-9} Torr (1.5×10^{-7} Pa), achieved by a combination of turbomolecular and ion pumps. Monochromatic Al-Kα radiation (hν = 1486.6 eV) is employed with the anode power set to 150 W. All spectra were collected at normal emission angle. Data analysis was done using the CasaXPS Version 2.3.19PR1.0 software package employing Shirley/Shirley Tougaard backgrounds and Scofield sensitivity factors.[49,50] Curve fits using combined Gaussian-Lorentzian peak shapes (GL(30)) were used to discern the components of detail spectra, except for the metallic Ni where an asymmetric LA(1.1,2.2,10) line shape was used. The binding energy scale was calibrated using sputter-etched Au, Ag and Cu standard samples, which exhibit Au $4f_{7/2}$, Ag $3d_{5/2}$ and Cu $2p_{3/2}$ peak positions at 83.96 eV, 368.21 eV and 932.62 eV, respectively. Hence, all binding energies are given with respect to the calibrated Fermi level at 0 eV. All content values shown are in units of a relative atomic percent (at. %), where the detection limit in survey measurements usually lies around 0.1-0.5 at. %, depending on the element. The accuracy of XPS measurements is around 10-20 % of the values shown. Assignment of different components was primarily done using Refs.[51,52] For the attenuated total reflection Fourier-transform Infrared spectroscopy (ATR-FTIR) measurements a PerkinElmer FTIR Spectral UATR-TWO with a spectrum two Universal ATR (Single Reflection Diamond) accessory was used. The X-ray Fluorescence Spectroscopy (XRF) chemical quantification analysis was performed with an Atomika 8030C X-ray fluorescence analyzer with a Molybdenum X-ray source monochromitized Kα-line. The excitation conditions were 50 kV and 47 mA, 100 s with a total reflection geometry and an Energy-dispersive Si(Li)-detector. For the sample preparation, all reflectors were washed thoroughly and measured to account for true blanks. 1 mg of the solid nano-powder was loaded on the clean reflectors and sealed with 5 µL of a 1 % PVA solution to avoid contamination of the detector. After drying for 5 min on a hot plate and cooling, the reflectors with the loaded samples were measured. For the data evaluation, Ti was set as a matrix with 100 % (wt. %) and relative amounts of Ni were acquired (wt. %). The accuracy of TXRF measurements is around 10 % of the values shown. An exemplary XRF spectrum of a Ni/TiO$_2$ sample is shown in **Figure**

17

S12. For the Diffuse Reflectance Ultraviolet Spectroscopy (DRS or DR-UV-Vis) a Jasco V-670 UV-Vis photo spectrometer was used and the reflectance spectra of the catalyst powders were acquired using an integration sphere accessory. The X-ray diffraction (XRD) was performed using an XPERT II: PANalytical XPert Pro MPD (Θ-Θ Diffractometer) for the experiments. The sample was placed on a sample holder and irradiated with a Cu X-ray source (8.04 keV, 1.5406 Å). The signal was acquired with Bragg-Brentano Θ/Θ-diffractometer geometry ranging from 5° to 80° degrees. The detector system was a semiconductor X'Celerator (2.1°) detector.

Conflicts of interest

There are no conflicts to declare.

Supporting Information

Supporting Information is available from the Wiley Online Library or from the author.

Acknowledgements

Received: ((will be filled in by the editorial staff))
Revised: ((will be filled in by the editorial staff))
Published online: ((will be filled in by the editorial staff))

References

[1] S. Zhu, D. Wang, *Adv. Energy Mater.* **2017**, *7*, 1700841.
[2] K. Takanabe, *ACS Catal.* **2017**, *7*, 8006.
[3] S. J. A. Moniz, S. A. Shevlin, D. J. Martin, Z.-X. Guo, J. Tang, *Energy Environ. Sci.* **2015**, *8*, 731.
[4] F. E. Osterloh, *ACS Energy Lett.* **2017**, *2*, 445.
[5] Y. Zhong, C. Peng, Z. He, D. Chen, H. Jia, J. Zhang, H. Ding, X. Wu, *Catal. Sci. Technol.* **2021**, *11*, 27.

[6] X. Li, J. Yu, J. Low, Y. Fang, J. Xiao, X. Chen, *J. Mater. Chem. A* **2015**, *3*, 2485.

[7] T. Liu, L. Bai, N. Tian, J. Liu, Y. Zhang, H. Huang, *Int. J. Hydrog. Energy* **2023**, *48*, 12257.

[8] R. Marschall, *Adv. Funct. Mater.* **2014**, *24*, 2421.

[9] M. R. Nellist, F. A. L. Laskowski, F. Lin, T. J. Mills, S. W. Boettcher, *Acc. Chem. Res.* **2016**, *49*, 733.

[10] H. Zhao, Q. Mao, L. Jian, Y. Dong, Y. Zhu, *Chin. J. Catal.* **2022**, *43*, 1774.

[11] K. Wenderich, G. Mul, *Chem. Rev.* **2016**, *116*, 14587.

[12] P. Ciambelli, G. La Guardia, L. Vitale, in *Stud. Surf. Sci. Catal.*, Elsevier, **2020**, pp. 97–116.

[13] K. P. de Jong, *Synthesis of Solid Catalysts*, Wiley, **2009**.

[14] P. Ayala, A. Giesriegl, S. P. Nandan, S. N. Myakala, P. Wobrauschek, A. Cherevan, *Catalysts* **2021**, *11*, 417.

[15] J. S. Schubert, L. Kalantari, A. Lechner, A. Giesriegl, S. P. Nandan, P. Alaya, S. Kashiwaya, M. Sauer, A. Foelske, J. Rosen, P. Blaha, A. Cherevan, D. Eder, *J. Mater. Chem. A* **2021**, *9*, 21958.

[16] X. Liu, H. Zhuang, *Int. J. Energy Res.* **2021**, *45*, 1480.

[17] Y. Xu, R. Xu, *Appl. Surf. Sci.* **2015**, *351*, 779.

[18] R. Shen, J. Xie, Q. Xiang, X. Chen, J. Jiang, X. Li, *Chin. J. Catal.* **2019**, *40*, 240.

[19] W.-T. Chen, A. Chan, D. Sun-Waterhouse, T. Moriga, H. Idriss, G. I. N. Waterhouse, *J. Catal.* **2015**, *326*, 43.

[20] A. Indra, P. W. Menezes, K. Kailasam, D. Hollmann, M. Schröder, A. Thomas, A. Brückner, M. Driess, *Chem. Commun.* **2015**, *52*, 104.

[21] J. Yu, Y. Hai, B. Cheng, *J. Phys. Chem. C* **2011**, *115*, 4953.

[22] S. Lv, M. Pei, Y. Liu, Z. Si, X. Wu, R. Ran, D. Weng, F. Kang, *Nano Res.* **2022**, *15*, 5848.

[23] J. S. Schubert, J. Popovic, G. M. Haselmann, S. P. Nandan, J. Wang, A. Giesriegl, A. S. Cherevan, D. Eder, *J. Mater. Chem. A* **2019**, DOI 10.1039/C9TA05637H.

[24] X. Chen, J. Xiong, J. Shi, S. Xia, S. Gui, W. Shangguan, *Front. Energy* **2019**, *13*, 684.

[25] A. L. Luna, D. Dragoe, K. Wang, P. Beaunier, E. Kowalska, B. Ohtani, D. Bahena Uribe, M. A. Valenzuela, H. Remita, C. Colbeau-Justin, *J. Phys. Chem. C* **2017**, *121*, 14302.

[26] J. L. Rodríguez, F. Pola, M. A. Valenzuela, T. Poznyak, *MRS Online Proc. Libr.* **2011**, *1279*, 53.

[27] W. Wang, S. Liu, L. Nie, B. Cheng, J. Yu, *Phys. Chem. Chem. Phys.* **2013**, *15*, 12033.

[28] M. Sakamoto, M. Fujistuka, T. Majima, *J. Photochem. Photobiol. C Photochem. Rev.* **2009**, *10*, 33.

[29] W.-C. Lin, W.-D. Yang, I.-L. Huang, T.-S. Wu, Z.-J. Chung, *Energy Fuels* **2009**, *23*, 2192.

[30] J. Schneider, D. W. Bahnemann, *J. Phys. Chem. Lett.* **2013**, *4*, 3479.

[31] V. Kumaravel, M. Imam, A. Badreldin, R. Chava, J. Do, M. Kang, A. Abdel-Wahab, *Catalysts* **2019**, *9*, 276.

[32] D. L. Howard, H. G. Kjaergaard, J. Huang, M. Meuwly, *J. Phys. Chem. A* **2015**, *119*, 7980.

[33] S. Sun, Y.-C. Zhang, G. Shen, Y. Wang, X. Liu, Z. Duan, L. Pan, X. Zhang, J.-J. Zou, *Appl. Catal. B Environ.* **2019**, *243*, 253.

[34] X. Qiu, M. Miyauchi, K. Sunada, M. Minoshima, M. Liu, Y. Lu, D. Li, Y. Shimodaira, Y. Hosogi, Y. Kuroda, K. Hashimoto, *ACS Nano* **2012**, *6*, 1609.

[35] L. P. Bevy, *Trends in Catalysis Research*, Nova Publishers, **2006**.

[36] M. Myilsamy, M. Mahalakshmi, V. Murugesan, N. Subha, *Appl. Surf. Sci.* **2015**, *342*, 1.

19

[37] S. Akel, R. Boughaled, R. Dillert, M. El Azzouzi, D. W. Bahnemann, *Molecules* **2020**, *25*, 249.

[38] H. Yu, J. Tian, F. Chen, P. Wang, X. Wang, *Sci. Rep.* **2015**, *5*, 13083.

[39] J. Choi, H. Park, M. R. Hoffmann, *J. Mater. Res.* **2010**, *25*, 149.

[40] H. Yu, H. Irie, K. Hashimoto, *J. Am. Chem. Soc.* **2010**, *132*, 6898.

[41] H. Irie, K. Kamiya, T. Shibanuma, S. Miura, D. A. Tryk, T. Yokoyama, K. Hashimoto, *J. Phys. Chem. C* **2009**, *113*, 10761.

[42] H. Irie, S. Miura, K. Kamiya, K. Hashimoto, *Chem. Phys. Lett.* **2008**, *457*, 202.

[43] X. Cai, Y. Cai, Y. Liu, S. Deng, Y. Wang, Y. Wang, I. Djerdj, *Ceram. Int.* **2014**, *40*, 57.

[44] E. Gallo, E. Gorelov, A. A. Guda, A. L. Bugaev, F. Bonino, E. Borfecchia, G. Ricchiardi, D. Gianolio, S. Chavan, C. Lamberti, *Inorg. Chem.* **2017**, *56*, 14408.

[45] M. C. Biesinger, L. W. M. Lau, A. R. Gerson, R. S. C. Smart, *Phys. Chem. Chem. Phys.* **2012**, *14*, 2434.

[46] M. C. Biesinger, *Surf. Interface Anal.* **2017**, *49*, 1325.

[47] M. C. Biesinger, B. P. Payne, A. P. Grosvenor, L. W. M. Lau, A. R. Gerson, R. St. C. Smart, *Appl. Surf. Sci.* **2011**, *257*, 2717.

[48] S. Kumar, K. Ojha, A. K. Ganguli, *Adv. Mater. Interfaces* **2017**, *4*, 1600981.

[49] S. Tougaard, *Surf. Interface Anal.* **1997**, *25*, 137.

[50] D. A. Shirley, *Phys. Rev. B* **1972**, *5*, 4709.

[51] C.D. Wagner, A.V. Naumkin, A. Kraut-Vass, J.W. Allison, C.J. Powell, J.R. Rumble, **2003**.

[52] David. Briggs, Graham. Beamson, *Anal. Chem.* **1992**, *64*, 1729.

112

Supporting Information

Nature of the active Ni state for photocatalytic hydrogen generation

Jasmin S. Schubert, Eva Doloszeski, Pablo Ayala, Stephen Nagaraju Myakala, Jakob Rath, Bernhard Fickl, Ariane Giesriegl, Dogukan H. Apaydin, Bernhard C. Bayer, Shun Kashiwaya, Alexey Cherevan, * Dominik Eder *

J.S. Schubert, E. Doloszeski, P. Ayala, S. N. Myakala, J. Rath, B. Fickl, A. Giesriegl, D. H. Apaydin, B. C. Bayer, A. Cherevan, D. Eder
Institute of Materials Chemistry, Technische Universität Wien (TU Wien), Getreidemarkt 9, 1060, Vienna, Austria
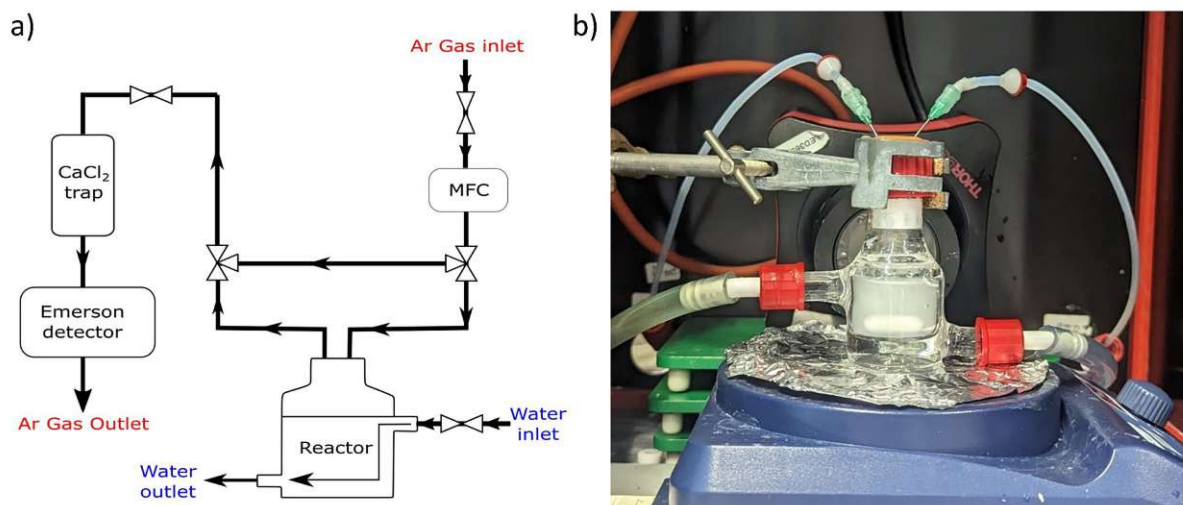E-mail: alexey.cherevan@tuwien.ac.at, dominik.eder@tuwien.ac.at

S. Kashiwaya
Materials Design, Department of Physics, Chemistry, and Biology (IFM), Linköping University, 58183, Linköping, Sweden

113

Table of Contents

1. Photocatalytic setup

Figure S1. Scheme of the photocatalytic setup used for the in-flow in-situ H_2- and CO_2-detection. a) Schematic representation of the experimental setup. b) A photograph of the reactor where the photocatalytic experiments were carried out.

2. TiO₂ benchmark experiments

To determine and consider the potential effects that high-temperature calcination can imply on the resulting crystallinity and defect level of TiO_2 – used throughout this work as a support material – we performed HER experiments by using a non-calcined TiO_2 powder (RT) and the one calcined at 400 °C. For the experiments, we used the same Ni(acac)$_2$ solution used for the PD samples (described in the main manuscript "experimental section/methods"). **Figure S2** shows that the HER performance of the resulting Ni/TiO_2 samples based on bare (RT) and calcined (400 °C) TiO_2 powders is almost identical, which strongly suggests that the temperatures used in this work (250 and 400 °C) are low enough to preserve crystallinity or defect levels of the supporting TiO_2 intact. This in turn, allows us to exclude these effects when discussing HER trends of the Ni/TiO_2 samples prepared via wet-impregnation and concentrate our discussion on the effect of Ni/TiO_2 interface and quality of the Ni species.
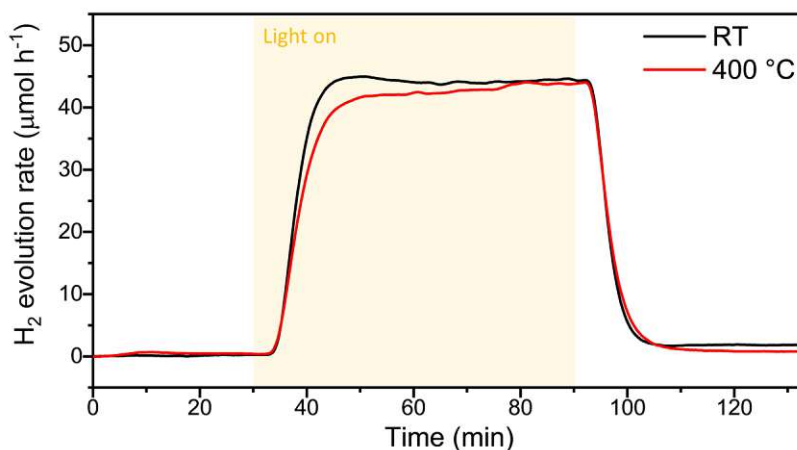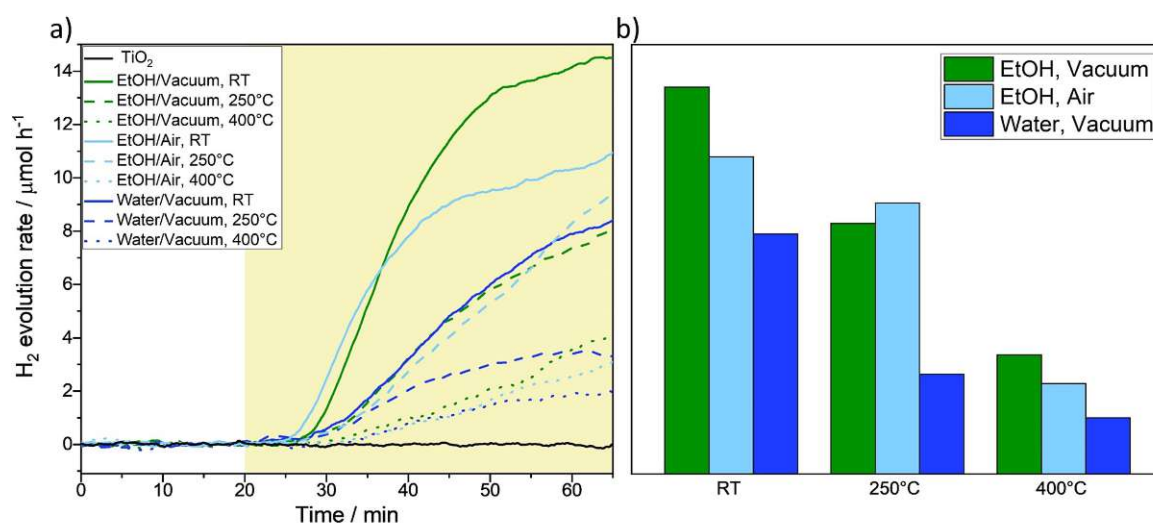

Figure S2. HER performance of TiO_2 samples (using Ni(acac)$_2$ as cocatalyst via photodeposition) based on bare TiO_2 (RT) and the one calcined at 400 °C. The yellow area shows the illumination period. The short delay between the start of illumination and the rise of H_2 signal is due to the experimental setup (see experimental section and **Figure S1**).

3. Variation of synthetic conditions and reproducibility tests

We investigated the effect of different synthetic parameters and the reproducibility of the Ni/TiO$_2$ photosystem. For this, we started with the same precursors, but used different solvents (ethanol or water) and two different ambient (under air or vacuum). These samples are: in ethanol under vacuum (EtOH/vacuum), ethanol under air (EtOH/air) and water under vacuum (H$_2$O/vacuum). Experimental details can be found in the experimental section of the main manuscript. Then, three different calcination protocols were applied to prepare non-calcined – i.e. as-prepared (RT) – as well as 250 °C and 400 °C calcined samples. All the samples were tested for the capacity to generate hydrogen, where the most active sample set was obtained with EtOH/vacuum (the sample set discussed in the main manuscript), followed by the EtOH/air and H$_2$O/vacuum (**Figure S3**). All samples were characterized by UV-Vis, ATR-IR, TEM, TXRF and XPS, revealing similarity in their structure and composition, so no major differences among the different sets could be concluded (see the corresponding sections).

3.1. HER

The HER rate analysis in **Figure S3** shows that all sample sets reveal the same trend: the RT sample is the most HER active and we observe gradually decreasing HER rate with increasing calcination temperature, independent of the synthetic protocol used.

Figure S3. HER performance of Ni/TiO$_2$ samples prepared using different solvent/ambient conditions and different post-calcination temperatures. a) In-situ H$_2$ generation profiles over the first 65 min of the experiment. b) Bar graph derived from the HER datasets in figure a, showing HER rates achieved for the samples after 65 minutes of experiment.

3.2. UV-Vis

UV-Vis data in **Figure S4** show a shift of the absorption band to higher wavelength in the range from 400 to 550 nm for the samples prepared using different protocols. This shift takes place in a reproducible way in all sample sets from the RT to 400 °C. In the range from 550 to 900 nm we see the characteristic Ni(II) d-d transition. The RT samples show the same band as pure Ni(acac)$_2$ for both samples synthesized in EtOH. The samples synthesized in water, however, show a shift to higher wavelength, which is probably induced by Ni forming an aqua complex ([Ni(H$_2$O)$_6$]$^{2+}$). At 250 °C all the profiles are quite similar, with the Ni species hydroxylated to the TiO$_2$ surface -OH groups, Ni-(OH)-Ti. Then, at 400 °C, the band flattens suggesting more hydroxylation and Ni-O-Ti bonds. The data show a slight change in the Ni coordination for the RT samples when using EtOH or H$_2$O, yet by gradually increasing the calcination temperature all samples start to resemble each other, which hints for a similar chemical environment and structure. Hence, the most probable cause of the different HER rate observed in **Figure S3**, is the difference in the initial chemical environment of Ni species and the way Ni transforms during the photocatalytic reaction.
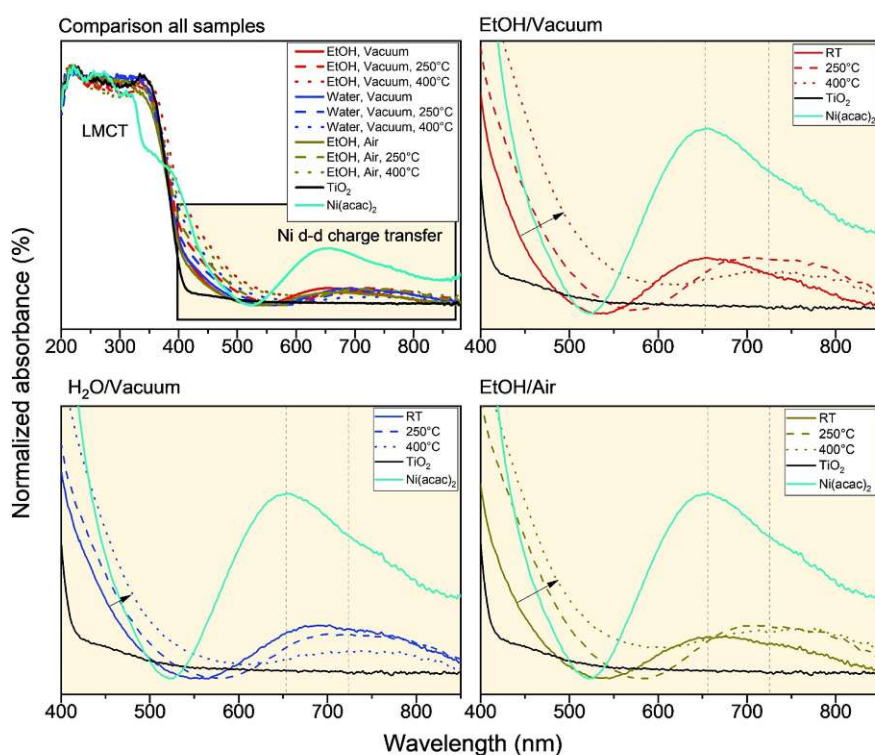
Figure S4. UV-Vis of Ni/TiO$_2$ samples prepared using different solvent/ambient conditions and different post-calcination temperatures.

6

3.3. ATR-FTIR

The ATR-FTIR spectra for the different RT samples (**Figure S5**) indicate the presence of the acetylacetonate rest, which signal is gradually vanishing by increasing the calcination temperature (independent of the sample set investigated). These observations are reproducible for all data sets.
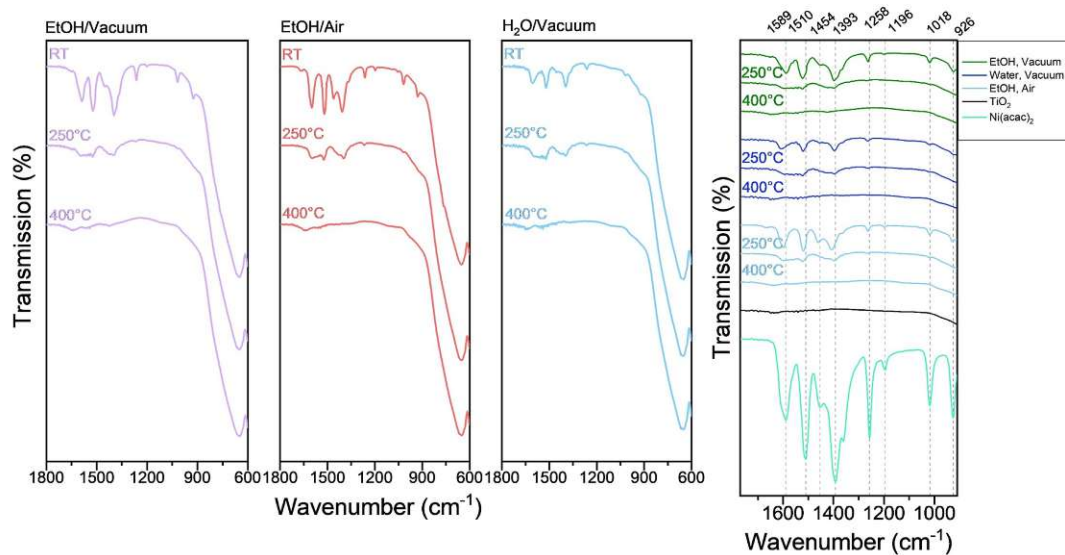
Figure S5. ATR-FTIR of Ni/TiO$_2$ samples prepared using different solvent/ambient conditions and different post-calcination temperatures.

7

119

3.4. TEM

The TEM micrographs in **Figure S6,** also show no major difference among the samples, neither to pure TiO_2.
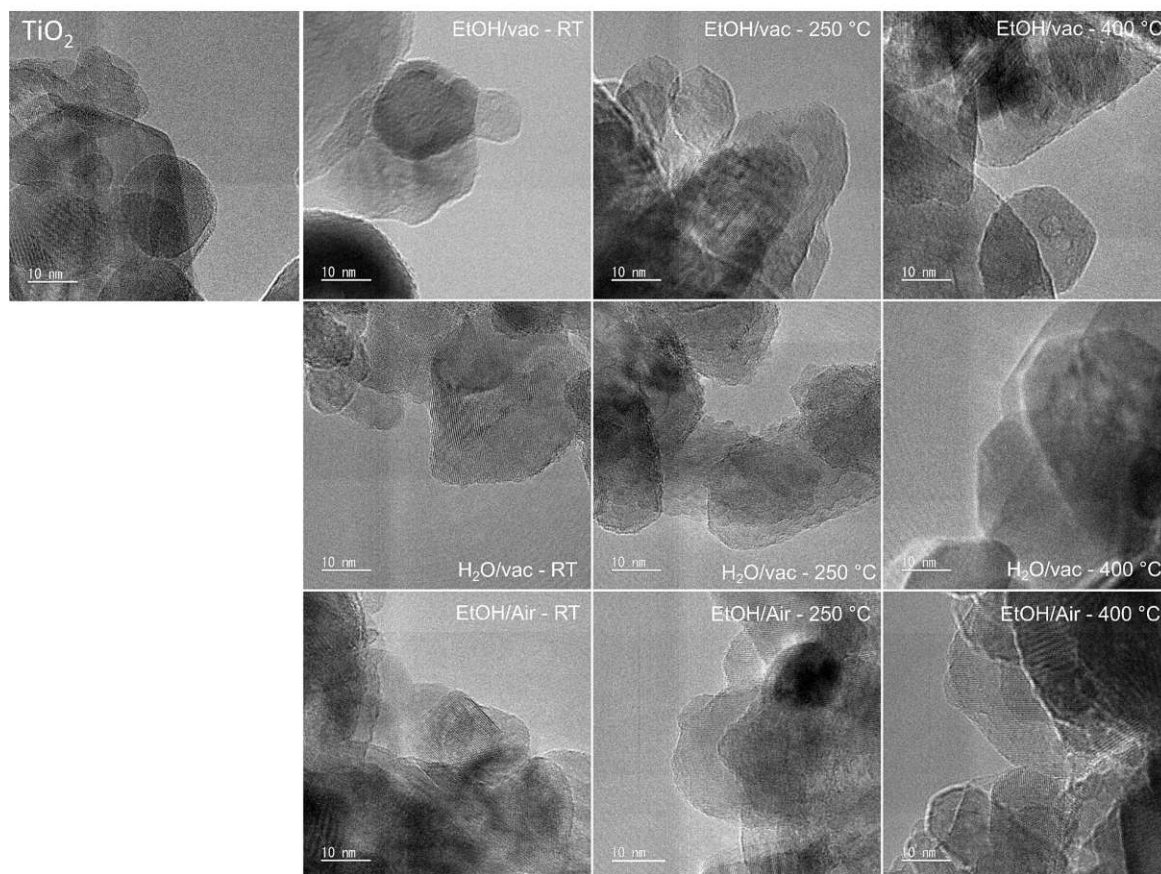
Figure S6. TEM images of Ni/TiO_2 samples prepared using different solvent/ambient conditions and different post-calcination temperatures.

3.5. XPS

The XPS data in **Figure S7** are consistent among the samples, with no significant changes observed when different post-treatment temperatures were applied.
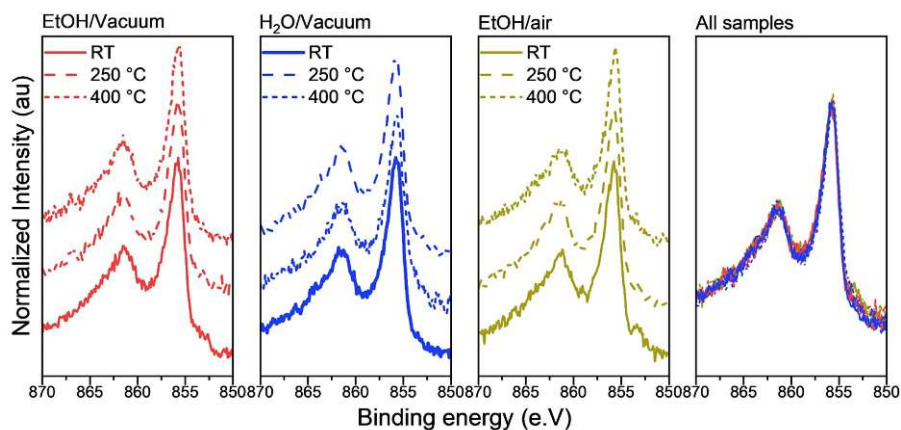
Figure S7. Ni2p XPS of Ni/TiO$_2$ samples prepared using different solvent/ambient conditions and different post-calcination temperatures.

3.6. Quantification of the Ni content in each sample by XRF and XPS surveys

Table S1. XRF of Ni/TiO$_2$ samples prepared using different solvent/ambient conditions and different post-calcination temperatures. Ni at. % in relation to TiO$_2$ (taken as 100 %).

	XRF	XPS
Sample	at. % Ni	
EtOH/Vacuum		
RT	6.3 ± 0.6	4.7 ± 0.5
250 °C	5.3 ± 0.5	2.6 ± 0.3
400 °C	4.8 ± 0.5	3.1 ± 0.3
H$_2$O/Vacuum		
RT	5.2 ± 0.5	5.2 ± 0.5
250 °C	5.2 ± 0.5	4.6 ± 0.5
400 °C	5.4 ± 0.3	3.3 ± 0.3
EtOH/Air		
RT	5.3 ± 0.3	2.8 ± 0.3
250 °C	5.3 ± 0.5	4.9 ± 0.5
400 °C	4.9 ± 0.4	3.6 ± 0.4

4. Further characterization data of the Ni/TiO₂ samples discussed in the main manuscript

4.1. Chronoamperometry measurements

To investigate the ability of the Ni species to extract electrons from TiO_2 substrate, we performed chopped-light chronoamperometry measurements of the RT sample and a TiO_2 benchmark (**Figure S8**). To perform the measurement TiO_2 and Ni/TiO_2 powders (RT sample) were deposited onto glassy carbon electrodes using an ink formulation that consisted of 10 mg of the corresponding powder, 50 µL of Nafion solution (5wt% in water and low aliphatic alcohols), and 950 µL of isopropyl alcohol. The mixture was briefly sonicated to obtain a homogeneous dispersion. Afterward, 50µL of the corresponding suspensions were taken and drop cast onto glassy carbon (GC) disk electrodes. GC/TiO_2 and GC/RT electrodes were used as working electrodes in a three-electrode setup in which Pt plate served as counter electrode and Ag/AgCl (in 3M KCl - E^0=0.210V) was used as the reference electrode. 0.1M Na_2SO_4 in water was used as the electrolyte. In order to simulate the photocatalytic reaction conditions, all the experiments were performed at open circuit conditions and the photocurrents was measured using a Thorlabs Solis 365C High-power LED light source.

The data show, that upon illumination TiO_2 delivers up to 4 $\mu A/cm^2$. The electrode behaves as a photoanode, which is expected considering the n-type character of TiO_2. The RT electrode delivers almost 10 times less photocurrent than the pure TiO_2 (**Figure S8**). This is something we have anticipated as the introduction of reductive co-catalysts into the structure of TiO_2 hinders it from conducting holes. When photocatalysts are illuminated, excitons (electron-hole pairs) are generated. These can either undergo (1) recombination in the catalyst core (bulk recombination), (2) recombination at the surface (surface recombination) or they might (3) be quenched by oxidants at the surface. When the surface does not contain any oxidants at higher energies than the conduction band edge, but sacrificial electron donors are available (such as methanol), holes in the valence band will be scavenged while electrons remain in the photocatalyst. This in return, results in negatively charged particles. These particles will generate anodic currents (the case of pure TiO_2 on GC). However, when electron acceptors (oxidants) are on the surface, they will take up these electrons balancing the charge and hindering the extraction of holes (the case of GC/RT) hence, causing a decrease in observed photoanodic current. In other words, the photocurrent data indicate that the presence of Ni in the photosystem enables the extraction of electrons, which is in line with its reductive co-catalytic nature.

10
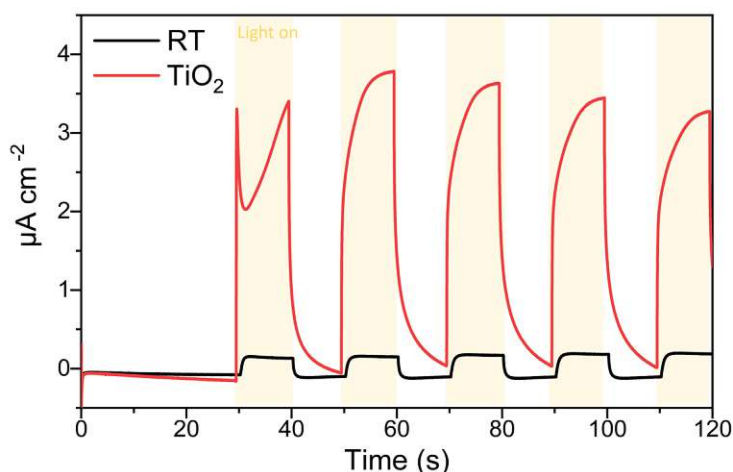
Figure S8. Chronoamperometry measurements of the RT sample and the TiO$_2$ benchmark. The yellow area shows the illumination period

4.2. Additional calculations of the H$_2$ and CO$_2$ evolution rate

We calculated the total amounts of H$_2$ and CO$_2$ generated during the photocatalytic reaction by integrating the activation- and stability-cycle areas obtained from the HER profiles presented in **Figure 1** as well as the H$_2$ and CO$_2$ evolution rate increase in the activation-cycle. This information is presented in **Table S2**. Furthermore, we estimated the theoretical maximum CO$_2$ amount that can be generated from the acetlyacetonate (acac) present in the reaction. For this calculation, we assumed the most oxidizing conditions, as the reaction mechanism – to the best of our knowledge – is not known under this condition. According to this, a single acac anion – with formula C$_5$H$_8$O$_2^-$– can generate a maximum of 5 CO$_2$;

$$C_5H_8O_2^- \rightarrow 5\ CO_2$$
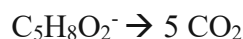
From **Table S1** we know that the RT sample contains 6.3 at. % Ni, which corresponds to 0.008 mmol Ni (10 mg of sample was used in the photocatalytic reaction). This corresponds to 0.016 mmol of acac from Ni(acac)$_2$. Thus, according to the equation above, we can generate a maximum of 78 µmol of CO$_2$ from acac considering its full oxidation. The RT/H$_2$O sample (**Table S2**) shows that acac after 17 h of illumination generated 0.58 µmols of CO$_2$ at a constant rate, as the curve in **Figure 1b** reveals. Thus, the amount of CO$_2$ generated is much below the theoretical one. The underlying cause of this effect is out of the scope of this work, yet most probably it is related to the reaction kinetics, as acac needs more time under this conditions to fully oxidize. The formation of CO$_2$ by the RT/H$_2$O and NiCl$_2$/TiO$_2$ reference samples (**Figure 1b**) clearly show that both carbon donors (acac and MeOH) contribute to the overall

11

123

CO_2 generation, while the steady increase of the CO_2 evolution rate mainly originates from MeOH oxidation.

Table S2. Integrated area of the activation- and stability-cycle along with the total area (i.e. total amount of H_2 and CO_2 generated) and the slope of the activation-cycle of the H_2 and CO_2 evolution profiles shown in **Figure 1**. See **Figure S9** for details how the slope was determined.

	H_2				CO_2			
	Integrate			slope	Integrate			slope
	activation-cycle	stability-cycle	Total		activation-cycle	stability-cycle	Total	
	μmol			$\mu mol\ h^{-2}$	μmol			$\mu mol\ h^{-2}$
RT	39.1	788.6	827.7	0.06	0.3	6.4	6.7	0.00056
250 °C	26.7	624.7	651.4	0.02	0.3	4.2	4.6	0.00090
400 °C	15.4	386.7	402.1	0.01	0.1	2.1	2.2	0.00020
PD	32.9	650.9	683.8	0.06	0.2	4.7	4.9	0.00020
RT/H_2O	0.0	0.0	0.0	0.00	0.1	0.5	0.6	0.00060
$NiCl_2/TiO_2$	33.9	339.8	373.7	0.04	0.03	0.9	0.9	0.00001

4.3. H_2 evolution rate profiles of the $NiCl_2/TiO_2$ and RT/H_2O samples

The H_2 evolution profile of $NiCl_2/TiO_2$ and RT/H_2O references are shown in **Figure S9**. The $NiCl_2/TiO_2$ sample shows that the anion present (i.e. the impurities of any kind, as the data discussed in **section 3, reproducibility test** revealed) also affects the overall activity and the reaction pathways of the Ni/TiO_2 photocatalyst, as the only difference between the Ni/TiO_2 and $NiCl_2/TiO_2$ samples is the composition of the Ni precursor ($NiCl_2$ or $Ni(acac)_2$). To reveal the effect of these anions is out of the scope of this work. Yet, most probably acac (and the solvent remnants from the synthesis) forms radicals and other reactive intermediates during the reaction, which affect the formation of the final active Ni species. [1–5] This data clearly shows that further parameters (like the anion decomposition intermediates) play a role in the overall activity and further research is necessary.
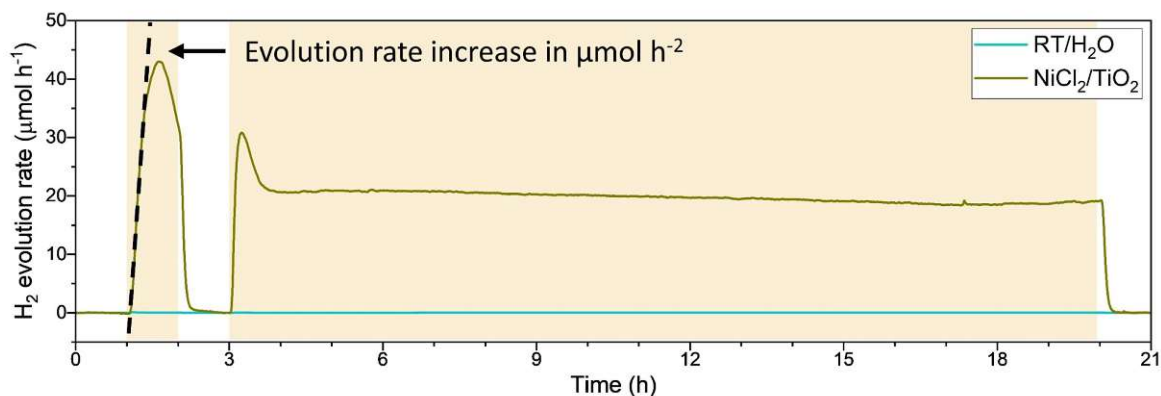
Figure S9. HER evolution rate of the RT sample tested only in water (i.e. without sacrificial agent, MeOH, RT/H$_2$O) and the NiCl$_2$/TiO$_2$ sample tested under standard conditions (in presence of MeOH) showing the full 21 h HER profile (activation- and stability-cycle). The illumination periods of the photocatalyst are indicated by the yellow region. In the figure is also shown how the evolution rate increase was determined for the H$_2$ and CO$_2$ data (**Table S2**).

4.4. ATR-FTIR

4.4.1. Full range ATR- FTIR spectra shown in Figure 1
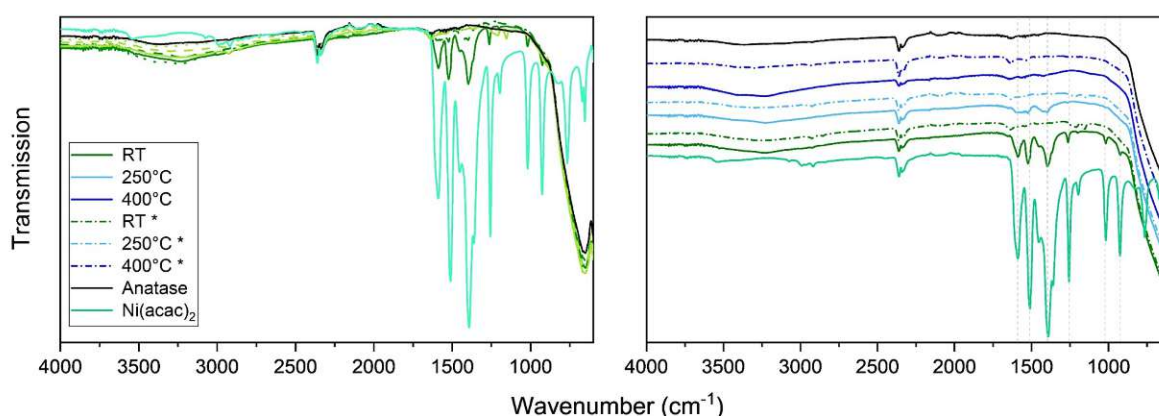
Figure S10. ATR-FTIR before and after HER (indicated by *) for the EtOH/Vac. Sample showing the OH band at 3000-3800 cm^{-1}.

4.4.2. Washing experiment of the RT sample

The aim of this experimental setup was to test how strong is the acac ion attached to the TiO$_2$ surface in the non-calcined, RT-derived sample. For this, the 10 mg of the RT sample was stirred in a MeOH/H$_2$O solution for 30 minutes, filtered and washed 3 times with 5 mL water. The data, shown in **Figure S11,** indicates strongly that acac is weakly attached on the TiO$_2$ surface, as no acac is visible after the washing experiments; the resulting FTIR spectrum resembles that of the pure TiO$_2$ reference. These data support the washing experiments and

13

XRF quantification data of Ni presented in the main manuscript (**Figure 2/Table S3**), showing that both, Ni and acac are weakly attached on the TiO_2 surface and once the powder is immersed in the reaction solution, both get dissolved.
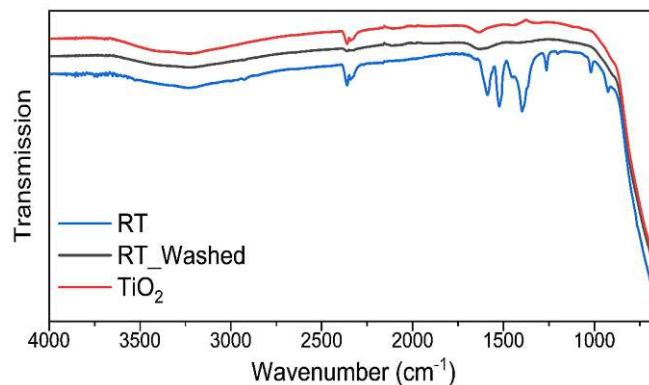
Figure S11. ATR-FTIR spectra of the RT sample before and after washing along with the TiO_2 reference.

4.5. XRF
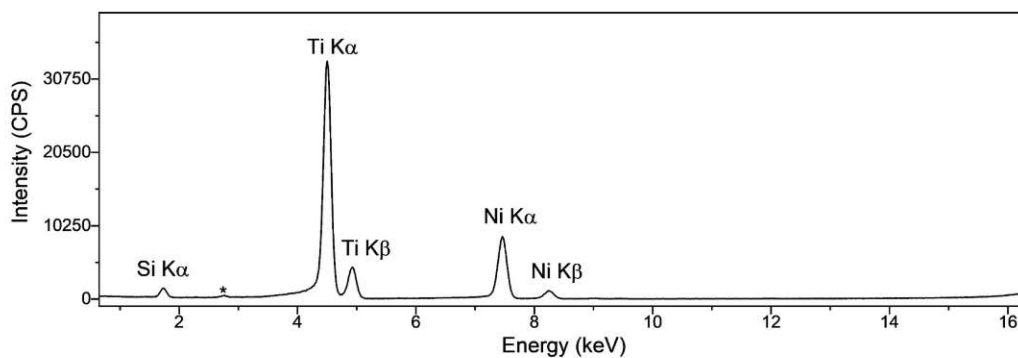
Figure S12. Example XRF spectrum of the EtOH/vac. sample.

14

Table S3. XRF and XPS Ni quantification of the Ni/TiO$_2$ samples prepared at different temperatures (RT, 250 and 400 C) and the photodeposited sample. Each sample is shown as-prepared, after washing, as well as after 2h (activation-cycle) and 21 h (stability-cycle) of HER run. Ni at. % is given in relation to TiO$_2$. The Ni % was calculated from the as-prepared (before HER) samples set as 100 %.

|		Units	RT	250 °C	400 °C	PD
XRF	Before HER		6.3 ± 0.5	5.2 ± 0.4	5.0 ± 0.4	-
	After washing	Ni	1.1 ± 0.1	2.7 ± 0.3	3.7 ± 0.4	-
	After 2 h HER	at. %	2.9 ± 0.2	2.9 ± 0.2	4.5 ± 0.3	3.3 ± 0.2
	After 21 h HER		3.5 ± 0.3	4.1 ± 0.3	4.8 ± 0.4	5.3 ± 0.4
	after washing	% of Ni	16.9 ± 1.7	52.2 ± 5.2	73.9 ± 7.4	-
	after 2 h HER		45.9 ± 4.6	55.1 ± 5.5	89.8 ± 9.0	-
	after 21 h HER		55.7 ± 5.6	78.3 ± 7.8	96.2 ± 9.6	-
XPS	Before HER	Ni	4.7 ± 0.5	2.6 ± 0.3	3.1 ± 0.3	-
	After 2 h HER	at. %	0.9 ± 0.1	0.3 ± 0.1	0.4 ± 0.1	0.7 ± 0.1
	After 21 h HER		0.7 ± 0.1	0.6 ± 0.1	1.8 ± 0.2	2.0 ± 0.2

4.6. XRD, HRTEM and EDX/STEM

To further elucidate on possible changes upon calcination and HER of the investigated samples, we analyzed them by XRD (**Figure S13**), HRTEM (**Figure S14**) and STEM/EDX mapping (**Figure S15**). The XRD data confirms that all samples correspond to a mixture of anatase – the major component – and rutile TiO$_2$, with no apparent changes in anatase/rutile ratio. Additionally, neither Ni-related-phase, nor other changes induced by calcination or photocatalysis could be observed. The HRTEM images revealed no visible changes (as discussed in the main manuscript), therefore we further analyzed them to determine the lattice spacing. This was done using the software "ImageJ" and is shown in **Figure S14** and **Table S4**. A fast Fourier transform (FFT) was applied, revealing the calculated diffraction pattern of the image and through masking individual diffraction spots the lattice direction of interest was chosen. After applying the inverse FFT on the masked pattern the specific lattice spacing could be measured with reasonably high precision. The analysis revealed no change in crystallinity upon calcination or HER, with all values interspacing values corresponding to the TiO$_2$ lattice, in line with the XRD data. The STEM/EDX observations are discussed in the main manuscript. Furthermore, our previous investigations – where we investigated a Ni(acac)$_2$ wet impregnated

TiO_2 (P25) with electron diffraction, TEM and XRD – revealed also that the deposited Ni salts are of amorphous nature. [9] Hereby, we can conclude that the Ni-species – and accordingly the acac anions – are homogeneously, randomly, amorphously and atomically dispersed on the TiO_2 surface. Hence, they are not visible using crystallographic methods.
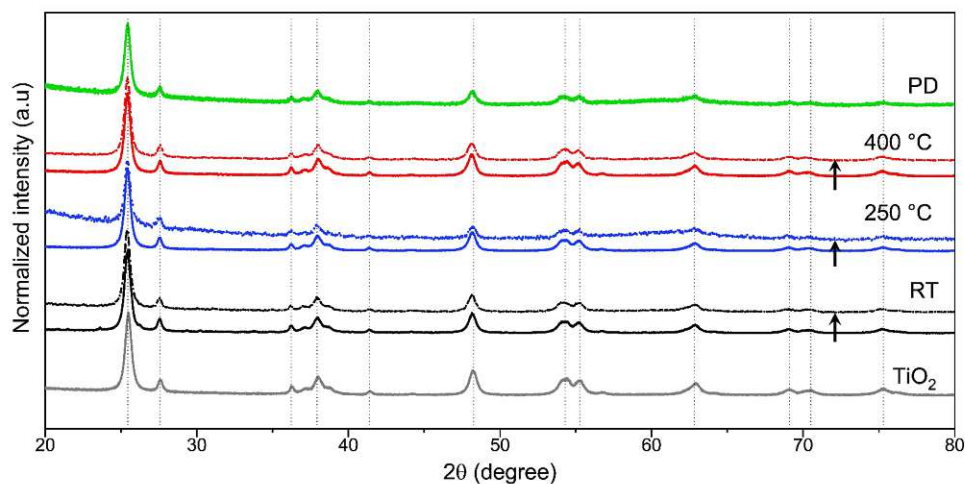
Figure S13. XRD of the EtOH/vac. samples before and after 21 h HER (indicated by the arrow, from before to after HER).
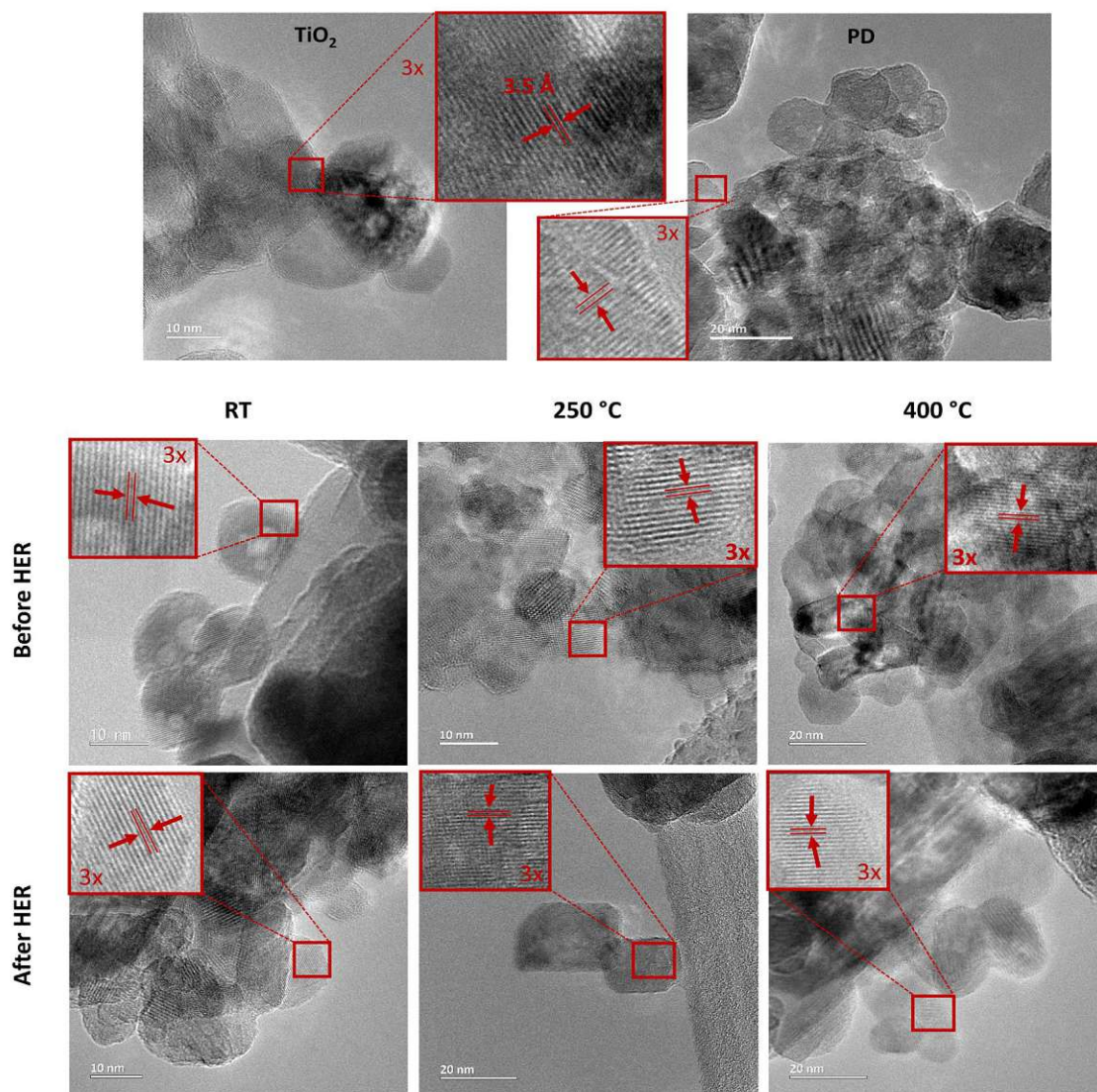
Figure S14. TEM image of the EtOH/vac. samples before and after 21h HER with the corresponding TiO₂ and the photodeposited (PD) samples as references. Highlighted are the areas taken to determine the atomic spacing with a 3 times magnification (3x) of the original image. The spacing between fringes for all samples is shown in **Table S4**.

Table S4. Atomic spacing determined of the EtOH/Vac. Samples before and after HER as well as the TiO₂ and PD reference samples. Values taken from the TEM images shown in **Figure S14**.

	Before HER	After HER
	Å	
TiO₂	3.5 ± 0.1	-
PD	-	3.5 ± 0.1
RT	3.5 ± 0.1	3.5 ± 0.1
250 °C	3.6 ± 0.1	3.5 ± 0.1
400 °C	3.5 ± 0.1	3.6 ± 0.1

17

129
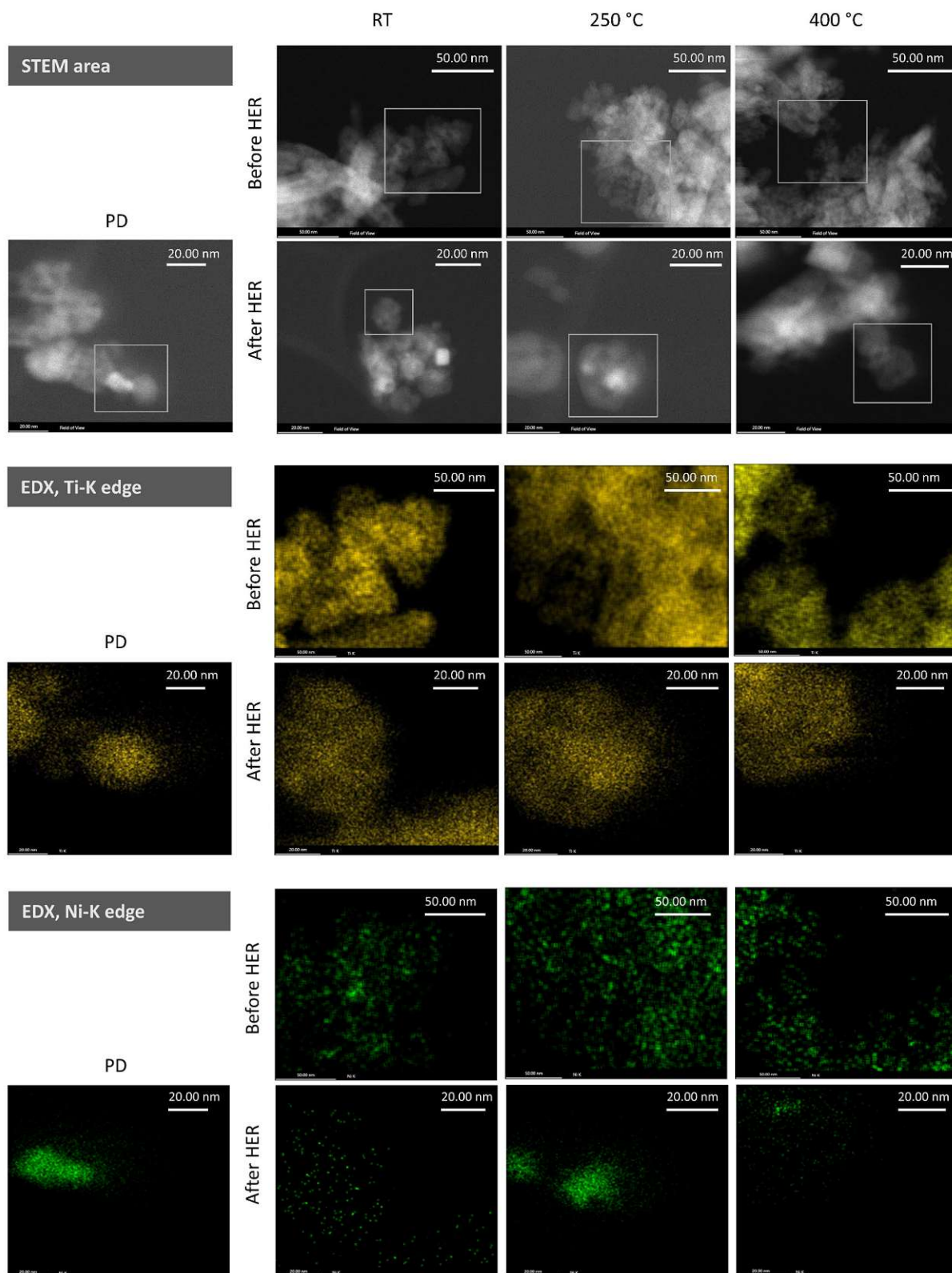
Figure S15. STEM and EDX elemental mapping of the Ni/TiO$_2$ and PD sample before and after HER (after 17 h of illumination).

4.7. XPS

Survey and detail spectra of all Ni/TiO$_2$ samples discussed in the main manuscript are shown in the following sections. For simplicity – and as no changes where observable between the spectra – only the as-prepared samples (i.e. before HER) are presented with regard to their detailed spectra.

4.7.1. Surveys
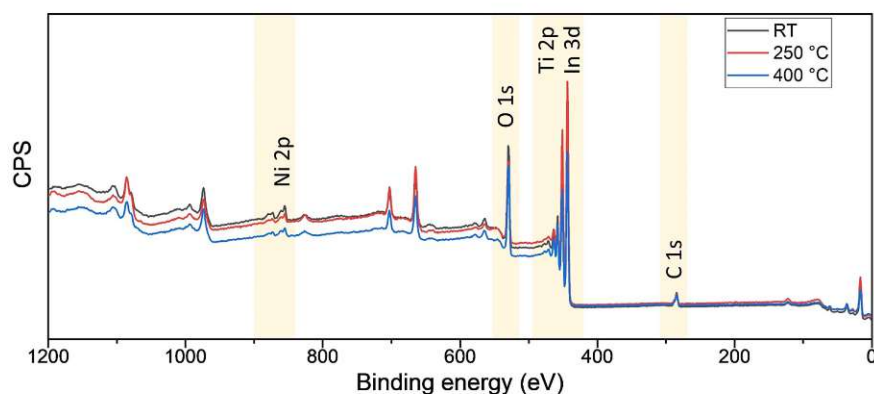
Figure S16. XPS survey of the as-prepared samples (i.e. before HER). Shadowed regions were used to acquire detail spectra; the rest of the signals belong to other In, Ti and O transitions.

4.7.2. C1s
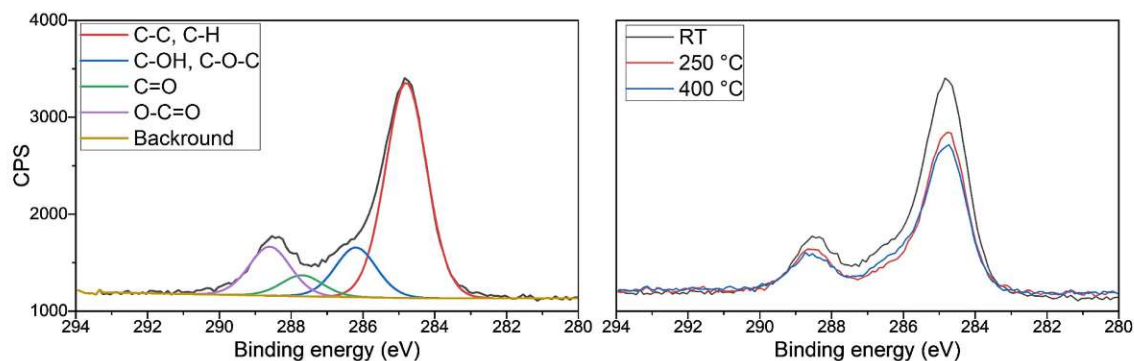
Figure S17. C1s detail spectrum of the as-prepared RT sample (left) along with different C-species, and the overlaid spectra of RT, 250 °C and 400 °C Ni/TiO$_2$ samples (right).

19

131

4.7.3. O1s
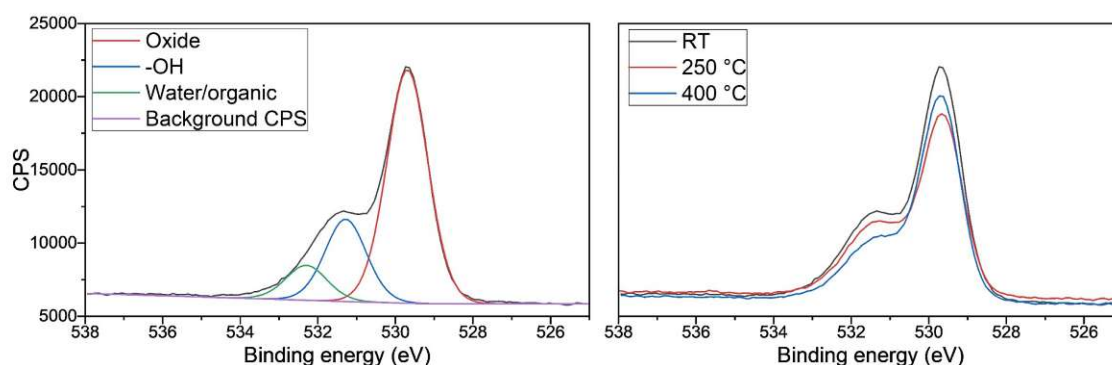
Figure S18. O1s detail spectrum of the as-prepared RT sample (left) along with the fits of different O-species, and the overlaid spectra of the RT, 250 °C and 400 °C Ni/TiO$_2$ samples (right).

4.7.4. Ti2p
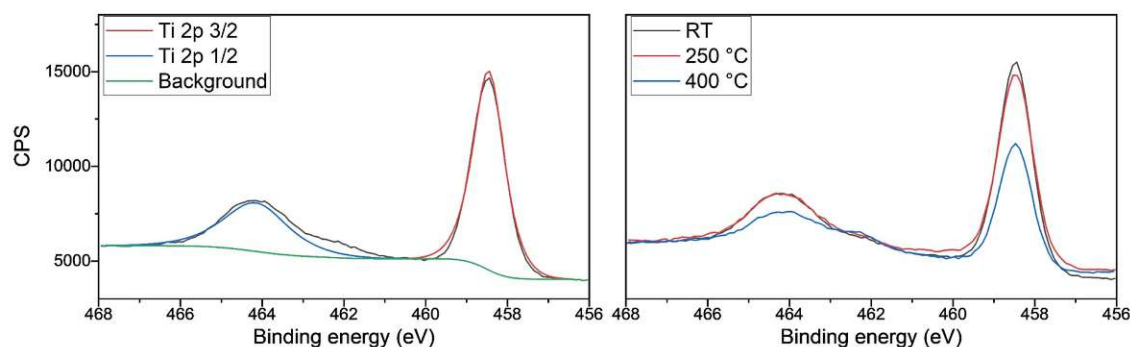
Figure S19. Ti2p detail spectrum of the as-prepared RT sample (left) along with the fitted Ti2p orbit splitting, and the overlaid spectra of the RT, 250 °C and 400 °C Ni/TiO$_2$ samples (right).

4.7.5. Ni 2p reference plots and quantification details

In order to determine the chemical surrounding of the Ni species in the investigated samples by XPS, we used for the data evaluation casaXPS and the constrains proposed by Biesinger et. al. [8]. In **Figure S20**, we show the spectra of the RT sample before HER with the typical Ni2p$_{3/2}$ peak with binding energy (B.E) of 855.8 eV and a small shoulder at 852.8 eV. With this sample, we show the different theoretical fits that correspond to a pure Ni(OH)$_2$, NiO and Ni^0 species and a mixture of those. [8,6,7] These different fits show that the Ni chemical surrounding in the

20

sample corresponds to a mixture of Ni(OH)$_2$ and metallic Ni. We also used NiO and NiOOH (only shown NiO in **Figure S20**), yet those ones did not show any improvement to the fits, and, thus, for simplicity we used the minimal required spectral fitting parameters.[9] Hereby, we can conclude that the main Ni species in the RT sample before HER is Ni(OH)$_2$ and Ni^0. The same applies for the 250 °C and 400 °C samples shown in **Figure S21**.
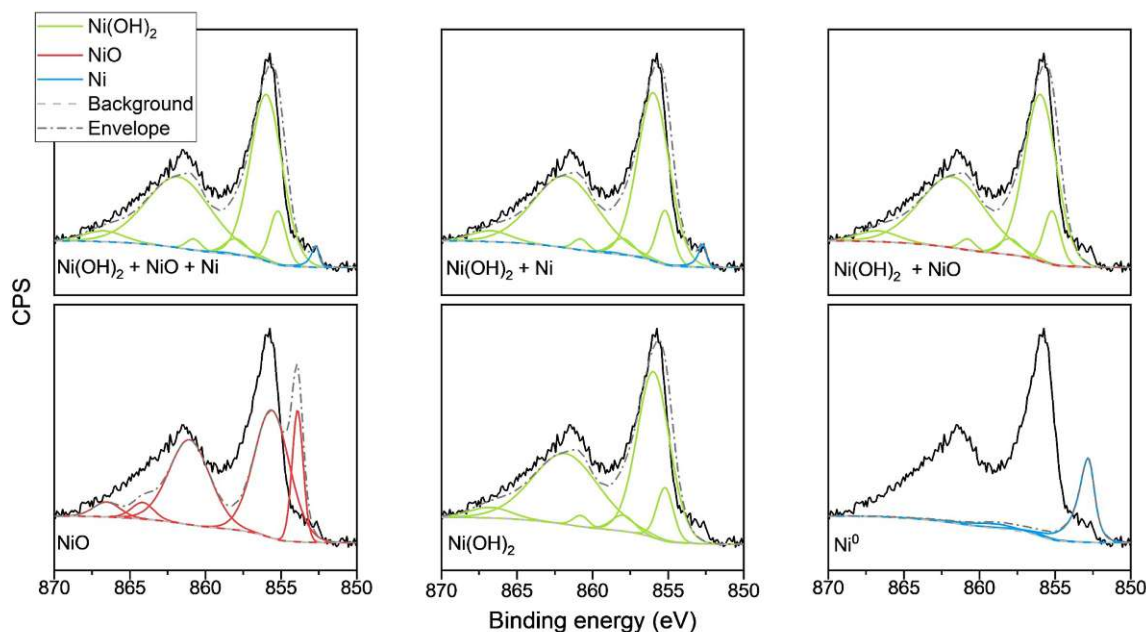
Figure S20. The as-prepared Ni/TiO$_2$ RT sample with different theoretical fits to elucidate the Ni chemical surrounding: pure Ni(OH)$_2$, NiO, metallic Ni and a mixture of those. Fitting data taken from Biesinger et al. [8]. We used the Shirley background and Gauss-Lorenzian line shape, GL(30), for Ni(OH)$_2$ and NiO and asymmetric line shape, LA(1.1,2.2,10), for metallic Ni.

To quantify the amount of Ni(II) and Ni^0 present in the samples, we used the spectral fitting parameters of Ni(OH)$_2$ and Ni^0. The corresponding fits can be seen in **Figure S21** and the calculated Ni(OH)$_2$ and Ni^0 quantification (in at.%) is shown in **Table S5**. Note that this quantification method bares an intrinsic error that is estimated 10 - 20 % for the samples before HER. For the XPS data after 1 h HER (activation-cycle), the error is estimated higher, as the data is more noise. For the data after the stability-cycle no adequate fitting was possible (see **Figure S21** after 17 h HER), and thus, the obtained values only provide qualitative information.
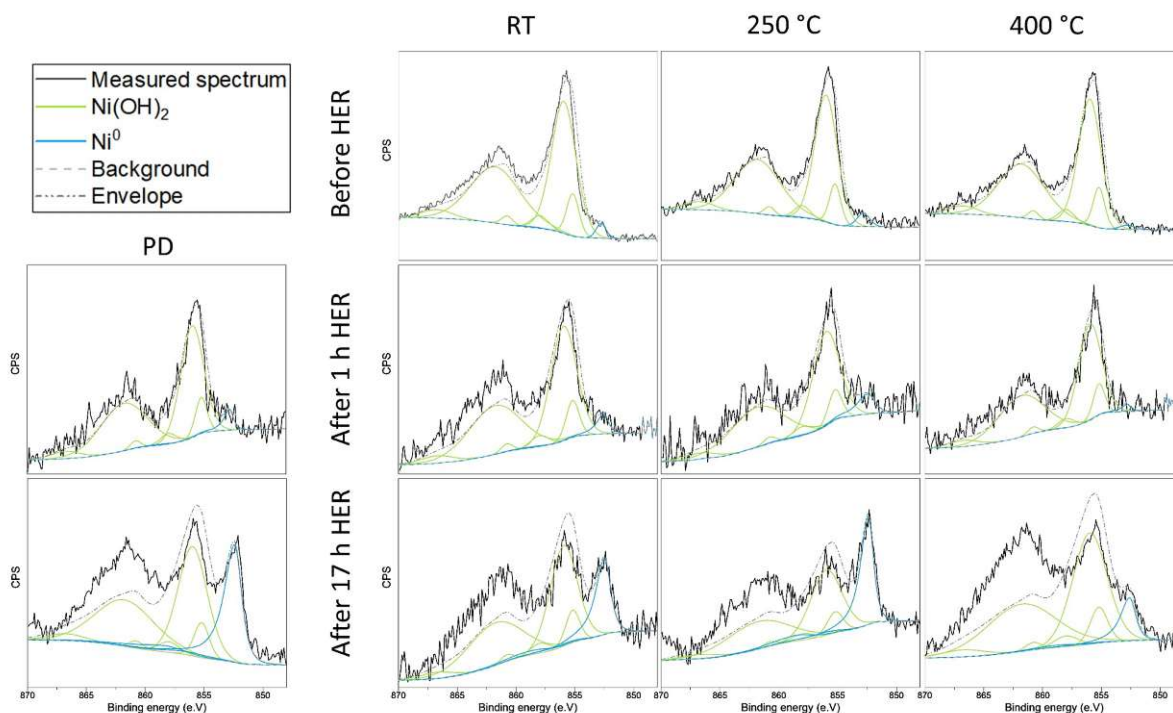
Figure S21. Spectral fits of the as-prepared Ni/TiO₂ samples (RT and 250 °C and 400 °C derived) and those after 1 h and 17 h of HER. The spectral fitting data were taken from Biesinger et. al [8] . We used the Shirley background and Gauss-Lorenzian line shape, GL(30), for Ni(OH)$_2$ and asymmetric line shape, LA(1.1,2.2,10), for metallic Ni.

WILEY-VCH

Table S5. Metallic Ni and Ni(II) quantification of the Ni/TiO$_2$ samples (RT and 250 °C and 400 °C derived) before HER and those after 1 h and 17 h of HER. The quantification was obtained from the spectral fitting data provided by Biesinger et. al [8] for the Ni(OH)$_2$ and Ni^0 fits. See **Figure S21** for the corresponding spectral fits. For the as-prepared samples (before HER), the error is estimated around 10-20 %; it is higher for the data after the activation-cycle as the data show more noise. The values shown for the samples after the stability-cycle is only qualitative, as no proper fit to the measured data was possible (see **Figure S21**).

	RT	250 °C	400 °C	PD
	at.%			
As-prepared				
Ni^0	17.0	26.7	13.7	-
Ni(II)	83.0	73.1	86.3	-
Activation-cycle				
Ni^0	38	52	19	38
Ni(II)	62	46	81	62
Stability-cycle				
Ni^0	77	85	57	83
Ni(II)	24	16	43	17

5. References

[1] Z. Lin, D. Han, S. Li, *J Therm Anal Calorim* **2012**, *107*, 471.

[2] J. V. Hoene, R. G. Charles, W. M. Hickam, *J. Phys. Chem.* **1958**, *62*, 1098.

[3] S. Yoda, Y. Takebayashi, K. Sue, T. Furuya, K. Otake, *The Journal of Supercritical Fluids* **2017**, *123*, 82.

[4] J. Schneider, D. W. Bahnemann, *J. Phys. Chem. Lett.* **2013**, *4*, 3479.

[5] V. Kumaravel, M. Imam, A. Badreldin, R. Chava, J. Do, M. Kang, A. Abdel-Wahab, *Catalysts* **2019**, *9*, 276.

[6] M. C. Biesinger, L. W. M. Lau, A. R. Gerson, R. S. C. Smart, *Phys. Chem. Chem. Phys.* **2012**, *14*, 2434.

[7] M. C. Biesinger, B. P. Payne, A. P. Grosvenor, L. W. M. Lau, A. R. Gerson, R. St. C. Smart, *Applied Surface Science* **2011**, *257*, 2717.

[8] M. C. Biesinger, B. P. Payne, L. W. M. Lau, A. Gerson, R. S. C. Smart, *Surface and Interface Analysis* **2009**, *41*, 324.

[9] J. S. Schubert, J. Popovic, G. M. Haselmann, S. P. Nandan, J. Wang, A. Giesriegl, A. S. Cherevan, D. Eder, *J. Mater. Chem. A* **2019**, DOI 10.1039/C9TA05637H.

4.3 Co-author Manuscripts

In my PhD thesis I further collaborated on different projects, in many of which my main contribution was the XPS data acquisition, evaluation, discussion and preparation of the corresponding manuscript parts. The full and updated list of my publications can be found in my GoogleScholar account (Jasmin S. Schubert).

In the moment of writing my thesis the list of my contributions is as follows:

1. Rabl, H.; Myakala, S. N.; Rath, J.; Fickl, B.; Schubert, J. S.; Apaydin, D. H. & Eder, D.; *Microwave-assisted synthesis of metal-organic chalcogenolate assemblies as electrocatalysts for syngas production*, Communications Chemistry, Nature Publishing Group, 2023, 6, 1-8.

2. Nandan, S. P.; Gumerova, N. I.; Schubert, J. S.; Saito, H.; Rompel, A.; Cherevan, A. & Eder, D.; *Immobilization of a [CoIIICoII(H2O)W11O39]7– Polyoxoanion for the Photocatalytic Oxygen Evolution Reaction*, ACS Materials Au, American Chemical Society, 2022, 2, 505-515.

3. Batool, S.; Nandan, S. P.; Myakala, S. N.; Rajagopal, A.; Schubert, J. S.; Ayala, P.; Naghdi, S.; Saito, H.; Bernardi, J.; Streb, C.; Cherevan, A. & Eder, D.; *Surface Anchoring and Active Sites of [Mo3S13]2– Clusters as Co-Catalysts for Photocatalytic Hydrogen Evolution*, ACS Catalysis, American Chemical Society, 2022, 12, 6641-6650.

4. Naghilou, A.; He, M.; Schubert, J. S.; Zhigilei, L. V. & Kautek, W.; *Femtosecond laser generation of microbumps and nanojets on single and bilayer Cu/Ag thin films* Physical Chemistry Chemical Physics, The Royal Society of Chemistry, 2019, 21, 11846-11860.

Conclusions and outlook

The focus of this thesis was to systematically compare different co-catalyst for their photocatalytic HER and OER capacity. The investigated metals were Ni, Mn, Co, Fe, and Cu that were attached on TiO_2. All photocatalyst were synthesized by impregnating TiO_2 with the corresponding metal salt ($Ni(acac)_2$, $Mn(acac)_2$, $Co(acac)_3$, $Fe(acac)_3$ and $Cu(ac)_2$) followed by calcination under air. Among these metals, only Ni and Cu showed enhanced HER performances – towards bare TiO_2 – while for the OER, Fe and Co showed co-catalytic effects, and Mn, a detrimental effect, as no O_2 was generated at all. Further investigation of the HER capacity of Ni and Cu revealed that calcination (from no-calcination up to 400 °C) of the photocatalysts had a detrimental effect on the overall HER performance. In both, Ni and Cu systems, the higher the calcination temperature was, the lower was the generated amount of H_2. A careful and extensive analysis of the photosystems – using a plethora of characterization methods – revealed that by increasing calcination temperature, Cu and Ni species got gradually stronger attached on TiO_2. These observations were followed by an extensive investigation to elucidate the structural and the oxidation state changes taking place upon calcination. For Cu, all samples revealed the same mixed oxidation state – Cu^0, Cu^+ and Cu^{2+} – with similar proportions of the three Cu species independent of the calcination protocol used. However, structural analyses showed that by increased temperature, Cu – in form of Cu^+ – diffuses into the TiO_2 lattice. This leads to a combination of effects, such as the addition of defects into the TiO_2 lattice that act as charge recombination centres, and the reduction of Cu concentration – i.e. catalytically active sites – available for the reactant on the TiO_2 surface. The analysis of the Ni-based photosystem, showed also a mixed oxidation state – Ni^0 and Ni^{2+} – independent of the sample preparation method. While for the Cu system, only the as-synthesised samples (i.e. before HER) were analysed, for the Ni system the samples were investigated before and after HER. This led to remarkable findings, as in literature – as well as in manuscript No.1 of this thesis – the HER performance is attributed to the presence of Ni^0, however, manuscript No.3 revealed that rather the mixed oxidation state of Ni^0 and Ni^{2+} is required[58,61–67] to promote HER effectively. Upon illumination, Ni acts a dynamic catalyst, where Ni^{2+} is gradually reduced by the TiO_2-CB electron to Ni^0, followed by the reduction of H^+ to H_2. To get regenerated and start the whole process again, Ni requires to get back to its original oxidation state ($Ni^0 \rightarrow Ni^{2+}$). However, when Ni is strongly attached to the support, it gets stabilized by the TiO_2 lattice, meaning the dynamic $Ni^{2+} \leftrightarrow Ni^0$ process is partially inhibited, leading to an ultimate decrease in the amount of H_2 to be generated. Hereby, this work highlights that post-synthetic calcination of a photocatalyst results in complex changes that can lead to a detrimental effect on the overall photocatalytic performance and that Ni and Cu as co-catalysts requires a dynamic redox shuttle to achieve superior HER performances. Thus, possible calcination side-effects, the right oxidation state ratio and the attachment strength of co-catalyst need to be considered in the design of these and similar photosystems.

This thesis, as any other scientific work, has left many open questions to fully understand the

systems under investigation. Hereby, I provide a small outlook for possible future investigations that could deliver a more in-depth understanding of the photosystems. Some of those open questions are: Cu oxidation state optimal for HER and the cumulative role of its different oxidation states (Cu^+, Cu^{2+} and Cu^0) during the photocatalytic process, as in the scientific community there is no consensus of the active Cu state for HER.[57,58,68–77] Furthermore, it is suggested to further clarify which is the right proportion of Ni^0 and Ni^{2+} required to achieve the highest HER performance and how is this optimal proportion dependent on the photocatalytic conditions. Useful methods would be in-situ experiments with electron paramagnetic resonance (EPR) – to determine the oxidation state transformation that takes place during HER for Ni and Cu – or the use of synchrotron sources, such as extended x-ray absorption fine structure spectroscopy (EXAFS), to determine the exact state and location of Ni and Cu, as well as the corresponding oxidation states. Other experiments that would further elucidate the nature of these systems could include reduction and oxidation experiments. That means, reducing all Cu and Ni to the metallic form (e.g. via mild H_2 reduction), or oxidizing them to the highest oxidation state (e.g. via controlled calcination), which ultimately would provide further hints about the optimal oxidation state and co-catalyst transformation mechanism. Additionally, this thesis demonstrated that the photosystems are very sensitive (the overall amount of generated H_2 and their long term HER profiles) to the choice of the anion and synthetic protocol such as the use of different solvents and atmospheres. In manuscript No. 2 we saw slight differences by using acetate or nitrate. In manuscript No. 3 we saw differences by using acetylacetonate or chloride, or by different synthesis parameters. Both sets of results leave an open question of what exact changes lead to the reduced/increased H_2 generation. Finally, the development of a more complex photosystem, such as that combining Ni and Cu co-catalysts in one photocatalyst, would further be interesting, as possibly the two types of metals have a synergistic effect with regard to their HER performance. On the other hand, the combination of Cu/Ni with Fe/Co would be of high interest, as this work has shown that these metals enable the HER and OER, respectively, thus possibly allowing to achieve overall water spiting photocatalysts.

Curriculum vitae

Personal Data

Date of Birth:	10.04.1988
LinkedIn:	www.linkedin.com/in/jasmin-s-schubert/
Google scholar:	scholar.google.at/citations?user=qiWZS8kAAAAJ&hl=en
ORCID:	0000-0002-1292-8485
E-mail:	jasmin.schubert2@gmail.com

Education

10.2018 – 12.2023	PhD candidate
	Vienna University of Technology, Vienna, Austria
10.2016 – 07.2018	Master of Science
	University of Vienna, Vienna, Austria
	Master thesis „*Synthesis and characterization of metal oxide clusters attached to TiO_2 nanoparticles for photocatalytic water splitting*"
10.2015 – 07.2016	Erasmus$^+$ Program
	University of Vienna, Austria
09.2011 – 07.2016	Bachelor in Chemistry
	Universitat Autónoma de Barcelona, Barcelona, Spain
	Bachelor Thesis „*Uranium extraction from aqueous solutions via ionic liquids*"

Awards and scholarships

Dec. 2019	ÖAW Otto-Vogl Award for my Master thesis
Jan. 2019	Merit scholarship (Leistungstipendium) from University of Vienna
Mar. 2017	Erwin Schrödinger Society for Nanosciences (ESG) Scholarship
Oct.2015 – Jul.2016	European Commission Erasmus$^+$ Scholarship

Internships

08.2016 – 03.2017	University of Vienna, Institute of physical chemistry
	Project: Characterization of laser-mater interaction
05.2015 – 08.2015	Ludwig Maximilian University
	Project: Organic synthesis of photo-switching molecules

Teachings

10.2018 – 10.2023	University assistant for Bachelor laboratory courses
	Vienna University of Technology
07.2018	Kinderuni - Workshop organizer
	Vienna University of Technology
10.2017 – 06.2018	Tutor for Bachelor laboratory courses
	Vienna University of Technology

Other contributions

06.2021 - 09.2021	FemChem Scientific Workshop 2021
	Organization and member of the abstract committee
10.2020 - 09.2022	FemChem
	Member of the Communication and information team

References

[1] IEA. The future of hydrogen - seizing today's opportunities. *Report prepared by the IEA for the G20, Japan*, june 2019. License: CC BY 4.0.

[2] Hui Song, Shunqin Luo, Hengming Huang, Bowen Deng, and Jinhua Ye. Solar-Driven Hydrogen Production: Recent Advances, Challenges, and Future Perspectives. *ACS Energy Letters*, 7(3):1043–1065, March 2022.

[3] Furat Dawood, Martin Anda, and G. M. Shafiullah. Hydrogen production for energy: An overview. *International Journal of Hydrogen Energy*, 45(7):3847–3869, February 2020.

[4] P. P. Edwards, V. L. Kuznetsov, W. I. F. David, and N. P. Brandon. Hydrogen and fuel cells: Towards a sustainable energy future. *Energy Policy*, 36(12):4356–4362, December 2008.

[5] Jan Willem Erisman, Mark A. Sutton, James Galloway, Zbigniew Klimont, and Wilfried Winiwarter. How a century of ammonia synthesis changed the world. *Nature Geoscience*, 1(10):636–639, October 2008.

[6] Andy Brown. Uses of hydrogen in industry. *The chemical Engineer*, July 2019.

[7] IEA. Global demand for pure hydrogen, 1975-2018, iea. 2019.

[8] Trade Ministry of Economy and Japan Industry. The strategic road map for hydrogen and fuel cells: Industry-academia-government action plan to realize a "hydrogen society". hydrogen and fuel cell stragegy council,. 2019.

[9] Nikkei Asia. Japan can win over investors by clarifying its hydrogen strategy, July 2023.

[10] Agata Godula-Jopek. *Hydrogen Production by Electrolysis*. Wiley-VCH Verlag GmbH & Co, 2015.

[11] Mazlan Abdul Hosseini, Seyed Ehsan Wahid. Hydrogen production from renewable and sustainable energy resources: Promising green energy carrier for clean development. *Renewable and Sustainable Energy Reviews*, 2016.

[12] Akira Fujishima and Kenichi Honda. Electrochemical Photolysis of Water at a Semiconductor Electrode. *Nature*, 238(5358):37–38, July 1972.

[13] Victor Gold, editor. *The IUPAC Compendium of Chemical Terminology: The Gold Book*. International Union of Pure and Applied Chemistry (IUPAC), Research Triangle Park, NC, 4 edition, 2019.

[14] Jacek K. Stolarczyk, Santanu Bhattacharyya, Lakshminarayana Polavarapu, and Jochen Feldmann. Challenges and Prospects in Solar Water Splitting and CO2 Reduction with Inorganic and Hybrid Nanostructures. *ACS Catalysis*, 8(4):3602–3635, April 2018.

141

[15] S. E. Braslavsky. Glossary of terms used in photochemistry, 3rd edition (IUPAC Recommendations 2006). *Pure and Applied Chemistry*, 79(3):293–465, January 2007.

[16] Frank E. Osterloh. Photocatalysis versus Photosynthesis: A Sensitivity Analysis of Devices for Solar Energy Conversion and Chemical Transformations. *ACS Energy Letters*, 2(2):445–453, February 2017.

[17] Kazuhiro Takanabe. Photocatalytic Water Splitting: Quantitative Approaches toward Photocatalyst by Design. *ACS Catalysis*, 7(11):8006–8022, November 2017.

[18] Blok K Bode H Frenz W Gather C Hanekamp G Imboden D Jahnke M Kost M Kurz R Nutzinger HG Ziesemer T Steger U, Achterberg W. The average global rate of photosynthesis is 130 tw. *Sustainable development and innovation in the energy sector*, 2005.

[19] Shasha Zhu and Dunwei Wang. Photocatalysis: Basic Principles, Diverse Forms of Implementations and Emerging Scientific Opportunities. *Advanced Energy Materials*, 7(23):1700841, 2017.

[20] Robert R. Crichton and Ricardo O. Louro. *Practical Approaches to Biological Inorganic Chemistry*. Elsevier, 2013.

[21] Anthony F. Collings and Christa Critchley. *Artificial Photosynthesis*. 2005.

[22] Jinhua Ye Gianluca Li Puma Jenny Schneider, Detlef Bahnemann and Dionysios D. Dionysiou. *Photocatalysis: Fundamentals and Perspectives*. The Royal Society of Chemistry, 2016.

[23] Jean-Luc Bredas. Mind the gap! *Materials Horizons*, 1(1):17–19, November 2013.

[24] Barkha Rani, Arpan Kumar Nayak, and Niroj Kumar Sahu. 1 - Fundamentals principle of photocatalysis. Micro and Nano Technologies, pages 1–22. Elsevier, January 2022.

[25] Junjie Chen. Homogeneous and heterogeneous catalysis:teachings of the thermal energy and power engineering course. *World Academy of Science, Engineering and Technology International Journal of Educational and Pedagogical Sciences*, 2014.

[26] Arabinda Baruah, Vandna Chaudhary, Ritu Malik, and Vijay K. Tomer. 17 - Nanotechnology Based Solutions for Wastewater Treatment. Micro and Nano Technologies, pages 337–368. Elsevier, January 2019.

[27] Akihiko Kudo and Yugo Miseki. Heterogeneous photocatalyst materials for water splittingw. *Chemical Society Reviews*, 2008.

[28] Min Liu, Xiaoqing Qiu, Masahiro Miyauchi, and Kazuhito Hashimoto. Cu(ii) oxide amorphous nanoclusters grafted ti3+ self-doped tio2: An efficient visible light photocatalyst. *Chemistry of Materials*, 2011.

[29] Kazuhiro Takanabe and Kazunari Domen. Toward Visible Light Response: Overall Water Splitting Using Heterogeneous Photocatalysts. 1(5-6):313–322, December 2011.

[30] Tsutomu Hirakawa and Prashant V. Kamat. Charge separation and catalytic activity of Ag@TiO2 core-shell composite clusters under UV-irradiation. *Journal of the American Chemical Society*, 127(11):3928–3934, March 2005.

[31] Wei-Kang Wang, Jie-Jie Chen, Wen-Wei Li, Dan-Ni Pei, Xing Zhang, and Han-Qing Yu. Synthesis of Pt-Loaded Self-Interspersed Anatase TiO2 with a Large Fraction of (001) Facets for Efficient Photocatalytic Nitrobenzene Degradation. *ACS Applied Materials & Interfaces*, 7(36):20349–20359, September 2015.

[32] E. Hussain, I. Majeed, M. Amtiaz Nadeem, A. Badshah, Yuxiang Chen, M. Arif Nadeem, and Rongchao Jin. Titania-Supported Palladium/Strontium Nanoparticles (Pd/Sr-NPs@P25) for Photocatalytic H2 Production from Water Splitting. *The Journal of Physical Chemistry C*, 120(31):17205–17213, August 2016.

[33] Savio J. A. Moniz, Stephen A. Shevlin, David James Martin, Zheng-Xiao Guo, and Junwang Tang. Visible-light driven heterojunction photocatalysts for water splitting – a critical review. *Energy & Environmental Science*, 8(3):731–759, March 2015.

[34] Jingrun Ran, Jun Zhang, Jiaguo Yu, Mietek Jaroniec, and Shi Zhang Qiao. Earth-abundant cocatalysts for semiconductor-based photocatalytic water splitting. *Chemical Society Reviews*, 43(22):7787–7812, October 2014.

[35] Roland Marschall. Semiconductor Composites: Strategies for Enhancing Charge Carrier Separation to Improve Photocatalytic Activity. *Advanced Functional Materials*, 24(17):2421–2440, 2014.

[36] Yi Zhong, Chundong Peng, Zetian He, Daimei Chen, Hailong Jia, Jinzhong Zhang, Hao Ding, and Xiangfeng Wu. Interface engineering of heterojunction photocatalysts based on 1D nanomaterials. *Catalysis Science & Technology*, 11(1):27–42, January 2021.

[37] Michael R. Nellist, Forrest A. L. Laskowski, Fuding Lin, Thomas J. Mills, and Shannon W. Boettcher. Semiconductor–Electrocatalyst Interfaces: Theory, Experiment, and Applications in Photoelectrochemical Water Splitting. *Accounts of Chemical Research*, 49(4):733–740, April 2016.

[38] Rakshit Ameta and Suresh C. Ameta. *Photocatalysis - Principles and application*. Taylor & Francis Group, 2017.

[39] Tongyao Liu, Liqi Bai, Na Tian, Jingang Liu, Yihe Zhang, and Hongwei Huang. Interfacial engineering in two-dimensional heterojunction photocatalysts. *International Journal of Hydrogen Energy*, 48(33):12257–12287, April 2023.

[40] Lin Che, Jialu Pan, Kexin Cai, Yanqing Cong, and Shi-Wen Lv. The construction of p-n heterojunction for enhancing photocatalytic performance in environmental application: A review. *Separation and Purification Technology*, 315:123708, June 2023.

[41] Dennis Y.C. Leung K. Sumathy Meng Ni, Michael K.H. Leung. A review and recent developments in photocatalytic water-splitting using tio2 for hydrogen production. *Renewable & sustainable energy reviews*, 2007.

[42] Alex Omo Ibhadon and Paul Fitzpatrick. Heterogeneous photocatalysis: Recent advances and applications. *Catalysts*, 2013.

[43] Mohammad Mansoob Khan. *Nanocomposites for Visible Light-induced Photocatalysis*. Springer, 2017.

[44] Jenny Schneider and Detlef W. Bahnemann. Undesired Role of Sacrificial Reagents in Photocatalysis. *The Journal of Physical Chemistry Letters*, 4(20):3479–3483, October 2013.

[45] Krishnamoorthy Sathiyan, Ronen Bar-Ziv, Vered Marks, Dan Meyerstein, and Tomer Zidki. The Role of Common Alcoholic Sacrificial Agents in Photocatalysis: Is It Always Trivial? *Chemistry – A European Journal*, 27(64):15936–15943, 2021.

[46] Jiaqi Zhao, Run Shi, Zhenhua Li, Chao Zhou, and Tierui Zhang. How to make use of methanol in green catalytic hydrogen production? *Nano Select*, 1(1):12–29, 2020.

[47] Greta M. Haselmann, Bettina Baumgartner, Jia Wang, Karin Wieland, Tushar Gupta, Christopher Herzig, Andreas Limbeck, Bernhard Lendl, and Dominik Eder. In Situ Pt Photodeposition and Methanol Photooxidation on Pt/TiO2: Pt-Loading-Dependent Photocatalytic Reaction Pathways Studied by Liquid-Phase Infrared Spectroscopy. *ACS Catalysis*, 10(5):2964–2977, March 2020.

[48] Felipe Guzman, Steven S. C. Chuang, and Cheng Yang. Role of Methanol Sacrificing Reagent in the Photocatalytic Evolution of Hydrogen. *Industrial & Engineering Chemistry Research*, 52(1):61–65, January 2013.

[49] James Highfield. Advances and Recent Trends in Heterogeneous Photo(Electro)-Catalysis for Solar Fuels and Chemicals. *Molecules*, 20(4):6739–6793, April 2015.

[50] Tahereh Jafari, Ehsan Moharreri, Alireza Shirazi Amin, Ran Miao, Wenqiao Song, and Steven L. Suib. Photocatalytic Water Splitting-The Untamed Dream: A Review of Recent Advances. *Molecules (Basel, Switzerland)*, 21(7):900, July 2016.

[51] Rayhan Hossain, Md Aslam Uddin, and M. Arif Khan. Mechanistic Understanding in Manipulating Energetics of TiO2 for Photocatalysis. *The Journal of Physical Chemistry C*, 127(23):10897–10912, June 2023.

[52] Alireza Shirazi Amin Ran Miao Wenqiao Song Tahereh Jafari, Ehsan Moharreri and Steven L. Suib. Photocatalytic water splitting—the untamed dream: A review of recent advances. *Molecules*, 2016.

[53] N. Serpone and A. V. Emeline. Semiconductor Photocatalysis — Past, Present, and Future Outlook. *The Journal of Physical Chemistry Letters*, 3(5):673–677, March 2012.

[54] Qi-Jun Liu, Zheng Ran, Fu-Sheng Liu, and Zheng-Tang Liu. Phase transitions and mechanical stability of TiO2 polymorphs under high pressure. *Journal of Alloys and Compounds*, 631:192–201, May 2015.

[55] Dennis Y. C. Leung, Xianliang Fu, Cuifang Wang, Meng Ni, Michael K. H. Leung, Xuxu Wang, and Xianzhi Fu. Hydrogen Production over Titania-Based Photocatalysts. *ChemSusChem*, 3(6):681–694, 2010.

[56] Seyedsina Hejazi, Manuela S. Killian, Anca Mazare, and Shiva Mohajernia. Single-Atom-Based Catalysts for Photocatalytic Water Splitting on TiO2 Nanostructures. *Catalysts*, 12(8):905, August 2022.

[57] Vatika Soni, Pardeep Singh, Aftab Aslam Parwaz Khan, Arachana Singh, Ashok Kumar Nadda, Chaudhery Mustansar Hussain, Quyet Van Le, Stanislav Rizevsky, Van-Huy Nguyen, and Pankaj Raizada. Photocatalytic transition-metal-oxides-based p–n heterojunction materials: synthesis, sustainable energy and environmental applications, and perspectives. *Journal of Nanostructure in Chemistry*, 13(2):129–166, April 2023.

[58] Solmaz Feizpoor, Shima Rahim Pouran, and Aziz Habibi-Yangjeh. Recent progress on photocatalytic evolution of hydrogen gas over TiO2-x-based emerging nanostructures. *Materials Science in Semiconductor Processing*, 162:107444, August 2023.

[59] Nguyen Hoang Ly, Yasser Vasseghian, and Sang-Woo Joo. Plasmonic photocatalysts for enhanced solar hydrogen production: A comprehensive review. *Fuel*, 344:128087, July 2023.

[60] Daisuke Fujita Elisabeth Mansfield, Debra L. Kaiser and Marcel Van de Voorde. *Metrology and Standardization for Nanotechnology*.

[61] Qin-Dong Huang Mei-Ting Fan You-Zhu Yuan Timothy Thatt-Yang Tan Dai-Wei Liao Jing-Dong Lin, Shi Yan. Tio2 promoted by two different non-noble metal cocatalysts for enhanced photocatalytic h2 evolution. *Applied Surface Science*, 2014.

[62] Yanyu Zhang-Hongxing Jia Zijun Sun Pingwu Du Zhiping Yan, Xingxing Yu. Enhanced visible light-driven hydrogen production from water by a noble-metal-free system containing organic dye-sensitized titanium dioxide loaded with nickel hydroxide as the cocatalyst. *Applied Catalysis B: Environmental*, 2014.

[63] Athira Krishnan, Akhila Ajith, Abhirami V Krishnan, Raina Elsa Saji, S. Syamli, and Sheik Muhammadhu Aboobakar Shibli. Ni-based Electro/Photo-Catalysts in HER – A Review. *Surfaces and Interfaces*, 36:102619, February 2023.

[64] Wan-Ting Chen, Andrew Chan, Dongxiao Sun-Waterhouse, Toshihiro Moriga, Hicham Idriss, and Geoffrey I. N. Waterhouse. Ni/TiO2: A promising low-cost photocatalytic system for solar H2 production from ethanol–water mixtures. *Journal of Catalysis*, 326:43–53, June 2015.

[65] Arindam Indra, Prashanth W. Menezes, Kamalakannan Kailasam, Dirk Hollmann, Marc Schröder, Arne Thomas, Angelika Brückner, and Matthias Driess. Nickel as a co-catalyst for photocatalytic hydrogen evolution on graphitic-carbon nitride (sg-CN): what is the nature of the active species? *Chemical Communications*, 52(1):104–107, December 2015.

[66] Jiaguo Yu, Yang Hai, and Mietek Jaroniec. Photocatalytic hydrogen production over cuo-modified titania. *Journal of Colloid and Interface Science*, 2011.

[67] Shangchun Lv, Mengxi Pei, Yuxiang Liu, Zhichun Si, Xiaodong Wu, Rui Ran, Duan Weng, and Feiyu Kang. An isolation strategy to anchor atomic Ni or Co cocatalysts on TiO2(A) for photocatalytic hydrogen production. *Nano Research*, 15(7):5848–5856, July 2022.

[68] Tushar Janardan Pawar, David Contreras López, José Luis Olivares Romero, and Javier Vallejo Montesinos. Surface modification of titanium dioxide. *Journal of Materials Science*, 58(16):6887–6930, April 2023.

[69] Yumin Zhang, Jianhong Zhao, Hui Wang, Bin Xiao, Wen Zhang, Xinbo Zhao, Tianping Lv, Madasamy Thangamuthu, Jin Zhang, Yan Guo, Jiani Ma, Lina Lin, Junwang Tang, Rong Huang, and Qingju Liu. Single-atom Cu anchored catalysts for photocatalytic renewable H2 production with a quantum efficiency of 56%. *Nature Communications*, 13(1):58, January 2022.

[70] Byoung-Hoon Lee, Sunghak Park, Minho Kim, Arun K. Sinha, Seong Chan Lee, Euiyeon Jung, Woo Je Chang, Kug-Seung Lee, Jeong Hyun Kim, Sung-Pyo Cho, Hyungjun Kim, Ki Tae Nam, and Taeghwan Hyeon. Reversible and cooperative photoactivation of single-atom Cu/TiO2 photocatalysts. *Nature Materials*, 18(6):620–626, June 2019.

[71] Yuqi Wu, Gongxuan Lu, and Shuben Li. The Role of Cu(I) Species for Photocatalytic Hydrogen Generation Over CuOx/TiO2. *Catalysis Letters*, 133(1):97–105, November 2009.

[72] Huilin Hou, Minghui Shang, Fengmei Gao, Lin Wang, Qiao Liu, Jinju Zheng, Zuobao Yang, and Weiyou Yang. Highly Efficient Photocatalytic Hydrogen Evolution in Ternary Hybrid TiO2/CuO/Cu Thoroughly Mesoporous Nanofibers. *ACS Applied Materials & Interfaces*, 8(31):20128–20137, August 2016.

[73] Qianqian Hu, Jiquan Huang, Guojing Li, Yabin Jiang, Hai Lan, Wang Guo, and Yongge Cao. Origin of the improved photocatalytic activity of Cu incorporated TiO2 for hydrogen generation from water. *Applied Surface Science*, 382:170–177, September 2016.

[74] Jiaxin Zhu, Jinyan Xiong, Gang Cheng, Weijie Li, and Shixue Dou. Promoting solar-to-hydrogen evolution on Schottky interface with mesoporous TiO2-Cu hybrid nanostructures. *Journal of Colloid and Interface Science*, 545:116–127, June 2019.

[75] Lucy M. Ombaka, Mariano Curti, James D. McGettrick, Matthew L. Davies, and Detlef W. Bahnemann. Nitrogen/Carbon-Coated Zero-Valent Copper as Highly Efficient Co-catalysts for TiO2 Applied in Photocatalytic and Photoelectrocatalytic Hydrogen Production. *ACS Applied Materials & Interfaces*, 12(27):30365–30380, July 2020.

[76] Gang Cheng, Mengmeng Zhang, Chao Han, Ying Liang, and Kai Zhao. Achieving solar-to-hydrogen evolution promotion using TiO2 nanoparticles and an unanchored Cu co-catalyst. *Materials Research Bulletin*, 129:110891, September 2020.

[77] Ya-Jie Feng, Yang Wang, Kai-Wen Wang, Jiang-Ping Ma, You-Yu Duan, Jie Liu, Xu Lu, Bin Zhang, Guo-Yu Wang, and Xiao-Yuan Zhou. Ultra-fine Cu clusters decorated hydrangea-like titanium dioxide for photocatalytic hydrogen production. *Rare Metals*, 41(2):385–395, February 2022.

[78] Mahmoud R. Saleh, Safinaz M. Thabet, Reem A. El-Gendy, Moushira Saleh, and Haitham M. El-Bery. MIL-53 (Fe) for constructing hydrogenated Fe3O4@C@TiO2 double core-shell nanocrystals as superior bifunctional photocatalyst. *Journal of Photochemistry and Photobiology A: Chemistry*, 432:114125, November 2022.

[79] Bingquan Xia, Bowen He, Jianjun Zhang, Laiquan Li, Yanzhao Zhang, Jiaguo Yu, Jingrun Ran, and Shi-Zhang Qiao. TiO2/FePS3 S-Scheme Heterojunction for Greatly Raised Photocatalytic Hydrogen Evolution. *Advanced Energy Materials*, 12(46):2201449, 2022.

[80] Sarika Sasidharan, Sumi Vijayakumari Sasidharan Nair, Abhilash Sudhakaran, and Rijith Sreenivasan. Insight into the Fabrication and Characterization of Novel Heterojunctions of Fe2O3 and V2O5 with TiO2 and Graphene Oxide for Enhanced Photocatalytic Hydrogen Evolution: A Comparison Study. *Industrial & Engineering Chemistry Research*, 61(7):2714–2733, February 2022.

[81] Ajit Sharma, Doan Van Thuan, Thanh-Dong Pham, Mai Hung Thanh Tung, Nguyen Thi Thanh Truc, and Dai-Viet N. Vo. Advanced Surface of Fibrous Activated Carbon Immobilized with FeO/TiO2 for Photocatalytic Evolution of Hydrogen under Visible Light. *Chemical Engineering & Technology*, 43(4):752–761, 2020.

References

[82] Nishijima Hiroaki-Yamamoto Hironori Fujishima Musashi Okuoka Shin ichi Hattori Takanori Sumida Yasutaka Kobayashi Hisayoshi Tada Hiroaki, Jin Qiliang. Titanium(iv) dioxide surface modified with iron oxide as a visible light photocatalyst. *Angewandte Chemie International Edition*, 2011.

[83] Jingjing Si, Shuying Xiao, Yu Wang, Lingbin Zhu, Xiaohong Xia, Zhongbing Huang, and Yun Gao. Sub-nanometer Co3O4 clusters anchored on TiO2(B) nano-sheets: Pt replaceable Co-catalysts for H2 evolution. *Nanoscale*, 10(5):2596–2602, February 2018.

[84] Zhanfen Chen, Jiaqi Pan, Jie Mei, Qi Yu, Panhong Wang, Peipei Wang, Jingjing Wang, Changsheng Song, Yingying Zheng, and Chaorong Li. Ternary Co3O4/CdS/SrTiO3 core-shell pn junctions toward enhanced photocatalytic hydrogen production activity. *Journal of Environmental Chemical Engineering*, 9(1):104895, February 2021.

[85] Xin Wu, Shouwei Zuo, Mei Qiu, Yang Li, Yongfan Zhang, Pengfei An, Jing Zhang, Huabin Zhang, and Jian Zhang. Atomically defined Co on two-dimensional TiO2 nanosheet for photocatalytic hydrogen evolution. *Chemical Engineering Journal*, 420:127681, September 2021.

[86] Hui Zhang, Weimin Wang, Huanxin Zhao, Lixia Zhao, Li-Yong Gan, and Liang-Hong Guo. Facet-Dependent Interfacial Charge Transfer in Fe(III)-Grafted TiO2 Nanostructures Activated by Visible Light. *ACS Catalysis*, 8(10):9399–9407, October 2018.

[87] Qian Wang and Kazunari Domen. Particulate Photocatalysts for Light-Driven Water Splitting: Mechanisms, Challenges, and Design Strategies. *Chemical Reviews*, 120(2):919–985, January 2020.

[88] Lichen Liu, Zeyang Ji, Weixin Zou, Xianrui Gu, Yu Deng, Fei Gao, Changjin Tang, and Lin Dong. In Situ Loading Transition Metal Oxide Clusters on TiO2 Nanosheets As Co-catalysts for Exceptional High Photoactivity. *ACS Catalysis*, 3(9):2052–2061, September 2013.

[89] Ang Li, Tuo Wang, Xiaoxia Chang, Weiting Cai, Peng Zhang, Jijie Zhang, and Jinlong Gong. Spatial separation of oxidation and reduction co-catalysts for efficient charge separation: Pt@tio2@mnox hollow spheres for photocatalytic reactions. *Chem. Sci.*, 2016.

[90] Pyroscience GmbH. *ttps://www.pyroscience.com (accessed 2023-04-04)*.

[91] Paul Van Der Heide. *X-RAY PHOTOELECTRON SPECTROSCOPY-An Introduction to Principles and Practices*. 2012.

[92] Paul Gabbott. *Principles and Applications of Thermal Analysis*. Blackwell Publishing, 2008.

[93] Barbara H.Stuart. *Infrared Spectroscopy: Fundamentals and Applications*. 2004.

[94] Kazuo Nakamoto John R. Ferraro and Chris W. Brown. *Introductory Raman Spectroscopy*. 2003.

[95] Philippe Colomban and Aneta Slodczyk. Raman intensity: An important tool in the study of nanomaterials and nanostructures. *Acta Physica Polonica A*, 116:7–12, 2009.

[96] Lawrence P. Bevy. *Focus on Catalysis Research*. Nova, 2006.

[97] John Humphreys Peter J. Goodhew and Richard Beanland. *ELECTRON MICROSCOPY AND ANALYSIS*. 2001.

[98] Jasmin S. Schubert, Janko Popovic, Greta M. Haselmann, Sreejith P. Nandan, Jia Wang, Ariane Giesriegl, Alexey S. Cherevan, and Dominik Eder. Immobilization of Co, Mn, Ni and Fe oxide co-catalysts on TiO2 for photocatalytic water splitting reactions. *Journal of Materials Chemistry A*, 7(31):18568–18579, August 2019.

[99] Jasmin S. Schubert, Leila Kalantari, Andreas Lechner, Ariane Giesriegl, Sreejith P. Nandan, Pablo Alaya, Shun Kashiwaya, Markus Sauer, Annette Foelske, Johanna Rosen, Peter Blaha, Alexey Cherevan, and Dominik Eder. Elucidating the formation and active state of Cu co-catalysts for photocatalytic hydrogen evolution. *Journal of Materials Chemistry A*, 9(38):21958–21971, October 2021.

[100] *Jasmin S. Schubert, Eva Doloszeski, Pablo Ayala, Stephen Nagaraju Myakala, Jakob Rath, Bernhard Fickl, Ariane Giesriegl, Dogukan H. Apaydin, Bernhard C. Bayer, Shun Kashiwaya, Alexey Cherevan, Dominik Eder. Nature of the active Ni state for photocatalytic hydrogen generation. Currently under 2on revision in Advanced Materials Interfaces, an Open Access journal that publishes under a CC BY-Creative Commons license.*